1-1-2015

# Noncovalent Interactions Between Alkali Metal Cation And Aza/thia-Crown Macrocycles: Mass Spectrometric Techniques And Theoretical Studies

Calvin A. Austin
*Wayne State University,*

## Recommended Citation

Austin, Calvin A., "Noncovalent Interactions Between Alkali Metal Cation And Aza/thia-Crown Macrocycles: Mass Spectrometric Techniques And Theoretical Studies" (2015). *Wayne State University Dissertations.* Paper 1304.

# NONCOVALENT INTERACTIONS BETWEEN ALKALI METAL CATION AND AZA/THIA-CROWN MACROCYCLES: MASS SPECTROMETRIC TECHNIQUES AND THEORETICAL STUDIES

by

**CALVIN A. AUSTIN**

**DISSERTATION**

Submitted to the Graduate School

of Wayne State University,

Detroit, Michigan

in partial fulfillment of the requirements

for the degree of

**DOCTOR OF PHILOSOPHY**

2015

MAJOR: CHEMISTRY (Analytical)

Approved By:

______________________________

Advisor/Date

______________________________

______________________________

______________________________

# ACKNOWLDEGEMENTS

I would like to thank the department of Chemistry, Wayne State University (WSU) for admitting me into the graduate program. I would also like thank the Rodgers Research group and Trimpin Research group; I have truly grown thru the experiences gain in the groups. I believe the skills gained and experience will play an important role in my future career. I would also like to thank my committee members for serving on my committee, providing support, and for their time. I also very grateful to other faculty and staff members in the chemistry department, they have truly made me feel accepted as part of the department. I will like to thank RanRan Wu, Jackie Baldyga, Nestor Ocampo, and Brian Newman, their support and advice have proven to be invaluable. The WSU Chemistry Dept has treated me as family and I am truly grateful. Without the strong supporting environment, I don't believe I could have completed my Ph.D. I will also like to thank Peter Norris, he always been there to remind me that I can complete the Ph.D. Lastly I want to acknowledge my Aunt Peggy Austin, she has been like a mother to me during my Ph.D. thesis. I was able maintain my weight and sanity through the home-cook meals and emotional support provided.

# TABLE OF CONTENTS

**CHAPTER 1 – INTRODUCTION**

**CHAPTER 2 – EXPERIMENTAL AND THEORETICAL SECTION**

**CHAPTER 3 – Alkali Metal Cation – Cyclen: Effects of Alkali Metal Cation Size on the Structure and Binding Energies**

**CHAPTER 4 – Infrared Multiple Photon Dissociation Action Spectroscopy of Alkali Metal Cation – Cyclen Complexes: Effects of Alkali Metal Cation Size on Gas-Phase Conformation**

**CHAPTER 5 – Alkali Metal Cation – Hexacyclen: Effects of Alkali Metal Cation Size on the Structure and Binding Energies**

**CHAPTER 6 – Alkali Metal Cation – Diaza-18-Crown-6: Effects of Alkali Metal Cation Size on the Structure and Binding Energies**

**CHAPTER 7 – Alkali Metal Cation – Hexathia-18-Crown-6: Effects of Alkali Metal Cation Size on the Structure and Binding Energies**

**CHAPTER 8 – CONCLUSTIONS AND FUTURE WORK**

LIST OF TABLES

LIST OF FIGURES

# CHAPTER 1

# INTRODUCTION

## 1.1. Macrocyclic Ligands

Since the pioneering work of the 1987 Nobel Prize Winners, Charles J. Pedersen, Donald J. Cram, and Jeanne-Marie Lehn, macrocyclic ligands have been extensively investigated and employed for a wide variety of molecular recognition applications as a result of their ability to strongly and selectively bind guest species including: metal and organic cations, anions, and neutral molecules [1]. Macrocyclic ligands are defined as molecules consisting of three or more donor atoms (O, N, S) in a ring at least nine atoms long [1]. Natural macrocycles are involved in several fundamental biological processes such as the mechanism of photosynthesis and the transport of oxygen in mammalian respiratory systems. Natural macrocycles were investigated extensively for their unique properties, such as enhanced kinetic and thermodynamic stabilities in relation to its binding to various guest species.

The vast majority of studies of macrocyclic ligands have been aimed at elucidation of the fundamental aspects of molecular recognition and self-assembly so as to determine the biological principles that control their behavior [1]. The biological and chemical insight gained from these studies has then been employed for the design and synthesis of intelligent artificial systems [2]. The molecular recognition between a host macrocycle and guest can be tuned by varying the size, nature, and electronic properties of both the host and guest species, many applications based on these complexes have already been realized [2–10]. In addition, there is enormous potential for new applications of macrocyclic complexes in many diverse fields including: bio- and nanotechnology, catalysis, chemical synthesis, environmental cleanup, molecular electronics and photonics, and medicine [11–20].

The vast majority of macrocyclic studies have been carried out in solution; but there is a growing emphasis on the use of mass spectrometry techniques for the study of molecular recognition because of it speed, sensitivity, and selectivity. In particular, mass spectrometry investigations are carried out in the gas phase and thus enable investigation of the fundamental intrinsic behavior in the absence of complicating solvent interactions. An understanding of intrinsic properties will contribute to the development of better models to understand molecular recognition and related processes.

### 1.1.1. 1,4,7,10-tetra-azacyclododecane (ta42C4) and 1,4,7,10,13,16-hexaazacyclooctadecane (ha18C6)

Cyclen (1,4,7,10-tetraazacyclododecane, ta12C4) and Hexacyclen (1,4,7,10,13,16-hexaazacyclooctadecane, ha18C6), the aza analogues of 12-crown-4 (1,4,7,10-tetraoxacyclodecane, 12C4) and 18-crown-6 (1,4,7,10,13,16-hexaoxacyclooctadecane, 18C6) have been extensively used in many applications. Similar to the crown ethers [1], aza-crown ethers are capable of selectively binding cations via noncovalent metal-ligand interactions or hydrogen bond interactions [8,21]. Crown ethers have been more extensively used as compared to the aza-analogues primarily because they are less expensive to make. In spite of their cost, aza-crown ethers find uses in various applications because they are generally more selective in its binding due to its ability to bind various guest species and act as a proton acceptor and donor. Transition and heavy metal cations tend to form stable complexes with aza-crown ethers, whereas the crown ethers preferentially bind alkali and alkaline earth metal cations [1].

Cyclen is used as a building block in the synthesis of magnetic resonance imaging (MRI) contrast agents [22]. Cyclen derivatives have also been used in medicinal applications including, drug delivery and chelators suitable for diagnosis and tumor therapy [5,23]. Cyclen in various derivatized forms has been used in many separations and molecular recognition applications [24,25]. Cyclen has also been used as a model system to investigate the synthesis of new materials related to nonlinear optical (NLO) properties [26]. All of these applications make use of functionalized cyclen, such that very limited thermodynamic information is available for the neutral cyclen ligand and its complexes to alkali metal cations in the gas phase.

Hexacyclen is a hexadentate macrocycle that is able to completely encapsulate the alkali metal cation, when compared to cyclen [8,27]. For most transition metal cations, ha18C6 forms a 1:1 metal-ligand complex [28–29, 30, 31, 32, 33], but in some cases a 2:1 complex is formed [34–35]. Hexacyclen also exhibits greater specificity due to its ability to act as a proton acceptor or donor, in contrast to 18C6. Protonated hexacyclen has been used to bind various organic and inorganic anions at varying pH [6, 36–44]. In addition, it has been shown to be a catalyst of ATP-hydrolysis and to be capable of acting as an enzyme mimic for phosphoryl transfer reactions [17,18,45]. Upon functionalization of the amine donor atoms of hexacyclen, binding interactions with amino acids, peptides, and dopamine have been observed [19,46]. Hexacyclen has also been functionalized with hexaacetic acid and has been utilized in layer-by-layer assemblies for water desalination [20,47]. To date, very little gas-phase thermochemical and spectroscopic information has been reported for hexacyclen and its alkali metal cations complexes.

### 1.1.2. 1,4,10,13-tetraoxa-7,16-diazacyclooctadecane (da18C6)

Diaza-18-crown-6 (1,4,10,13-tetraoxa-7,16-diazacyclooctadecane (da18C6)) is analogous to 18-crown-6 (18C6), except that nitrogen donor atoms have replaced two oxygen donor atoms. The properties attributed to the presence of two types of donor atoms symmetrically placed in the macrocycle have been investigated using solution phase methods [48]. The da18C6 ligand exhibits binding to the alkali and alkaline earth metal cations as well as several transitions metal cations, such as $Cu^+$ and $Ag^+$ in methanol and acetonitrile solutions [48–50]. The stability of metal cation–da18C6 complexes decreases in aqueous solution due to the competition between the metal cation binding to da18C6 vs. water molecules, primarily a result of the nitrogen donor atoms ability to act as strong proton acceptors. Diaza-18-crown-6 has been functionalized with various groups to investigate its fluorescence behavior [51], the modulation of its two-photon absorption cross-section by metal cations [52], as a ratiometric probe for the selective time-gated luminescence detection of potassium in water [53], and specific membrane transport of $Ag^+$ and $Cu^+$ ions through a supported membrane [54].

### 1.1.3. 1,4,7,10,13,16-hexathiacyclooctadecane (ht18C6)

Hexathia 18-crown-6 (1,4,7,10,13,16-hexathiacyclooctadecane, ht18C6) is the sulfur analogue of 18-crown-6 (1,4,7,10,13,16-hexaoxacyclooctadecane, 18C6). Similar to hexacyclen, hexathia 18-crown-6 form stable 1:1 complexes with the transitions metal cations [1] but it differs in that it is generally selective for soft metal cations such as $Ag^+$, $Hg^{2+}$, $Cu^+$, and $Pd^{2+}$ [55,56]. The fundamental processes that govern the complexation of the metal cations have been investigated [56–61]. The facilitated transfer of heavy metals ion across two immiscible electrolyte solutions have also been investigated using ht18C6 [62,63]. There has been considerable interest in hexathia 18-crown-6 for the removal of heavy metal cations such as $Ag^+$, $Hg^{2+}$, $Au^{3+}$, and $Au^+$ [64–68]. In addition, hexathia 18-crown-6 has been used to model systems for the blue copper protein [57,69,70,] and vitamins [71].

## 1.2. Alkali Metal Cations

The alkali metals are a group in the periodic table characterized by having one electron in the outermost s-oribital. Alkali metals are interesting from a practical point-of-view. The alkali metal cations ($Na^+$, $K^+$, $Rb^+$, and $Cs^+$) have many applications. $Na^+$ is used as light source [72,73], whereas Na metal is used as a reducing agent of transitions metals [74]. $Na^+$ and $K^+$ are both important as they have major biological roles relative to nerve and heart function in animals [75,76]. $Na^+$ and $K^+$ control the osmotic pressure of cells; neutralize the negative charges of intracellular anions and transferring ions across bio-membranes. $Rb^+$ and $Cs^+$ don't have any direct biological roles in living systems and both can be toxic [77,78]. In the case of $Cs^+$, the metal cation will readily interfere with $K^+$ in animal cell [77,78]. $Rb^+$ and $Cs^+$ do have applications in living systems, with $Rb^+$ having been shown to stimulate metabolism [79] and $Cs^+$ has been investigated as a therapeutic cancer agent [80]. $Rb^+$ and $Cs^+$ are also used in atomic clocks [81], with the seconds being defined in reference to the Cesium 133 atom [82].

### 1.3. Noncovalent Metal Ligand Interactions

Noncovalent interactions play major roles in modern chemistry including; condensation and solvation, organization and stabilization of organometallic compounds, folding of proteins, specific recognition of substrates, and the transport of ions and molecules. Nonconvalent interaction does not involve the sharing of an electron as with covalent interactions, or the electrons stayed paired in the reactants and products, and no change is observed in the type of chemical bonding in the products and reactants [83]. Covalent interactions are generally stronger than nonconvalent interaction and are the dominant factors that hold molecules together in specific geometries. Although weak compared to covalent interactions, noncovalent interactions contribute to the ability of molecules to undergo changes in conformation, which provides specific conditions for substances that bind and react with each other. The different types of noncovalent interactions include hydrogen bonding [84–86], ionic interactions [87,88], Van der Waals interactions [89], cation-π [90–93], and hydrophobic interactions [89].

Noncovalent metal-ligand interactions are of the ionic type. For the macrocycle discussed previously, it has been shown that oxygen donor atoms bind the alkali metal cation, where the nitrogen donor atoms bind the transition metal cations [1]. The alkali metals are grouped as hard metal cations, which have a high tendency to form noncovalent bonds. Soft metal cations, such as the transitions metal cations, have a higher tendency to form covalent bonds. Noncovalent interactions are important in molecular recognition; the macrocycles and their interactions with metals can be used to understand molecular recognition [94].

## 1.4. Importance of Model System

Model systems are important because they allow for a focus on one particular aspect of a biological structure, complex, or pathway. Model systems allow for the separation of factors that contribute to stability and reactivity. For example, macrocycles and their metal complexes have been extensively studied in solution, where separating out intrinsic and extrinsic binding behavior can be difficult [8–10]. The size of the metal cation and the cavity size of the macrocyclic ligand are two principle components that contribute to observed selectivity. In some cases, as with the crown ethers, size of the metal cation and size of the macrocycle cavity does not explain observed selectivity [95]. Armentrout and co-workers investigated alkali metal cation interactions with several crown ethers including 1,4,7,10-tetraoxaclododecane (12-crown-4 or 12C4), 1,4,7,10,13-pentaoxacyclododecane (15-crown-5 or 15C5), and 1,4,7,10,13,16-hexaoxacyclododecane (18-crown-6 or 18C6) using GIBMS techniques, with complementary electronic structure calculations performed by Feller and co-workers [96–102]. In general, good agreement between the measured and calculated binding energies was found. However, interactions between $Rb^+$ and $Cs^+$ with 12C4 and 15C5 appeared to be underestimated in the experiments. Theoretical analysis of these systems suggested that excited conformations may have been accessed in the experiments, but this was never proven. Recently in collaboration with Armentrout, the alkali metal cation binding to 12C4 and 15C5 was revisited and showed that ground-state species could be accessed using an alternative ionization technique, electrospray ionization (ESI), such that accurate binding energies for these systems were able to be determined [103,104]. From these studies, observed selectivity could be better understood due to the complementary gas phase data.

## 1.5. Motivation and Systems Investigated

The focus of my Ph.D. studies has been on the determination of accurate structural and thermochemical information regarding the binding between host macrocyclic ligands and metal and organic cations to provide detailed insight into the factors that control the selectivity of the complexation process. These studies involve both experimental and theoretical investigations of the structures of these complexes and their fragmentation behavior. Using energy-resolved collision-induced dissociation (CID) techniques carried out in a guided ion beam tandem mass spectrometer (GIBMS) and theoretical electronic structure calculations, we are able to characterize the various binding geometries available to cation-macrocycle complexes and their relative stabilities, as well as to accurately determine their absolute binding affinities. In addition, using complementary infrared multiple photon dissociation (IRMPD) action spectroscopy experiments, supported by complementary theoretical electronic structure calculations, to characterize the IR spectra of the cation-macrocycle complexes and definitively determine the structures of the complexes accessed under our experimental conditions. Very little gas-phase thermochemical and spectroscopic information has been reported to date, we have thus far focused on systematic studies of the interactions between relatively simple macrocycles and alkali metal and organic cations.

### 1.5.1. Alkali Metal Cation Binding Affinities of ta12C4, ha18C6, da18C6, ht18C6

In this thesis, the noncovalent interactions between alkali metal cations ($Na^+$, $K^+$, $Rb^+$, and $Cs^+$) and ta12C4 and ha18C6, the nitrogen azacrown ether analogues of 12-crown-4 and 18-crown-6, ht18C6, the sulfur thiacrown ether analogues of 18-crown-6, and the mixed donor atom ligand da18C6 are investigated. Energy-resolved collision-induced dissociation (CID) techniques were used in conjunction with theoretical electronic structure calculations to characterize the structures, binding interactions, and stability of the $M^+$(macrocycle) complexes where the macrocycle is ta12C4, ha18C6, ht18C6, or da18C6. Guided ion beam tandem mass spectrometry techniques (GIBMS) were used to characterize the energy dependence of the CID of the $M^+$(macrocycle) complexes, which allowed the bond dissociation energies (BDEs) of the complexes to be determined. Density functional theory calculations at the B3LYP/6-31+G*_HW and def2/TZVPPD levels of theory were used to determine the structures of all the neutrals azacrown ethers and the $M^+$(macrocycle) complexes. Theoretical BDEs are determined from single point energy calculations at the B3LYP and MP2 (full) levels of theory using the B3LYP/6-31+G*_HW and def2/TZVPPD optimized geometries.

### 1.5.2. IRMPD Action Spectroscopy of Alkali Metal Cation – ta12C4

The gas phase structures of alkali metal cationized complexes of cyclen (1,4,7,10-tetra-azacyclododecane) were examined via infrared multiple photon dissociation (IRMPD) action spectroscopy and theoretical electronic structure calculations. Complexes involving four of the alkali metal cations, $Na^+$, $K^+$, $Rb^+$, and $Cs^+$, are examined. The photodissociation experiments were carried out in a 4.7 T Fourier transform ion cyclotron resonance mass spectrometer (FT-ICR MS). The mass-selected alkali metal cation-cyclen complexes were irradiated using a wavelength tunable free electron laser (FEL) over the range of wavelengths extending from ~600 to 1600 $cm^{-1}$. Theoretical methods were employed to characterize the structures and relative stabilities of isolated cations and aza-crowns as well as the nonconvalently bound complexes comprised of these species. The measured IRMPD action spectra of the $M^+$(cyclen) complexes were compared to the theoretical linear IR spectra computed for the various stable low-energy conformations of these species to determine the structures accessed in the experiments.

## 1.6. References

[1] L.F. Lindoy, The Chemistry of Macrocyclic Ligand Complexes; Cambridge University Press, Cambridge, 1989, p. 13.

[2] R. Delgado, V. Félix, L.M.P. Lima, D.W. Price, Dalton Trans. (2007) 2734.

[3] M. Kim, J.W. Jeon, J. Suh, J. Biol. Inorg. Chem. 10 (2005) 364.

[4] C.A. Boswell, X. Sun, W. Niu, G.R. Weisman, E.H. Wong, A.L. Rheingold, C.J. Anderson, J. Med. Chem. 47 (2004) 1465.

[5] T. Chen, X. Wang, Y. He, C. Zhang, Z. Wu, K. Liao, J. Wang, Z. Guo, Inorg. Chem. 48 (2009) 5801.

[6] E. Kimura, A. Watanabe, M.A. Kodama, J. Am. Chem. Soc. 105 (1983) 2063.

[7] M.W. Hosseini, J.M. Lehn, M.P. Mertes, Helv. Chim. Acta 66 (1983) 2454.

[8] R.M. Izatt, K. Pawlak, J.S. Bradshaw, Chem. Rev. 95 (1995) 2529.

[9] H.K. Frensdorff, J. Am. Chem. Soc. 93 (1971) 600.

[10] A. D'Aprano, B. Sesta, J. Phys. Chem. 91 (1987) 2415.

[11] A. Prokhorov, N.L. Bris, G. Bernard, H. Henri, Synth. Commun. 36 (2006) 3271.

[12] E. Kinoshita-Kikuta, E. Kinoshita, N. Harada, T. Koike, Anal Biochem. 408 (2011) 34.

[13] J. Geduhn, T. Walenzyk, B. Koenig, Curr. Org. Synth. 23 (2007) 390.

[14] H. Kubo, T.N. Player, S. Shinoda, H. Tsukube, H. Nariai, T. Takeuchi, Anal. Chim. Acta 504 (2004) 137.

[15] T.Y. Lee, J. Suh, Pure Appl. Chem. 81 (2009) 255.

[16] J. Suh, W.S. Chei, Curr. Opin. Chem. Biol. 12 (2008) 207.

[17] M.W. Hosseini, J.M. Lehn, J. Am. Chem. Soc. 109 (1987) 7047.

[18] M.W. Hosseini, J.M. Lehn, K.C. Jones, K.E. Plute, K.B. Mertes, M.P. Mertes, J. Am. Chem. Soc. 111 (1989) 6330.

[19] M. Kodama, Bull. Chem. Soc. Jpn. 69 (1996) 3179.

[20] A. El-Hashani, A. Toutianoush, B. Tieke, J. Membr. Sci. 318 (2008) 65.

[21] R. Kataky, K.E. Matthes, P.E. Nicholson, D. Parker, J. Chem. SOC. PERKIN TRANS. 2 (1990) 1425.

[22] D.E. Reichert, J.S. Lewis, C.J. Anderson, Coord. Chem. Rev. 184 (1999) 3.

[23] R. Delgado, V. Félix, L.M.P. Lima, D.W. Price, Dalton Trans. (2007) 2734.

[24] A. Prokhorov, N.L. Bris, G. Bernard, H. Henri, Synth. Commun. 36 (2006) 3271.

[25] H. Kubo, T.N. Player, S. Shinoda, H. Tsukube, H. Nariai, T. Takeuchi, Anal. Chim. Acta 504 (2004) 137.

[26] Z.J. Li, Z.R. Li, F. Wang, C. Luo, F. Ma, D. Wu, Q. Wang, X. Huang, J. Phys. Chem. A 113 (2009) 2961.

[27] M.G.B. Drew, M.A. Santos, Struct. Chem. 4 (1993) 5.

[28] Y. Yoshikawa, Chem. Lett. (1978) 109.

[29] D.J. Royer, G.J. Grant, D.G. Van Derveer, M.J. Castillo, Inorg. Chem. 21 (1982) 1902.

[30] S. Chandrasekhar, D.G. Fortier, A. McAuley, Inorg. Chem. *32* (1992) 1424.

[31] M.A.A.F.deC.T. Corrondo, V. Félix, M.T. Durate, M.A. Santos, Polyhedron 12 (1993) 931.

[32] M. Nierlich, J. –M. Sabattie, N. Keller, L. Monique, J.D. Vigner, Acta Cryst. Sect. C 50 (1994) 52.

[33] X.–H. Bu, S.–L. Lu, R.–H. Zhang, W.–G. Wang, X.–K. Yao, Polyhedron 16 (1997) 3247.

[34] A. McAuley, T.W. Whitcombe, M.J. Zaworotko, Inorg. Org. 30 (1991) 3513.

[35] J.E. Barker, Y. Liu, N.D. Martin, T. Ren, J. Am. Chem. Soc. 125 (2003) 13332.

[36] J. Cullinane, R.I. Gelb, T.N. Margulis, L.J. Zompa, J. Am. Chem. Soc. 104 (1982) 3048.

[37] E. Kimura, A. Sakonaka, M.A. Kodama, J. Am. Chem. Soc. 104 (1982) 4984.

[38] E. Kimura, M. Kodama, T. Yatsunami, J. Am. Chem. Soc. 104 (1982) 3182.

[39] R.I. Gelb, L.M. Schwartz, L. Zompa, Inorg. Chem. 25 (1986) 1527.

[40] P. Thuery, N. Keller, M. Lance, J.D. Vigner, M. Nierlich, Acta Crystallogr., Sect. C: Cryst. Struct. Commun. 51 (1995) 1407.

[41] C. Bazzicalupi, A. Bencini, A. Bianchi, M. Cecchi, B. Escuder, V. Fusi, E. Garcia-España, C. Giorgi, S.V. Luis, G. Maccagni, V. Marcelino, P. Paoletti, B. Valtancoli, J. Am. Chem. Soc. 121 (1999) 6807.

[42] A.C. Warden, M. Warren, M.T.W. Hearn, L. Spiccia, Inorg. Chem. 43 (2004) 6936.

[43] A.C. Warden, M. Warren, M.T.W. Hearn, L. Spiccia, New J. Chem. 28 (2004) 1160.

[44] A.C. Warden, M. Warren, M.T.W. Hearn, L. Spiccia, New J. Chem. 28 (2004)1301.

[45] M.W. Hosseini, J.M. Lehn, M.P. Mertes, Helv. Chim. Acta 66 (1983) 2454.

[46] K. Kimura, H. Fujioka, K. Kodama, J. Chem. Soc. Chem. Commun. (1986) 1158.

[47] K. Hoffmann, B. Tieke, J. Membr. Sci. 341 (2009) 261.

[48] H.K. Frensdorff, J. Am. Chem. Soc. 93 (1971) 600.

[49] A. D'Aprano, B. Sesta, J. Phys. Chem. 91 (1987) 2415.

[50] B.G. Cox, P. Firman, I. Schneider, H. Schneider, Inorg. Chem. 27 (1998) 4018.

[51] H. Sulowska, W. Wiczk, J. Mlodzianowski, M. Przyborowska, T. Ossowski, J. Photoch. Photobio. A 150 (2002) 249.

[52] A. Jana, A.K. De, D. Goswami, P.K. Bharadwaj, J. Organomet. Chem. 693 (2008) 1186.

[53] E.A. Weitz, V.C. Pierre, Chem. Comm. 47 (2011) 541.

[54] A. Gherrou, H. Kerdjoudj, Desalination 151 (2002) 87.

[55] S. Patai, Supplement E: The Chemsitry of Ehters, Crown Ethers, Hydroxyl Groups and their Sulphur Analogue Part (II); John Wiley & Sons, New York, 1980.

[56] T.E. Jones, LS.W.L. Sokol, D.R. Rorabacher, M.D. Glick, J. Chem. Soc., Chem. Commun. (1979) 140.

[57] P.W.R. Corfield, C. Ceccarelli, M.D. Glick, I.W.Y. Moy, L.A. Ochrymowycz, D.B. Rorabacher, J. Am. Chem. Soc. 107 (1985) 2399.

[58] P.J. Blower, J.A. Clarkson, S.C. Rawle, J.R. Hartman Jr., R.E. Wolf, R. Yagbasan, S.G. Bott, S.R. Copper, Inorg. Chem. 28 (1989) 4040.

[59] W.N. Setzer, Y. Tang, G.J. Grant, D.G. VanDerveer, Inorg. Chem. 30 (1991) 3652.

[60] W.N. Setzer, Y. Tang, G.J. Grant, D.G. VanDerveer, Inorg. Chem. 31 (1992) 1116.

[61] R. Alberto, W. Nef, A. Smith, T.A. Kaden, M. Neuburger, M. Zehnder, A. Frey, U. Abram, P.A. Schubiger, Inorg. Chem. 35 (1996) 3420.

[62] H. Katano, M. Senda, Anal. Sci. 12 (1996) 683.

[63] H. Katano, M. Senda, Anal. Sci. 15 (1999) 1179.

[64] M. Shamsipur, G. Azimi, M. H. Mashhadizadeh, S. S. Madaeni, Anal. Sci. 17 (2001) 491.

[65] B. Saad, C.C. Chong, A.S.M. Ali, M.F. Bari, I.A. Rahman, N. Mohamad, M.I. Saleh, Anal. Chim. Acta 555 (2006) 146.

[66] A.J. Nelson, J.G. Reynolds, T.F. Baumann, G.A. Fox, Appl. Surf. Sci. 167 (2000) 205.

[67] A. Gherrou, H. Kerdjoudj, Desalination 144 (2002) 231.

[68] A. Gherrou, H. Kerdjoudj, R. Molinari, P. Seta, E. Drioli, J. Membr. Sci. 228 (2004) 149.

[69] L.L. Diaddario, Jr., E.R. Dockal, M.D. Glick, L.A. Ochrymowyez, D.B. Rorabacher, Inorg. Chem. 24 (1985) 356.

[70] V.B. Pett, L.L. Diaddario, Jr., E.R. Dockal, P.W. Corfield, C. Ceercarelli, M.D. Glick, L.A. Ochrymowyez, D.B. Rorabacher, Inorg. Chem. 22 (1983) 3661.

[71] R. Shivdas, P.B. Desai, A.K. Srivastava, J. Chem. Eng. Data 49 (2004) 1738.

[72] J.L. Lindsey, Applied Illumination Engineering; Fairmont Press Inc., Liburn, 1997, p. 112.

[73] R. Kane, H. Sell, Revolution in Lamps: A Chronicle of 50 Years of Progress; Fairmont Press Inc., Liburn, 2001, p. 241.

[74] N.N. Greenwood, A. Earnshaw, Chemistry of the Elements (2nd ed.); Burrweorth-Heninemann, Oxfoxd, 1997.

[75] M. Winter, WebElements Periodic Table of the Elements | Sodium | Biological Information, http://www.webelements.com.

[76] M. Winter, WebElements Periodic Table of the Elements | Potassium | Biological Information, http://www.webelements.com.

[77] M. Winter, WebElements Periodic Table of the Elements | Rubidium| Biological Information, http://www.webelements.com.

[78] M. Winter, WebElements Periodic Table of the Elements | Cesium | Biological Information, http://www.webelements.com.

[79] H.L. Meltzer, J. Clin. Pharmacol. 31 (1991) 179.

[80] H.E. Sartori, Pharmacol. Biochem. Be. 21 (1984) 11.

[81] Time Service Department—U.S. Navel Obsevatory—Department of the Navy, http://tycho.usno.navy.mil/cesium.html.

[82] The NIST reference on Constants, Units, and Uncertainty, NIST, http://physics.nist.gov/cuu/Units/second.html

[83] P.A. Kollman, Acc. Chem. Res. 10 (1977) 365.

[84] R. Chidamaram, M. Ramabadham, Physica B, 174 (1991) 300.

[85] P. Auffinger, F.A. Hays, A. Westhof, P. ShingHo, Proc. Natl. Acad. Sci. USA, 48 (2004) 16789.

[86] A.S. Borovik, Acc. Chem. Res. 38(1) (2005) 54.

[87] H. Nicholson, W.J. Becktel, B.W. Mathews, Nature 336 (1998) 651.

[88] J. Sancho, L. Serrano, A. Fersht, Biochemistry 31 (1992) 2253.

[89] R. Sutton, B.W. Rockett, P. Swindells, Chemistry for the Life Sciences; Taylor & Francis Inc., New York , 2000, p. 28.

[90] J.C. Ma, D.A. Dougherty, Chem. Rev. 97 (1997) 1303.

[91] S. Yamada, Y. Morimoto, T. Misono, Tetrahedron Lett. 46 (2005) 5673.

[92] Y. Inagaki, T.T. Pham, F. Fujiwara, T. Kohno, D.A. Osborne, Y. Igarashi, G. Tigyi, L.A. Parrill, Biochem J. 389 (2005) 187.

[93] W. Zhong, J.P. Gallivan, Y. Zhang, L. Li, H.A. Lester, D.A. Dougherty, Proc. Natl. Acad. Sci. USA 95 (1998) 12088.

[94] A.D. Buckingham, A.C. Legon, S.M. Roberts, Principles of Molecular Recognition, Blackie Academic, Glasgow, 1993.

[95] G.W. Gokel, D.M. Goli, C. Minganti, L. Echegoyen, J. Am. Chem. Soc. 105 (1983) 6786.

[96] D. Ray, D. Feller, M.B. More, E.D. Glendening, P.B. Armentrout, J. Phys. Chem. 100 (1996) 16116.

[97] M.B. More, D. Ray, P.B. Armentrout, J. Phys. Chem. A 101 (1997) 831.

[98] M.B. More, D. Ray, P.B. Armentrout, J. Phys. Chem. A 101 (1997) 4254.

[99] M.B. More, D. Ray, P.B. Armentrout, J. Phys. Chem. A 101 (1997) 7007.

[100] S.E. Hill, D. Feller, E.D. Glendening, J. Phys. Chem. A. 102 (1998) 3813.

[101]M.B. More, D. Ray, P.B. Armentrout, J. Am. Chem. Soc. 121 (1999) 417.

[102] E.D. Glendening, D. Feller, M.A. Thompson, J. Am. Chem. Soc. 116 (1994) 10657.

[103] P.B. Armentrout, C.A. Austin, M.T. Rodgers, Int. J. Mass Spectrom. 330-332 (2012) 16.

[104] P.B. Armentrout, C.A. Austin, M.T. Rodgers, J. Phys. Chem. A. dx.doi.org/10.1021/jp4116172.

# CHAPTER 2

# Experimental and Theoretical Methods

## 2.1. General Procedures

A schematic diagram of the guided ion beam tandem mass spectrometer is shown in **Figure 2.1.** Cross sections for collision-induced dissociation (CID) of $M^+$(ligand), where $M^+ = Na^+, K^+, Rb^+$, and $Cs^+$, and ligand = ta12C4, ha18C6, da18C6, and ht18C6, are measured using a guided ion beam tandem mass spectrometer that has been described in detail previously [1]. The $M^+$(ligand) complexes are generated by electrospray ionization (ESI). The macrocyclic ligand and alkali metal cation salt are dissolved in a 90–95%/10–5% by volume MeOH/$H_2O$ or ACN/$H_2O$ mixture to produce a solution that is ~0.2 – 0.5 mM in each species., which was delivered via syringe pump using peek tubing to a home built electrospray ionization (ESI) source as describe previously [2,3]. An ESI voltage between 1.4 and 2.5 kV and flow rates in the range from 0.1 to 2 μL/min were employed for the $M^+$(L) complexes. Ionized droplets are transferred into the vacuum region via a SS capillary biased at ~20-50 V, with the capillary temperature ranging from 70 to 125 °C to depending on solution conditions. Ions are initially focused using rf ion funnel based on a design similar to that of Smith and coworkers, [4,5] and has been described in detail elsewhere [2]. Ions then enter a hexapole ion guide, where thermalization of the ions is achieved through collisions with the background gases. The ions emanating from the hexapole ion guide are then focused, accelerated, and focused into a magnetic sector momentum analyzer for mass selection of the reactant ion. The mass-selected ions are decelerated to a desired kinetic energy before entering an octopole ion beam guide, which traps the ions in the radial direction. Trapping is efficient such that the loss of scattered reactant and product ions in the octopole region is virtually eliminated. [6,7] The octopole ion beam guide passes through a static gas cell containing Xe. Xe pressures in the range from 0.025 to 0.2 mTorr are used for CID. At these pressures, multiple ion-neutral collisions are improbable. Unreacted beam and products ions drift to the end of the octopole, are focused into a quadrupole mass filter for mass analysis, and subsequently detected with a secondary electron scintillation (Daly) detector using standard pulse counting techniques.

## 2.2. Data Acquisition System

The GIBMS is control by a computer equipped with a Pentium 133 MHz processor. A commercial GPIB interface board with 12-bit resolution (Keithley PCI-488) and a custom digital I/O board provide the hardware control functions. The GPIB board controls the Canberra dual counter timer 2071A (used in ion detection) and a Kepco BOP 100-IM power supply (used to control the dc voltage applied to the reaction region). The Kepco BOP has two modes with high (0 to ±100 eV) and low (0 to ±10 eV) ranges, such that the 12-bit resolution of the GPIB results in a minimum energy step size of 0.002 eV below 10 eV and 0.024 eV above 10 eV. The quardupole mass filter m/z value was set by a 16-bit optically isolated DAC contained in the custom digital I/O board, with a minimum step size of 0.0153 Da. The two digital outputs used to control the electropneumatic valves that direct the neutral reactant gas to the collision gas cell or reaction chamber are also contained in the custom digital I/O board connected by solid-state relays. The pressure output is read digitally by interfacing the custom digital I/O board to the Baratron through an SCSI cable. The gas flow rates in the source and interaction regions and all other lens potentials in the instrument are not automated because they do not vary with the ion interaction energy. Manual control leak valves (Granville Philips, model 203) are used to control the collision gas flow rates and a custom-built voltage dividers powered by standard dc power supplies provide the lens potentials.

Two 32-bit multithreaded graphical user interface programs, MSCAN and EMP (energy, mass, and pressure) are used for data acquisition. Compaq Vision FORTRAN

6.1 A was used to write these two programs. A lower level device interfaces written in C are used to acquire data during experiments. The quadrupole mass filter was scanned at fixed octopole interaction energy and records the intensity of detected ions as a function of the mass-to-charge ratio by the MSCAN program. The octopole interaction energy was scanned and records the intensity of the specified reactant and product ions as a function of this energy by the EMP program. A real-time graphical display, I/O windows, a control panel, and a color and symbol palette are common features of both programs. User input was required for control of the instrument and to set up experiments through the control panel. The control panel also reports details and the progress of the current experiment and allows changes to be made in the graphical display window during data acquisition.

## 2.3. Absolute Cross Sections

Measured ion intensities are converted to absolute cross sections using Beer's law. The experimental total reaction cross section, $\sigma_{tot}$, was determined by the relation,

$$I_r = \left(I_r + \sum I_p\right) e^{-\sigma_{tot} n L} \tag{2.1}$$

where $I_R$ and $I_P$ and are the measured transmitted intensities of the reactant and product ions, respectively, $n$ is the gas density, and $L$ was the effective collision gas cell length. Individual product cross sections are calculated using the following formula

$$\sigma_p = \sigma_{tot}\left(I_p / \sum I_p\right) \tag{2.2}$$

**Equations 2.1** and **2.2** presume that the sum of the transmitted reactant and product ions are equal to the incident ion intensity, that is, $I_0 = I_r + \sum I_p$. Due to the 4π collection characteristics of the octopole, this assumption was valid as long as all significant channels are monitored.

There are errors in the cross sections associated with the pressure measurements and the effective length of the interaction region, leading to ± 20% absolute uncertainties in the cross section measurements. Relative Uncertainties are approximately ± 5%.

Ion kinetics energies in the laboratory frame, $E_{\mathrm{lab}}$, are converted to energies in the center of mass frame, $E_{\mathrm{CM}}$, using the formula $E_{\mathrm{CM}} = E_{\mathrm{lab}}\, m/(m + M)$, where $M$ and $m$ are the masses of the ionic and neutral reactants, respectively. All energies reported in this study are in the center-of-mass frame unless otherwise noted. The absolute zero and distribution of ion kinetic energies are determined using the octopole ion guide as a retarding potential analyzer as previously described [1]. The nominal laboratory ion kinetic energy is the potential difference between the ESI capillary and the interaction region (i.e., the dc voltage of the octopole). In addition, the octopole ion guide serves as a highly efficient retarding energy analyzer. The ion beam intensity, $I_0$, is monitored as the dc voltage of the octopole was swept through the ion energy zero, producing a retardation curve such as that shown in **Figure 2.3**. This figure shows the ion intensity of the $\mathrm{Rb}^+$(18C6) complex as a function of the laboratory kinetic energy. Due to the trapping efficiency of the octopole, dispersion of low energies ions, the result of space charge effects, are virtually eliminated. Further, because reactions take place in the same region as the energy analysis, there was no ambiguity in the interaction determination due to contact potential differences. For the ESI source, the experimental primary ion kinetic energy distribution, as determined by the retarding energy analysis, was nearly Gaussian. A Gaussian curve fitted to the experimental distribution from the retarding energy analysis of **Figure 2.3** is shown in **Figure 2.4**, where the ion beam energy distribution was obtained by taking the derivative with respect to energy of the retarding energy analysis curve. The solid line shows a Gaussian curve fitted to the data points. The apparent full width at half-maximum (FWHM) from the retardation curve adequately describes the width of the Gaussian fit. For most experiments performed here, the distribution of ion kinetic energies was nearly Gaussian with a FWHM typically between 0.2 and 0.7 eV (lab). The uncertainty in the absolute energy scale is ±0.10 eV (lab).

The effect of multiple collisions can significantly influence the shape of CID cross sections as observed in previous studies [8]. Predicting the presence and magnitude of these pressure effects are difficult, therefore pressure-dependent studies have been performed for all cross sections examined in this study. Data free from pressure effects was obtained by extrapolating to zero reactant pressure, as described previously [8]. Thus, results reported in these studies are due to single bimolecular encounters.

## 2.4. Thermochemical Analysis

The threshold regions of the measured CID cross sections are modeled using an empirical threshold law, **Equation 2.3**,

$$\sigma(E) = \sigma_0 \sum_i g_i (E + E_i - E_0)^n / E \qquad (2.3)$$

where $\sigma_0$ was an energy independent scaling factor, $E$ is the relative translational energy of the reactants, $E_0$ was the threshold for reaction of the ground electronic and ro-vibrational state, and $n$ was an adjustable parameter that was inversely correlated with the efficiency of kinetic to internal energy transfer [8]. The summation was over the ro-vibrational states of the reactant ions, $i$, where $E_\mathrm{i}$ is the excitation energy, and $g_\mathrm{i}$ was the populations of those states ($\sum g_\mathrm{i} = 1$ ). The relative reactivity of all ro-vibrational states, as reflected by $\sigma_0$ and $n$, was assumed to be equivalent. The Beyer-Swinehart algorithm [9–11], was used to evaluate the density of the ro-vibrational states and the relative populations, $g_\mathrm{i}$, are calculated for a Maxwell Boltzmann distribution at 298 K, the internal temperature of the reactant ions. The calculated frequencies are increased and decreased by 10% to evaluate the sensitivity of the experimental analysis to the deviations from true frequencies [12,13]. One standard deviation of the uncertainty in the vibrational energy was assumed from the observed change in the average vibrational energy.

The time scale for dissociation was within ~$10^{-4}$ s, which corresponds to the time the complex takes to pass from the collision cell to the quadrupole mass filter. As the size of the reactant ion increases, the probability that CID reaction will take place within the experimental time scale was small. In such cases, the apparent thresholds are shifted to higher in energies, resulting in a kinetic shift. Statistical theories for unimolecular dissociation are used in the analysis to quantify and correct for the kinetic shift, more specifically Rice-Ramsperger-Kassel-Marcus (RRKM) theory was incorporated into equation 2.3, resulting in **Equation 2.4**, as described in detail elsewhere [14,15].

$$\sigma(E) = (n\sigma_0 / E)\sum_i g_i \int_0^{E+E_i-E_0} (\Delta E)^{n-1}\left[1 - e^{-k(E+E_i-\Delta E)\tau}\right] d(\Delta E) \qquad (2.4)$$

τ was the experimental time available for dissociation, and $k$ was the unimolecular dissociation rate constant. The term $\Delta E$ is the energy that remains in translation after the collision between the reactants. Thus, $E - \Delta E$ energy transferred to the internal modes of the dissociating ion by this collision at a relative translational energy was the energy $E$. The internal energy of the energized molecule after the collision was therefore $E + E_i - \Delta E$. The unimolecular dissociation rate constant, $k$, is defined in the usual manner by the RRKM theory. The ro-vibrational frequencies appropriate for the energized molecules and the transition states (TSs) leading are needed for **equation 2.4**. The TSs are assumed to be loose and product-like because the interaction between the metal ions and the macrocycle is largely electrostatic, thus the TSs are modeled using the ro-vibrational frequencies of the products. This treatment of the TSs is refered to as the phase space limit and assumes the TS occurs at the centrifugal barrier for dissociation as described in detail elsewhere [14]. To give optimized values for the parameters $\sigma_0$, $E_0$, and $n$, **Equation 2.3** and **2.4** are convoluted with the kinetic and internal energies distributions of the reactants and a nonlinear least-squares analysis of the data is preformed. The range of threshold values determined for the zero-pressure-extrapolated data sets for each complex, variations associated with uncertainties in the vibrational frequencies, and the error in the absolute energy scale, ±0.05 eV (lab) are used to calculate the errors associated with the measurement of $E_0$. For analyses that include the RRKM lifetime analysis, the uncertainties in the reported $E_0$(PSL) values also include the effects of increasing and deceasing the time assumed available for dissociation (~ $10^{-4}$ s) by a factor of 2.

**Equations 2.3** and **2.4** explicitly include the internal energy of the reactant, $E_i$. The ro-vibrational energy of the reactants was redistributed throughout the reactant upon interaction with Xe, therefore all energy available was treated statistically. The CID processes examined here corresponds to simple noncovalent bond cleavage reactions, the $E_0$(PSL) values determined from analysis with **Equations 2.3** and **2.4** can be equated to 0 K BDEs [16,17]. Results obtained by this modeling procedure have been verified for many systems by comparing values derived from other experimental techniques and ab initio calculations [18].

## 2.5. Conversion from 0 to 298 K

To allow comparison to commonly employed experimental conditions, we convert the 0 K bond energies determined here to 298 K bond enthalpies and free energies. The enthalpy and entropy conversions are calculated using standard formulas (assuming harmonic oscillator and rigid rotor models) and vibrational and rotational constants determined for the B3LYP/def2-TZPPD optimized geometries. Enthalpic and entropic are determined by ±10% variation in all vibrational frequencies and additionally by ±50% variation in the frequencies associated with the $M^+$–donor atom, donor atom = N, O, and S, interactions responsible for the binding in these $M^+$(L) complexes.

## 2.6. FT–ICR MS–FEL Instrument Overview

Infrared multiple photon dissociation (IRMPD) action spectroscopy experiments are performed using a Fourier transform ion cyclotron resonance mass spectrometer (FTICR MS) coupled to the free electron laser (FEL), **Figure 2.4**.

### 2.6.1. Free Electron Laser

An electron gun is used to generate electrons, which are accelerated in a linear accelerator to relativistic speeds and injected into an undulator. The oscillating trajectory of the electron beam in the magnetic field results in the irradiation of the infrared beam. The light generated was captured in an optical cavity where freshly injected electrons are allowed to interact with the circulating light pulses to generate stimulated emission. FEL resonance condition was controlled by the wavelength of the stimulated radiation. The magnetic field strength in the undulator dictates the deviation from the straight path of the electron beam. Higher magnetic field induces greater electron deviation from the straight path, resulting in a longer resonance wavelength.

The output wavelength of the FEL depends on the strength of the magnetic field. Adjustment of the gap between the two arrays of magnets forming the undulator allows the strength of the magnetic field to be varied, and the wavelength of the irradiation to be tuned. The FEL has been described in detail elsewhere [19–21].

### 2.6.2. Fourier Transform Ion Cyclotron Resonance Mass Spectrometer

IRMPD action spectra of four $M^+$(cyclen) complexes were measured using 4.7 T Fourier transform ion cyclotron resonance mass spectrometer (FT-ICR MS) coupled to the free electron laser (FEL) that was housed at the FOM Institute for Plasma Physics, Rijnhuizen. The $M^+$(cyclen) complexes, where $M^+ = Na^+$, $K^+$, $Rb^+$, and $Cs^+$, were formed by electrospray ionization (ESI) using a Micromass "Z-spray" source and solutions containing 1mM of the corresponding alkali metal hydroxide salt and 1mM of cyclen in an approximately 85–90%:15–10% $CH_3CN$:$H_2O$ mixture. A solution flow rate of 10 μL/min was used and the electrospray needle was held at a voltage in the range between 2.0 and 2.8 kV. Ions emanating from the source were focused into a hexapole ion trap and accumulated for several seconds before being injected into the ICR cell via a quad bender and radiofrequency (rf) octopole ion guide through electrostatic switching of the dc bias on the octopole. This dc bias switching method allows ions to be captured in the ICR cell in the absence of a gas pulse, thus avoiding collisional heating of the ions as described in detail elsewhere [20]. Isolation of the precursor ions was achieved using stored waveform inverse Fourier transform (SWIFT) techniques prior to irradiation by the FEL at pulse energies of ~50 mJ per macropulse of 5 μs duration at a repetition rate of 10 Hz. The irradiation time was varied between 2 and 5 seconds for the complexes investigated here due to the number of photos required to effect efficient dissociation of the M+(cyclen) complexes varies inversely with the size of the alkali metal cation. Therefore, the interaction period corresponds to 20 to 50 macropulses over the wavelength region extending from 16.7 μm (600 $cm^{-1}$) to 6.3 μm (1600 $cm^{-1}$).

The IRMPD yield for each complex was determined using **Equation 2.5**,

$$\text{IRMPD yield} = I_{M^+}/(I_{M^+(\text{cyclen})} + I_{M^+}) \qquad (2.5)$$

where the $M^+$ fragment ion intensity ($I_{M^+}$) after laser irradiation was divided by the total ion intensity ($I_{M^+(\text{cyclen})} + I_{M^+}$). The IRMPD yield was not corrected for variations in the laser power as a function of the wavelength of the FEL because the uncorrected spectra provide a better match to the relative intensities of the linear IR spectra predicted.

## 2.7. Theoretical Calculations

Molecular dynamics simulated annealing procedures and density functional theory calculations are performed using Hyperchem [22] and the Gaussian 03 and 09 suite of programs [23, 24], respectively, to obtain model structures, vibrational frequencies, rotational constants, and energetics for the neutral ligand and $M^+$(ligand) complexes. These calculations also provide theoretical estimates of the bond dissociation energies for comparison to experimentally determined values investigated here. The first stage of calculations involved a simulated annealing process to generate potential low-energy candidate structures for the neutral ligand using Hyperchem. A three phase annealing process was used, with each cycle beginning and ending at 0 K, lasting for 0.8

ps, and achieving a simulation temperature of 1000 K. Heating and cooling times for each cycle were 0.3 ps, allowing the neutral ligand to sample conformational space for 0.2 ps at the simulation temperature. In some cases, the lowest energy conformer found during the first stage of simulated was subjected to a second stage at 298 K. The 15 lowest energy structures determined in the annealing process were chosen for higher-level optimization at 1000 K. When a second stage annealing was used, the 15 most stable structures found from simulated annealing at 298 K were also chosen for higher-level optimization, for a total of 30 conformations of neutral ligand.

Geometry optimizations of neutral ligand and the $M^+$(ligand) complexes were performed using the def2 triple zeta valence basis sets of Rappoport and Furche, def2–TZVPPD, which include polarization and diffuse functions, and use an ECP for the rubidium and cesium atoms developed by Leininger et al [25,26]. The def2-TZVPPD basis set is a balanced basis set on all atoms at the triple-zeta level. All structures were optimized using density functional theory with the B3LYP functional. In addition to the def2-TZVPPD basis set, geometry optimizations were also preformed using 6-31+G*_HW. HW indicates the ECP and valence basis sets of Hay and Wadt were used to describe the complexes to $Rb^+$ and $Cs^+$ [27], while the 6-31+G* basis sets were used for the C, N, $Na^+$, and $K^+$, and H atoms. A single polarization (d) function was added to the Hay-Wadt valence basis set for Rb and Cs, with exponents of 0.24 and 0.19, respectively, as recommended by Glendening et al. [28]. The def2-TZVPPD basis set, the ECP and valence basis sets of Hay and Wadt were obtained from the EMSL basis set exchange [29,30]. In cases where the B3LYP/6-31+G* frequencies are used to model the data, the vibrational frequencies are scaled by 0.9804 [31] whereas no scale was used for the B3LYP/def2-TZVPPD frequencies. Theoretical linear IR spectra were generated using the calculated vibrational frequencies (scaled by a factor of 0.9704) and IR intensities at the B3LYP/def2-TZVPPD level of theory. For comparison to the measured

IRMPD action spectra, the theoretical linear IR spectra were broadened using a 20 $cm^{-1}$ full width at half maximum (FWHM) Gaussian line shape.

Single point energy calculations were performed at the B3LYP and MP2(full) levels of theory using 6-311+G(2d,2p)_HW and def2-TZVPPD basis sets and the B3LYP/6-31+G*_HW and B3LYP/def2-TZVPPD optimized geometries, respectively. To obtain accurate BDEs, zero point energy (ZPE) corrections scaled by 0.98 were applied and basis set superposition errors (BSSE) were subtracted from the computed BDEs in the full counterpoise correction [32,33]. Results of the single point energy calculations will be compared to experimentally determined BDEs. The polarizabilities of the stable low-energy conformers of the neutral ligand were calculated at the PBE0/def2-TZVPPD level of theory using the B3LYP/def2-TZVPPD optimized geometries. In addition, the polarizabilties for the stable low-energy conformers of the neutral ligand were calculated at the PBE0/6-311+G(2d,2p) level of theory using the B3LYP/6-31+G*_HW optimized geometries. This level of theory has been shown to accurately reproduce experimental polarizabilities [34].

## 2.8. References

[1] M.T. Rodgers, J. Phys. Chem. A 105 (2001) 2374.

[2] Y. Chen, M.T. Rodgers, J. Am. Chem. Soc. 134 (2012) 2313.

[3] R.M. Moison, P.B. Armentrout, J. Am. Chem. Soc. 18 (2007) 1124.

[4] S.A. Shaffer, D.C. Prior, G.A., Anderson, H.R. Udseth, R.D. Smith, Anal. Chem. 70 (1998) 4111.

[5] S.A. Shaffer, A. Tolmachev, D.C. Prior, G.A., Anderson, H.R. Udseth, R.D. Smith, Anal. Chem. 71 (1999) 2957.

[6] E. Teloy, D. Gerlich, Chem. Phys. 4 (1974) 417.

[7] D. Gerlich, Adv. Chem. Phys. 82 (1992) 1.

[8] M.T. Rodgers, P.B. Armentrout, Int. J. Mass Spectrom. 185/186/187 (1999) 359.

[9] T.S. Beyer, D.F. Swinehart, Commun. ACM 16 (1979) 379.

[10] S.E. Stein, B.S. Rabinovitch, J. Chem. Phys. 58 (1973) 2438.

[11] S.E. Stein, B.S. Rabinovitch, Chem. Phys. Lett. 49 (1977) 183.

[12] J.A. Pople, B.H. Schlegel, K. Raghavachari, D.J. DeFrees, J.F. Binkley, M.J. Frisch, R.F. Whitesides, R.F. Hout, W.J. Hehre, Int. J. Quantum Chem. Symp. 15 (1981) 269.

[13] D.J. DeFrees, A.D. McLean, J. Chem. Phys. 82 (1985) 333.

[14] M.T. Rodgers, K.M. Ervin, P.B. Armentrout, J. Chem. Phys. 106 (1997) 4499.

[15] F.A. Khan, D.E. Clemmer, R.H. Schultz, P.B. Armentrout, J. Phys. Chem. 97 (1993) 7978.

[16] J. Simons, P.B. Armentrout, J. Am. Chem. Soc. 114 (1992) 8627.

[17] N.F. Dalleska, K. Honma, P.B. Armentrout, J. Am. Chem. Soc. 115 (1993) 12125.

[18] M.T. Rodgers, P.B. Armentrout, Mass Spectrom Rev. 19 (2000) 215.

[19] J.J. Valle, J.R. Eyler, J. Oomens, D.T. Moore, A.F.G. van der Meer, G. von Heldon, G. Meijer, C.L. Hendrickson, A.G. Marshall, G.T. Blakney, Rev. Sci. Instrum. 76 (2005) 023103.

[20] N.C. Polfer, J. Oomens, D.T. Moore, G. von Heldon, G. Meijer, R.C. Dunbar, J. Am. Chem. Soc. 128 (2006) 517.

[21] N.C. Polfer, J. Oomens, J. Phys. Chem. Chem. Phys. 9 (2007) 3804.

[22] HyperChem$^{TM}$ Molecluar Modeling Software Package, Version 7.5, Hypercube Inc., 2002.

[23] M.J. Frisch, G.W. Trucks, H.B. Schlegel, G.E. Scuseria, M.A. Robb, J.R. Cheeseman, J.A. Montgomery Jr., T. Vreven, K.N. Kudin, J.C. Burant, J.M. Millam, S.S. Iyengar, J. Tomasi, V. Barone, B. Mennucci, M. Cossi, G. Scalmani, N. Rega, G.A. Petersson, H. Nakatsuji, M. Hada, M. Ehara, K. Toyota, R. Fukuda, J. Hasegawa, M. Ishida, T. Nakajima, Y. Honda, O. Kitao, H. Nakai, M. Klene, X. Li, J.E. Knox, H.P. Hratchian, J.B. Cross, V. Bakken, C. Adamo, J. Jaramillo, R, Gomperts, R.E. Stratmann, O. Yazyev, A.J. Austin, R. Cammi, C. Pomelli, J.W. Ochterski, P.Y. Ayala, K. Morokuma, G.A. Voth, P. Salvador, J.J. Dannenberg, V.G. Zakrzewski, S. Dapprich, A.D. Daniels, M.C. Strain, O. Farkas, D.K.

Malick, A. Rabuck, K. Raghavachari, J.B. Foresman, J.V. Ortiz, Q. Cui, A.G. Baboul, S. Clifford, J. Cioslowski, B.B. Stefanov, G. Liu, A. Liashenko, P. Piskorz, I. Komaromi, R.L. Martin, D.J. Fox, T. Keith, M.A. Al-Laham, C.Y. Peng, A. Nanayakkara, M. Challacombe, P.MW. Gill, B. Johnson, W. Chen, M.W. Wong, C. Gonzalez, J.A. Pople, Gaussian 03, Revision D.01, 2005, Gaussian, Inc., Pittsburgh, PA.

[24] M.J. Frisch, G.W. Trucks, B.H. Schlegel, G.E. Scuseria, M.A. Robb, J.R. Cheeseman, G. Scalmani, V. Barone, B. Mennucci, G.A. Petersson et al. Gaussian 09, revision A.1; Gaussian, Inc., Wallingford CT, 2009

[25] D. Rappoport. F. Furche, J. Chem. Phys. 133 (2010) 134105.

[26] T. Leininger, A. Nicklass, W. Kuechle, H. Stoll, M. Dolg, A. Bergner, Phys. Lett. 255 (1996) 274.

[27] P.J. Hay, W.R. Wadt, J. Chem. Phys. 82 (1985) 299.

[28] E.D. Glendening, D. Feller, M.A. Thompson, J. Am. Chem. Soc. 116 (1994) 10657.

[29] D. Feller, J. Comp. Chem. 17 (1996) 1571.

[30] K.L. Schuchardt, B.T. Didier, T. Elsenthagen, L. Sun, V. Gurumoorthi, J. Chase, J. Li, T.L. Windus, J. Chem. Inf. Model. 47 (2007) 1045.

[31] J.B. Foresman, A.E. Frisch, Exploring Chemistry with Electronic Structure Methods; 2nd ed. Gaussian, Pittsburgh (1996) 64.

[32] S.F. Boys, R. Bernardi, Mol. Phys. 19 (1979) 553.

[33] F.B. van Duijneveldt, J.G.C.M. van Duijneveldt-van de Rijt, J.H. van Lenthe, Chem. Rev. 94 (1994) 1873.

[34] S.M. Smith, A.N. Markevitch, D.A. Romanov, X. Li, R.J. Levis, H.B. Schlegel, J. Phys. Chem. A 108 (2004) 11063.

## 2.9. Figure Captions

Figure 2.1. Schematic diagram of the guided ion beam tandem mass spectrometer.

Figure 2.2. Retarding potential analysis of the $Rb^+$(18C6) complex ion beam as a function of the laboratory ion kinetic energy.

Figure 2.3. Kinetic energy distribution of the $Rb^+$(18C6) complex ion beam.

Figure 2.4 Schematic diagram of the Fourier transform ion cyclotron resonance mass spectrometer coupled to the FELIX free electron laser.

Figure 2.1.

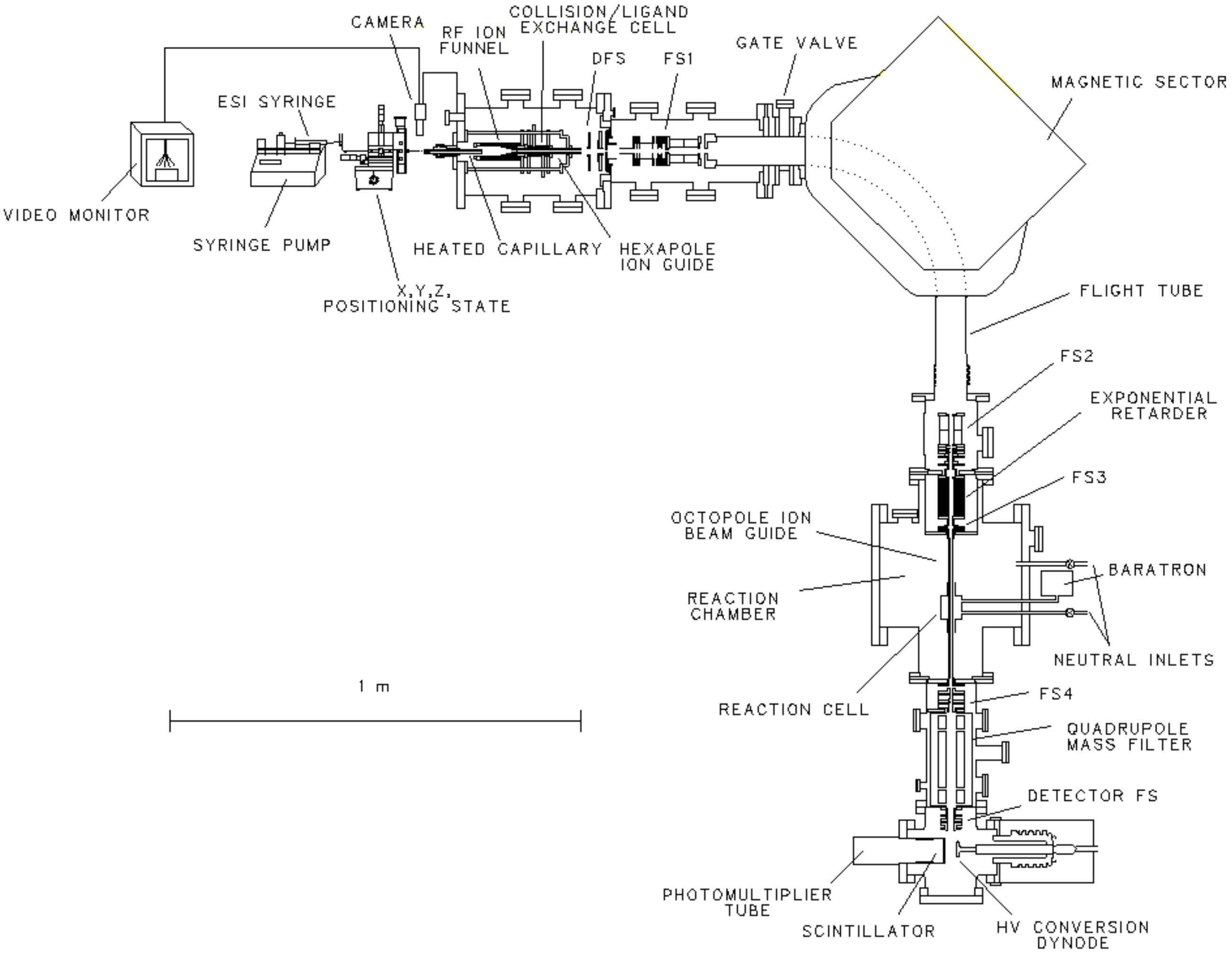
CAMERA
RF ION FUNNEL
COLLISION/LIGAND EXCHANGE CELL
DFS
FS1
GATE VALVE
MAGNETIC SECTOR
ESI SYRINGE
VIDEO MONITOR
SYRINGE PUMP
HEATED CAPILLARY
HEXAPOLE ION GUIDE
X,Y,Z, POSITIONING STATE
FLIGHT TUBE
FS2
EXPONENTIAL RETARDER
FS3
OCTOPOLE ION BEAM GUIDE
BARATRON
REACTION CHAMBER
NEUTRAL INLETS
1 m
REACTION CELL
FS4
QUADRUPOLE MASS FILTER
DETECTOR FS
PHOTOMULTIPLIER TUBE
SCINTILLATOR
HV CONVERSION DYNODE

Figure 2.2.

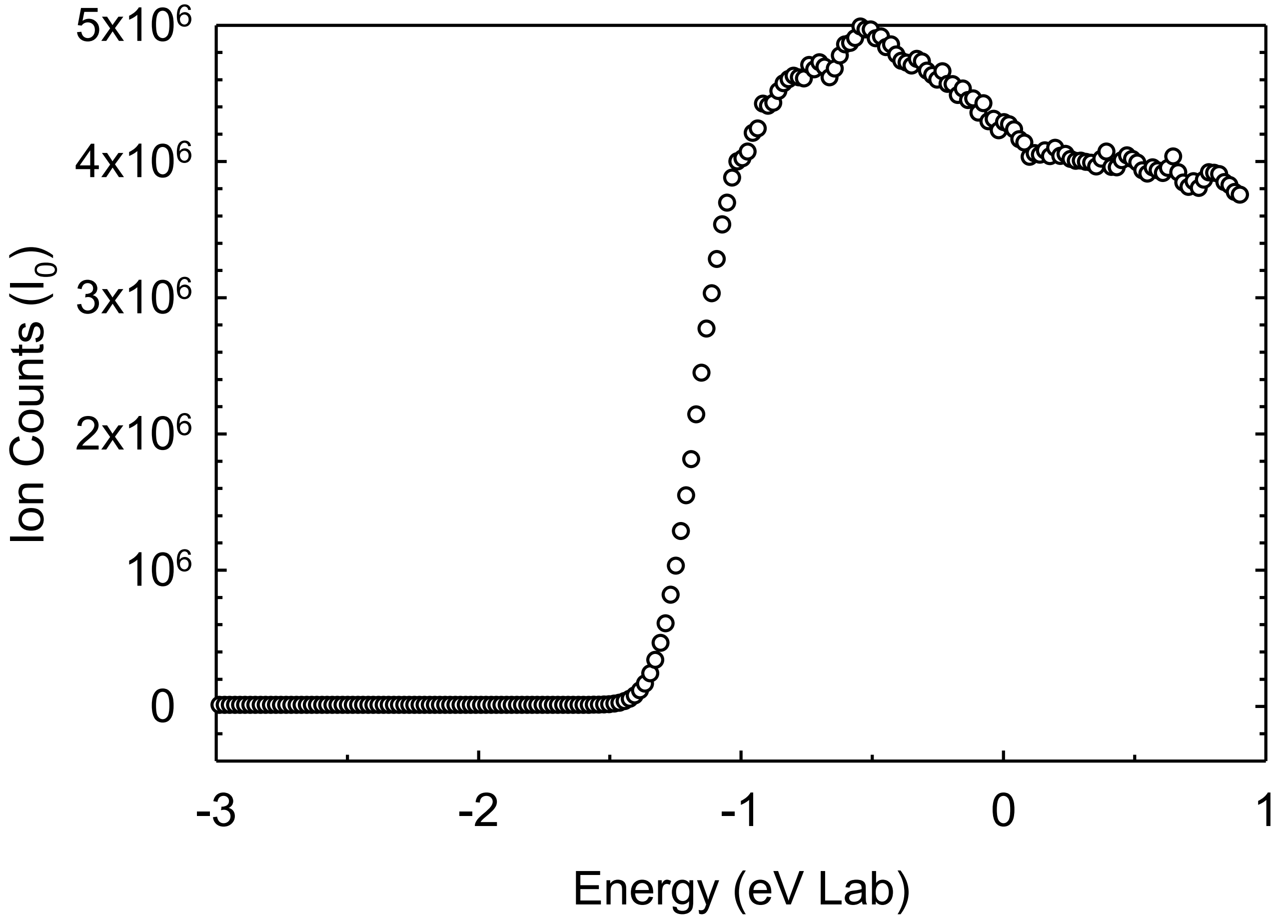
5x10$^6$
4x10$^6$
3x10$^6$
2x10$^6$
10$^6$
0
Ion Counts (I$_0$)
-3
-2
-1
0
1
Energy (eV Lab)

Figure 2.3.

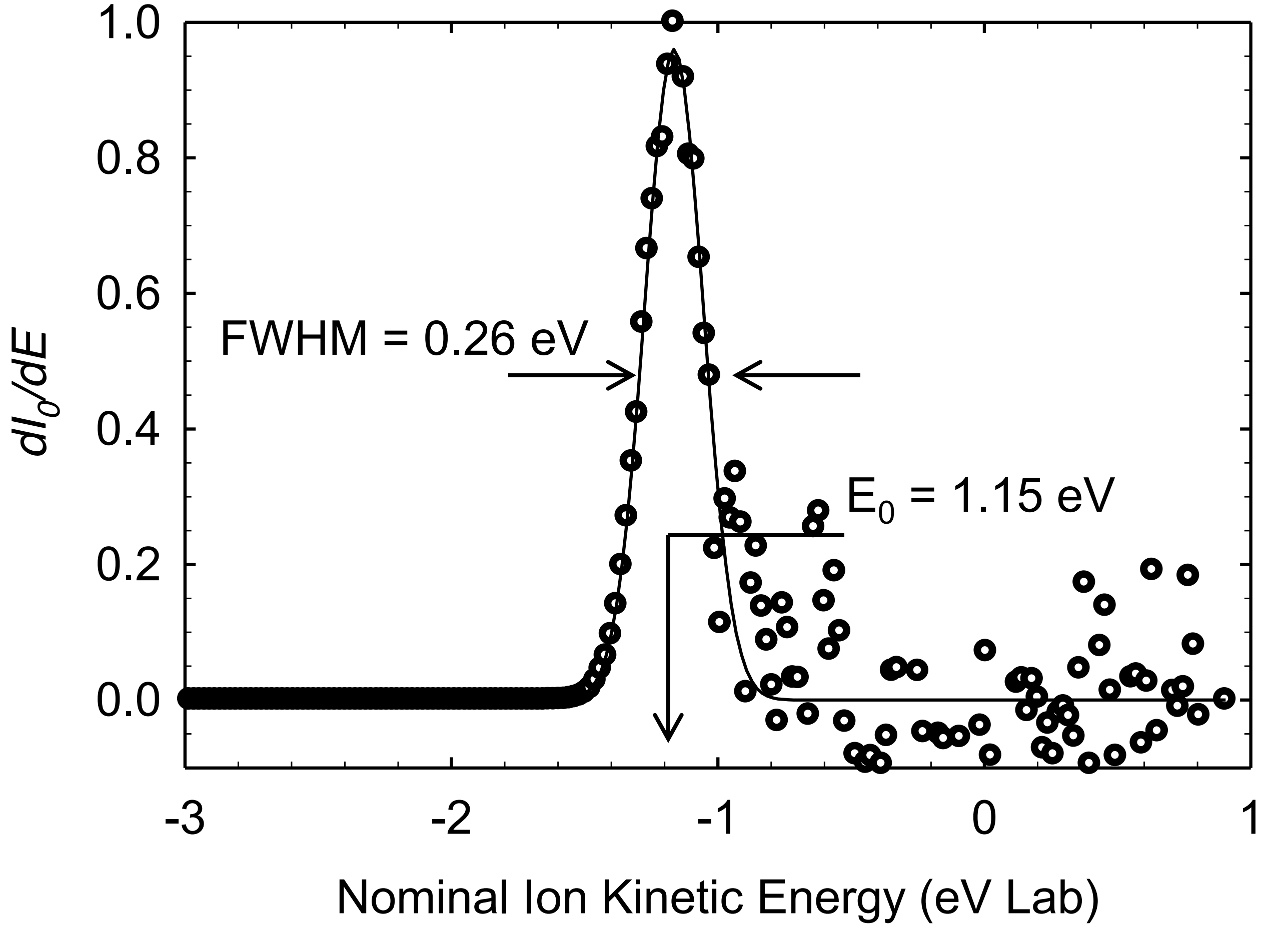
$dI_0/dE$
1.0
0.8
0.6
0.4
0.2
0.0
FWHM = 0.26 eV
$E_0$ = 1.15 eV
-3
-2
-1
0
1
Nominal Ion Kinetic Energy (eV Lab)

Figure 2.4.

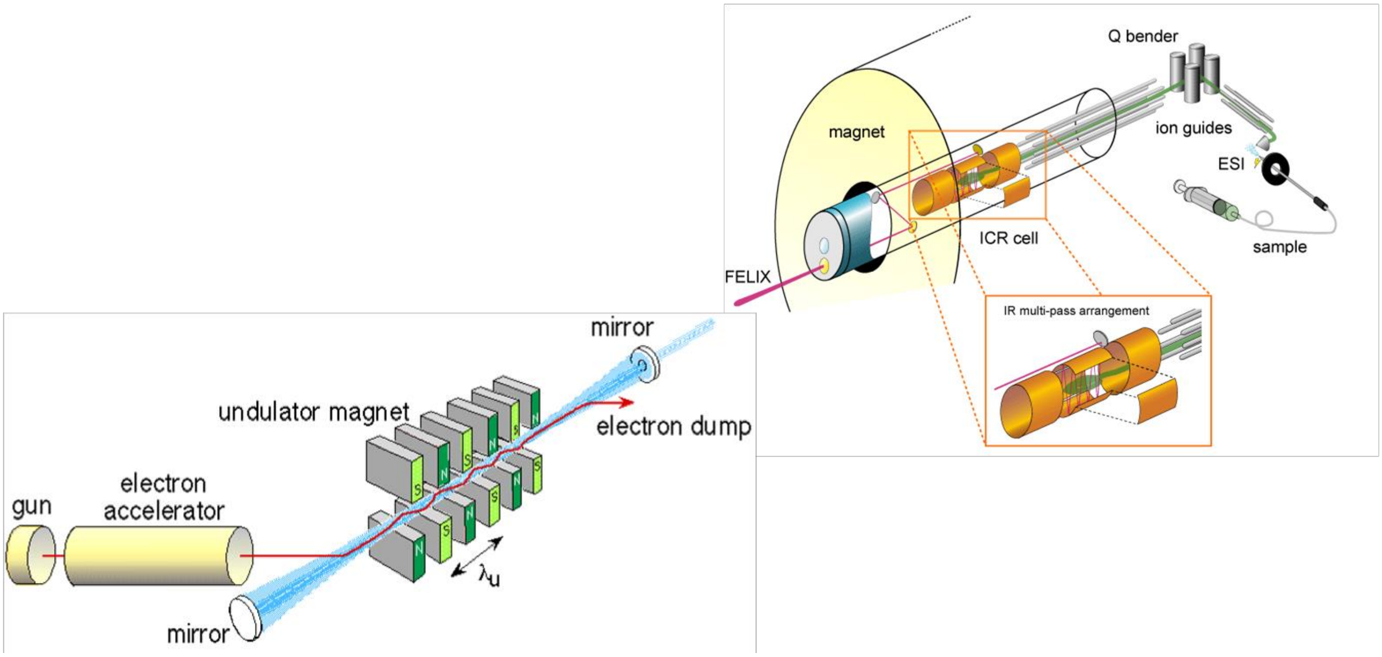
Q bender
ion guides
magnet
ESI
ICR cell
sample
FELIX
IR multi-pass arrangement
mirror
undulator magnet
electron dump
electron accelerator
gun
S
N
$\lambda_u$
mirror

# CHAPTER 3

## Alkali Metal Cation – Cyclen: Effects of Alkali Metal Cation Size on the Structure and Binding Energies

Portions of this chapter were reprinted with permission from Austin, C.A., Chen, Y., and Rodgers M.T. Alkali Metal Cation – ta12C4: Effects of Alkali Metal Cation Size on the Structure and Binding Energies. Int. J. Mass Spectrom. 330-332 (2012) 27. Copyright 2012 Elsevier B.V.

### 3.1. Introduction

Cyclen (1,4,7,10-tetraazacyclododecane (ta12C4)) is a macrocycle and the aza analogue of 12-crown-4 (1,4,7,10-tetraoxacyclododecane (12C4)). The structure of ta12C4 along with its measured [1,2] and calculated dipole moment and polarizability are shown in **Figure 3.1**. Alkali metal cation-ta12C4 complexes are interesting from a practical point of view. Several studies using both experimental and theoretical methods have examined the fundamental interactions between ions and neutral ta12C4 based molecules in solution [3-4]. Rode and Hannongbua studied the neutral and complexed forms of ta12C4 in solution using experimental and theoretical methods [5-10]. Separating out intrinsic properties from those that can be attributed to the local environment, in this case solution, is challenging. One way to study the intrinsic properties of the binding is to study these systems in the gas phase.

There have been fewer experimental studies of ions and neutral ta12C4 in the gas phase. Brodbelt and co-workers examined alkali metal cation selectivity and measured the gas phase basicities of polyamine complexes using H/D exchange and the bracketing method, respectively [11,12]. In their studies, $Li^+$ and $Na^+$ were the only alkali metal cations investigated. However, there is a lack of quantitative information relating the strength of binding to the complete alkali metal cation series.

The purpose of this study was to probe the nature of the binding interactions in alkali metal cation-ta12C4 complexes and provide accurate binding energies for the series of alkali metal cations including $Na^+$, $K^+$, $Rb^+$, and $Cs^+$. Results for the $M^+$(ta12C4) complexes were compared to the analogous $M^+$(12C4) complexes to elucidate the influence of the donor atoms (N versus O) on the nature and strength of binding [13–18].

## 3.2. Collision-Induced Dissociation Experiments

Cross sections for collision-induced dissociation (CID) of four $M^+$(ta12C4) complexes, where $M^+ = Na^+$, $K^+$, $Rb^+$, and $Cs^+$, were measured using a guided ion beam tandem mass spectrometer that was described in detail Chapter 2. The $M^+$(ta12C4) complexes were generated by electrospray ionization (ESI) [19]. Thermochemical analyses of the experimental results are explicitly discussed in **Chapter 2**.

## 3.3. Theoretical Calculations

To obtain model structures, vibrational frequencies, rotational constants, and energetics for the neutral ta12C4 ligand and for the $M^+$(ta12C4) complexes, molecular dynamics simulated annealing procedures and density functional theory calculations were performed using Hyperchem [20] and the Gaussian 03 suite of programs [21], respectively, and is describe in detail in **Chapter 2**.

Initial candidate structures for the $M^+$(ta12C4) complexes were generated using four of the low-energy neutral ta12C4 structures; those that were expected to provide the most favorable geometries for interaction with the alkali metal cation. The alkali metal cation was placed in various positions to exhaustively probe the range of geometries that allow interaction with one, two, three, or all four of the nitrogen donor atoms. Also included as an initial candidate structure for the $M^+$(ta12C4) complexes were structures analogous to the previously published ground-state conformations of the $M^+$(12C4) complexes [13–18].

Vibrational analyses of the geometry-optimized structures were performed to determine the vibrational frequencies for the neutral ta12C4 ligand and $M^+$(ta12C4) complexes. Single point energy calculations were performed at the B3LYP and MP2(full) levels of theory using the 6-311+G(2d,2p) and def2-TZVPPD basis sets and the B3LYP/6-31+G* and the B3LYP/def2-TZVPPD optimized geometries, respectively. To obtain accurate BDEs, zero point energy (ZPE) corrections being scaled by 0.9804 were applied and basis set superposition errors (BSSE) were subtracted from the computed dissociation energies in the full counterpoise correction [22,23]. The polarizabilties of the stable low-energy conformers of ta12C4 were calculated at the PBE0/def2-TZVPPD level of theory using the B3LYP/def2-TZVPPD optimized geometries.

## 3.4. Results

### 3.4.1. Collision-Induced Dissociation Experiments

Cross sections were measured for the interaction of Xe with four $M^+$(ta12C4) complexes, where $M^+ = Na^+, K^+, Rb^+$, and $Cs^+$. **Figure 3.2a** shows representative data for the $Na^+$(ta12C4) complex. The complexes to $K^+$, $Rb^+$, and $Cs^+$ exhibit similar relative behavior, and are provided as **Figure 3.3a-c**. In all cases, $M^+$ is the only ionic product observed corresponding to endothermic loss of the intact ta12C4 ligand in the CID reactions 3.1.

$$M^+(\text{ta12C4}) + Xe \rightarrow M^+ + \text{ta12C4} + Xe \tag{3.1}$$

### 3.4.2. Threshold Analysis.

The model of **Equation 2.4** was used to analyze the thresholds for CID reactions 3.1 in four $M^+$(ta12C4) systems. The results of these analyses are provided in **Table 3.1**. A representative analysis of the $Na^+$(ta12C4) complex is shown in **Figure 3.2b.** An analogous set of figures for the complexes to $K^+$, $Rb^+$, and $Cs^+$ are provided as **Figure**

**3.3d-f**. In all cases, the experimental cross sections for CID reactions 3.1 are accurately reproduced using a loose PSL TS model [24]. Previous work has shown that this model provides the most accurate assessment of the kinetic shifts for CID processes for noncovalently bound metal-ligand complexes. Good reproduction of the data is obtained over energy ranges exceeding 4.5 eV and cross section magnitudes of at least a factor of 100 for the complexes to $Na^+$ and $K^+$, and 50 for the complexes to $Rb^+$ and $Cs^+$. **Table 3.1** also includes threshold values, $E_0$, obtained without including the RRKM lifetime analysis. The difference between these values and the $E_0$(PSL) values provides a measure of the kinetic shifts for these systems, which increase from 0.42 eV for the $Cs^+$(ta12C4) complex to 2.20 eV for the $Na^+$(ta12C4) complex. All of the $M^+$(ta12C4) complexes possess the same number of vibrational modes, the observed kinetic shifts directly correlate with the measured $M^+$–ta12C4 BDE as observed (**Table 3.1**).

The entropy of activation, $\Delta S^\dagger$, is a measure of the looseness of the TS, but also depends on the threshold energy. The $\Delta S^\dagger$(PSL) values for these systems at 1000 K exhibit modest variation, as expected on the basis of the similarity of these systems, and vary between 57 and 72 J $K^{-1}$ $mol^{-1}$. The $\Delta S^\dagger$(PSL) values decrease with increasing size of the alkali metal in accord with the decrease in the threshold energy. These entropies of activation compare favorably to those previously determined for a wide variety of noncovalently bound complexes that dissociate via simple noncovalent bond cleavage [13–16, 18, 19, 25–31].

### 3.4.3. Theoretical Results

Theoretical structures were calculated for the ground-state and stable low-energy structures of ta12C4 and the $M^+$(ta12C4) complexes as described in the Theoretical Calculations in **Chapter 2**. $M^+$–ta12C4 BDEs calculated at the B3LYP and MP2(full) levels of theory using the def2-TZVPPD basis set and the B3LYP/def2-TZVPPD optimized geometries are summarized in **Table 3.2**. Also included are values calculated at the B3LYP and MP2(full) levels of theory using the B3LYP/6-311+G(2d,2p) basis set and the B3LYP/6-31+G* optimized geometries. ZPE and BSSE corrections were also included in the computed BDEs.

### 3.4.3.1. Neutral ta12C4

The B3LYP/def2-TZVPPD optimized structures of the five low energy conformers of ta12C4 along with their calculated dipole moments and molecular polarizabilities are shown **Figure 3.1**. The nomenclature employed to describe these structures is taken from the Bosnich *et al*, where the (+) and (-) describe the positions of the amine hydrogen atoms as lying above (+) or below (-) the plane of the ring [32]. Energetics computed using the B3LYP/def2-TZVPPD level of theory were found to be the most reliable. Therefore, the following discussion will focus on the geometries and energetics calculated at the B3LYP/def2-TZVPPD level of theory, unless otherwise noted. Due to the size of the alkali metal cations investigated, the plane created by the donor atoms is slightly distorted, but the position of the amine hydrogen atoms is consistent with this nomenclature. Five distinct stable low-energy geometries were found for the neutral ta12C4 ligand. The ground-state conformer is of $C_1$+++– symmetry and surprisingly exhibits a relatively large dipole moment, 1.27 D. Three of the nitrogen atoms are oriented towards the cavity of the ring while one nitrogen atom is oriented down and away from the cavity. This is due to the amine hydrogen interacting with the adjacent nitrogen donor atom. This conformation gains additional stabilization via a N–H···N hydrogen-bonding interaction. The next most stable conformer is the $C_s$+++–, which is calculated to lie 8.8 kJ/mol higher in energy. In the $C_s$+++– structure, the calculated dipole moment is 2.56 D, three of the nitrogen atoms lie in the same plane with one N donor atom below the plane leading to the large dipole moment. In the $^*C_2$+–+– and $C_2$+–+– structures the local dipoles are anti-aligned and oriented towards the center of the cavity, leading to cancelation of the local dipole and no overall dipole moment due to symmetry, which is calculated to lie 19.4 and 41.6 kJ/mol, respectively. The $^{*}C_2$+–+– conformer has been reported as the crystal structure of ta12C4 trihydrate [33]. The $^{*}C_2$+–+– conformer was also previously reported as the ground-state structure by Bultinck et al. [34]. Surprisingly, calculations performed here find that the $^{*}C_2$+–+– conformation lies 19.4 kJ/mol higher in energy than the ground-state conformer. The $C_{2V}$++++ structure lies 44.5 kJ/mol higher in energy, and the nitrogen donor atoms are all aligned in the same plane leading to a calculated dipole moment of 0.26 D. For both the $C_2$+–+– and the $C_{2V}$++++ conformations imaginary frequencies are encountered. In both cases, the imaginary frequencies arise from ring breathing motions where the amino hydrogens move back and forth towards the center of the cavity. Therefore, the stabilities of these conformations are underestimated. The PBE0/def2-TZVPPD computed polarizabilities of the stable conformers of ta12C4 exhibit only modest variation as expected and lie between 20.10 and 20.61 $Å^3$ (**Figure 3.1**). At the B3LYP/6-31+G* level of theory results are highly parallel, but the $C_s$+++– conformer is found to be less stable then the B3LYP/def2-TZVPPD results. The next most stable conformer at the B3LYP/6-31+G* level of theory is the $^{*}C_2$+–+– conformer calculated to lie 19.1 kJ/mol higher in energy, while the $C_s$+++– is calculated to lie 25.2 kJ/mol higher in energy.

#### 3.4.3.2. $M^+$(ta12C4)

Optimized geometries of the ground-state and low-energy structures of the $Na^+$(ta12C4) complex at the B3LYP/def2-TZVPPD are provided in **Figure 3.4**. Similar conformations were found for the complexes to the other alkali metal cations and are provided **Figures 3.5-3.7**.

As can be seen in **Figure 3.4,** for the $Na^+$(ta12C4) complex, the $C_4$++++ conformation where all 4 nitrogen donor atoms are oriented toward the sodium cation is the ground-state conformation. As indicated earlier, the (++++) indicates that the amine hydrogen atoms are all located above the plane of the ring. In this conformation the local dipoles of the 4 amino groups are oriented toward the metal cation. The analogous conformations are also observed as the ground-state conformations of the other alkali metal cations investigated (**Figures 3.5-3.7**). The cavity of ta12C4 is too small to accommodate the metal cation as seen by the metal cation sitting above the ring. The four alkali metal cation metal-nitrogen bond distances are equal in all complexes and increase with the size of the alkali metal cation from 2.434 Å for $Na^+$ to 3.190Å for $Cs^+$. The longer $M^+$–N bond distances lead to concomitant decreases in the $\angle NM^+N$ bond angles from 76.4 to 57.7 ° for the complexes to $Na^+$ and $Cs^+$. The structure of the ta12C4 ligand is very similar in all complexes as can be seen by the small differences in the ∠CNCC and ∠NCCN dihedral angles, which vary from -161.4 to -160.5 ° and 61.1 to 64.3 °, respectively (**Figures 3.5-3.7**).

The $C_{2v}$++++ conformation of $Na^+$(ta12C4) lies 21.7 kJ/mol above the ground-state conformation. In this conformation the alkali metal cation-nitrogen distances are not equal, and the ∠NCCN dihedral angles alternate between positive and negative values leading to the $C_{2v}$ symmetry. For the complexes of ta12C4 to the other alkali metal cations, the $C_s$+++– is the next most stable conformer lying 26.1, 24.1, and 23.4 kJ/mol above the ground-state conformer for the complexes to $K^+$, $Rb^+$, and $Cs^+$, respectively. In the $C_s$+++– conformation, one of the amino groups is further away from the metal cation than the other three, but the local dipole for this amino group is still oriented towards the metal cation, suggesting that the binding to this donor atom is weaker than to the other three nitrogen atoms. Another structure with $C_{2V}$ symmetry was also found (+–+–), but lies 52.1 kJ/mol higher in energy. The variation in the relative Gibbs free energies of the various conformations of the $M^+$(ta12C4) complexes at 298 K as a function of size of alkali metal cation is provided as **Figure 3.8**.

## 3.5. Discussion

### 3.5.1. Comparison of Theory and Experiment

The $M^+$–ta12C4 BDEs at 0 K measured here by guided ion beam mass tandem spectrometry techniques are summarized in **Table 3.2**. Also listed in **Table 3.2** are the $M^+$–ta12C4 BDEs calculated at the B3LYP and MP2(full) levels of theory using 6-311+G(2d,dp)_HW and def2-TZVPPD basis sets, including independent ZPE and BSSE corrections. The agreement between the calculated and measured BDEs is illustrated in **Figure 3.9**. As can be seen in the figure, all four levels of theory do a reasonably good job of describing the energetics of binding in these systems. Overall, the B3LYP/def2-TZVPPD results exhibit the best agreement with the measured values. The mean absolute deviation (MAD) between theory and experiment is 8.8 ± 4.4 kJ/mol. The MAD is only slightly larger than the average experimental uncertainty (AEU) in these values, 7.4 ± 3.1 kJ/mol. The 6-311+G(2d,dp)_HW basis set does not perform quite as well. The MAD between B3LYP/6-311+G(2d,dp)_HW theory and experiment is 14.3 ± 7.8 kJ/mol, almost double the AEU in these values. In contrast, the agreement between MP2(full) theory and experiment is much less sensitive to the basis set used. The MAD is 10.6 ± 6.4 kJ/mol when the def2-TZVPPD basis set is used and 10.5 ± 9.2 kJ/mol when the 6-311+G(2d,dp)_HW basis set is used.

Based on comparisons between theory and experiment, it appears that MP2(full) theory describes the binding in the $Na^+$(ta12C4) complex most effectively, while B3LYP theory performs slightly better than MP2(full) for the larger alkali metal cations, $K^+$–$Cs^+$. It is also clear that the Hay–Wadt ECP does not perform as well as the def2-TZVPPD ECP for Cs+, and underestimates the strength of binding. Similar behavior has been found for $Rb^+$ and $Cs^+$ interacting with a wide variety ligands [35, 36].

### 3.5.2. Trends in the Binding of Alkali Metal Cations to ta12C4

The experimental and calculated $M^+$–ta12C4 BDEs at 0 K are summarized in **Table 3.2** and shown pictorially in **Figure 3.10**. The $M^+$–ta12C4 BDEs are found to decrease monotonically as the size of the alkali metal cation increases from $Na^+$ to $Cs^+$. This is the expected trend for binding based primarily on electrostatic (ion-dipole and ion-induced dipole) interactions, because the increasing size of the alkali metal cation [37] leads to longer metal-ligand bond distances. The alkali metal cations have $s^0$ electron configurations such that their electron densities are spherically symmetric. Therefore, the metal-ligand bond distance is primarily determined by the size of the alkali metal cation. The smaller cations lead to shorter metal-ligand bond distances and stronger electrostatic interactions.

### 3.5.3. Comparison with 12-crown-4

In a series of independent and collaborative studies Armentrout, Feller, Glendening and coworkers investigated the structures and determined binding energies of complexes of alkali metal cations to 12C4 using electronic structure and TCID methods [13–17, 38]. The $M^+$(12C4) systems have been recently revisited and re-measured the $Rb^+$(12C4) and $Cs^+$(12C4) BDEs using the same experimental methods employed here because excited conformers were accessed in that work. In addition, earlier data was also reinterpreted and theoretical electronic structure calculations using the same four levels of theory examined here for all four alkali metal cation–12C4 complexes were preformed [18]. By comparing the results of these studies to current work, insight into the binding specificity of these complexes as a function of the nature of the donor atoms in the macrocyclic ring, N vs O, can be gained. Based on the gas basicities of these two ligands, 1004 kJ/mol for ta12C4 and 890.5 kJ/mol [39] for 12C4, one would expect harder metal cations to bind more strongly to ta12C4. Indeed this is the observed trend as can be seen in **Figure 3.11**. Preferential binding to ta12C4 is observed for the $Na^+$ cation as compared to 12C4. All of the other alkali metal cations examined, $K^+$, $Rb^+$, and $Cs^+$, bind slightly more strongly to 12C4 then to ta12C4. Both B3LYP and MP2(full) theories also suggest that ta12C4 binds the harder alkali metal cations more strongly than 12C4, but that this preference should also hold true for $K^+$. As a result of its preference over 12C4 for smaller, harder alkali metal cations, ta12C4 will likely prove more useful for selective binding to most transition metal cations.

### 3.6. Conclusion

The kinetic energy dependence of the collision-induced dissociation of four $M^+$(ta12C4) complexes where $M^+ = Na^+$, $K^+$, $Rb^+$, and $Cs^+$ with Xe, was examined in a guided ion beam tandem mass spectrometer. Only simple CID leading to loss of the intact ta12C4 ligand is observed for all four complexes. Thresholds for these CID reactions were determined after careful consideration of the effects of the kinetic and internal energy distributions of the reactants, multiple collisions with Xe, and the lifetime of the activated $M^+$(ta12C4) complexes using a loose PSL TS model. Molecular parameters needed for the analysis of experimental data as well as structures and theoretical estimates for the $M^+$–ta12C4 BDEs are obtained from Theoretical calculations preformed at the B3LYP/6-311+G(2d,2p)//B3LYP/6-31+G*, B3LYP/def2-TZVPPD//B3LYP/def2-TZVPPD, MP2(full)/6-311+G(2d,2p)//B3LYP/6-31+G*, and MP2(full)/def2-TZVPPD//B3LYP/def2-TZVPPD levels of theory. Reasonably good agreement is found for all levels of theory, but is best for the B3LYP/def2-TZVPPD calculated values. Trends in the measured and calculated BDEs suggest that binding is based primarily on electrostatic interactions. The structures of the $M^+$(ta12C4) complexes are very similar to those determined for the analogous $M^+$(12C4) complexes with only minor variations arising from the presence of the amino hydrogen atoms. Ta12C4 binds $Na^+$ more strongly than 12C4. In contrast, binding to $K^+$, $Rb^+$, and $Cs^+$ is slightly stronger to 12C4 than ta12C4. These results suggest that the N donor atoms of ta12C4 are more selective for hard metal cations whereas 12C4 is more selective for soft metal cations.

### 3.7. References

[1] G.J. Reibnegger, B.M. Rode, Inorg. Chim. Acta 72 (1983) 47

[2] S.V. Hannongbua, B.M. Rode, Inorg. Chim. Acta 96 (1985) 91

[3] K.H. Chalmers, E. De Luca, N.H.M. Hogg, A.M. Kenwright, I. Kuprov, D. Parker, M. Botta, J.I. Wilson, A.M. Blamire, Chem. Eur. J. 16 (2010) 134

[4] U. Cosentino, A. Villa, D. Pitea, G. Moro, V. Barone, A. Maiocchi, J. Am. Chem. Soc. 124 (2002) 4901

[5] V.W. Ruangpornvisuti, M.M. Probst, B.M. Rode, Inorg. Chim. Acta 134 (1987) 21

[6] S.V. Hannongbua, B.M. Rode, Faraday Trans. 2 82 (1986) 1021

[7] V.W. Ruangpornvisuti, , M.M. Probst, B.M. Rode, Inorg. Chim. Acta 144 (1988) 297

[8] S.V. Hannongbua, J. Phys. Chem. 100 (1996) 17655

[9] S. Udomsub, S.V. Hannongbua, Faraday Trans 93 (1997) 3045

[10] S.V. Hannongbua, Inorg. Chem. 42 (2003) 4147

[11] M.L. Reyzer, J.S. Brodbelt, J. Am. Soc. Mass. Spectrom. 9 (1998) 1043

[12] M.L. Reyzer, J.S Brodbelt, J. Am. Soc. Mass. Spectrom. 11 (2000) 711

[13] D. Ray, D. Feller, M.B. More, E.D. Glendening, P.B. Armentrout, J. Phys. Chem. 100 (1996) 16116

[14] M.B. More, D. Ray, P.B. Armentrout, J. Phys. Chem. A 101 (1997) 831

[15] M.B. More, D. Ray, P.B. Armentrout, J. Phys. Chem. A 101 (1997) 4254

[16] M.B. More, D. Ray, P.B. Armentrout, J. Phys. Chem. A 101 (1997) 7007

[17] S.E. Hill, D. Feller, E.D. Glendening, J. Phys. Chem. A. 102 (1998) 3813

[18] P.B. Armentrout, C.A. Austin, M.T. Rodgers, Int. J. Mass Spectrom. 330-332 (2012) 16.

[19] Y. Chen, M.T. Rodgers, J. Am. Chem. Soc. 134 (2012) 2313

[20] HyperChemTM Molecluar Modeling Software Package, Version 7.5, Hypercube Inc., 2002.

[21] M.J. Frisch, G.W. Trucks, H.B. Schlegel, G.E. Scuseria, M.A. Robb, J.R. Cheeseman, J.A. Montgomery, T. Vreven Jr, K.N. Kudin, J.C. Burant, J.M. Millam, S.S. Iyengar, J. Tomasi, V. Barone, B. Mennucci, M. Cossi, G. Scalmani, N. Rega, G. A. Petersson, H. Nakatsuji, M. Hada, M. Ehara, K. Toyota, R. Fukuda, J. Hasegawa, M. Ishida, T. Nakajima, Y. Honda, O. Kitao, H. Nakai, M. Klene, X. Li, J.E. Knox, H.P. Hratchian, J.B. Cross, C. Adamo, J. Jaramillo, R. Gomperts, R.E. Stratmann, O. Yazyev, A.J. Austin, R. Cammi, C. Pomelli, J.W. Ochterski, P.Y. Ayala, K. Morokuma, G.A. Voth, P. Salvador, J.J. Dannenberg, V.G. Zakrzerski, S. Dapprich, A.D. Daniels, M.C. Strain, O. Farkas, D.K. Malick, A.D. Rabuck, K. Raghavachari, J.B. Foresman, J.V. Ortiz, Q. Cui, A.G. Baboul, S. Clifford, J. Cioslowski, B.B. Stefanov, G. Liu, A. Liashenko, P. Piskorz, I. Komaromi, R.L. Martin, D.J. Fox, T. Keith, M.A. Al–Laham, C.Y. Peng, A. Nanayakkara, M. Challacombe, P.M.W. Gill, B. Johnson, W. Chen, M.W. Wong, C. Gonzalez, J.A. Pople, Gaussian 03, Revision B.03, Gaussian, Inc., Wallingford, CT, 2004.

[22] S.F. Boys, R. Bernardi, Mol. Phys. 19 (1979) 553

[23] F.B. van Duijneveldt, J.G.C.M. van Duijneveldt–van de Rijt, J.H. van Lenthe, Chem. Rev. 94 (1994) 1873

[24] M.T. Rodgers, K.M. Ervin, P.B. Armentrout, J. Chem. Phys. 106 (1997) 4499

[25] M.T. Rodgers, P.B. Armentrout, Mass Spectrom. Rev. 19 (2000) 215

[26] F. Muntean, P.B. Armentrout, J. Chem. Phys. 115 (2001) 1213

[27] F.A. Khan, D.E. Clemmer, R.H. Schultz, P.B. Armentrout, J. Phys. Chem. 97 (1993) 7978

[28] M.T. Rodgers, P.B. Armentrout, J. Phys. Chem. A 101 (1997) 2614

[29] P.B. Armentrout, J. Simons, J. Am. Chem. Soc. 114 (1992) 8627

[30] M.T. Rodgers, P.B. Armentrout, Mass Spectrom. Rev. 19 (2000) 215

[31] P.B. Armentrout, Int. J. Mass Spectrom. 193 (1999) 227

[32] B. Bosnich., C.K. Poon, R.D. Tobe, Inorg. Chem. 4 (1965) 1102

[33] J.H. Reibenspies, Acta Cryst. C48 (1992) 1717

[34] P. Bultinck, C. van Alsenoy, A. Gorminne, D. van de Vondel, J. Phys. Chem. A 104 (2000) 11801

[35] C. Ruan, Z. Yang, M.T. Rodgers, Int. J. Mass Spectrom. 267 (2007) 233

[36] C. Ruan, Z. Yang, N. Hallowita, M.T. Rodgers, J. Phys. Chem. A 109 (2007) 11539

[37] R.G. Wilson, G.R. Brewer, Wiley: New York, (1973) 118

[38] P.B. Armentrout, Int. J. Mass Spectrom. 193 (1999) 227

[39] E.P. Hunter, S.G. Lias, J. Phys. Chem. Ref. Data 27 (1998) 413

**Table 3.1.** Fitting Parameters of Equation 2.4, Threshold Dissociation Energies at 0 K, and Entropies of Activation at 1000 K of $M^+$(cyclen) Complexes[a]

| $M^+$ | $\sigma_0$[b] | n[b] | $E_0$[c] (eV) | $E_0$(PSL)[b] (eV) | Kinetic Shift (eV) | $\Delta S^\dagger$(PSL)[b] (J $mol^{-1}$ $K^{-1}$) |
|---|---|---|---|---|---|---|
| $Na^+$ | 75.3 (5.5) | 0.9 (0.1) | 5.11 (0.07) | 2.91 (0.12) | 2.20 | 79 (2) |
| $K^+$ | 18.3 (2.3) | 1.4 (0.1) | 2.63 (0.07) | 1.83 (0.08) | 0.80 | 70 (2) |
| $Rb^+$ | 10.8 (1.8) | 1.2 (0.1) | 2.07 (0.06) | 1.52(0.05) | 0.55 | 68 (2) |
| $Cs^+$ | 17.9 (1.3) | 1.3 (0.1) | 1.78 (0.05) | 1.36 (0.06) | 0.42 | 63 (2) |

[a] Present results, uncertainties are listed in parentheses. [b] Average values for loose PSL TS.
[c] No RRKM analysis.

**Table 3.2.** Bond Dissociation Enthalpies of $M^+$(cyclen) Complexes at 0 K in kJ/mol[a]

| $M^+$ | TCID | B3LYP[b] | | | MP2[c] | | |
|---|---|---|---|---|---|---|---|
| | | $D_e$ | $D_0$[d] | $D_{0,BSSE}$[d,e] | $D_e$ | $D_0$[d] | $D_{0,BSSE}$[d,e] |
| $Na^+$ | 280.8 (11.5) | 307.1 | 294.5 | 292.8 | 317.9 | 305.3 | 282.4 |
| | | 311.2 | 298.1 | 292.6 | 309.7 | 296.5 | 277.6 |
| $K^+$ | 176.4 (7.8) | 200.9 | 191.2 | 188.3 | 223.1 | 213.4 | 192.1 |
| | | 206.3 | 196.5 | 194.5 | 217.4 | 207.5 | 197.2 |
| $Rb^+$ | 146.7 (4.6) | 164.6 | 156.0 | 155.4 | 203.0 | 194.4 | 161.4 |
| | | 152.5 | 143.5 | 142.1 | 176.6 | 167.6 | 144.5 |
| $Cs^+$ | 131.3 (5.6) | 141.9 | 134.2 | 134.0 | 170.0 | 162.3 | 141.5 |
| | | 118.4 | 110.5 | 108.8 | 145.2 | 137.3 | 115.7 |
| MAD[f] | 7.4 (3.1) [g] | | | 8.8 (4.4) | | | 10.6 (6.4) |
| | | | | 14.3 (7.8) | | | 10.5 (9.2) |

[a]Present results, uncertainties are listed in parentheses. [b]Calculated at B3LYP/def2-TZVPPD and B3LYP/6-311+G(2d,2p)_HW level of theory. [c]Calculated at MP2(full)/def2-TZVPPD and MP2(full)/6-311+G(2d,2p)_HW level of theory using B3LYP optimized geometries. [d]Including ZPE corrections with the B3LYP/6-31+G* and B3LYP/def2-TZVPPD frequencies scaled by a factor of 0.9804. [e]Also includes BSSE corrections. [f]Mean absolute deviation. [g]Average experimental uncertainty.

## 3.8. Figure Captions

**Figure 3.1.** Structure of cyclen (1,4,7,10-tetraazacyclododecane, ta12C4). B3LYP/def2-TZVPPD optimized structures for low-energy conformations of ta12C4. Relative energies determined at the B3LYP/def2-TZVPPD level of theory are shown. The PBE0/def-TZVPPD calculated polarizabilities ($\alpha$) are also shown along with the calculated dipole moments ($\mu$).

**Figure 3.2.** Cross section for collision-induced dissociation of $Na^+$(ta12C4) with Xe as a function of kinetic energy in the center-of-mass frame (lower *x*-axis) and the laboratory frame (upper *x*-axis). Data are shown for a Xe pressure of ~0.2 mTorr, part a. Zero-pressure extrapolated cross section for collision-induced dissociation of the $Na^+$(ta12C4) complex with Xe in the threshold region as a function of kinetic energy in the center-of-mass frame (lower *x*-axis) and the laboratory frame (upper *x*-axis). The solid lines show the best fit to the data using the model of equation 2.4 convoluted over the neutral and ion kinetic and internal energy distributions. The dashed lines show the model cross section in the absence of experimental kinetic energy broadening for reactants with an internal energy of 0 K, part b

**Figure 3.3.** Cross sections for collision-induced dissociation of $M^+$(ta12C4) complexes, where $M^+ = K^+$, $Rb^+$, and $Cs^+$, with Xe as a function of kinetic energy in the center-of-mass frame (lower *x*-axis) and the laboratory frame (upper *x*-axis). Data are shown for a Xe pressure of ~0.2 mTorr, parts a-c, respectively. Zero-pressure extrapolated cross sections for collision-induced dissociation of $M^+$(ta12C4) complexes, where $M^+ = K^+$. $Rb^+$, and $Cs^+$. The solid lines show the best fits to the data using the model of equation 2.4 convoluted over the neutral and ion kinetic and internal energy distributions. The dashed lines show the model cross sections in the absence of experimental kinetic energy broadening for reactants with an internal energy of 0 K.

**Figure 3.4.** B3LYP/def2-TZVPPD optimized geometries and relative stabilities (in kJ/mol) of the stable low-energy conformers of the $Na^+$(ta12C4) complex.

**Figure 3.5.** B3LYP/def2-TZVPPD optimized geometries and relative stabilities (in kJ/mol) of the stable low-energy conformers of the $K^+$(ta12C4) complex.

**Figure 3.6.** B3LYP/def2-TZVPPD optimized geometries and relative stabilities (in kJ/mol) of the stable low-energy conformers of the $Rb^+$(ta12C4) complex.

**Figure 3.7.** B3LYP/def2-TZVPPD optimized geometries and relative stabilities (in kJ/mol) of the stable low-energy conformers of the $Cs^+$(ta12C4) complex.

**Figure 3.8.** Gibbs free energies (kJ/mol) calculated at the B3LYP/def2-TZVPPD level of theory of three conformations of $M^+$(ta12C4) complexes as a function of alkali metal cation identity relative to the energy of the ground-state conformer.

**Figure 3.9.** MP2(full) and B3LYP calculated versus TCID measured $M^+$-ta12C4 BDEs at 0 K (in kJ/mol), where $M^+ = Na^+$, $K^+$, $Rb^+$, and $Cs^+$. Calculated using the def2-TZVPPD basis set (●) and the 6-311+G(2d,2p)_HW basis set (○). All values are determined here and taken from Table 4.2.

**Figure 3.10.** Measured and Theoretical bond dissociation energies at 298 K (in kJ/mol) of the $M^+$(ta12C4) (blue) and $M^+$(12-crown-4) (red) complexes plotted versus the ionic radius of $M^+$ [39]. All values for the $M^+$(ta12C4) complexes are determined here and taken from Table 4.2. Values for the $M^+$(12C4) complexes are taken from [18].

**Figure 3.11.** Comparison of TCID measured and calculated $M^+$–ta12C4 and $M^+$–12C4 BDEs at 0 K (in kJ/mol), where $M^+ = Na^+$, $K^+$, $Rb^+$, and $Cs^+$. All values for the $M^+$(ta12C4) complexes are determined here and taken from Table 4.2. Values for the $M^+$(12C4) complexes are taken from [18].

Figure 3.1.

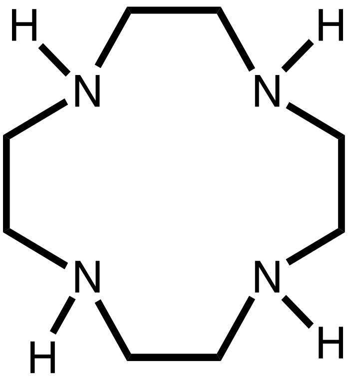

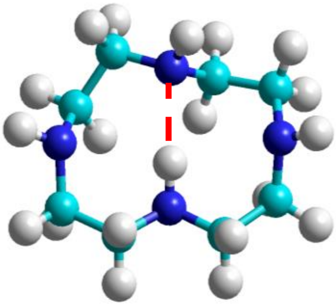

$C_1$ +++-
0.0 kJ/mol
$\mu = 1.27$ D
$\alpha = 20.16$ Å$^3$

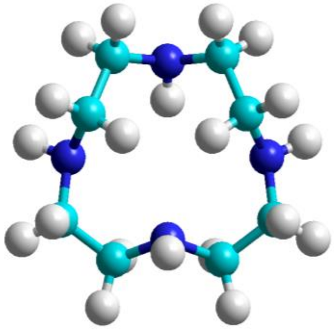

$C_s$ +++-
8.8 kJ/mol
$\mu = 2.27$ D
$\alpha = 20.09$ Å$^3$

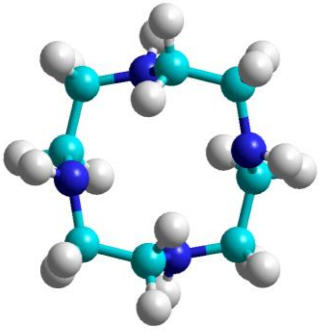

$^*C_2$ +-+-
19.4 kJ/mol
$\mu = 0.0$ D
$\alpha = 20.10$ Å$^3$

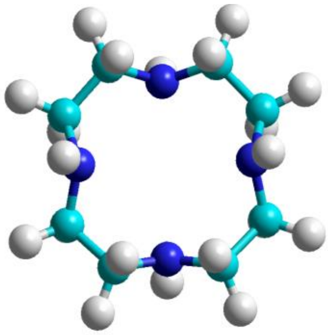

$C_2$ +-+-
41.6 kJ/mol
$\mu = 0.0$ D
$\alpha = 20.61$ Å$^3$
IM = 1

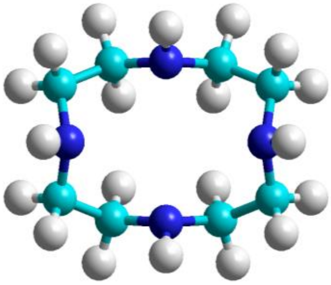

$C_{2v}$ ++++
44.5 kJ/mol
$\mu = 0.26$ D
$\alpha = 20.34$ Å$^3$
IM = 1

Cyclen (1,4,7,10-tetraazacyclododecane)

Figure 3.2.

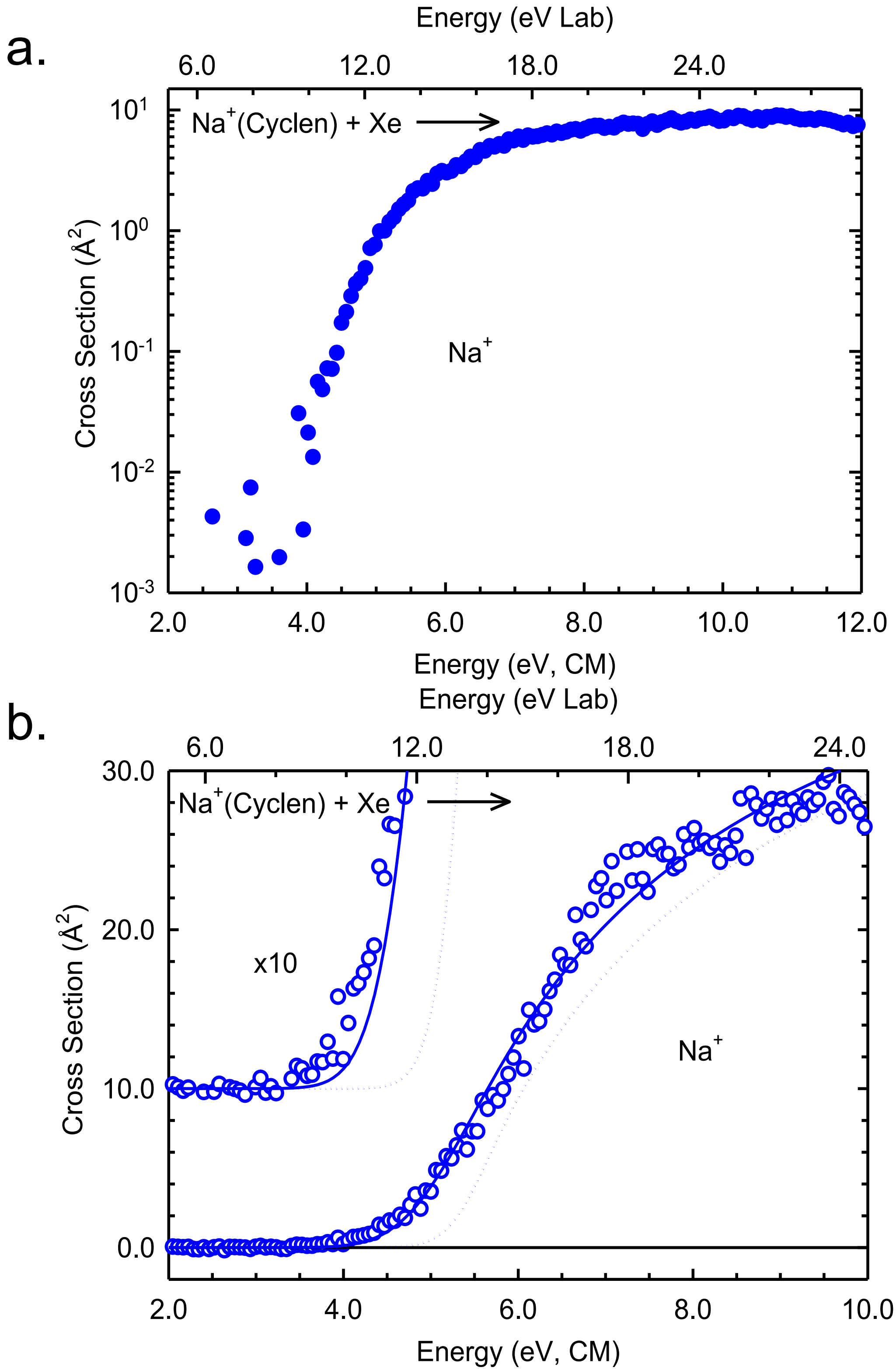
a.
Energy (eV Lab)
6.0
12.0
18.0
24.0
$10^1$
$10^0$
$10^{-1}$
$10^{-2}$
$10^{-3}$
Cross Section (Å$^2$)
Na$^+$(Cyclen) + Xe
Na$^+$
2.0
4.0
6.0
8.0
10.0
12.0
Energy (eV, CM)
b.
Energy (eV Lab)
6.0
12.0
18.0
24.0
30.0
20.0
10.0
0.0
Cross Section (Å$^2$)
Na$^+$(Cyclen) + Xe
x10
Na$^+$
2.0
4.0
6.0
8.0
10.0
Energy (eV, CM)

Figure 3.3.

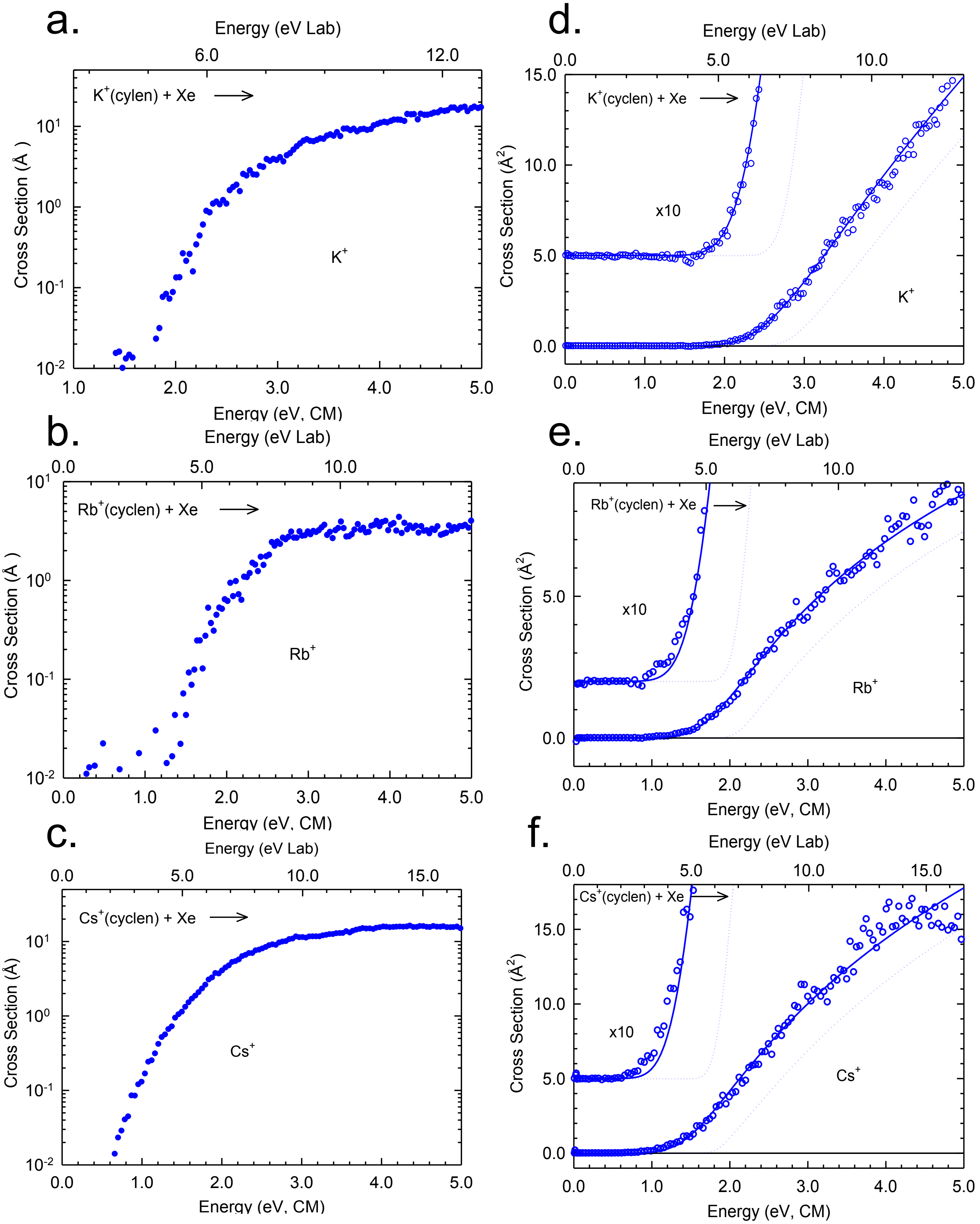
a.
Energy (eV Lab)
6.0
12.0
K$^+$(cylen) + Xe →
$10^1$
$10^0$
$10^{-1}$
$10^{-2}$
Cross Section (Å )
K$^+$
1.0
2.0
3.0
4.0
5.0
Energy (eV, CM)
b.
Energy (eV Lab)
0.0
5.0
10.0
Rb$^+$(cyclen) + Xe →
$10^1$
$10^0$
$10^{-1}$
$10^{-2}$
Cross Section (Å )
Rb$^+$
0.0
1.0
2.0
3.0
4.0
5.0
Energy (eV, CM)
c.
Energy (eV Lab)
0.0
5.0
10.0
15.0
Cs$^+$(cyclen) + Xe →
$10^1$
$10^0$
$10^{-1}$
$10^{-2}$
Cross Section (Å)
Cs$^+$
0.0
1.0
2.0
3.0
4.0
5.0
Energy (eV, CM)
d.
Energy (eV Lab)
0.0
5.0
10.0
15.0
10.0
5.0
0.0
K$^+$(cyclen) + Xe →
x10
Cross Section (Å$^2$)
K$^+$
0.0
1.0
2.0
3.0
4.0
5.0
Energy (eV, CM)
e.
Energy (eV Lab)
0.0
5.0
10.0
Rb$^+$(cyclen) + Xe →
5.0
0.0
x10
Cross Section (Å$^2$)
Rb$^+$
0.0
1.0
2.0
3.0
4.0
5.0
Energy (eV, CM)
f.
Energy (eV Lab)
0.0
5.0
10.0
15.0
Cs$^+$(cyclen) + Xe →
15.0
10.0
5.0
0.0
x10
Cross Section (Å$^2$)
Cs$^+$
0.0
1.0
2.0
3.0
4.0
5.0
Energy (eV, CM)

Figure 3.4.

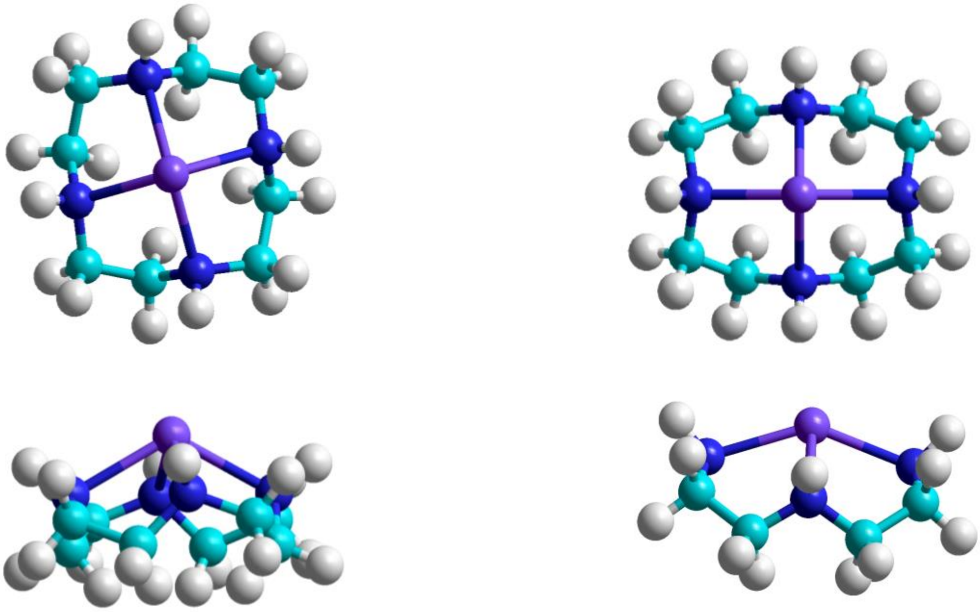

$C_4$ ++++
0.0 kJ/mol

$C_{2v}$ ++++
21.7 kJ/mol

$Na^+$(cyclen)

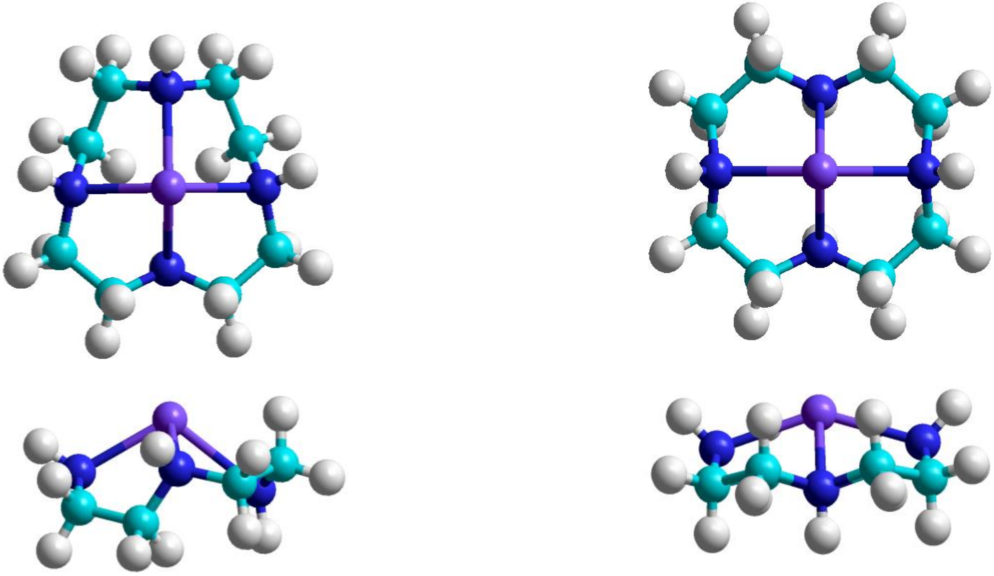

$C_s$ +++-
30.6 kJ/mol

$C_{2v}$ +-+-
52.1 kJ/mol

Figure 3.5.

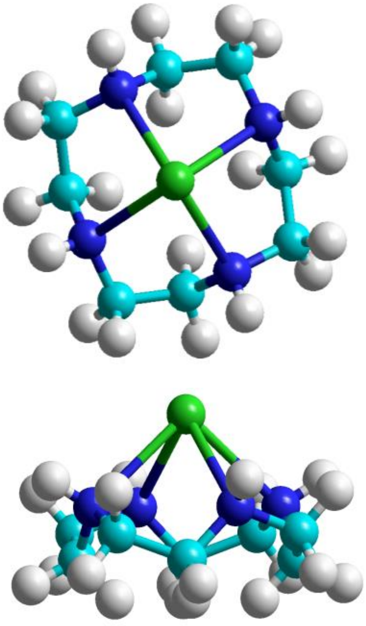

$C_4$ ++++
0.0 kJ/mol

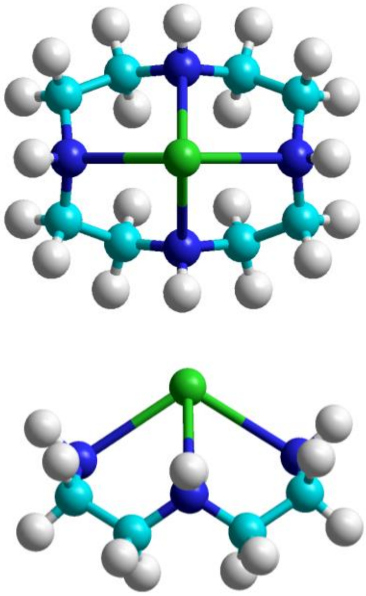

$C_{2v}$ ++++
26.9 kJ/mol

$K^+$(cyclen)

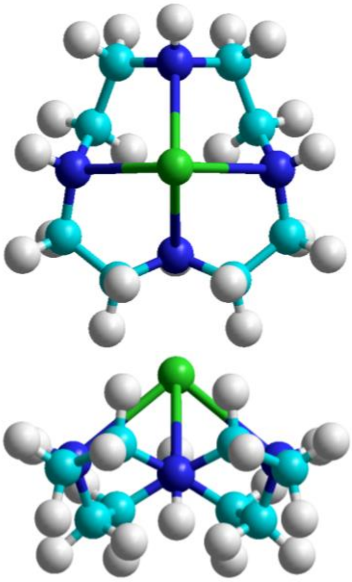

$C_s$ +++-
26.1 kJ/mol

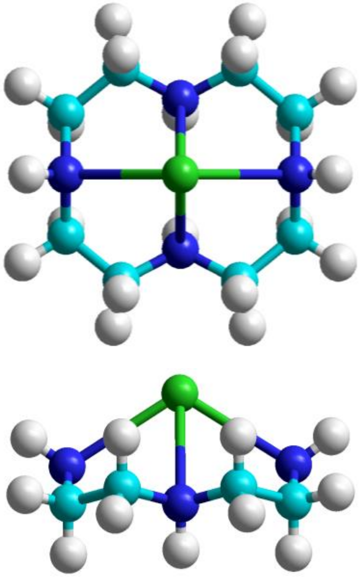

$C_{2v}$ +-+-
47.9 kJ/mol

Figure 3.6.

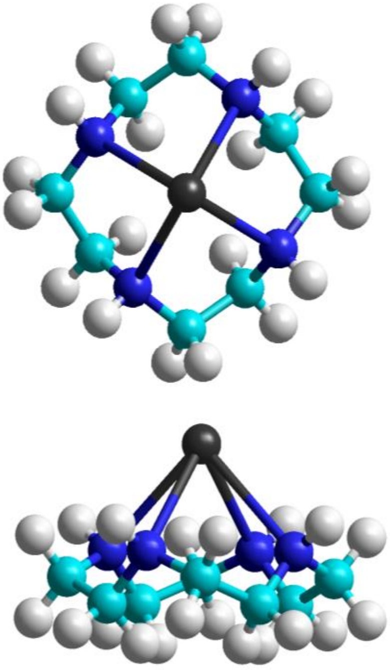

$C_4$ ++++
0.0 kJ/mol

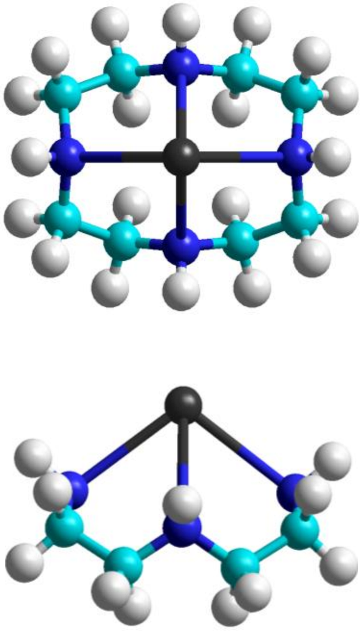

$C_{2v}$ ++++
28.1 kJ/mol

Rb$^+$(cyclen)

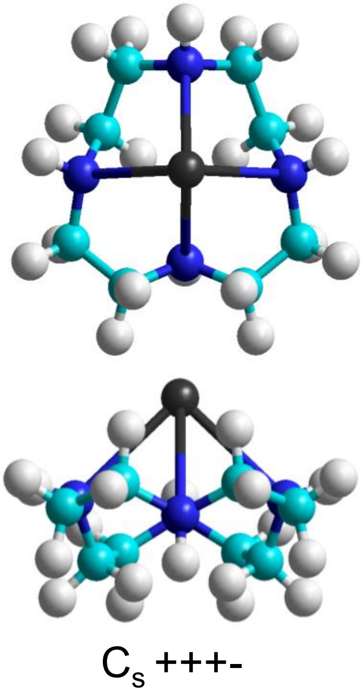

$C_s$ +++-
24.1 kJ/mol

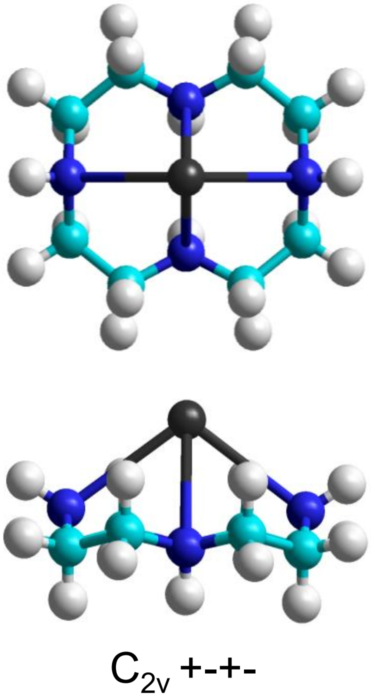

$C_{2v}$ +-+-
45.9 kJ/mol

Figure 3.7.

Cs$^+$(cyclen)

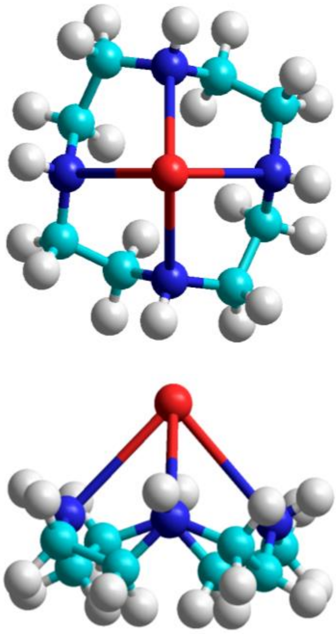

$C_4$ ++++
0.0 kJ/mol

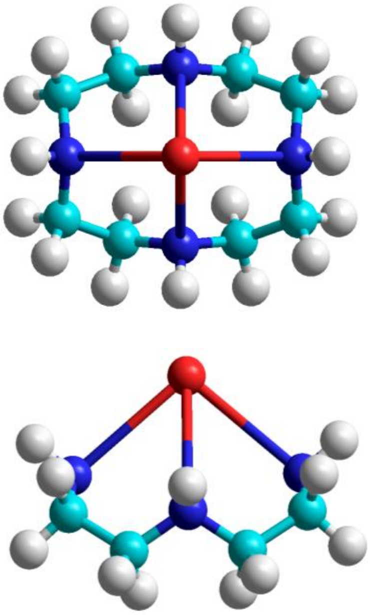

$C_{2v}$ ++++
28.4 kJ/mol

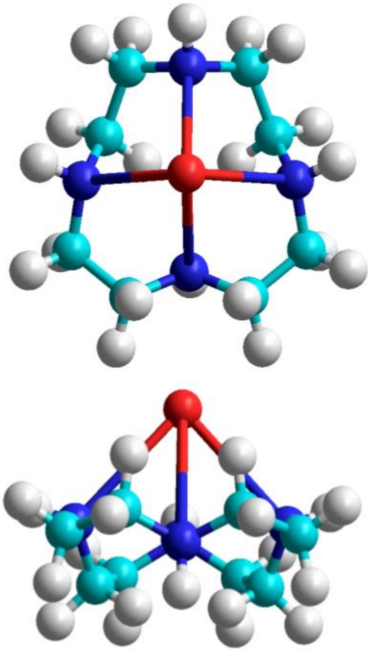

$C_s$ +++-
23.8 kJ/mol

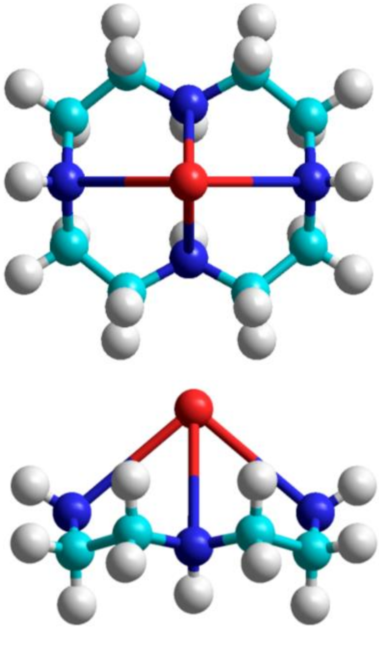

$C_{2v}$ +-+-
44.5 kJ/mol

Figure 3.8.

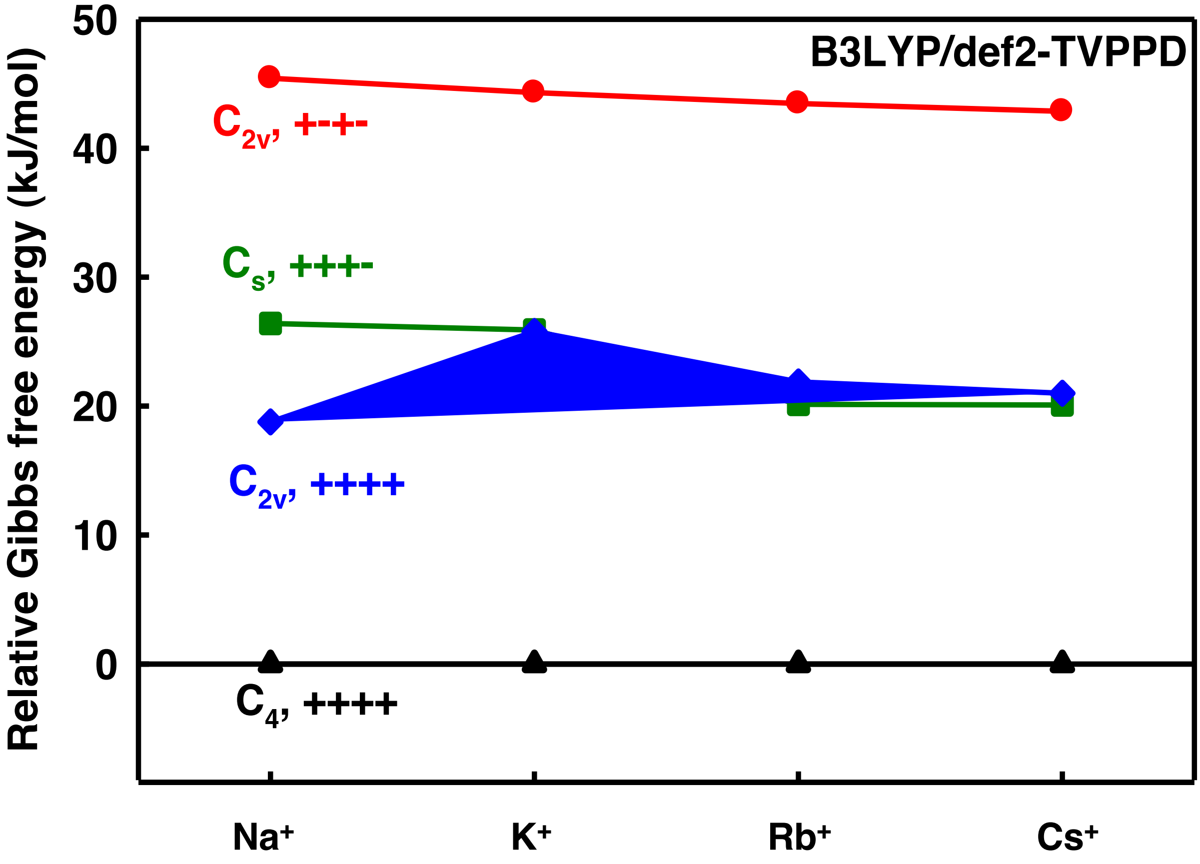
B3LYP/def2-TVPPD
C2v, ++-+-
Cs, +++-
C2v, ++++
C4, ++++
Relative Gibbs free energy (kJ/mol)
50
40
30
20
10
0
Na+
K+
Rb+
Cs+

Figure 3.9.

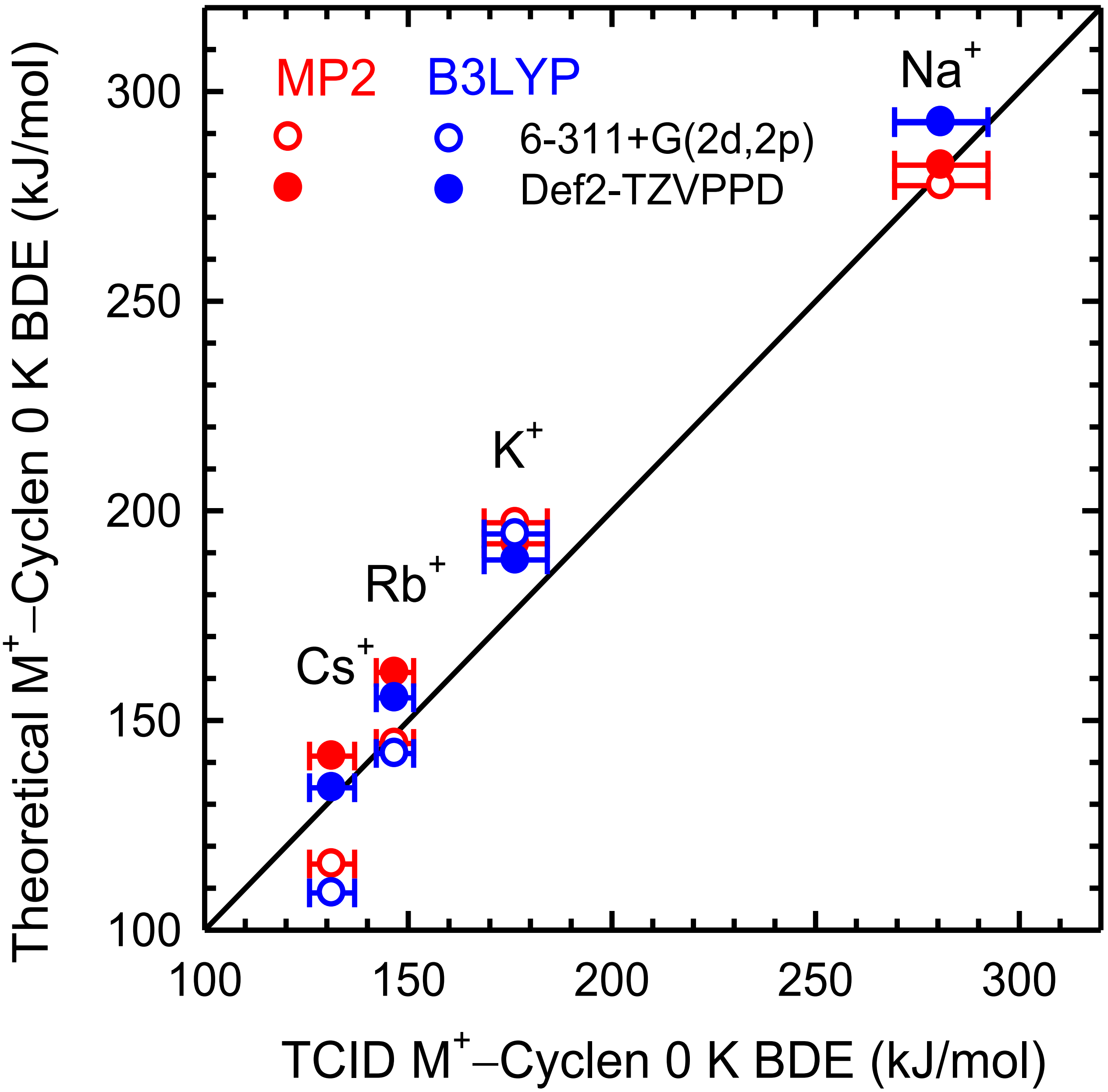
MP2
B3LYP
6-311+G(2d,2p)
Def2-TZVPPD
Na$^+$
K$^+$
Rb$^+$
Cs$^+$
Theoretical M$^+$–Cyclen 0 K BDE (kJ/mol)
TCID M$^+$–Cyclen 0 K BDE (kJ/mol)
100
150
200
250
300
100
150
200
250
300

Figure 3.10.

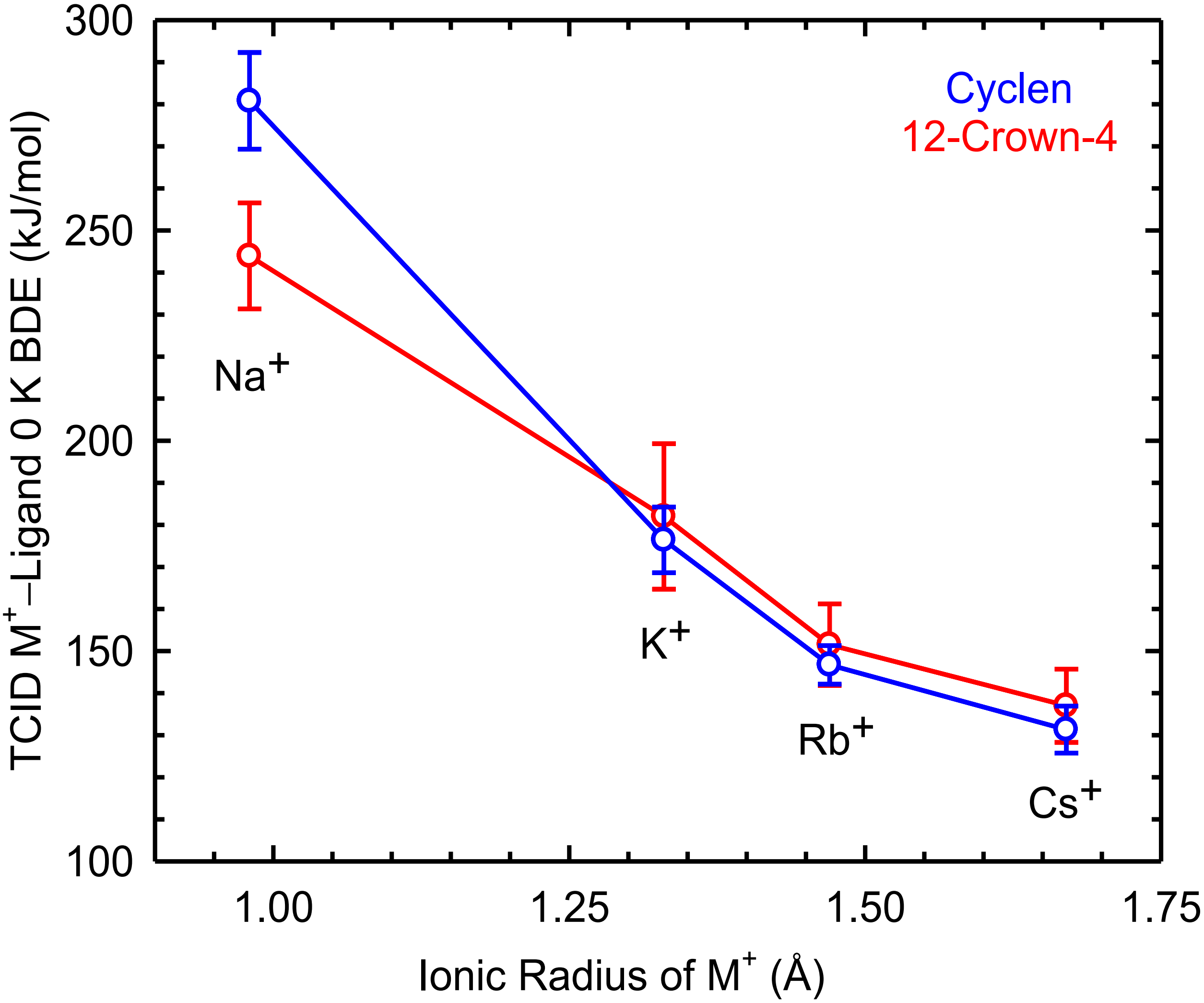

Cyclen
12-Crown-4
Na+
K+
Rb+
Cs+
TCID M+–Ligand 0 K BDE (kJ/mol)
300
250
200
150
100
1.00
1.25
1.50
1.75
Ionic Radius of M+ (Å)

Figure 3.11.

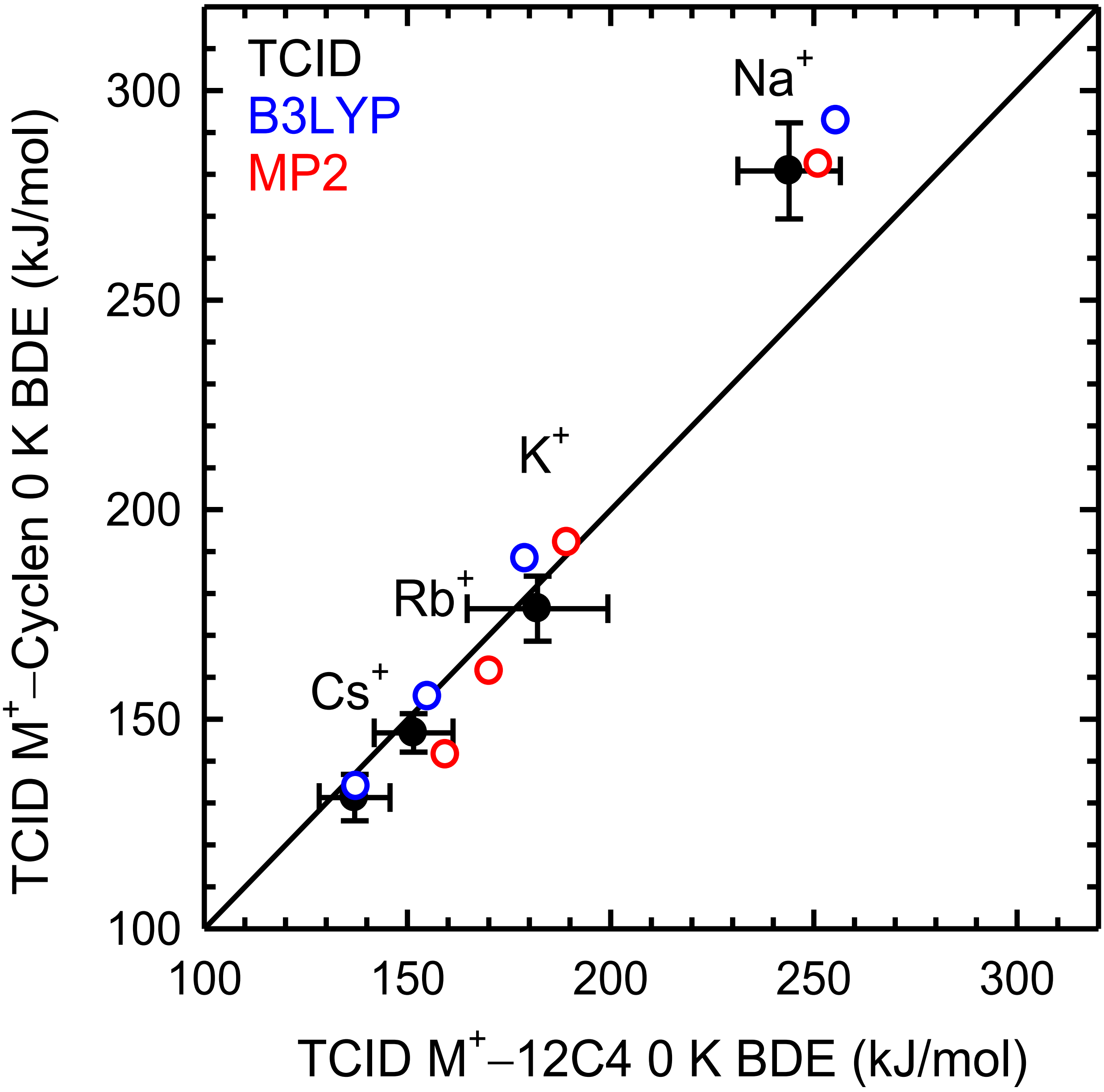
TCID
B3LYP
MP2
Na$^+$
K$^+$
Rb$^+$
Cs$^+$
300
250
200
150
100
100
150
200
250
300
TCID M$^+$–Cyclen 0 K BDE (kJ/mol)
TCID M$^+$–12C4 0 K BDE (kJ/mol)

# CHAPTER 4

# INFRARED MULTIPLE PHOTON DISSOCIATION ACTION SPECTROSCOPY OF ALKALI METAL CATION – CYCLEN COMPLEXES: EFFECTS OF ALKALI METAL CATION SIZE ON GAS-PHASE CONFORMATION

Portions of this chapter were reprinted with permission Austin, C.A., Chen, Y., Kaczan, C.M., Berden, G., Oomens, J., and Rodgers, M.T. Infrared Multiple Photon Dissociation Action Spectroscopy of Alkali Metal Cation – Cyclen Complexes: Effects of Alkali Metal Cation Size on Gas-Phase Conformation. Int. J. Mass Spectrom. 354–355 (2013) 346.

## 4.1. Introduction

Cyclen (1,4,7,10-tetraazacyclododecane, ta12C4), the aza analogue of 12-crown-4 (1,4,7,10-tetraoxacyclodecane) is extensively used in many applications ranging from biomedical imaging [1–4] to many different areas of chemistry including synthetic, analytical, and pharmaceutical chemistry [5–10]. For most applications, the backbone of ta12C4 is highly functionalized to effect very strong binding to transition metal cations.

IRMPD action spectroscopy has previously been used to investigate crown ether interactions with protons [11], metal cations [12–15], and small organic cations [16–19]. All of the studies reported to date have involved crown ethers possessing oxygen donor atoms, and have primarily focused on the 18-membered ring, 18-crown-6, rather than the nitrogen analogs and smaller 12-membered ring of ta12C4 examined here. For the alkali metal cation complexes of 18-crown-6, the ground-state conformation changes as a function of the size of the alkali metal cation, and in most cases evidence for a small population of excited conformers is found in the IRMPD experiments [14]. For the 12-membered ring, 12-crown-4, Armentrout and co-workers investigated complexes with the dications, $Zn^{2+}$ and $Cd^{2+}$ [16]. In this study, results were compared to the interactions with 15-crown-5 and 18-crown-6, and showed that the conformation of the metal-crown ether complex is highly dependent on the size and charge of the metal cation as well as the flexibility of the crown ether [16].

In this chapter, the IRMPD action spectra were measure for the dissociation of four $M^+$(ta12C4) complexes, where $M^+ = Na^+$, $K^+$, $Rb^+$, and $Cs^+$. Identification of the conformation(s) accessed in the experiments was achieved by comparison to linear IR spectra derived from quantum chemical calculations of the stable low-lying structures of the $M^+$(ta12C4) complexes with structures optimized and vibrational frequencies determined at the B3LYP/def2-TZVPPD level of theory. Relative energies for these complexes were calculated at the B3LYP/def2-TZVPPD and MP2(full)/def2-TZVPPD levels of theory, and for the largest alkali metal cations, $Rb^+$ and $Cs^+$, an ECP was used to describe the alkali metal cation.

## 4.2. Infrared Multiple Photon Dissociation Action Spectroscopy Experiments

IRMPD action spectra of four $M^+$(ta12C4) complexes were measured using a 4.7 T Fourier transform ion cyclotron resonance mass spectrometer (FT-ICR MS) coupled to the FELIX free electron laser (FEL) previously located at the FOM Institute for Plasma Physics, Rijnhuizen, but recently moved to the Radboud University of Nijmegen. The experimental setup used in these experiments has been described in detail elsewhere [20,21]. The $M^+$(ta12C4) complexes, where $M^+ = Na^+$, $K^+$, $Rb^+$, and $Cs^+$, were formed by electrospray ionization (ESI) using a Micromass "Z-spray" source and accumulated in a hexapole trap for several seconds followed by pulsed extraction through a quadrupole bender and injected in the ICR cell via rf octopole ion guide through electrostatic switching of the dc bias on the octopole. This dc bias switching method allows ions to be captured in the ICR cell in the absence of a gas pulse, thus avoiding collisional heating of the ions as described in detail elsewhere [22]. Isolation of the precursor ions was achieved using stored waveform inverse Fourier transform (SWIFT) techniques prior to irradiation by the FEL at pulse energies of ~50 mJ per macropulse of 5 μs duration at a repetition rate of 10 Hz. The number of photons required to effect efficient dissociation of the $M^+$(ta12C4) complexes varies inversely with the size of the alkali metal cation such that the irradiation time was varied between 2 and 5 s for the complexes investigated here, corresponding to interaction with 20 to 50 macropulses over the wavelength region extending from 16.7 μm (600 $cm^{-1}$) to 6.3 μm (1600 $cm^{-1}$).

## 4.3. Theoretical Calculations

Initial candidate structures for the $M^+$(ta12C4) complexes were generated using five of the low-energy neutral ta12C4 structures, i.e., those that were expected to provide the most favorable geometries for interaction with the alkali metal cation, and placing the alkali metal cation in various positions to exhaustively probe the range of geometries that allow interaction with one, two, three, and all four of the nitrogen donor atoms. In addition, structures analogous to the ground-state conformations of the $M^+$(12-crown-4) complexes previously reported were also used [23-27]. Again, the 15 most stable structures of each of the $M^+$(ta12C4) complexes from the simulated annealing cycles performed were chosen for higher-level geometry optimization.

Geometry optimizations of neutral ta12C4 and the $M^+$(ta12C4) complexes, where $M^+$ = $Na^+$, $K^+$, $Rb^+$, and $Cs^+$, were performed using the def2 triple zeta valence basis sets of Rappoport and Furche, def2–TZVPPD, which include polarization and diffuse functions, and use an ECP for the rubidium and cesium atoms developed by Leininger et al [28–29]. The def2-TZVPPD basis set was obtained from the EMSL basis set exchange [30–31]. All structures were optimized at the B3LYP/def2-TZVPPD level of theory using the Gaussian 03 suite of programs [32]. Theoretical linear IR spectra were generated using the calculated harmonic vibrational frequencies (scaled by a factor of 0.9704) and IR intensities. For comparison to the measured IRMPD action spectra, the theoretical linear IR spectra were broadened using a 20 $cm^{-1}$ full width at half maximum (fwhm) Gaussian line shape.

## 4.4. Results

### 4.4.1. IRMPD Action Spectra

Photodissociation of $M^+$(ta12C4), where $M^+ = Na^+$, $K^+$, $Rb^+$, and $Cs^+$, results in loss of the intact neutral ta12C4 ligand and detection of the alkali metal cation. The IRMPD yield for each complex was determined using Eq. (4.1),

$$IRMPD\ yield = I_{M^+} / ( I_{M^+(cyclen)} + I_{M^+} ) \tag{4.1}$$

where the $M^+$ fragment ion intensity ($I_{M^+}$) after laser irradiation is divided by the total ion intensity $(I_{M^+(cyclen)} + I_{M^+})$. The IRMPD yield was not corrected for variations in the laser power as a function of the wavelength of the FEL because the uncorrected spectra provide a better match to the relative intensities of the linear IR spectra predicted. The IRMPD behavior was investigated over the range of wavelengths extending from 6.3 μm (1600 $cm^{-1}$) to 16.7 μm (600 $cm^{-1}$) for all four $M^+$(ta12C4) complexes.

The IRMPD action spectra of the four alkali metal cation–ta12C4 complexes investigated here are compared in **Figure 4.1**. As can be seen in the figure, the features observed for the $Na^+$(ta12C4) complex are retained for all of the other alkali metal cation-ta12C4 complexes. New spectral features appear in the IRMPD spectrum of $K^+$(ta12C4), and become very obvious in the spectra of the larger alkali metal cation-ta12C4 complexes, $Rb^+$(ta12C4), and $Cs^+$(ta12C4). The IRMPD yields for the $M^+$(ta12C4) complexes increase as the size of the alkali metal cation increases, consistent with the decrease in the strength of binding with increasing size of the alkali metal cation. The IRMPD yield of the most intense spectral feature(s) increases by more than a factor of 10 from $Na^+$(ta12C4) to $K^+$(ta12C4), while increasing by a factor of three from $K^+$(ta12C4) to $Rb^+$(ta12C4), and 1.5 from $Rb^+$(ta12C4) to $Cs^+$(ta12C4). Small systematic shifts in the peak positions are observed across these systems, consistent with observations reported in previous studies of alkali metal cations interacting with a variety of amino acid and nucleobase ligands [33-42]. The spectral features that are retained throughout the IRMPD spectra of the four $M^+$(ta12C4) complexes examined here are increasingly blue shifted as the size of the alkali metal cation increases, except for the spectral feature centered at 805 $cm^{-1}$ in the spectrum of the $Na^+$(ta12C4) complex. A slight blue shift of this feature (to 808 $cm^{-1}$) is observed for $K^+$(ta12C4), whereas no shift is observed for the $Rb^+$(ta12C4) and $Cs^+$(ta12C4) complexes.

## 4.4.2. Theoretical Results

Structures for the complexes of ta12C4 to the alkali metal cations, $Na^+$, $K^+$, $Rb^+$, and $Cs^+$ were calculated as describe in the Theoretical Calculations section of **Chapter 2**. The nomenclature used to identify the different conformations is adopted from a previous study by Bosnich *et al*, where (+) and (-) signs are used to designate the positions of the amine hydrogen atoms as lying above or below the plane of the ring [43]. The optimized ground-state structures obtained for the $M^+$(ta12C4) complexes, where $M^+$ = $Na^+$, $K^+$, $Rb^+$, and $Cs^+$, along with the calculated binding energies are shown in **Figure 4.2**. Similar figures for the three most stable excited low-energy conformers are provided as **Figures 4.3–4.5**. Relative enthalpies and Gibbs free energies as well as estimated populations for Maxwell-Boltzmann distributions at 298 K calculated at the B3LYP and MP2(full) levels of theory, using the B3LYP/def2-TZVPPD optimized geometries and the def2-TZVPPD basis set are given in **Table 4.1**. For both levels of theory, the relative enthalpies and Gibbs free energies at 298 K of these complexes vary with the size of the metal cation, see **Table 4.1** and **Figure 4.6**. Both B3LYP and MP2(full) theories find that for all four alkali metal cation-ta12C4 complexes, the $C_4$(++++) conformer is the ground-state conformation, while the $C_{2v}$(+-+-) conformer is the least stable among the four stable low-energy conformations computed. In contrast, the relative stabilities of the $C_{2v}$(++++) and $C_s$(+++-) conformers vary with the size of the alkali metal cation and the level of theory employed. At the B3LYP level of theory, there is little variation in the relative Gibbs free energy as a function metal cation identity, **Figure 4.6a**. In contrast, the MP2(full) level of theory predicts greater variation in the relative Gibbs free energies as a function metal cation identity, **Figure 4.6b**, where the relative stabilities become closer as the size of the alkali metal cation increases. It was previously shown that B3LYP/def2-TZVPPD results exhibit the best agreement with the experimentally determined binding affinities of the alkali metal cation–ta12C4 complexes [44]. Therefore, the following discussion focuses on the geometries optimized at the B3LYP/def2-TZVPPD level of theory, while energetics computed at the B3LYP and MP2(full) levels of theory using the def2-TZVPPD basis set are compared.

For all of the alkali metal cation–ta12C4 complexes at both the B3LYP and MP2(full) levels of theory, the lowest energy structure is the $C_4$(++++) conformation, where all four nitrogen donor atoms are oriented towards the metal cation (**Figure 4.2**). For all of the alkali metal cation–ta12C4 complexes, the four $M^+$–N bond distances are equal and increase with the size of the alkali metal cation from 2.434 Å for $Na^+$ to 3.190 Å for $Cs^+$. The $\angle NM^+N$ bond angles decrease with the size of the cation from 76.4° to 57.7° for the complexes to $Na^+$ through $Cs^+$, consistent with the elongations of the $M^+$–N bond distances. In concert with these changes, the ∠NCCN and ∠CNCC dihedral angles increase and decrease from 61.1° to 64.3° and -161.4° to -160.5°, respectively, for the complexes to $Na^+$ through $Cs^+$. For the $C_{2v}$(++++) conformer of the $Na^+$(ta12C4) complex, all four $M^+$–N bond distances are equal, whereas the four $M^+$-N bond distances are split into two groups that differ by 0.07, 0.10, and 0.17 Å in length for the complexes to $K^+$, $Rb^+$, and $Cs^+$, respectively, (**Figures 4.3**). In the $C_{2v}$(++++) conformations, and the ∠NCCN dihedral angles alternate between positive and negative values. For the $C_s$(+++-) conformations (**Figure 4.4**), one of the amino groups is further away from the metal cation than the other three, suggesting a weaker interaction with the fourth donor atom. In the $C_{2v}$(+-+-) conformers (**Figure 4.5**), the amine hydrogen atoms alternate up and down with respect to the position of the alkali metal cation, and the ∠NCCN dihedral angles alternate between positive and negative values. The four ∠NCCN dihedral angles of the $C_{2v}$(+-+-) conformer of $Na^+$(ta12C4) are equal, but are again split into two groups that differ by 0.10°, 7.0°, and 6.0° for the complexes to $K^+$, $Rb^+$, and $Cs^+$, respectively.

## 4.5. Discussion

### 4.5.1. Comparison of Experimental IRMPD and Theoretical IR Spectral of $Na^+$(ta12C4)

**Figure 4.7** compares the experimental IRMPD action spectrum with the theoretical IR spectra for the four low-energy conformers found for the $Na^+$(ta12C4) complex. Because the experimental IRMPD yields are based on multiple photon processes, while the theoretical IR intensities are based on a single photon absorption process, the relative intensities predicted by theory do not always correspond well with the measured action spectrum. Good agreement between the IRMPD action spectrum and the calculated IR spectrum for the ground-state $C_4$(++++) conformer is obtained for the bands that are observed experimentally, suggesting that the ground-state $C_4$(++++) conformer is accessed in the experiments. For the $C_4$(++++) conformer, the bands centered at 812 and 933 $cm^{-1}$ are blue shifted by 7 $cm^{-1}$ relative to the measured IRMPD spectrum, while the band centered at 1366 $cm^{-1}$ is blue shifted by 21 $cm^{-1}$. The peak centered at 1068 $cm^{-1}$ in the theoretical spectrum for the $C_4$(++++) conformer is red shifted by 2 $cm^{-1}$ relative to the measured IRMPD spectrum. However, many additional bands of lower intensity were predicted that are not observed, indicating that the IRMPD efficiency at these wavelengths is poor for the strongly bound $Na^+$(ta12C4) complex. For the $C_{2v}$(++++) conformer, the bands centered at 814, and 927, and 1355 $cm^{-1}$ are blue shifted by 9, 1, and 10 $cm^{-1}$, respectively, relative to the measured IRMPD spectrum. The peak centered at 1061 $cm^{-1}$ in the theoretical spectrum for the $C_{2v}$(++++) conformer is red shifted by 9 $cm^{-1}$ relative to the measured IRMPD spectrum. The presence of the $C_{2v}$(++++) conformer in the experiments is difficult to rule out without a more careful analysis. The $C_{2v}$(++++) conformer lies 18.9 and 19.6 kJ/mol higher in free energy than the ground-state $C_4$(++++) conformer at the B3LYP and MP2(full) levels of theory, respectively. Assuming that the computed energies are reliable and that an equilibrium distribution at 298 K were present, the $C_{2v}$(++++) conformer would comprise less than 0.05% of the reactant population. A broad spectral feature between 760 and 860 $cm^{-1}$ is predicted in the theoretical IR spectrum of the $C_s$(+++-) conformer instead of the relatively narrower band observed at 805 $cm^{-1}$ in the IRMPD action spectrum. The bands centered at 900, 1068, and 1357 $cm^{-1}$ in the theoretical spectrum of the $C_s$(+++-) conformer are red shifted by 26, 2, and 12 $cm^{-1}$, respectively, relative to the measured IRMPD spectrum. The $C_s$(+++-) conformer lies 26.4 and 20.8 kJ/mol above the ground state $C_4$(++++) conformer at the B3LYP and MP2(full) levels of theory, and would thus comprise less than 0.1% of the reactant ion population in a 298 K Maxwell-Boltzman distribution, suggesting this conformer was not accessed in this experiments. The spectra calculated for the $C_{2v}$(+-+-) conformer also exhibits intense spectral features near those observed in the IRMPD action spectrum, but in most cases the computed bands are moderately red shifted, suggesting that this conformer was not accessed in the experiments. The absence in the measured IRMPD spectrum of the very intense band centered at 674 $cm^{-1}$ in the predicted IR spectrum, and the relatively high free energy computed for this conformer are probably the most diagnostic for confirming that this conformer was not accessed in the experiments.

The agreement between the experimental IRMPD action spectrum and the theoretical IR spectrum for the ground-state $C_4$(++++) conformer allows for a qualitative assignment of the vibrational features for the $Na^+$(ta12C4) complex (**Table 4.2**). The most intense band observed at 805 $cm^{-1}$ in the IRMPD spectrum for $Na^+$(ta12C4) corresponds to a complex mode comprised of $M^+$–N stretching, N–H bending, and CNC scissoring. The next most intense spectral feature, at 1070 $cm^{-1}$, corresponds to a mode comprised of $CH_2$ stretching and a C–N torsion that is doubly degenerate and is red shifted by 2 $cm^{-1}$ relative to the measured IRMPD spectrum. The very weak band observed at 926 $cm^{-1}$ is also doubly degenerate and corresponds to a mode of mixed character arising from N–H and $CH_2$ rocking. The weak band observed at 1345 $cm^{-1}$ corresponds to doubly degenerate $CH_2$ scissoring modes.

### 4.5.2. Comparison of Experimental IRMPD and Theoretical IR Spectral of $K^+$(ta12C4)

The IRMPD action spectrum of $K^+$(ta12C4) is similar to that of $Na^+$(ta12C4), see **Figure 4.1**. However, the IRMPD yield has increased by more than an order of magnitude such that new bands are now evident at 835, 888, 1126, 1244, and 1451 $cm^{-1}$. This is primarily the result of enhanced sensitivity associated with more facile dissociation of this less strongly bound system. The $K^+$-ta12C4 bond dissociation energy (BDE) is 176.4 ± 7.8 kJ/mol, and is substantially weaker than the $Na^+$–ta12C4 BDE, 280.8 ± 11.5 kJ/mol [44]. Based on the measure BDEs, 63% fewer photons are needed to dissociate the $K^+$(ta12C4) complex as compared to the $Na^+$(ta12C4) complex.

Good agreement between the measured IRMPD action spectrum and the calculated IR spectrum for the ground-state $C_4$(++++) conformer is found, as can be seen in the comparison of **Figure 4.8**. The band positions are well reproduced, suggesting that the ground-state structure is accessed in the experiments. In most cases, the bands in the theoretical IR spectrum for the $C_4$(++++) conformer are slightly red shifted as compared to the measured IRMPD spectrum, e.g., the bands centered at 808, 888, 1075, 1126, and 1244 $cm^{-1}$ in the measured spectrum are red shifted by 2, 6, 6, 15, and 5 $cm^{-1}$, respectively, in the calculated spectrum. In contrast, the bands that are centered at 835, 1354, and 1451 in the measured IRMPD spectrum are blue shifted in the predicted spectrum for the $C_4$(++++) conformer by 4, 13, and 3 $cm^{-1}$, respectively. For the calculated spectrum of the $C_{2v}$(++++) conformer, overlapping spectral features are also observed, but most of the spectral features are red shifted as compared to experiment.

Bands centered at 793, 863, 1058, and 1432 cm$^{-1}$ in the theoretical IR spectrum for the $C_{2v}$(++++) conformer are red shifted by 17-25 cm$^{-1}$, while the bands centered at 928 and 1351 cm$^{-1}$ are red shifted by 9 and 3 cm$^{-1}$, respectively, relative to the measured IRMPD spectrum. The bands at 1134 and 1260 cm$^{-1}$ in the theoretical IR spectrum for the $C_{2v}$(++++) conformer are blue shifted by 8 and 16 cm$^{-1}$, respectively, relative to the measured IRMPD spectrum. The $C_{2v}$(++++) conformer lies 25.8 and 25.7 kJ/mol above the ground-state $C_4$(++++) conformer at the B3LYP and MP2(full) levels of theory, respectively, an increase in the relative Gibbs free energy difference for the ground-state and first-excited conformers as compared to those of the Na$^+$(ta12C4) complex. The spectrum computed for the $C_s$(+++-) conformer exhibits a broad feature between 760 and 860 cm$^{-1}$ that does not match well with the peak observed at 808 cm$^{-1}$ in the experimental IRMPD spectrum of the K$^+$(ta12C4) complex. Other features observed in the low frequency region between 600 and 1000 cm$^{-1}$ are not reproduced or are blue shifted as compared to experiment for the $C_s$(+++-) conformer. The three bands observed at 1075, 1126, and 1354 cm$^{-1}$ are in good agreement with the $C_s$(+++-) conformer in position, but not in relative intensity. The $C_s$(+++-) conformer lies 25.9 and 18.8 kJ/mol above the ground-state $C_4$(++++) conformer at the B3LYP and MP2(full) levels of theory respectively, a decrease in the relative Gibbs free energy difference for the ground-state and second-excited conformers as compared to those of the Na$^+$(ta12C4) complex. Based on the relative Gibbs free energies, the $C_{2v}$(++++) and $C_s$(+++-) conformers would comprise less than 0.1% of the K$^+$(ta12C4) population at 298 K. The observed spectral differences and relative stabilities suggest that these conformers are not accessed in the experiments. There are several spectral features predicted for the $C_{2v}$(+-+-) conformer that overlap with those observed in the low frequency region, i.e., those centered at 811, 886, and 937 cm$^{-1}$, that are only slightly blue shifted (by less than 3 cm$^{-1}$) relative to the measured IRMPD spectrum, but the relative intensities differ markedly. Spectral features matching those that are observed at 1075, 1354, and 1451 cm$^{-1}$ are red shifted in the theoretical IR spectrum for the $C_{2v}$(+-+-) conformer by 9, 10, and 6 $cm^{-1}$, respectively. There are several intense spectral features predicted in the theoretical IR spectrum for the $C_{2v}$(+-+-) conformer (i.e., the peaks centered at 640, 740, 1136, and 1483 $cm^{-1}$) that are not observed in the IRMPD action spectrum, suggesting that this conformer is not accessed in the experiments. In addition, the $C_{2v}$(+-+-) conformer lies 44.3 and 41.4 kJ/mol higher in free energy at the B3LYP and MP2(full) levels of theory, respectively, further confirming that this conformer was not accessed in the experiments.

Assignments for the bands observed in the $K^+$(ta12C4) action spectrum based on comparison to the IR spectrum computed for the ground state $C_4$(++++) conformer are consistent with those assigned for the $Na^+$(ta12C4) complex. The most intense spectral feature is now centered at 1075 and corresponds to a mode of mixed character comprised of a C–N torsion and $CH_2$ stretching. The peak observed at 808 $cm^{-1}$, corresponds to a complex mode comprised of $M^+$–N stretching, N–H bending, and CNC scissoring. The peak observed at 937 $cm^{-1}$, corresponds to a doubly degenerate N–H and $CH_2$ rocking modes. The new spectral feature observed at 888 $cm^{-1}$ corresponds to a $CH_2$ rocking and N–H bending mixed character mode. The band centered at 835 $cm^{-1}$ corresponds to N–H bending coupled with $CH_2$ rocking. The peak at 1451 $cm^{-1}$ corresponds to a mixture of singly and doubly degenerate N–H wagging and $CH_2$ scissoring modes. The feature at 1354 $cm^{-1}$ corresponds to doubly degenerate $CH_2$ wagging modes. The peak centered at 1126 $cm^{-1}$ is the result of a doubly degenerate C–N stretch. The peak with the lowest IRMPD yield, at 1244 $cm^{-1}$, corresponds to a mode of mixed character comprised of doubly degenerate $CH_2$ twisting and N–H wagging.

### 4.5.3. Comparison of Experimental IRMPD and Theoretical IR Spectral of $Rb^+$(ta12C4)

The experimental IRMPD action spectrum for the $Rb^+$(ta12C4) complex is shown in **Figure 4.9**, and is the most complicated spectrum thus far. Compared to the experimental IRMPD spectrum of K$^+$(ta12C4), the Rb$^+$(ta12C4) complex retains all the same bands, but new features are observed at 752, 1008, and 1284 cm$^{-1}$, **Figure 4.1**. For the major feature centered at 805 cm$^{-1}$, there is the appearance of small shoulder at 787 cm$^{-1}$. In addition, there is a notable increase in the relative intensity of the peaks observed, more so in the frequency range between 1100 and 1600 cm$^{-1}$; peaks in this region increase by approximately 2 orders of magnitude. As previously stated, the appearance of new bands could be the result of better sensitivity associated with more facile dissociation of this more weakly bound system, or could be evidence of additional conformers being accessed in the experiments. The Rb$^+$–ta12C4 BDE, 146.7 ± 4.6 kJ/mol, is substantially weaker than that those of Na$^+$(ta12C4) and K$^+$(ta12C4) [44]. Based on the measured BDEs, only 52 and 83% as many photons are needed to dissociate the Rb$^+$(ta12C4) complex, as compared to the Na$^+$(ta12C4) and K$^+$(ta12C4) complexes, respectively.

Excellent agreement between the measured IRMPD action spectrum and the calculated IR spectrum for the ground-state $C_4$(++++) conformer is found, as can be seen from the comparison in **Figure 4.9**. The band positions are well reproduced, suggesting that the ground-state conformer is accessed in the experiments. The most intense spectral feature appears at 1075 cm$^{-1}$ and is red shifted by 6 cm$^{-1}$ in the calculated spectrum for the ground-state conformer. The bands centered at 805, 838, 889, 1008, 1075, 1121, 1241, and 1284 cm$^{-1}$ in the measured IRMPD spectrum are red shifted by 2, 7, 9, 7, 6, 9, 2, and 9 cm$^{-1}$, respectively, while the bands centered at 1357 and 1446 cm$^{-1}$ are blue shifted by 4 and 2 cm$^{-1}$ in the theoretical IR spectrum predicted for the $C_4$(++++) conformer. As found for the K$^+$(ta12C4) complex, the spectral features observed in the low frequency region between 600 and 1000 cm$^{-1}$ are not reproduced, or are blue shifted in the predicted IR spectrum of the $C_s$(+++-) conformer as compared to experiment. The three bands centered at 1075, 1121, and 1357 cm$^{-1}$ are in good agreement with the $C_s$(+++-) conformer in position, but not in relative intensity, and are red or blue shifted by less than 3 $cm^{-1}$. The bands predicted at 788 and 842 $cm^{-1}$ that contribute to the broad feature in the theoretical IR spectrum for the $C_s$(+++-) conformer match well with the features observed in the experimental spectrum at 787 and 838 $cm^{-1}$, respectively. The difference in the Gibbs free energy at the B3LYP level of theory, 20.1 kJ/mol, suggests the conformer would comprise less than 0.1% of the $Rb^+$(ta12C4) population at 298 K. In contrast, the difference in the Gibbs free energy at the MP2(full) level of theory, 9.7 kJ/mol, suggests the conformer would comprise 2.1% of the $Rb^+$(ta12C4) population at 298 K. The absence of the intense band predicted at 703 $cm^{-1}$ in the IRMPD spectrum is probably the most diagnostic for ruling out a significant presence of the $C_s$(+++-) conformer in the experiments. However, the appearance of the shoulder at 787 $cm^{-1}$ in the measured IRMPD spectrum matches well with the feature observed at 789 $cm^{-1}$ in the predicted IR spectrum for the $C_s$(+++-) conformer, suggesting that a very small population of this conformation may have been accessed in the experiments. For the calculated spectrum of the $C_{2v}$(++++) conformer, overlapping spectral features are observed, but most of the spectral features in the ranges between 600 and 1000 $cm^{-1}$ and from 1200 to 1600 $cm^{-1}$ are red shifted as compared to experiment, similar to that observed for the $K^+$(ta12C4) complex. Bands centered at 805, 937, 1075, 1357, and 1446 $cm^{-1}$ in the measured IRMPD spectrum are red shifted by 20, 13, 17, 6, and 14 $cm^{-1}$, while the bands observed at 838, 1121, and 1241 $cm^{-1}$ are blue shifted by 23, 14, and 16 $cm^{-1}$ in the theoretical spectrum predicted for the $C_{2v}$(++++) conformer. The $C_{2v}$(++++) conformer lies 21.9 and 18.1 kJ/mol above the ground-state at the B3LYP and MP2(full) levels of theory, respectively, such that it would comprise less than 0.1% of the reactant ion population in a 298 K Maxwell-Boltzmann distribution. The spectral and energetic differences suggest that this conformer was not accessed in the experiments. The absence of the intense spectral features predicted at 623 and 735 $cm^{-1}$ and virtually no peak-to-peak overlap indicates that the $C_{2v}$(+-+-) conformer is not accessed in the experiments. The large difference in the relative Gibbs free energies computed for these conformers at both the B3LYP and MP2(full) levels of theory, 43.5 and 32.1 kJ/mol, respectively, also suggest that the $C_{2v}$(+-+-) conformer is not accessed in the experiments.

Assignments for the bands observed in the $Rb^+$(ta12C4) action spectrum based on comparison to the IR spectrum computed for the ground state $C_4$(++++) conformer are consistent with those assigned for the $Na^+$(ta12C4) and $K^+$(ta12C4) complexes. The new spectral feature centered at 752 $cm^{-1}$ is a mixed character mode comprised of doubly degenerate N–H bending with contributions from $CH_2$ rocking. The feature at 787 $cm^{-1}$ can be attributed to a very minor population of the $C_s$(+++-) conformer and this band is assigned as N-H wagging. This now completes the assignment of all the main bands observed in the experimental spectrum as summarized in **Table 4.2**. Vibrational modes that were previously more rigid due to stronger interactions with the smaller metal cations are contributing more to the IRMPD yield. There is a change in the most intense peak as compared to the $Na^+$(ta12C4) and $K^+$(ta12C4) complexes. The most intense spectral peak occurs at 1446 $cm^{-1}$ and corresponds to a complex mixed character mode comprised of N–H wagging and $CH_2$ scissoring. Similarly, the IRMPD yields of the C–N stretch at 1121 $cm^{-1}$, the $CH_2$ twisting and N–H wagging mixed character mode at 1241 $cm^{-1}$, and the doubly degenerate $CH_2$ scissoring mode centered at 1357 $cm^{-1}$ also increased significantly in the IRMPD spectrum. Theory generally does a very good job of reproducing the peak intensities as compared to experimental IRMPD spectrum, but predicts the mixed character mode comprised of $M^+$–N stretching, N–H bending, and CNC scissoring to be the relatively more intense than the other spectral features in the IR spectrum of the $C_4$(++++) conformer.

### 4.5.4. Comparison of Experimental IRMPD and Theoretical IR Spectral of $Cs^+$(ta12C4)

**Figure 4.10** compares the experimental IRMPD action spectrum to the calculated IR spectra for the four most stable conformers found for the $Cs^+$(ta12C4) complex.

Compared to the experimental spectrum of $Rb^+$(ta12C4), $Cs^+$(ta12C4) retained all the same bands, but overall the spectral features observed in the experimental spectrum of $Cs^+$(ta12C4) were better resolved. In addition, there was a notable increase in the IRMPD yield of the peaks observed as compared to the $M^+$(ta12C4) complexes to the smaller alkali metal cations. The $Cs^+$–ta12C4 BDE, 131.3 ± 5.6 kJ/mol, is substantially weaker than that those of $Na^+$(ta12C4), $K^+$(ta12C4), and $Rb^+$(ta12C4) [44]. Based on the measured BDEs, only 47, 74 and 90% as many photons were needed to dissociate the $Cs^+$(ta12C4) complex, as compared to the $Na^+$(ta12C4), $K^+$(ta12C4), and $Rb^+$(ta12C4) complexes, respectively.

Excellent agreement between the measured IRMPD action spectrum and the calculated IR spectrum for the ground-state $C_4$(++++) conformer is clearly evident in the comparison in **Figure 4.10**. The band positions are well reproduced, suggesting that the ground-state conformer is accessed in the experiments. The most intense spectral feature appears at 805 $cm^{-1}$ in both the IRMPD spectrum and predicted IR spectrum. The bands centered at 752, 835, 889, 938, 1008, 1081, 1123, and 1240 $cm^{-1}$ in the measured IRMPD spectrum are red shifted by 8, 2, 9, 2, 7, 11, 10, and 2 $cm^{-1}$, respectively, while the bands centered at 1288, 1358 and 1447 $cm^{-1}$ are blue shifted by 5, 3, and 5 $cm^{-1}$ in the theoretical IR spectrum predicted for the $C_4$(++++) conformer. As found for the $K^+$(ta12C4) and $Rb^+$(ta12C4) complexes, the spectral features observed in the low frequency region between 600 and 1000 $cm^{-1}$ are not reproduced or, are blue shifted as compared to experiment in the IR spectrum of the $C_s$(+++-) conformer. The two bands centered at 1081 and 1123 $cm^{-1}$ are in good agreement with the $C_s$(+++-) conformer in position, and are red or blue shifted by less than 3 $cm^{-1}$. In contrast, the feature centered at 1358 $cm^{-1}$ is not well reproduced in shape or relative intensity. The bands predicted at 788 and 845 $cm^{-1}$ that contribute to the broad feature in the theoretical IR spectrum for the $C_s$(+++-) conformer are only blue and red shifted by 5 and 10 $cm^{-1}$ as compared to the features in experimental spectrum at 783 and 835 $cm^{-1}$, respectively, however, the central feature at 818 $cm^{-1}$ is much less intense and blue shifted by 13 $cm^{-1}$. The difference in the Gibbs free energy at the B3LYP level of theory, 20.1 kJ/mol, suggests the conformer would comprise less than 0.1% of the $Cs^+$(ta12C4) population at 298 K. In contrast, the difference in the Gibbs free energy at the MP2(full) level of theory, 6.3 kJ/mol, suggests the conformer would comprise 8.9% of the $Cs^+$(ta12C4) population at 298 K. The absence of the intense band predicted at 699 $cm^{-1}$ in the IRMPD spectrum is probably most diagnostic for ruling out a significant presence of the $C_s$(+++-) conformer in the experiments. However, the appearance of the shoulder at 783 $cm^{-1}$ in the measured IRMPD spectrum matches well with the feature at 788 $cm^{-1}$ in the predicted IR spectrum for the $C_s$(+++-) conformer, suggesting that a small population of this conformation may have been accessed in the experiments. For the calculated spectrum of the $C_{2v}$(++++) conformer, overlapping spectral features are observed, but most of the spectral features in the ranges between 600 and 1000 $cm^{-1}$ and from 1200 to 1600 $cm^{-1}$ are red shifted as compared to experiment, similar to that observed for the $K^+$(ta12C4) and $Rb^+$(ta12C4) complexes. Bands centered at 805, 938, 1081, 1358, and 1447 $cm^{-1}$ in the measured IRMPD spectrum are red shifted by 20, 8, 23, 9, and 21 $cm^{-1}$, while the bands observed at 835, 1123, and 1240 $cm^{-1}$ are blue shifted by 25, 15, and 21 $cm^{-1}$ in the theoretical spectrum predicted for the $C_{2v}$(++++) conformer. The $C_{2v}$(++++) conformer lies 21.0 and 11.4 kJ/mol above the ground-state at the B3LYP and MP2(full) levels of theory, respectively, such that it would comprise less than 0.1 and 1.0% of the reactant ion population in a 298 K Maxwell-Boltzmann distribution, suggesting that a significant population of this conformer was not accessed in this experiment. However, the appearance of the shoulder at 783 $cm^{-1}$ in the measured IRMPD spectrum matches well with the intense feature at 788 $cm^{-1}$ in the predicted IR spectrum for the $C_{2v}$(+++-) conformer suggesting that a very small population of this conformation may have been accessed in the experiments. However, this shoulder more likely arises from the presence of a small population of the $C_s$(+++-) conformer. The absence of intense spectral features at 623 and 735 cm$^{-1}$ and virtually no peak-to-peak overlap indicates that the $C_{2v}$(+-+-) conformer is not accessed in the experiments. The large difference in the relative Gibbs free energies computed for this conformer at both the B3LYP and MP2(full) levels of theory, 42.9 and 25.8 kJ/mol, respectively, also suggest that the $C_{2v}$(+-+-) conformer is not accessed in the experiments.

Assignments for the bands observed in the $Cs^+$(ta12C4) action spectrum based on comparison to the IR spectrum computed for the ground state $C_4$(++++) conformer, and possibly a minor contribution from the $C_s$(+++-) conformer, exactly parallel those for $Rb^+$(ta12C4), **Table 4.2**.

### 4.5.5. Effects of Alkali Metal Cation Size of Gas-Phase Conformation

Based on comparison of the measured IRMPD action spectra for the $M^+$(ta12C4) complexes and calculated IR spectra and energetics for the stable low-energy conformations of these complexes, it is clear that the symmetry and mode of binding are not altered by the size of the alkali metal cation. The $C_4$(++++) conformation remains the ground-state conformation for all four alkali metal cations and is the dominant species accessed in the experiments. However, as can be seen in **Figure 4.1** the strength of interaction between the alkali metal cation and ta12C4 does vary with the cation as evidenced by the systematic shifts in several of the spectral features observed in the IRMPD spectra of these complexes, in agreement with the measured $M^+$-ta12C4 BDEs [44]. Indeed, the strength of binding and the shifting of the frequencies of the spectral features are strongly correlated with the size of the metal cation. The smaller the metal cation, the more closely it can approach the ta12C4 ligand, resulting in stronger binding and larger spectral shifts as observed. The systematic variation in the $M^+$-N bond lengths, which increase with the size of the alkali metal cation from 2.434 Å for $Na^+$ to 3.190 Å for $Cs^+$, and the $\angle NM^+N$ bond angles, which decrease with the size of the cation from 76.4° for $Na^+$ to 57.7° for $Cs^+$, is nicely illustrated in the ground-state $C_4$(++++)

conformers shown in **Figure 4.2**. The ta12C4 ring is sufficiently small that even the $Na^+$ cation is not quite able to insert itself in the ring, while the larger alkali metal cations occupy sites further and further above the ta12C4 ring with increasing size. To optimize the alkali metal cation-N donor binding interactions in these complexes, ta12C4 curves toward the $Na^+$ cation. However, as the size of the alkali metal cation increases, the ta12C4 ring becomes slightly flatter to accommodate the binding. This is easily seen from the comparison of the N1-N7 and N4-N10 distances, which increase from 4.268 Å for $Na^+$ to 4.348 Å for $Cs^+$. The presence of a minor population of the first excited $C_s$(+++-) conformers for $Rb^+$ and $Cs^+$, clearly indicates that the size of the alkali metal cation is important in determining the conformations accessed in the experiments, and suggest that larger, more flexible azacrown ether analogs may exhibit greater variation in the preferred alkali metal cation binding modes.

## 4.6. Conclusions

IRMPD action spectra of alkali metal cation-ta12C4 complexes in the region extending from 600 to 1600 $cm^{-1}$ have been obtained for four $M^+$(ta12C4) complexes where $M^+ = Na^+, K^+, Rb^+$, and $Cs^+$. For all four complexes, the loss of the intact neutral ta12C4 ligand is the only dissociation pathway observed, consistent with simple CID fragmentation behavior [44]. The binding energies were found to decrease monotonically with the size of the alkali metal cation [44]. Binding of alkali metal cations to ta12C4 produces similar IRMPD action spectra. The IRMPD yields for the $M^+$(ta12C4) complexes increase as the size the alkali metal cation increases, in accordance with the trends in the strength of alkali metal cation binding in these systems. Spectral features in the IRMPD action spectra are retained throughout the entire series, while new spectral features are observed for the complexes to the larger alkali-metal cations. Comparison with IR spectra calculated at the B3LYP/def2-TZVPPD level of theory allows the conformations present in the experiments to be identified. For the larger alkali metal cations $K^+$, $Rb^+$, and $Cs^+$, the IRMPD action spectrum is well reproduced by the calculated spectrum for the most-stable conformation, $C_4$(++++). Evidence for the presence of a minor population of excited conformations is observed for the complexes to $Rb^+$ and $Cs^+$. For the $Na^+$(ta12C4) complex, the lack of spectral features, which is a result of the IRMPD yield being low for this complex, makes identifying the conformations accessed in the experiment less definitive, but trends for the larger metal cations suggest that only the ground state $C_4$(++++) conformation was accessed in the experiments. This behavior is in sharp contrast to that found for the alkali and transition metal cation complexes to 15-crown-5 and 18-crown-6, where the conformation(s) accessed vary with the size of the metal cation. It is presently unclear whether this difference arises from the size of the crown (12 versus 15 and 18-membered rings) or the nature of the donor atoms (N versus O).

## 4.7. References

[1] R. Delgado, V. Félix, L.M.P. Lima, D.W. Price, Dalton Trans. (2007) 2734.

[2] M. Kim, J.W. Jeon, J. Suh, J. Biol. Inorg. Chem. 10 (2005) 364.

[3] C.A. Boswell, X. Sun, W. Niu, G.R. Weisman, E.H. Wong, A.L. Rheingold, C.J. Anderson, J. Med. Chem. 47 (2004) 1465.

[4] T. Chen, X. Wang, Y. He, C. Zhang, Z. Wu, K. Liao, J. Wang, Z. Guo, Inorg. Chem.48 (2009) 5801.

[5] A. Prokhorov, N.L. Bris, G. Bernard, H. Henri, Synth. Commun. 36 (2006) 3271.

[6] E. Kinoshita-Kikuta, E. Kinoshita, N. Harada, T. Koike, Anal Biochem.498 (2011) 34.

[7] J. Geduhn, T. Walenzyk, B. Koenig, Curr. Org. Synth. 23(2007) 390.

[8] H. Kubo, T.N. Player, S. Shinoda, H. Tsukube, H. Nariai, T. Takeuchi, Anal. Chim. Acta 504 (2004) 137.

[9] T.Y. Lee, J. Suh, Pure Appl. Chem. 81 (2009) 255.

[10] J. Suh, W.S. Chei, Curr. Opin. Chem. Biol. 12 (2008) 207.

[11] A. Colorado, J.X. Shen, V.H. Vartanian, J. Brodbelt, Anal. Chem. 68 (1996) 4033.

[12] B. Martínez-Haya, P. Hurtado, A.R. Hortal, S. Hamad, J.D. Steill, J. Oomens, J. Phys. Chem. A 114 (2010) 7048.

[13] F. Gamez, P. Hurtado, B. Martínez-Haya, G. Berden, J. Oomens, Int. J. Mass Spectrom. 308 (2011) 217.

[14] T.E. Cooper, D.R. Carl, J. Oomens, J.D. Steill, P.B. Armentrout, J. Phys. Chem. A 115 (2011) 5408.

[15] D.M. Peiris, Y. Yang, R. Ramanathan, K.R. Williams, C.H. Watson, J.R. Eyler, Int. J. Mass Spectrom. 157/158 (1996) 365.

[16] P.Hurtado, F. Gamez, S. Hamad, B. Martínez-Haya, J.D. Steill, J. Oomens, J. Phys. Chem. A 115 (2011) 7275.

[17] P. Hurtado, F. Gamez, S. Hamad, B. Martínez-Haya, J.D. Steill, J. Oomens, J. Chem. Phys.136 (2012) 114301.

[18] C.N. Stedwell, J.F. Galindo, K. Gulyuz, A.E. Roitberg, N.C. Polfer, J. Phys. Chem. A 117 (2013) 1181.

[19] C.N. Stedwell, A.L. Partick, K. Gulyuz, N.C. Polfer, Anal. Chem. 84 (2012) 9907.

[20] D. Oepts, A.F.G. van der Meer, P.W. van Amersfoort, Infrared Phys. Technol. 36 (1995) 297.

[21] J.J. Valle, J.R Eyler, J. Oomens, D.T. Moore, A.F.G. van der Meer, G. von Heldon, G. Meijer, C.L. Hendrickson, A.G. Marshall, G.T. Blakney, Rev. Sci. Instrum.76 (2005) 023103.

[22] N.C. Polfer, J. Oomens, D.T. Moore, G. von Helden, G. Meijer, R.C. Dunbar, J. Am. Chem. Soc. 128 (2006) 517.

[23] D. Ray, D. Feller, M.B. More E.D. Glendening, P.B. Armentrout, J. Phys. Chem. 100 (1996) 16116.

[24] M.B. More, D. Ray, P.B. Armentrout, J. Phys. Chem. A 101 (1997) 831.

[25] M.B. More, D. Ray, P.B. Armentrout, J. Phys. Chem. A 101 (1997) 4254.

[26] M.B. More, D. Ray, P.B. Armentrout, J. Phys. Chem. A 101 (1997) 7007.

[27] S.E. Hill, D. Feller, E.D. Glendening, J. Phys. Chem. A102 (1998) 3813.

[28] D. Rappoport. F. Furche, J. Chem. Phys. 133 (2010) 134105.

[29] T. Leininger, A. Nicklass, W. Kuechle, H. Stoll, M. Dolg, A. Bergner, Phys. Lett. 255 (1996) 274.

[30] D. Feller, J. Comp. Chem. 17 (1996) 1571.

[31] K.L. Schuchardt, B.T. Didier, T. Elsenthagen, L. Sun, V. Gurumoorthi, J. Chase, J. Li, T.L. Windus, J. Chem. Inf. Model. 47 (2007) 1045.

[32] M.J. Frisch, G.W. Trucks, H.B. Schlegel, G.E. Scuseria, M.A. Robb, J.R. Cheeseman, J.A. Montgomery Jr., T. Vreven, K.N. Kudin, J.C. Burant, J.M. Millam, S.S. Iyengar, J. Tomasi, V. Barone, B. Mennucci, M. Cossi, G. Scalmani, N. Rega, G.A. Petersson, H. Nakatsuji, M. Hada, M. Ehara, K. Toyota, R. Fukuda, J. Hasegawa, M. Ishida, T. Nakajima, Y. Honda, O. Kitao, H. Nakai, M. Klene, X. Li, J.E. Knox, H.P. Hratchian, J.B. Cross, V. Bakken, C. Adamo, J. Jaramillo, R, Gomperts, R.E. Stratmann, O. Yazyev, A.J. Austin, R. Cammi, C. Pomelli, J.W. Ochterski, P.Y. Ayala, K. Morokuma, G.A. Voth, P. Salvador, J.J. Dannenberg, V.G. Zakrzewski, S. Dapprich, A.D. Daniels, M.C. Strain, O. Farkas, D.K. Malick, A. Rabuck, K. Raghavachari, J.B. Foresman, J.V. Ortiz, Q. Cui, A.G. Baboul, S. Clifford, J. Cioslowski, B.B. Stefanov, G. Liu, A. Liashenko, P. Piskorz, I. Komaromi, R.L. Martin, D.J. Fox, T. Keith, M.A. Al-Laham, C.Y. Peng, A. Nanayakkara, M. Challacombe, P.MW. Gill, B. Johnson, W. Chen, M.W. Wong, C. Gonzalez, J.A. Pople, Gaussian 03, Revision D.01, 2005, Gaussian, Inc., Pittsburgh, PA.

[33] N.C. Polfer, J. Oomens, R.C. Dunbar, Phys. Chem. Chem. Phys. 8 (2006) 2744.

[34] M.W. Forbes, M.F. Bush, N.C. Polfer, J. Oomens, R.C. Dunbar, E.R. Williams, R.A. Jockusch, J. Phys. Chem. A 111 (2007) 11759.

[35] P.B. Armentrout, M.T. Rodgers, J. Oomens, J.D. Steill, J. Phys. Chem. A 112 (2008) 2248.

[36] M.T. Rodgers, P.B. Armentrout, J. Oomens, J.D. Steill, J. Phys. Chem. A 112 (2008) 2258.

[37] J.T. O'Brien, J.S. Prell, J.D. Steill, J. Oomens, E.R. Williams, J. Phys. Chem. A 112 (2008) 10823.

[38] A.L. Heaton, V.N. Bowman, J. Oomens, J.D. Steill, P.B. Armentrout, J. Phys. Chem. A 113 (2009) 5519.

[39] D.R. Carl, T.E. Cooper, J. Oomens, J.D. Steill, P.B. Armentrout, Phys. Chem. Chem. Phys. 12 (2010) 3384.

[40] M. Citir, E.M.S. Stennett, J. Oomens, J.D. Steill, M.T. Rodgers, P.B. Armentrout, Int. J. Mass Spectrom.297 (2010) 9.

[41] M. Citir, C.S. Hinton, J. Oomens, J.D. Steill, P.B. Armentrout, J. Phys. Chem. A 116 (2012) 1532.

[42] B. Yang, R.R. Wu, G. Berden, J. Oomens, M.T. Rodgers, J. Am. Soc. Mass Spectrom. (2013) *submitted for publication.*

[43] B. Bosnich. C.K. Poon, R.D. Tobe, Inorg. Chem. 4 (1965) 1102.

[44] C.A. Austin, Y. Chen, M.T. Rodgers, Int. J. Mass Spectrom. 330-332 (2012) 27.

**Table 4.1.** Relative enthalpies and Gibbs free energies (in kJ/mol) and Maxwell-Boltzmann populations (%) at 298 K of stable low-energy conformers of M$^+$(cyclen)$^a$

| Complex | Conformer | B3LYP/def2-TZVPPD$^b$ | | | MP2(full)/ def2-TZVPPD$^c$ | | |
|---|---|---|---|---|---|---|---|
| | | $\Delta H_{298}$ | $\Delta G_{298}$ | $Pop_{298}$ | $\Delta H_{298}$ | $\Delta G_{298}$ | $Pop_{298}$ |
| Na$^+$(cyclen) | **$C_4$ (++++)** | **0.0** | **0.0** | **100** | **0.0** | **0.0** | **100** |
| | $C_{2v}$ (++++) | 21.9 | 18.8 | < 0.1 | 22.7 | 19.6 | < 0.1 |
| | $C_s$ (+++–) | 31.2 | 26.4 | < 0.1 | 25.6 | 20.8 | < 0.1 |
| | $C_{2v}$ (+–+–) | 53.6 | 45.4 | < 0.1 | 56.6 | 48.4 | < 0.1 |
| K$^+$(cyclen) | **$C_4$ (++++)** | **0.0** | **0.0** | **100** | **0.0** | **0.0** | **100** |
| | $C_{2v}$ (++++) | 27.2 | 25.8 | < 0.1 | 27.1 | 25.7 | < 0.1 |
| | $C_s$ (+++–) | 26.4) | 25.9 | < 0.1 | 19.3 | 18.8 | < 0.1 |
| | $C_{2v}$ (+–+–) | 49.6 | 44.3 | < 0.1 | 46.7 | 41.4 | < 0.1 |
| Rb$^+$(cyclen) | **$C_4$ (++++)** | **0.0** | **0.0** | **100** | **0.0** | **0.0** | **98** |
| | $C_{2v}$ (++++) | 28.6 | 21.9 | < 0.1 | 24.8 | 18.1 | < 0.1 |
| | $C_s$ (+++–) | 24.5 | 20.1 | < 0.1 | 14.1 | 9.7 | 2.1 |
| | $C_{2v}$ (+–+–) | 45.6 | 43.5 | < 0.1 | 34.3 | 32.1 | < 0.1 |
| Cs$^+$(cyclen) | **$C_4$ (++++)** | **0.0** | **0.0** | **100** | **0.0** | **0.0** | **90** |
| | $C_{2v}$ (++++) | 28.8 | 21.0 | < 0.1 | 19.1 | 11.4 | 1.0 |
| | $C_s$ (+++–) | 24.0 | 20.1 | < 0.1 | 10.2 | 6.3 | 8.9 |
| | $C_{2v}$ (+–+–) | 43.9 | 42.9 | < 0.1 | 26.9 | 32.1 | < 0.1 |

[a] Geometries optimized at the B3LYP/def2-TZVPPD level of theory.
[b] Calculated at B3LYP/def2-TZVPPD level of theory.
[c] Calculated at the MP2(full)/def2-TZVPPD level of theory.

**Table 4.2.** Observed band positions (in $\text{cm}^{-1}$) of the vibrational modes of $M^+$(cyclen) complexes in the IR fingerprint region[a]

| Vibrational mode | $Na^+$(cyclen) | $K^+$(cyclen) | $Rb^+$(cyclen) | $Cs^+$(cyclen) |
|---|---|---|---|---|
| N–H bending , $CH_2$ rocking | – | – | 752 | 752 |
| N–H wagging[b] | | | 787 | 783 |
| $M^+$–N stretching,<br>N–H bending, CNC scissoring | 805 | 808 | 805 | 805 |
| $CH_2$ rocking, N–H bending | – | 835 | 838 | 835 |
| N–H bending, $CH_2$ rocking | – | 888 | 889 | 889 |
| N–H bending, $CH_2$ rocking | 926 | 937 | 937 | 938 |
| $CH_2$ rocking, N–H wagging | – | – | 1008 | 1008 |
| $CH_2$ stretching, C–N torsion | 1070 | 1075 | 1075 | 1081 |
| C–N stretching | – | 1126 | 1121 | 1123 |
| $CH_2$ twisting, N–H wagging | – | 1244 | 1241 | 1240 |
| $CH_2$ wagging | – | – | 1284 | 1288 |
| $CH_2$ scissoring | 1345 | 1354 | 1357 | 1358 |
| N–H wagging, $CH_2$ scissoring | – | 1451 | 1446 | 1447 |

[a] Assignments based on comparison of the IRMPD action spectra and theoretical IR spectra of the ground-state $C_4$(++++) conformers optimized at the B3LYP/def2-TZVPPD level of theory, except as noted.

[b] Assignments based on $C_s$(+++–) conformers.

## 4.8. Figure Captions

**Figure 4.1**. Measured infrared multiple photon dissociation action spectra of $M^+$(cyclen) complexes, where $M^+ = Na^+$, $K^+$, $Rb^+$ and $Cs^+$.

**Figure 4.2.** B3LYP/def2-TZVPPD ground state $C_4$(++++) conformers and B3LYP/def2-TZVPPD and *MP2(full)/def2-TZVPPD* Gibbs free energies of binding at 298 K (in kJ/mol) of $M^+$(cyclen) complexes, where $M^+ = Na^+$, $K^+$, $Rb^+$, and $Cs^+$.

**Figure 4.3.** $C_{2v}$ (++++) conformer and Gibbs free energies at 298 K (in kJ/mol) of the $M^+$(cyclen) complexes, where $M^+ = Na^+$, $K^+$, $Rb^+$, and $Cs^+$, at the B3LYP/def2-TZVPPD and *MP2(full)/def2-TZVPPD* using structures optimized at the B3LYP/def2-TZVPPD level of theory.

**Figure 4.4.** $C_s$ (+++-) conformer and Gibbs free energies at 298 K (in kJ/mol) of the $M^+$(cyclen) complexes, where $M^+ = Na^+$, $K^+$, $Rb^+$, and $Cs^+$, at the B3LYP/def2-TZVPPD and *MP2(full)/def2-TZVPPD* using structures optimized at the B3LYP/def2-TZVPPD level of theory.

**Figure 4.5.** $C_{2v}$ (+-+-) conformer and Gibbs free energies at 298 K (in kJ/mol) of the $M^+$(cyclen) complexes, where $M^+ = Na^+$, $K^+$, $Rb^+$, and $Cs^+$, at the B3LYP/def2-TZVPPD and *MP2(full)/def2-TZVPPD* using structures optimized at the B3LYP/def2-TZVPPD level of theory.

**Figure 4.6.** Variation in the B3LYP/def2-TZVPPD and MP2(full)/def2-TZVPPD relative Gibbs free energies at 298 K (in kJ/mol) of the four most stable conformations of the

$M^+$(cyclen) complexes determined at the B3LYP/def2-TZVPPD level of theory as a function of the alkali metal cation.

**Figure 4.7.** Comparison of the experimental IRMPD action spectrum of $Na^+$(cyclen) with linear IR spectra for the four most stable conformations predicted at the B3LYP/def2-TZVPPD level of theory. B3LYP/def2-TZVPPD and *MP2(full)/def2-TZVPPD* relative Gibbs free energies at 298 K are also shown.

**Figure 4.8.** Comparison of the experimental IRMPD action spectrum of $K^+$(cyclen) with linear IR spectra for the four most stable conformations predicted at the B3LYP/def2-TZVPPD level of theory. B3LYP/def2-TZVPPD and *MP2(full)/def2-TZVPPD* relative Gibbs free energies at 298 K are also shown.

**Figure 4.9.** Comparison of the experimental IRMPD action spectrum of $Rb^+$(cyclen) with linear IR spectra for the four most stable conformations predicted at the B3LYP/def2-TZVPPD level of theory. B3LYP/def2-TZVPPD and *MP2(full)/def2-TZVPPD* relative Gibbs free energies at 298 K are also shown.

**Figure 4.10.** Comparison of the experimental IRMPD action spectrum of $Cs^+$(cyclen) with linear IR spectra for the four most stable conformations predicted at the B3LYP/def2-TZVPPD level of theory. B3LYP/def2-TZVPPD and *MP2(full)/def2-TZVPPD* relative Gibbs free energies at 298 K are also shown.

Figure 4.1.

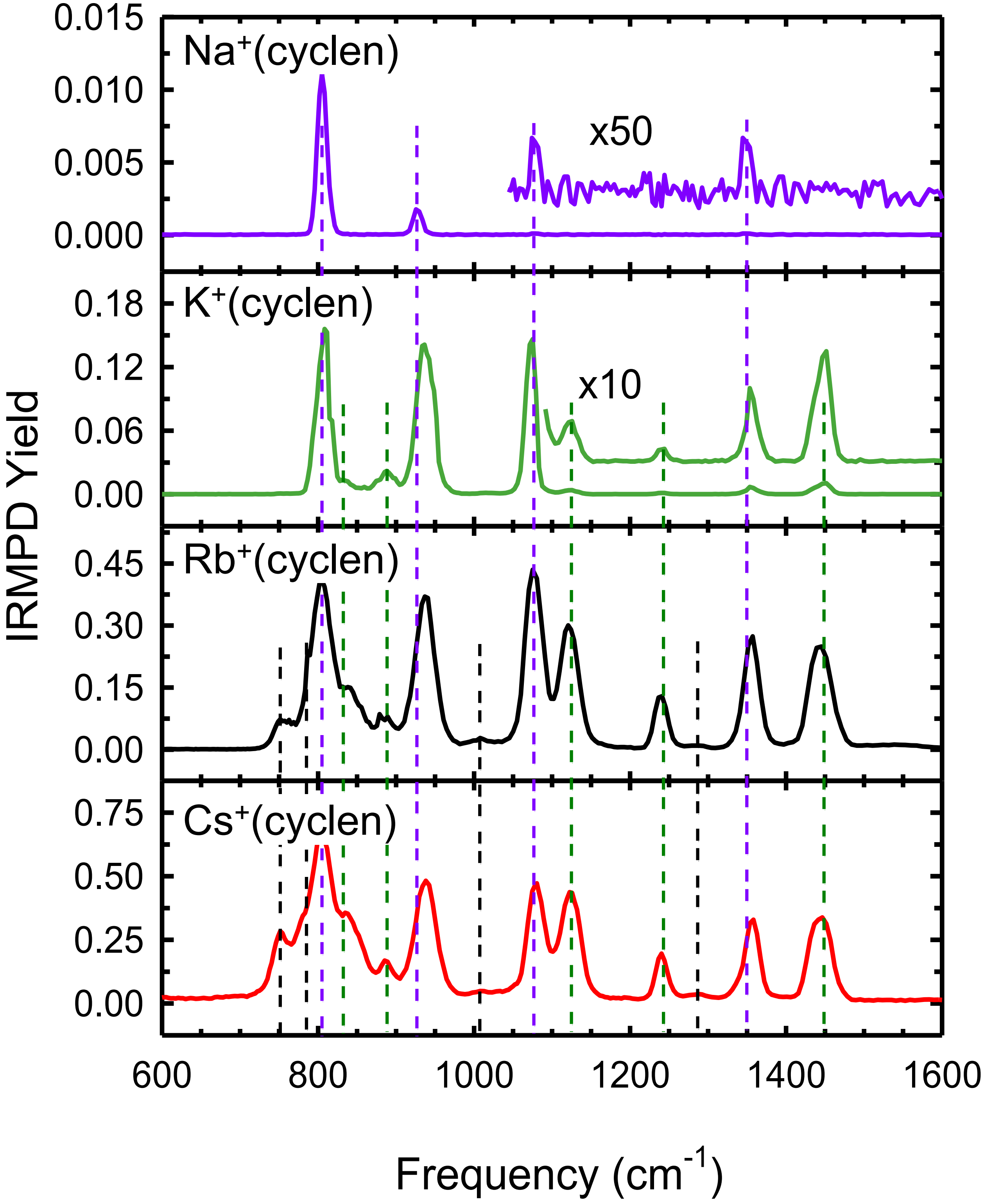
Na⁺(cyclen)
x50
K⁺(cyclen)
x10
Rb⁺(cyclen)
Cs⁺(cyclen)
0.015
0.010
0.005
0.000
0.18
0.12
0.06
0.00
0.45
0.30
0.15
0.00
0.75
0.50
0.25
0.00
IRMPD Yield
600
800
1000
1200
1400
1600
Frequency (cm-1)

Figure 4.2.

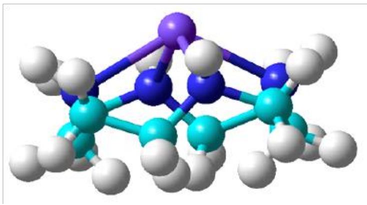

Na$^+$(cyclen)
292.8 kJ/mol
*282.4 kJ/mol*

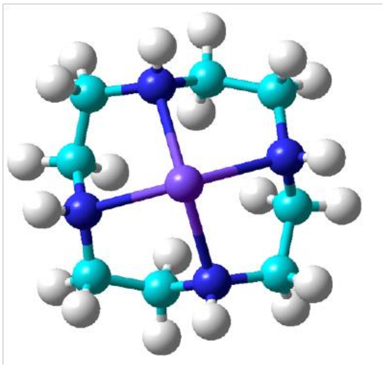

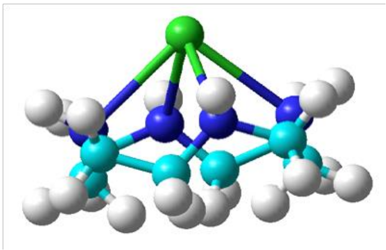

K$^+$(cyclen)
188.3 kJ/mol
*192.1 kJ/mol*

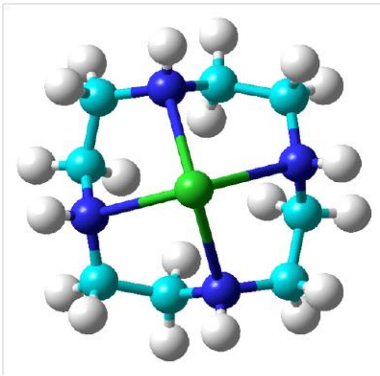

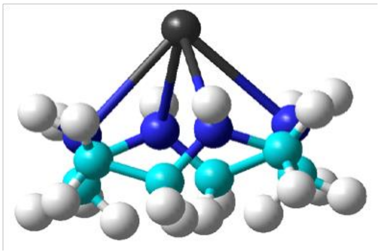

Rb$^+$(cyclen)
155.4 kJ/mol
*161.4 kJ/mol*

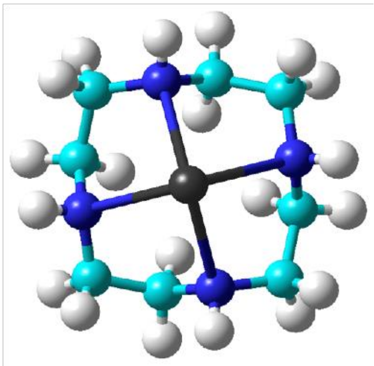

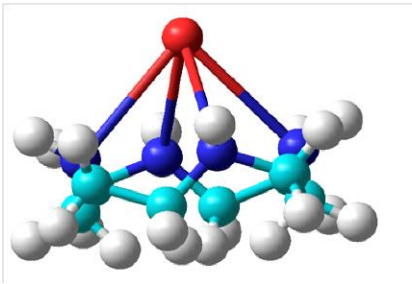

Cs$^+$(cyclen)
134.0 kJ/mol
*141.5 kJ/mol*

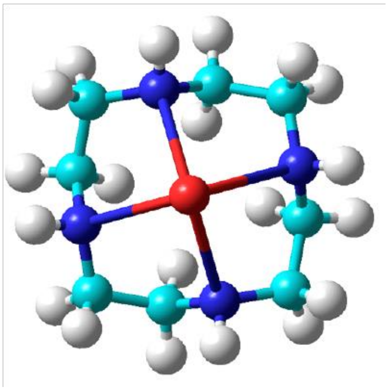

$C_4$(++++)

Figure 4.3.

$C_{2v}$ (++++)

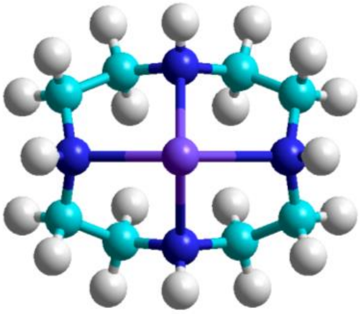

Na(cyclen)
18.8 (*19.6*) kJ/mol

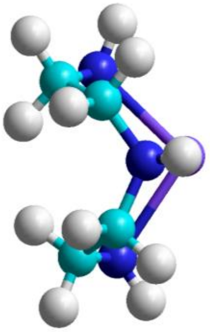

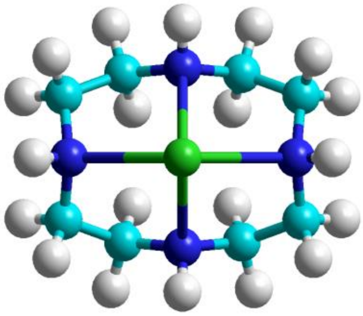

K$^+$(cyclen)
25.8 (*25.7*) kJ/mol

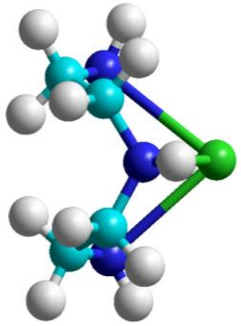

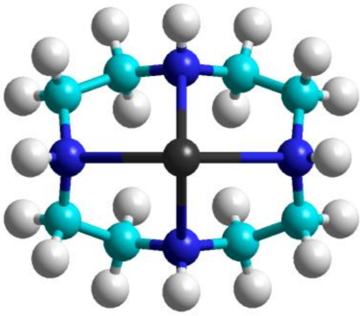

Rb$^+$(cyclen)
21.9 (*18.1*) kJ/mol

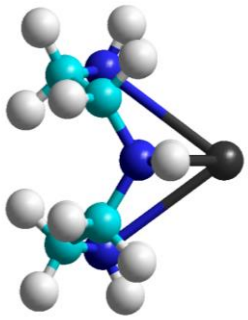

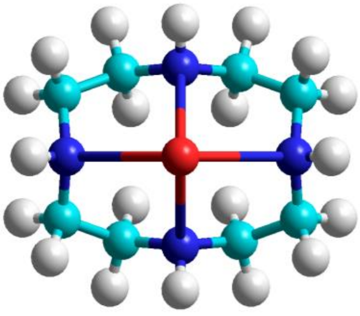

Cs$^+$(cyclen)
21.0 (*11.4*) kJ/mol

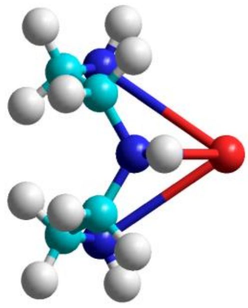

Figure 4.4.

$C_s$ (+++-)

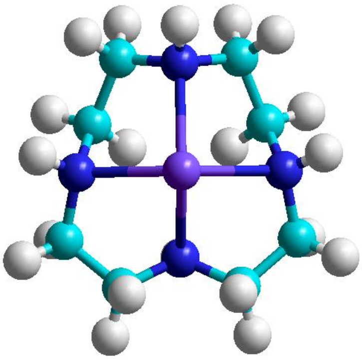

Na(cyclen)
26.4 (*20.8*) kJ/mol

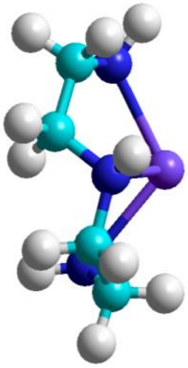

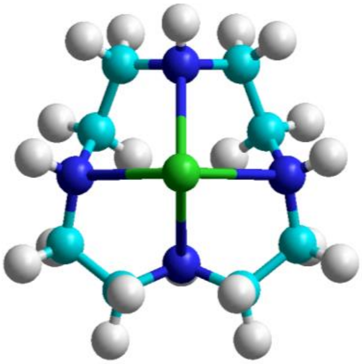

K$^+$(cyclen)
25.9 (*18.8*) kJ/mol

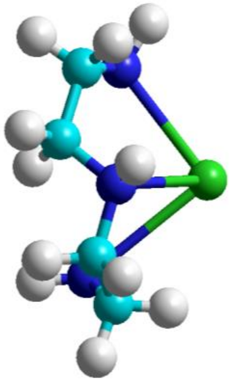

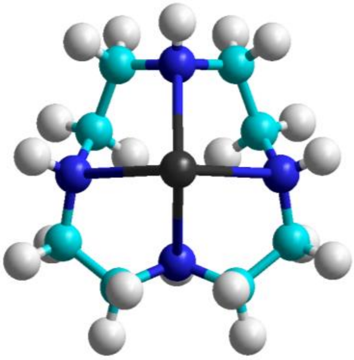

Rb$^+$(cyclen)
20.1 (*9.7*) kJ/mol

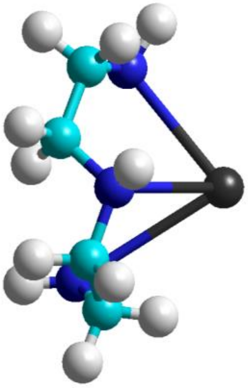

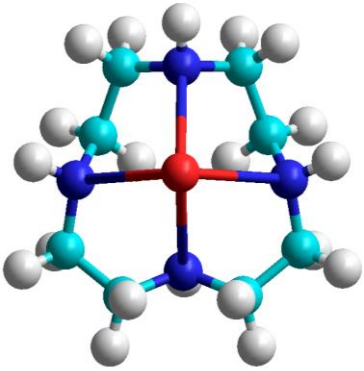

Cs$^+$(cyclen)
20.1 (*6.3*) kJ/mol

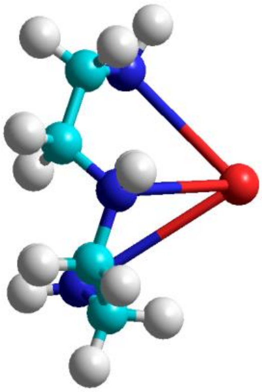

Figure 4.5.

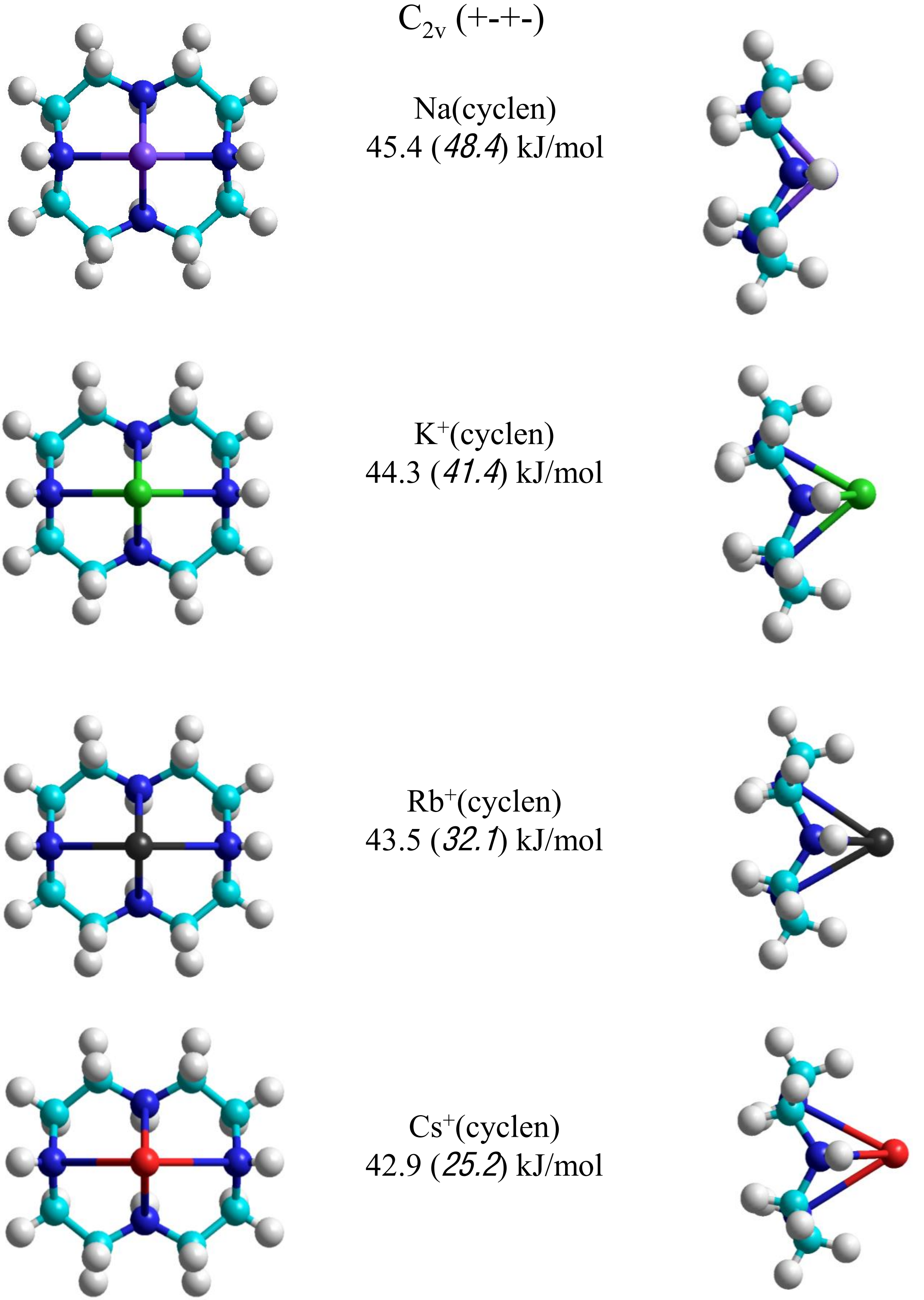

$C_{2v}$ (+-+-)

Na(cyclen)
45.4 (*48.4*) kJ/mol

$K^+$(cyclen)
44.3 (*41.4*) kJ/mol

$Rb^+$(cyclen)
43.5 (*32.1*) kJ/mol

$Cs^+$(cyclen)
42.9 (*25.2*) kJ/mol

Figure 4.6.

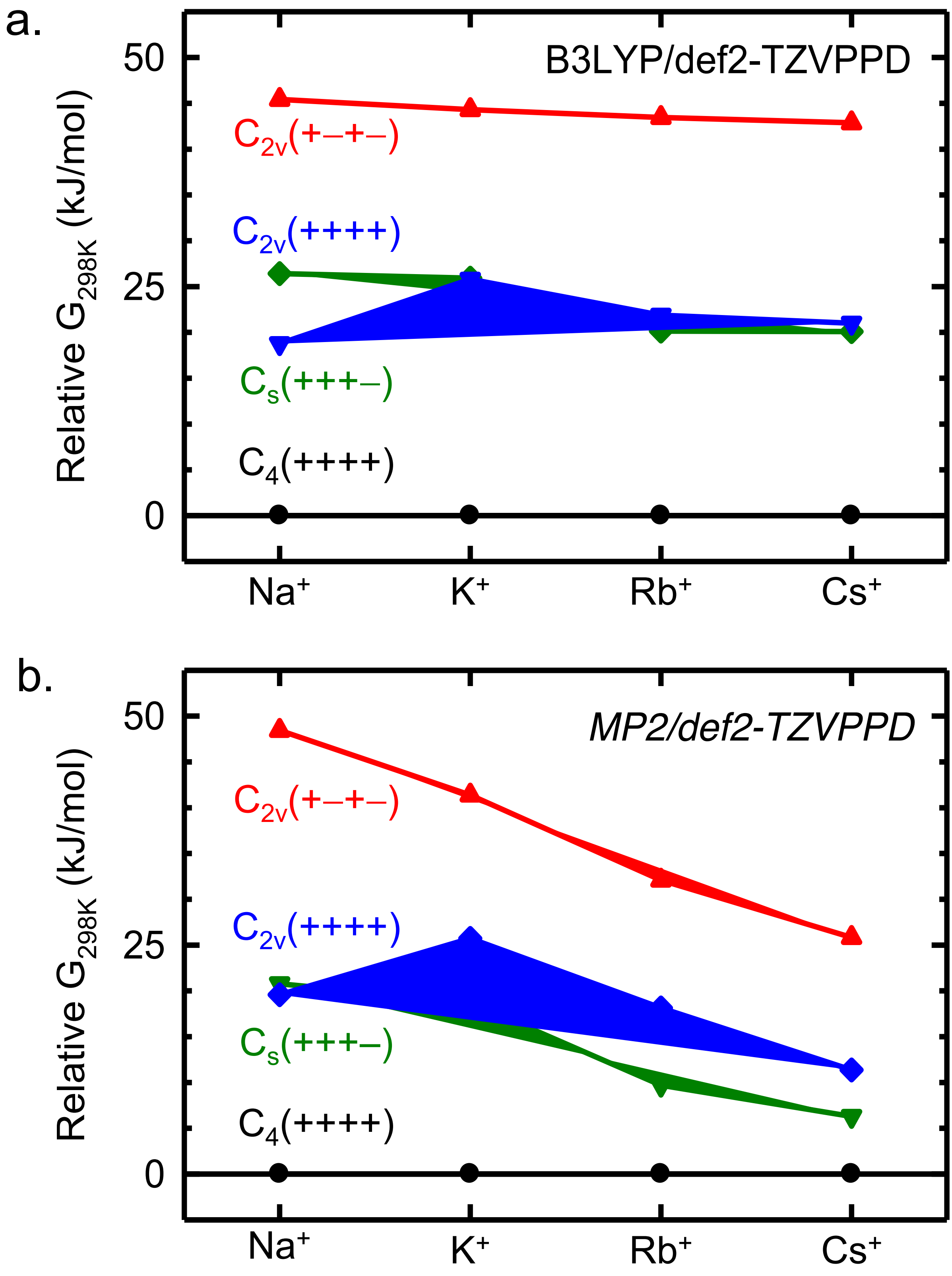
a.
B3LYP/def2-TZVPPD
Relative $G_{298K}$ (kJ/mol)
50
25
0
$C_{2v}$(+–+–)
$C_{2v}$(++++)
$C_s$(+++–)
$C_4$(++++)
Na⁺
K⁺
Rb⁺
Cs⁺
b.
MP2/def2-TZVPPD
Relative $G_{298K}$ (kJ/mol)
50
25
0
$C_{2v}$(+–+–)
$C_{2v}$(++++)
$C_s$(+++–)
$C_4$(++++)
Na⁺
K⁺
Rb⁺
Cs⁺

Figure 4.7.

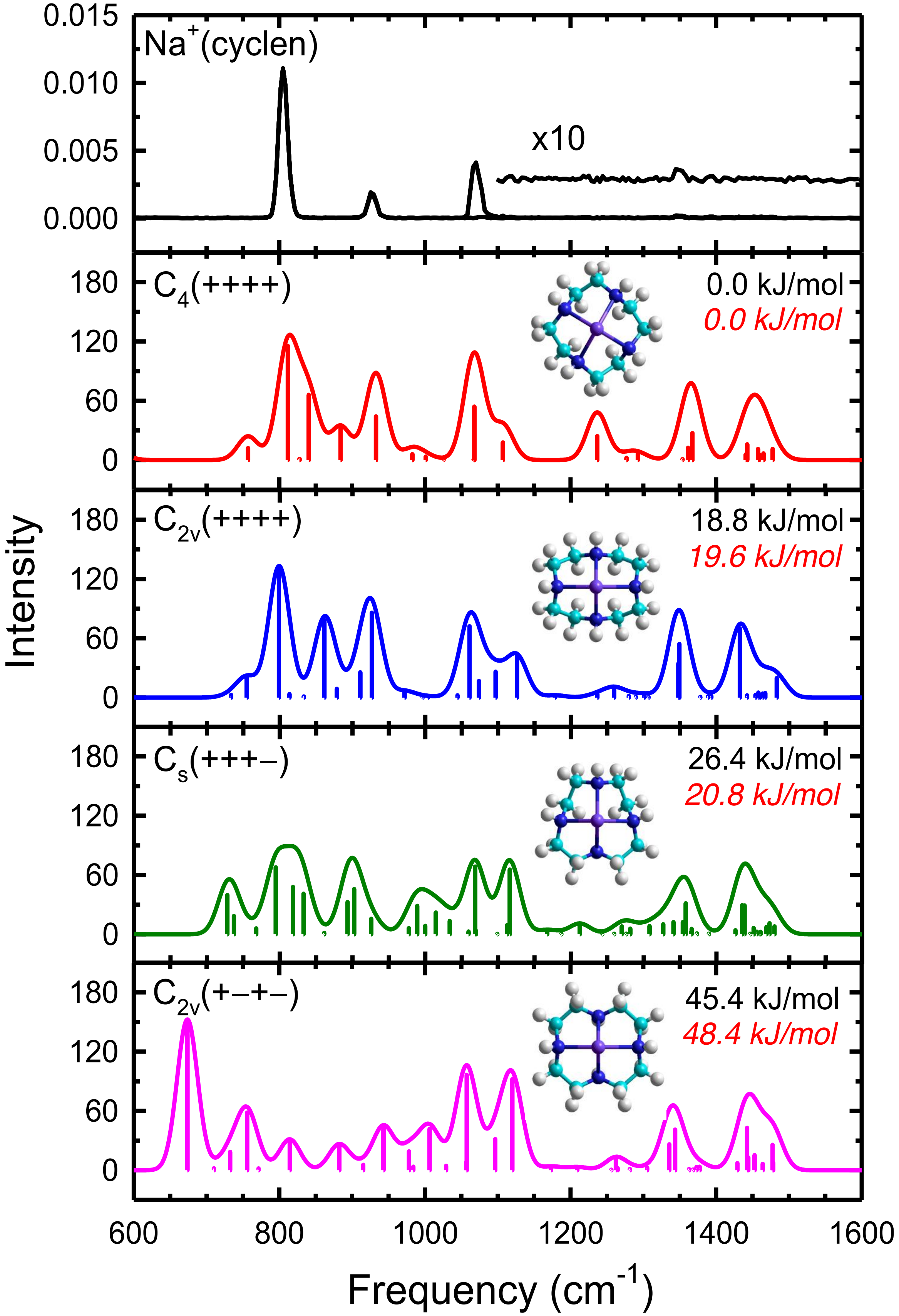
Na+(cyclen)
x10
0.015
0.010
0.005
0.000
C4(++++)
0.0 kJ/mol
0.0 kJ/mol
C2v(++++)
18.8 kJ/mol
19.6 kJ/mol
Cs(+++–)
26.4 kJ/mol
20.8 kJ/mol
C2v(+–+–)
45.4 kJ/mol
48.4 kJ/mol
180
120
60
0
Intensity
600
800
1000
1200
1400
1600
Frequency (cm-1)

Figure 4.8.

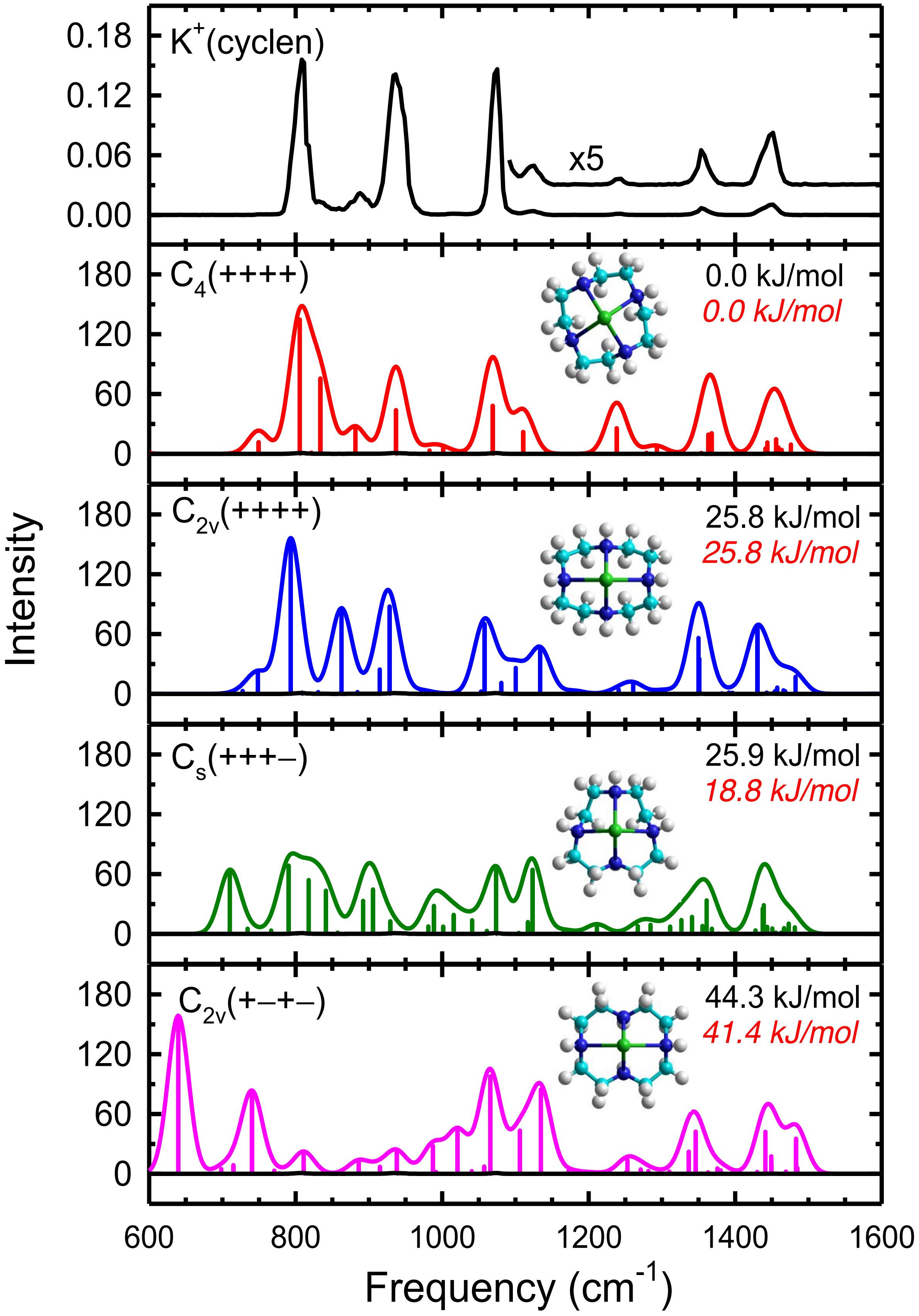
K$^+$(cyclen)
x5
0.18
0.12
0.06
0.00
$C_4$(++++)
0.0 kJ/mol
0.0 kJ/mol
$C_{2v}$(++++)
25.8 kJ/mol
25.8 kJ/mol
$C_s$(+++–)
25.9 kJ/mol
18.8 kJ/mol
$C_{2v}$(+–+–)
44.3 kJ/mol
41.4 kJ/mol
180
120
60
0
Intensity
600
800
1000
1200
1400
1600
Frequency (cm$^{-1}$)

Figure 4.9.

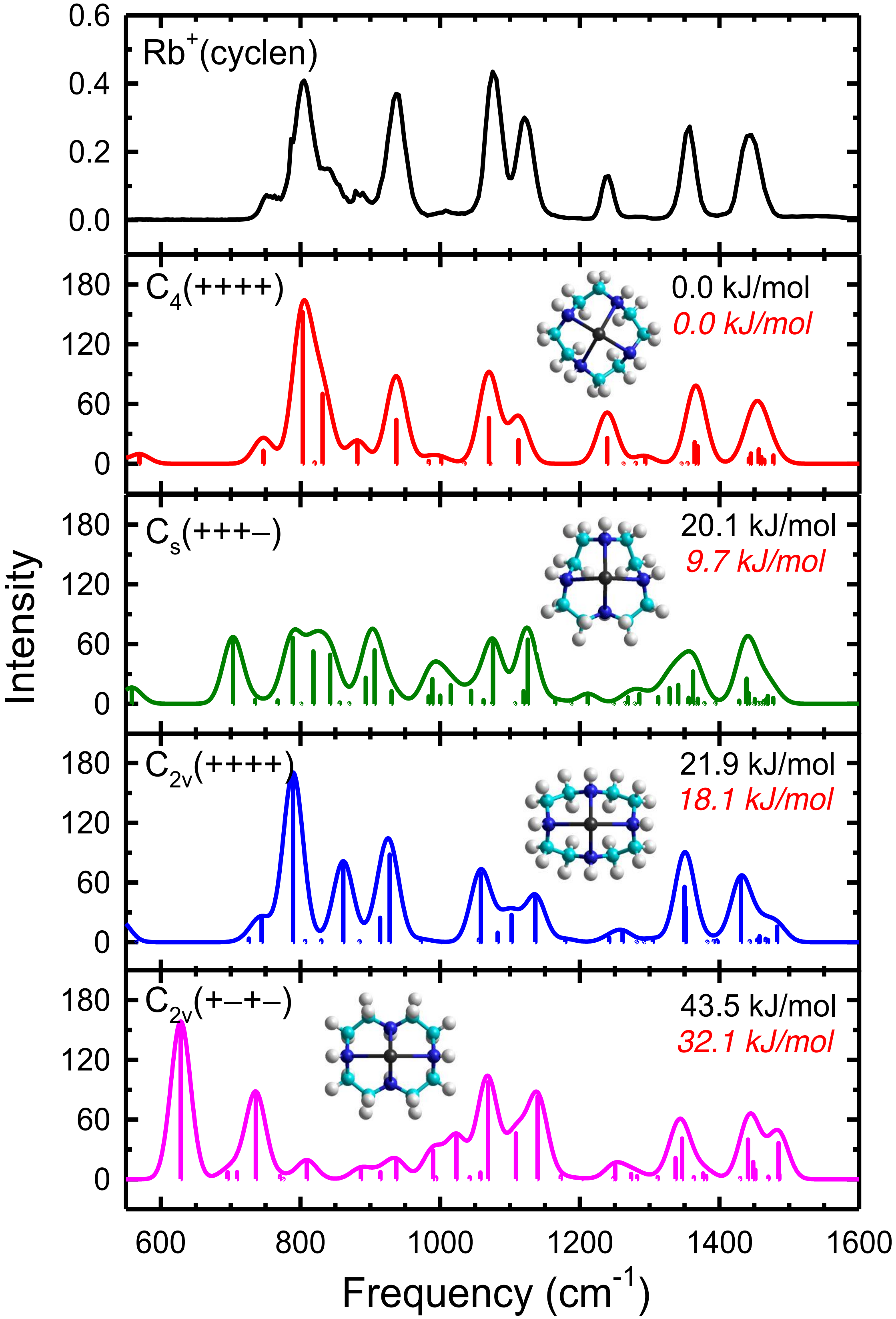
Rb$^+$(cycln)
C$_4$(++++)
0.0 kJ/mol
0.0 kJ/mol
C$_s$(+++–)
20.1 kJ/mol
9.7 kJ/mol
C$_{2v}$(++++)
21.9 kJ/mol
18.1 kJ/mol
C$_{2v}$(+–+–)
43.5 kJ/mol
32.1 kJ/mol
Intensity
Frequency (cm$^{-1}$)
0.6
0.4
0.2
0.0
180
120
60
0
600
800
1000
1200
1400
1600

Figure 4.10.

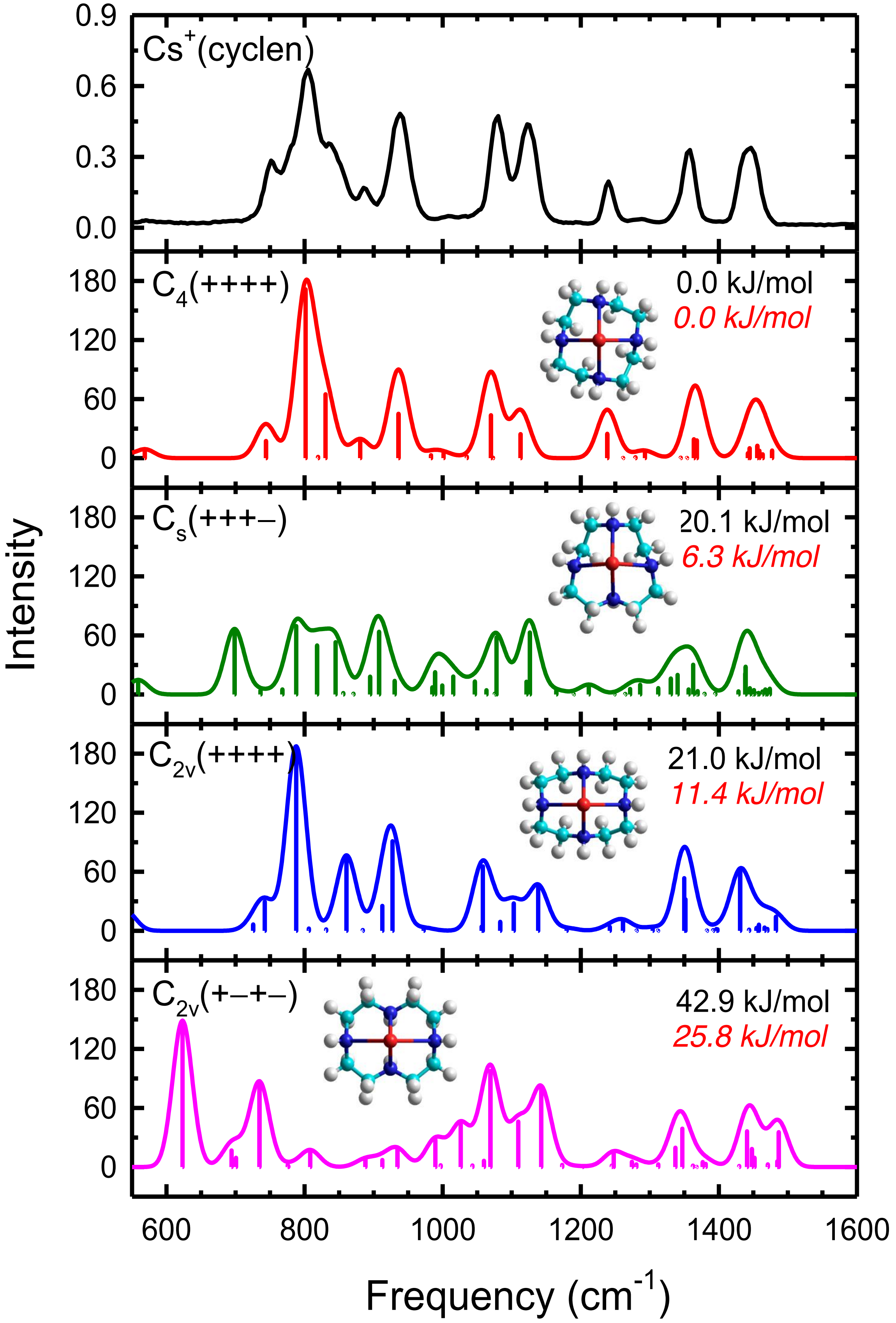
Cs$^+$(cyclen)
$C_4$(++++)
0.0 kJ/mol
0.0 kJ/mol
$C_s$(+++–)
20.1 kJ/mol
6.3 kJ/mol
$C_{2v}$(++++)
21.0 kJ/mol
11.4 kJ/mol
$C_{2v}$(+–+–)
42.9 kJ/mol
25.8 kJ/mol
Intensity
0.9
0.6
0.3
0.0
180
120
60
0
600
800
1000
1200
1400
1600
Frequency (cm$^{-1}$)

# CHAPTER 5

# ALKALI METAL CATION – HEXACYCLEN: EFFECTS OF ALKALI METAL CATION SIZE ON THE STRUCTURE AND BINDING ENERGIES

Portions of this chapter were reprinted with permission Austin, C.A. and Rodgers, M.T. Alkali Metal Cation – Hexacyclen: Effects of Alkali Metal Cation Size on the Structure and Binding Energies. J. Phys. Chem. A 118 (2014) 5488.

## 5.1. Introduction

Hexacyclen (1,4,7,10,13,16-hexaazacyclooctadecane, hexaaza-18-crown-6, ha18C6) is a multidentate amine macrocycle, and the aza analogue of 18-crown-6 (1,4,7,10,13,16-hexaoxacyclooctadecane, 18C6). The structure of ha18C6 is shown in **Figure 5.1**.

Theoretical investigations of the interactions of hexacyclen with neutral and anionic species [1], and a range of transition metal cations including $Co^{3+}$, $Hg^{2+}$, and $Sn^{2+}$ [2], and the late first row divalent transition metal cations ($Mn^{2+}$, $Fe^{2+}$, $Co^{2+}$, $Ni^{2+}$, $Cu^{2+}$, and $Zn^{2+}$) [3] have been reported. To date, very little gas phase thermochemical and spectroscopic information has been reported for hexacyclen interactions with alkali metal cations.

The studies of molecular recognition of metal cations by macrocyclic ligands have been extended by probing the nature of the binding interactions in alkali metal cation−ha18C6 complexes and providing accurate binding energies for the series of alkali metal cations including $Na^+$, $K^+$, $Rb^+$, and $Cs^+$. Results for the $M^+$(ha18C6) complexes are compared to the analogous $M^+$(18C6) and $M^+$(ta12C4) complexes to elucidate the influence of the donor atoms (N versus O) and the number of donor atoms (six vs. four) on the nature and strength of binding. In aqueous solution, alkali metal cations preferentially bind to crown ethers over the analogous nitrogen macrocycles [4]. Investigating the $M^+$(ha18C6) complexes in the gas phase and in solvent (via use of a polarizable continuum solvent model) thus allows separation of the intrinsic binding interactions and effects due to solvation. In addition, the effects of the alkali metal cations on the conformation of their complexes to ha18C6 are investigated. Previous work indicates that the ha18C6 ligand encapsulates metal cations in different geometric environments that depend on the size of the metal cation [2].

### 5.2. Collision–Induced Dissociation Experiments

Cross sections for collision-induced dissociation (CID) of four $M^+$(ha18C6) complexes, where $M^+ = Na^+$, $K^+$, $Rb^+$, and $Cs^+$, are measured using a guided ion beam tandem mass spectrometer that has been described in detail Chapter 2. The $M^+$(ha18C6) complexes are generated by electrospray ionization (ESI) [5]. Thermochemical analyses of the experimental results are explicitly discussed in **Chapter 2**.

### 5.3. Theoretical Calculations

To obtain model structures, vibrational frequencies, rotational constants, and energetics for the neutral ha18C6 ligand and the $M^+$(ha18C6) complexes, molecular dynamics simulated annealing procedures and ab initio and density functional theory calculations were performed using Hyperchem [6] and the Gaussian 09 suite of programs [7], respectively, and is describe in detail in **Chapter 2**.

Initial candidate structures chosen for higher-level optimization for the $M^+$(ha18C6) complexes were generated using five of the low-energy neutral ha18C6 structures, those that were expected to provide the most favorable geometries for interaction with the alkali metal cation, and those similar to the crystal structures of transition metal cation−ha18C6 complexes previously reported [8,9]. The neutral ha18C6 geometries used to bind to the metal cation were chosen on the basis of their similarities to crystal structures and their ability to fully encapsulate the metal cation (i.e., the $C_{3v}$ and $D_{3d}$ structures of **Figure 5.1**). In all cases the metal cation was placed in the center of the neutral ha18C6 ligand, such that all of the $M^+$−N bond distances were approximately equal, and subjected to geometry optimization.

Vibrational analyses of the geometry-optimized structures were performed to determine the vibrational frequencies of the neutral ha18C6 ligand and $M^+$(ha18C6) complexes. When used to model the data or to calculate thermal energy corrections, the computed frequencies were scaled by a factor of 0.9804 [10]. Single-point energy calculations were performed at the B3LYP and MP2(full) levels of theory using 6-311+G(2d,2p)_HW and def2-TZVPPD basis sets and the B3LYP/6-31+G* _HW and B3LYP/def2-TZVPPD optimized geometries, respectively. To obtain accurate BDEs, zero-point energy (ZPE) corrections scaled by 0.98 were applied, and basis set superposition errors (BSSE) were subtracted from the computed BDEs in the full counterpoise correction [11,12]. The BSSE corrections are much smaller for B3LYP than MP2(full) calculations. Because previous calculations for the $M^+$(18C6) complexes were performed at a lower level of theory [13], analogous calculations for the $M^+$(18C6) complexes were also performed here to enable effective comparisons to the $M^+$(ha18C6) systems. $M^+$−18C6 BDEs are summarized in **Table 5.1**. The polarizabilities for the stable low-energy conformers of ha18C6 were calculated at the PBE0/6-311+G(2d,2p) level of theory using the B3LYP/6-31+G* optimized geometries. This level of theory has been shown to accurately reproduce experimental polarizabilities [14]. In addition, the polarizabilities for the stable low-energy conformers of ha18C6 were also calculated at the PBE0/def2-TZVPPD level of theory.

To further assess the effects of dispersion on the binding in the $M^+$(ha18C6) complexes, limited calculations were also performed at the B3LYP-D/def2-TZVPPD level of theory. Likewise, to examine the effects of solvent on the binding, limited calculations at the B3LYP/def2-TZVPPD level of theory using a polarizable continuum model (PCM) in water and acetonitrile were also performed. Included among these calculations were the stable low-energy conformations of the neutral ha18C6 ligand and

$Na^+$(ha18C6) complex as well as the ground-state conformations of the $M^+$(ha18C6) complexes of the larger alkali metal cations. Calculations for the $Cs^+$(ha18C6) complex in both water and acetonitrile, and the $Rb^+$(ha18C6) complex in acetonitrile were unsuccessful as the PCM calculations required more memory than available to us. B3LYP-D calculations could not be performed for the $Cs^+$(ha18C6) complex as no van der Waals radius is available in Gaussian09 for $Cs^+$.

## 5.4. Results

### 5.4.1. Cross Sections for Collision–Induced Dissociation

Cross sections were measured for the interaction of Xe with four $M^+$(ha18C6) complexes, where $M^+ = Na^+$, $K^+$, $Rb^+$, and $Cs^+$. **Figure 5.2a** shows representative data for the $K^+$(ha18C6) complex. The complexes to $Na^+$, $Rb^+$, and $Cs^+$ exhibit similar behavior, and are provided as **Figure 5.3a**. In all cases, $M^+$ is the only ionic product detected corresponding to endothermic loss of the intact ha18C6 ligand in the CID reactions 5.1.

$$M^+(\text{ha18C6}) + Xe \rightarrow M^+ + \text{ha18C6} + Xe \qquad (5.1)$$

The magnitudes of the cross sections generally increase as the size of the alkali metal cation increases from $Na^+$ to $Cs^+$, which is primarily a result of the CID thresholds decreasing in that order.

### 5.4.2. Threshold Analysis.

The model of **Equation 2.4** was used to analyze the thresholds for CID reactions 5.1 in four $M^+$(ha18C6) systems. The results of these analyses are provided in **Table 5.2**. The molecular parameters of the ground-state structures of the $M^+$(ha18C6) complexes at 0 K were used in the modeling procedures. A representative analysis is shown in **Figure**

**5.2b** for the $K^+$(ha18C6) complex. An analogous set of figures for the complexes to $Na^+$, $Rb^+$, and $Cs^+$ are provided as **Figure 5.3b**. In all cases, the experimental cross sections for CID reactions 5.1 are accurately reproduced using a loose PSL TS model [15]. Previous work has shown that this model provides the most accurate assessment of the kinetic shifts for CID processes for noncovalently bound metal− ligand complexes [16–23].

Good reproduction of the experimental data is obtained over energy ranges exceeding 3 eV and cross-section magnitudes >3 orders of magnitude for the $M^+$(ha18C6) complexes. **Table 5.2** also includes threshold values, $E_0$, obtained without including the RRKM lifetime analysis in the modeling procedures. The difference between these values and the $E_0$(PSL) values provides a measure of the kinetic shifts for these systems, which vary from 1.47 eV for the $Cs^+$(ha18C6) complex to 5.10 eV for the $Na^+$(ha18C6) complex. All four $M^+$(ha18C6) complexes possess the same number of degrees of freedom, the kinetic shifts should directly correlate with the measured $M^+$−ha18C6 BDEs (**Table 5.2**), as observed.

The entropy of activation, $\Delta S^\dagger$, is a measure of the looseness of the TS. $\Delta S^\dagger$ is largely determined by the molecular parameters (vibrational frequencies and rotational constants) used to model the energized $M^+$(ha18C6) complex and the TS, but also depends on the threshold energy. The $\Delta S^\dagger$(PSL) values for these systems at 1000 K exhibit modest variation, as expected on the basis of the similarity of these systems, and vary between 58 and 78 $J \cdot K^{-1} \cdot mol^{-1}$. The larger value for the $Na^+$(ha18C6) complex is a consequence of both the larger threshold energy and different conformation of the energized molecule, Na3(6N), versus that of other complexes, M1(6N). These entropies of activation compare favorably to those previously determined in our laboratory for a wide variety of noncovalently bound complexes that dissociate via simple noncovalent bond cleavage [21–30].

### 5.4.3. Theoretical Results

The ground–state and stable low energy conformations of the ha18C6 ligand and $M^+$(ha18C6) complexes were determined as described in the Theoretical Calculations section of **Chapter 2**. $M^+$–ha18C6 BDEs calculated at the B3LYP, B3LYP-D, and MP2(full) levels of theory using the def2-TZVPPD and 6-311+G(2d,2p)_HW basis sets are summarized in **Table 5.3**, whereas B3LYP/def2-TZVPPD results using the PCM model in acetonitrile and water are listed in **Table 5.4**. Independent ZPE and BSSE corrections are also included in the computed BDEs.

#### 5.4.3.1. Neutral ha18C6

The B3LYP/def2-TZVPPD optimized structures of the neutral ha18C6 ligand along with the calculated dipole moments are shown **Figure 5.1**. Four distinct stable geometries were found. Energetics computed using the B3LYP/def2-TZVPPD level of theory was determined to be the most reliable in a previous study of the analogous $M^+$(ta12C4) complexes [22]. Therefore, the following discussion will focus on the geometries and energetics calculated at the B3LYP/def2-TZVPPD level of theory unless otherwise noted. The ground-state conformer of ha18C6 is of $C_{3v}$ symmetry and surprisingly exhibits a relatively large dipole moment of 2.98 D. Three of the amine hydrogen atoms of the ground-state conformer are oriented toward the cavity of the ring with corresponding ∠CNCC dihedral angles of 175.9°, whereas the other three amine hydrogen atoms are oriented perpendicular to the cavity of the ring with corresponding ∠CNCC dihedral angles of −178.1°. In this conformation all of the amine hydrogen atoms are located on the same side of the neutral ligand such that by the ∠HNCC dihedral angles are all positive and vary from 51.2 to 60.0°. Santos and Drew [1] previously reported this structure as the ground state.

The next most stable conformer is of $C_{2h}$ symmetry and was previously reported as the ground-state structure by Varadwaj et al [3]. The $C_{2h}$ conformer lies 7.9 kJ/mol higher in energy than the $C_{3v}$ ground–state conformer. In the $C_{2h}$ conformer, the amine hydrogen atoms alternate up and down, two amine donor atoms are oriented away from the cavity of the ligand, whereas the other four amine hydrogen atoms are oriented toward the cavity of the ligand with corresponding ∠HNCC dihedral angles of ~ ± 60°. The local dipoles of the $C_{2h}$ conformer are anti–aligned and oriented toward the center of the cavity, leading to cancellation of the local dipoles and no overall dipole moment due to symmetry. Two additional stable conformers are found that are of $C_i$ and $D_{3d}$ symmetry that lie 33.8 and 58.9 kJ/mol, respectively, higher in energy than the $C_{3v}$ ground–state conformer. Similar to the $C_{2h}$ conformer, the dipoles are anti–aligned for the $C_i$ and $D_{3d}$ conformers leading to cancellation, and no net dipole moment. The $C_i$ and $D_{3d}$ conformers are similar in that the nitrogen donor atoms alternate up and down in the ring, but differ in the positions of the amine hydrogen atoms. For the $D_{3d}$ conformer, the amine hydrogen atoms are off set to a greater extent from the plane of the ring with smaller average ∠CNCC and ∠NCCN dihedral angles of 169.2° and 46.6°, respectively, than the $C_i$ conformer with corresponding dihedral angles of 172.3° and 52.6°, respectively. This is further illustrated by the differences in the average ∠HNCC dihedral angles, which are 68.8° for the $C_i$ conformer, and only 37.2° for the $D_{3d}$ conformer. Similar results are found at the MP2(full)/def2-TZVPPD and B3LYP/6-311+G(2d,2p)_HW levels of theory. In contrast, and in agreement with the results of Varadwaj et al. [3], the MP2(full)/6-311+G(2d,2p)_HW level of theory finds the $C_{2h}$ conformation to be the lowest–energy structure, whereas the $C_{3v}$ conformer lies a mere 0.4 kJ/mol higher in energy at this level of theory.

### 5.4.3.2. $M^+$(ha18C6)

The B3LYP/def2-TZVPPD optimized geometries and relative Gibbs free energies at 298 K of the stable low-energy conformers of the $K^+$(ha18C6) complex are shown in **Figure 5.4**. Similar conformations were also found for the $M^+$(ha18C6) complexes to the other alkali metal cations investigated and are provided as **Figures 5.5–5.7**. The nomenclature employed to describe these structures is of the form Mx(y,*y*N), where M identifies the metal cation, x indicates the relative order of stability among the stable low–energy conformers of the $K^+$(ha18C6) complex, yN is the number of N donor atoms coordinated to the alkali metal cation and describes the $M^+$–N interactions as having relatively short (y) or relatively longer (*y*) $M^+$–N bond lengths (versus the average $M^+$–N bond lengths). The ground–state conformation of $M^+$(ha18C6) varies with the size of the alkali metal cation. Similar results have been found for complexes of transition metal cations to 1,5,9,13-tetracyclohexadecane, whereupon changing the size of the metal cation, more highly strained conformers are observed to form more stable complexes [31]. The ground–state conformation of the $M^+$(ha18C6) complexes at 0 K determined at the B3LYP/def2-TZVPPD level of theory is very similar for the $K^+$, $Rb^+$, $Cs^+$ complexes, but differs from that found for $Na^+$, **Figures 5.4–5.7**. However, at 298 K the most stable conformation of $Na^+$(ha18C6) is a structure parallel to that found for the other alkali metal cations. The relative energies and free energies follow the same order for $K^+$, $Rb^+$, and $Cs^+$, whereas the relative ΔH and ΔG values differ markedly for $Na^+$, **Figure 5.5**. At the MP2 level of theory (using the def2-TZVPPD basis set) the relative energies and Gibbs free energies are similar to those determined at the B3LYP level of theory. In contrast, the ground–state conformations transition at $Cs^+$ for calculations performed at the B3LYP and MP2 levels of theory using the 6-311+G(2d,2p)_HW basis set. Similar behavior was found for the $M^+$(18C6) complexes, where the relative stabilities of the stable low-energy conformers were also found to vary with the level of theory employed [13].

### 5.4.3.2.1. $K^+$(ha18C6)

In the ground-state conformation of the $K^+$(ha18C6) complex, K1(6N), the $K^+$ metal cation sits in the center of the nearly planar ring created by the amine donor atoms at an average $K^+$–N bond distance of 2.991 Å. There are small differences in the average ∠NCCN and ∠CNCC dihedral angles that describe the skeletal backbone of the macrocycle that occur upon binding of $K^+$, **Table 5.5**. The ∠HNCC dihedral angles are influenced the most and increase from 55.6° in neutral ha18C6 to 64.9° in $K^+$(ha18C6). There is no change in the average N–H bond distances, whereas the C–N bonds are elongated by 0.011 Å. Previously, Santos et al. concluded that for $M^+$(ha18C6) complexes to small metal cations such that the $M^+$–N bond distances are <2.6 Å, a more bent structure (trigonal prismatic) is preferred, whereas for larger metal cations a planar hexagonal conformer is preferred, similar to that found for the $K^+$(ha18C6) complex [1,2]. The next most stable conformer, K2(6N), is calculated to lie 44.0 kJ/mol higher in free energy and has an average $K^+$–N bond distance of 3.153 Å. In the K2(6N) conformer, three of the amine hydrogen atoms are oriented toward the cavity with corresponding averages ∠HNCC dihedral angle of −74.4° , such that the metal cation sits slightly above the plane created by the nitrogen donor atoms. The K2(6N) conformer skeletal backbone dihedral angles differ from the ha18C6 conformer by 11 to 27° , with the ∠NCCN and ∠CNCC dihedral angles contracting and the ∠HNCC dihedral expanding. The N–H bonds of the K2(6N) conformer shorten by 0.004 Å, whereas the C–N bonds are elongated by 0.012 Å versus the ground–state K1(6N) conformer. The K3(6N) conformer lies 71.5 kJ/mol higher in free energy and is similar to the trigonal prismatic structure observed for ha18C6 interactions with small metal cations as much greater distortions of the neutral ligand occur upon binding of $K^+$ in this conformation[9,32,33]. The K3(6N) conformer has an average $K^+$–N bond distance of 2.847 Å. The K4(6N) conformer is more compact such that the average $K^+$–N bond distance is the shortest among the low–energy conformers computed, 2.642 Å, and is calculated to lie 199.1 kJ/mol higher in free energy! The K4(6N) conformer exhibits the greatest distortion upon binding of $K^+$ of all of the stable conformers computed, see **Table 5.5**. Similar trends in the geometric parameters are found for all of the other alkali metal cation–hexacyclen complexes. The K4(6N) conformer possesses an imaginary frequency corresponding to a ring-breathing mode where the metal cation moves up and down in the center of the ring as the ring stretches and shrinks. Calculations were performed using tight convergence in an attempt to remove this imaginary frequency; however, even tight convergence failed to eliminate the imaginary frequency.

#### 5.4.3.2.2. $Rb^+$(ha18C6) and $Cs^+$(ha18C6)

For $Rb^+$ and $Cs^+$, the Cs complexes, M1(6N) are preferred as found for the $K^+$(ha18C6) complex. The cavity of ha18C6 is too small to accommodate these larger metal cations such that the metal cation sits above the ring in the complexes to $Rb^+$ and $Cs^+$, **Figure 5.6–5.7**. At the B3LYP/def2-TZVPPD level of theory, M2(3N) conformers are calculated to lie 18.8 and 7.5 kJ/mol higher in free energy for $Rb^+$ and $Cs^+$ than the ground–state M1(6N) conformers, respectively. As previously discussed, at the B3LYP/6-311+G(2d,2p)_HW level of theory, the Cs2(3N) conformer, with an average $Cs^+$–N bond distance of 3.363 Å, is calculated to be the lowest–energy structure of the $Cs^+$ (ha18C6) complex, whereas the Cs1(6N) conformer is calculated to lie 7.1 kJ/mol higher in free energy. The Cs1(6N) conformer has an average $Cs^+$–N bond distance of 3.246 Å, slightly shorter than that found for the Cs2(3N) conformer. In contrast, the Rb1(6N) conformer is the ground state for the $Rb^+$(ha18C6) complex at all levels of theory. The Rb1(6N) conformer has an average $Rb^+$–N bond distance of 3.082 Å, whereas the Rb2(3N) conformer has an average $Rb^+$–N bond distance of 3.200 Å. The Rb3(4,2N) and Cs3(2,2N) conformers are more highly distorted than the more symmetric M3(6N) complexes found for $Na^+$ and $K^+$, with average $M^+$–N bond distances of 3.123 and 3.381 Å, respectively. For $Rb^+$(ha18C6), the Rb3(4,2N) conformer is calculated to lie 71.0 kJ/mol higher in free energy than the ground–state Rb1(6N) conformer. For $Cs^+$(ha18C6), the Cs3(2,2N) conformer is calculated to lie 42.6 kJ/mol higher in free energy than the ground–state Cs1(6N) conformer. The M4(6N) conformers are calculated to lie 272.9 and 358.8 kJ/mol higher in free energy for $Rb^+$ and $Cs^+$, respectively. Similar to the K4(6N) conformer, the shortest bond distances are found for the Rb4(6N) (2.756 Å) and Cs4(6N) (2.875 Å) conformers, which also possess an imaginary frequency corresponding to a ring-breathing mode in which the metal cation moves up and down in the center of the ring as the ring expands and contracts, respectively. Again, calculations were performed using tight convergence, but attempts failed to eliminate the imaginary frequency.

#### 5.4.3.2.3. $Na^+$(ha18C6)

Similar structures are found for the $Na^+$(ha18C6) complex at the B3LYP level of theory, however the relative stability order of the conformers changes significantly versus the larger alkali metal cations, **Figure 5.5**. As shown in **Figure 5.5**, conformers Na1(6N) and Na3(6N) are of very similar stability (free energy). At 0 K Na3(6N) is the ground–state conformation, whereas Na1(6N) is more stable at 298 K. For the Na1(6N) conformation, the average $Na^+$–N bond distance is 2.918 Å, suggesting a more weakly bound complex than the Na3(6N) conformation where the average $Na^+$–N bond distance is 2.571 Å. In the Na1(6N) conformation, the amine groups alternate up and down in the ring, and the local dipoles of the amine donor atoms are oriented toward the metal cation. This is clearly indicated by the sign of the ∠HNCC dihedral angles ~ −68.3° for the amine donor atoms facing down and 68.3° for the nitrogen donor atoms that face up. The next most stable conformer, Na3(6N), is calculated to lie 7.1 kJ/mol higher in free energy than the ground–state Na1(6N) conformer. In this conformation the local dipoles of all six amino groups are oriented toward the metal cation with an average $Na^+$–N bond distance of 2.571 Å. Several crystal structures have been reported in the literature where ha18C6 encapsulates small transition metal cations such as $Hg^{2+}$, $Co^{3+}$, and $Cu^{2+}$ in structures similar to that computed for the Na3(6N) conformer of the $Na^+$ (ha18C6) complex[9,32,33]. In most of these cases, the complex is octacoordinate due to the presence of counteranions, versus the hexacoordinate ionic complex reported here. We identified another high–energy structure also of $D_{3d}$ symmetry, Na4(6N), that lies 45.2 kJ/mol higher in free energy than the ground-state Na1(6N) conformer. A crystal structure similar to the Na4(6N) conformer was reported by Chandrasekhar et al. for the Cr(III)[(ha18C6)]$Br^{3-}$ complex [8]. The Na2(6N) conformer was found to possess two imaginary frequencies associated with the metal cation bouncing back and fourth in the plane of the macrocycle created by the nitrogen donor atoms and is calculated to lie 70.0 kJ/mol higher in free energy than the ground–state Na1(6N) conformer. In this conformation, the amino hydrogen atoms are all located on the same side of the macrocyclic ring, whereas in the three more stable conformations, the amine hydrogen atoms alternate up and down. Again, re-optimization using tight convergence failed to eliminate the imaginary frequencies.

## 5.5. Discussion

### 5.5.1. Comparison of Theory and Experiment

The $M^+$–ha18C6 BDEs at 0 K measured here by threshold CID techniques are summarized in **Table 5.3**. Also listed in **Table 5.3** are the $M^+$–ha18C6 BDEs calculated at the B3LYP, B3LYP-D, and MP2(full) levels of theory using the def2-TZVPPD and 6-311+G(2d,2p)_HW basis sets, including independent ZPE and BSSE corrections. The agreement between the calculated and measured BDEs is illustrated in **Figure 5.8**. As can be seen in the figure, the B3LYP/def2-TZVPPD values exhibit very good agreement with the measured values for $K^+$, $Rb^+$, and $Cs^+$, but underestimate the strength of binding to $Na^+$. The mean absolute deviation (MAD) between theory and experiment is 13.1 ± 16.4 kJ/mol. The MAD is somewhat larger than the average experimental uncertainty (AEU) in these values, 8.9 ± 3.0 kJ/mol. When BSSE corrections are not included (values not shown in **Figure 5.8**), the MAD between the B3LYP/def2-TZVPPD calculated and the TCID measured values improves slightly to 11.9 ± 15.6 kJ/mol. In contrast, the MAD between the calculated and measured values is almost twice as large at the B3LYP/6-311+G(2d,2p)_HW level of theory, 22.9 ± 14.6 kJ/mol. B3LYP theory underestimates the strength of interaction in all cases, except for the $K^+$(ha18C6) complex, when the 6-311+G(2d,2p)_HW basis set is used. The agreement between MP2(full) theory, using both the def2-TZVPPD and 6-311+G(2d,2p)_HW basis sets, and measured $M^+$–ha18C6 BDEs is intermediate between the B3LYP results using these basis sets with MADs of 16.8 ± 9.4 and 16.2 ± 12.0 kJ/mol, respectively. MP2(full) theory overestimates the strength of interaction in all cases, except for the $Na^+$(ha18C6) complex, when the def2-TZVPPD basis set is used. MP2(full) theory underestimates the strength of interaction in all cases, except for the $K^+$(ha18C6) complex, when the 6-311+G(2d,2p)_HW basis set is used, similar to the trend observed at the B3LYP level of theory, and as reported previously for other ligands binding to the $Rb^+$ and $Cs^+$ cations when the Hay–Wadt ECP is used. [21–23, 34–41] When dispersion corrections are included in the B3LYP model, i.e., B3LYP-D, the BDEs increase significantly, and exhibit much poorer agreement with the measured values. The MAD between the B3LYP-D and measured BDEs is 45.2 ± 5.9 kJ/mol, much larger than the AEU in these values, 10 ± 2.6 kJ/mol. Clearly the B3LYP-D model is significantly over-correcting for dispersion effects in the binding.

### 5.5.2. Trends in the Binding of Alkali Metal Cations to ha18C6

The experimental and calculated $M^+$–ha18C6 BDEs at 0 K are summarized in **Table 5.3**. The variation in the measured BDEs with the size of the alkali metal cation [42] is shown in **Figure 5.9**. Similar to behavior observed for many alkali metal cation–ligand complexes including $M^+$(ta12C4) [22] and $M^+$(18C6) [20], the $M^+$–ha18C6 BDEs are found to decrease monotonically as the size of the alkali metal cation increases from $Na^+$ to $Cs^+$. This is the expected trend for binding based primarily on electrostatic interactions because the metal–ligand bond distances are primarily determined by the size of the metal cation. Smaller cations lead to shorter metal–ligand bond distances and stronger electrostatic interactions [43]. The difference in the $M^+$–ha18C6 BDEs for adjacent metal cations becomes smaller as the size of the metal cation increases from $Na^+$ to $Cs^+$ because the relative change in the ionic radii for the alkali metal cations becomes smaller.

### 5.5.3. Comparison with 18-crown-6

The experimentally determined $M^+$–ha18C6 and $M^+$–18C6 [20] BDEs are plotted as a function of the ionic radii of the alkali metal cations in **Figure 5.9a**, whereas the measured and calculated $M^+$–ha18C6 and $M^+$–18C6 BDEs are listed in **Tables 5.3** and **5.1**, and are compared in **Figure 5.9b**. Experimentally, the $Na^+$ cation is found to bind ha18C6 more strongly than 18C6. In contrast, for all of the larger alkali metal cations, the measured $M^+$–18C6 BDEs slightly exceed the $M^+$–ha18C6 BDEs, but are equal within the experimental errors in these measurements, suggesting that the differences in the binding are not significant. In contrast, both B3LYP and MP2 theory suggest that the alkali metal cations should bind to 18C6 more strongly than ha18C6, and that the preference for 18C6 should increase with the size of the alkali metal cation. Interestingly, although theory overestimates the preference for 18C6, the relative trend in the experimental data is reproduced as illustrated in **Figure 5.9b**.

Highly parallel results were found for the comparison of the analogous four–donor system previously investigated, where ta12C4 exhibits preferential binding to $Na^+$, whereas the experiments suggest that 12C4 binds slightly more strongly to the larger alkali metal cations, $K^+$, $Rb^+$, and $Cs^+$ [22]. In contrast, B3LYP and MP2 theory suggest that the alkali metal cations should bind to 12C4 more strongly than ta12C4 as the hardness of the metal decreases with the size of the alkali metal cation. However, again the measured differences are smaller than the experimental errors in these measurements and the expected accuracy of the theoretical methods applied, similar to the behavior observed here for ha18C6 and 18C6. These trends suggest that the N donor atoms of ha18C6 exhibit a strong preference for hard metal cations, and help explain their selectivity for transition metal cations.

### 5.5.4. Comparison with ta12C4

The experimentally determined $M^+$–ha18C6 and $M^+$–ta12C4 BDEs are plotted as a function of the ionic radii of the alkali metal cation in **Figure 5.10a**. Although the trends in binding are highly parallel, ha18C6 binds the alkali metal cations more strongly than ta12C4. **Figure 5.10b** compares the TCID measured and theoretically calculated $M^+$–ha18C6 and $M^+$–ta12C4 BDEs at 0 K. Solely on the basis of the number of $M^+$–N donor interactions, ha18C6 should bind 50% stronger than ta12C4, whereas the enhancement in the binding from ta12C4 to ha18C6 is much smaller (19 ± 6%). Theory suggests even smaller enhancements in the binding of ha18C6 versus ta12C4 of 9 ± 8% and 16 ± 7% at the B3LYP and MP2 levels of theory using def2-TZVPPD basis set, respectively. This behavior is not unexpected as ha18C6 provides six alkali metal cation–nitrogen donor interactions, whereas ta12C4 only provides four, and the strength of the $M^+$–N donor interactions should fall off with increasing ligation.

### 5.5.5. Solvent Effects

Comparison of the results for the isolated $M^+$(ha18C6) complexes to those determined using a PCM model for water or acetonitrile provide an opportunity to gain insight into both the intrinsic nature and strength of the binding as well as effects of solvent on the binding. The measured $M^+$(ha18C6) BDEs are quite strong in the absence of solvent, and decrease as the size of the alkali metal cation increases, from 325.8 ($Na^+$) to 221.8 ($K^+$) to 186.1 ($Rb^+$) to 149.0 ($Cs^+$) kJ/mol. As expected, the binding becomes much weaker in the presence of solvent as it shields and competes with the ha18C6 ligand for interactions with the alkali metal cation. The $M^+$–ha18C6 BDEs are weaker in water than acetonitrile as expected on the basis of the dielectric constants of these solvents, ε = 78.3 for water, and 35.7 for acetonitrile (as implemented in Gaussian09). In water, the $M^+$–ha18C6 BDEs increase from 5.8 kJ/mol for $Na^+$ to 27.7 kJ/mol for $K^+$, and then decrease to 9.8 kJ/mol for $Rb^+$. In acetonitrile, the $M^+$–ha18C6 are only slightly larger, and increase from 10.5 kJ/mol for $Na^+$ to 31.5 kJ/mol for $K^+$. Thus, both solvents lead to a change in the relative binding order. The intrinsic binding is inversely correlated with the size of the metal cation, whereas both solvents exhibit selectivity for $K^+$ over the other alkali metal cations. Parallel intrinsic and solution behavior has also been reported for alkali metal cation binding to 18C6 [13,20].

### 5.6. Conclusion

The kinetic energy dependences of the collision-induced dissociation of four $M^+$(ha18C6) complexes, where $M^+$ = $Na^+$, $K^+$, $Rb^+$, and $Cs^+$, with Xe are examined in a guided ion beam tandem mass spectrometer. The only dissociation pathway observed for all four complexes is loss of the intact ha18C6 ligand. Thresholds for these dissociation reactions are determined after careful consideration of the effects of the kinetic and internal energy distributions of the reactants, multiple collisions with Xe, and the lifetime of the activated $M^+$(ha18C6) complexes using a loose-phase space limit TS model. Molecular parameters needed for the analysis of the experimental data as well as structures and theoretical estimates for the $M^+$–ha18C6 BDEs are obtained from theoretical calculations performed at the B3LYP and MP2(full) levels of theory using the def2-TZVPPD and 6-311+G(2d,2p)_HW basis sets. Good agreement between theory and experiment is found for the B3LYP/def2-TZVPPD results, and suggest that calculations using the hybrid basis set, 6-311+G(2d,2p)_HW, are less worthwhile. MP2(full) theory does a reasonable job but does not perform quite as well at B3LYP theory with either basis set. Inclusion of dispersion effects in the B3LYP functional, B3LYP-D, leads to a gross overestimate in the strength of the binding. Trends in the measured and calculated $M^+$–ha18C6 BDEs suggest that the binding is based primarily on electrostatic interactions. For the larger alkali metal cations, $K^+$, $Rb^+$, and $Cs^+$, the nature of the binding to ha18C6 is similar, resulting in highly parallel stable low-energy conformations of these complexes. The ha18C6 ligand binds $Na^+$ more strongly than 18C6 as previously found for ta12C4 vs 12C4. In contrast, a slight preference for binding of 18C6 over ha18C6 to $K^+$, $Rb^+$, and $Cs^+$ is found, but this preference is smaller than the experimental error in these measurements for $K^+$ and $Cs^+$, suggesting that this binding preference is not very significant. Overall, the gas-phase trends in the binding suggest that the N donors atoms of ha18C6 bind more strongly to hard metal cations, whereas the O donor atoms of 18C6 bind slightly more strongly to softer metal cations. In contrast, the B3LYP and MP2(full) levels of theory suggest preferential binding of the alkali metal cations to 18C6. Binding of the alkali metal cations to ha18C6 is found to be 19 ± 6% stronger than to ta12C4, indicating that the number of donor atoms, the cavity size, and the flexibility of the ligand allow alkali metal cations to bind more strongly but that the enhancement in the binding falls off monotonically with each additional $M^+$–N interaction. In solvent, the binding interactions are weakened significantly, and the competition between the ha18C6 ligand and the solvent for the alkali metal cations leads to a change in the relative binding order such that ha18C6 is selective for $K^+$ over the other alkali metal cations, parallel to the behavior reported for 18C6.

## 5.7. References

[1] M.A. Santos, M.G.B. Drew, J. Chem. Soc., Faraday Trans. 87 (1991)1321.

[2] M.G.B. Drew, M.A. Santos, Struct. Chem. 4 (1993) 5.

[3] P.R. Varadwaji, A. Varawaj, G.H. Peslherbe, H.M. Marques, J. Chem. Phys. A 115 (2011) 13280.

[4] L.F. Lindoy, The Chemistry of Macrocyclic Ligand Complexes; Cambridge University Press, Cambridge, 1989, p. 13.

[5] Y. Chen, M.T. Rodgers, J. Am. Chem. Soc. 134 (2012) 2313

[6] HyperChem Molecular Modeling Software Package, Version 7.5; Hypercube Inc.: Gainesville, FL, 2002.

[7] Frisch, M. J.; et al. Gaussian 09, revision A.1; Gaussian, Inc.: Wallingford CT, 2009.

[8] S. Chandrasekhar, D.G. Fortier, A. McAuley, Inorg. Chem. 32 (1992) 1424.

[9] M.A.A.F. de C.T. Corrondo, V. Félix, M.T. Durate, M.A. Santos, Poly-hedron 12 (1993) 931.

[10] J.B. Foresman, M.J. Frisch, Exploring Chemistry  with Electronic Structure Methods, 2nd ed, Gaussian; Pittsburgh, 1996, p. 64.

[11] S.F. Boys, R. Bernardi, Mol. Phys. 19 (1979) 553.

[12] F.B. van Duijneveldt, J.G.C.M. van Duijneveldt-van de Rijt, J.H. van Lenthe, Chem. Rev. 94 (1994) 1873.

[13] E.D. Glendening, D. Feller, M.A. Thompson, J. Am. Chem. Soc. 116 (1994) 10657.

[14] S.M. Smith, A.N. Markevitch, D.A. Romanov, X. Li, R.J. Levis, H.B. Schlegel, J. Phys. Chem. A 108 (2004) 11063.

[15] M.T. Rodgers, K.M. Ervin, P.B. Armentrout, J. Chem. Phys. 106 (1997) 4499.

[16] D. Ray, D. Feller, M.B. More, E.D. Glendening, P.B. Armentrout, J. Phys. Chem. 100 (1996) 16116.

[17] M.B. More, D. Ray, P.B. Armentrout, J. Phys. Chem. A 101 (1997) 831.

[18] M.B. More, D. Ray, P.B. Armentrout, J. Phys. Chem. A 101 (1997) 4254.

[19] M.B. More, D. Ray, P.B. Armentrout, J. Phys. Chem. A 101 (1997) 7007.

[20] M.B. More, D. Ray, P.B. Armentrout, J. Am. Chem. Soc. 121 (1999) 417.

[21] P.B. Armentrout, C.A. Austin, M.T. Rodgers, Int. J. Mass Spectrom. 330–332 (2012) 16.

[22] C.A. Austin Y. Chen. M.T. Rodgers, Int. J. Mass Spectrom. 330–332 (2012) 27.

[23] P.B. Armentrout, C.A. Austin, M.T. Rodgers, J. Phys. Chem. A DOI: 10.1021/jp4116172.

[24] M.T. Rodgers, J. Phys. Chem. A 105 (2001) 2374.

[25] Y. Chen, M.T. Rodgers, J. Am. Chem. Soc. 134 (2012) 2313.

[26] Y. Chen, M.T. Rodgers, J. Am. Chem. Soc. 134 (2012) 5863.

[27] M.T. Rodgers, P.B. Armentrout, Mass Spectrom. Rev. 19 (2000) 215.

[28] M.T. Rodgers, P.B. Armentrout, J. Phys. Chem. A 103 (1999) 4955.

[29] J.R. Stanley, R. Amunugama, M.T. Rodgers, J. Am. Chem. Soc. 122 (2000) 10969.

[30] M.T. Rodgers, P.B. Armentrout, Int. J. Mass Spectrom. 185/186/187 (1999) 359.

[31] R, Luckay, T.E. Chantson, J.H. Reibenspies, R.D. Hancock, J. Chem. Soc., Dalton 8 (1995) 1363.

[32] M. Morooka, S. Ohba, K. Toriumi, Acta Crystallogr. Sect. B 48 (1992) 459.

[33] L. Ballester, A. Gutiérrez, M.F. Perpiñán, A.E. Sánchez, M. Fonari, M. Gdaniec, Inorg. Chem. 46 (2007) 3946.

[34] C. Ruan, H. Huang, M.T. Rodgers, J. Am. Soc. Mass Spectrom 19 (2008) 305.

[35] C. Ruan, Z. Yang, M.T. Rodgers, Int. J. Mass Spectrom. 276 (2007) 233.

[36] C. Ruan, H. Huang, M.T. Rodgers, J. Phys. Chem. A 111 (2007) 13521.

[37] C. Ruan, Z. Yang, N. Hallowita, M.T. Rodgers, J. Phys. Chem. A 109 (2007) 11539.

[38] P.B. Armentrout. Y. Chen, M.T. Rodgers, J. Phys. Chem. A 116 (2012) 3989.

[39] P.B. Armentrout, M. Citir, Y. Chen, M.T. Rodgers, J. Phys. Chem. A 116 (2012) 11823.

[40] P.B. Armentrout, B. Yang, M.T. Rodgers, J. Phys. Chem. A 117 (2013) 3771.

[41] P.B. Armentrout, B. Yang, M.T. Rodgers, J. Phys. Chem. A 118 (2014) 4300.

[42] Ionic radii are taken from: CRC Handbook of Chemistry and Physics; http://www.hbcpnetbase.com.

[43] R.G. Wilson, G.R. Brewer, Ion Beams: With Applications to Ion Implantation; Wiley, New York, 1973 p 118.

**Table 5.1.** Bond Dissociation Enthalpies of $M^+(18C6)$ Complexes at 0 K in kJ/mol[a]

| $M^+$ | TCID | B3LYP[b] | | | | MP2[c] | | | |
|---|---|---|---|---|---|---|---|---|---|
| | | $D_e$ | $D_0^{d}$ | $D_{0,BSSE}^{d,e}$ | $D_{0,BSSE}^{,e}$ | $D_e$ | $D_0^{d}$ | $D_{0,BSSE}^{d,e}$ | $D_{0,BSSE}^{,e}$ |
| $Na^+$ | 296.2 (19.3) | 332.1 | 324.0 | 322.4 | **341.8**[f] | 351.7 | 343.6 | 327.3 | **349.0**[f] |
| | | *338.8* | *331.2* | *324.6* | | *351.2* | *343.6* | *326.1* | |
| $K^+$ | 234.5 (12.5) | 279.1 | 272.0 | 269.0 | **284.9**[f] | 313.9 | 306.8 | 282.4 | **301.3**[f] |
| | | *283.4* | *276.2* | *272.4* | | *303.9* | *296.8* | *281.4* | |
| $Rb^+$ | 191.0 (12.5) | 236.6 | 230.7 | 230.0 | **231.0**[f] | 298.7 | 292.9 | 248.6 | **247.7**[f] |
| | | *225.1* | *219.3* | *217.2* | | *262.0* | *256.2* | *224.4* | |
| $Cs^+$ | 167.9 (8.7) | 204.4 | 198.5 | 197.7 | **186.6**[f] | 261.0 | 255.2 | 227.5 | **207.5**[f] |
| | | *183.2* | *178.4* | *176.0* | | *224.5* | *219.7* | *189.6* | |

[a] TCID bond dissociation enthalpies of $M^+(18C6)$ complexes results from More et al. reference 36, uncertainties are listed in parentheses. [b] Calculated at B3LYP/def2-TZVPPD and *B3LYP/6-311+G(2d,2p)_HW//B3LYP/6-31+G*_HW* levels of theory. [c] Calculated at MP2(full)/def2-TZVPPD and *MP2(full)/6-311+G(2d,2p)_ HW//B3LYP/ 6-31+G*_HW* levels of theory. [d] Including ZPE corrections with the B3LYP/6-31+G*_HW and B3LYP/def2-TZVPPD frequencies scaled by a factor of 0.9804. [e] Also includes BSSE corrections. [f] B3LYP/6-31+G(d) and MP2(full)/6-31+G(d)//B3LYP/6-31+G(d) (**bold**) results from Glendening et. al. reference 37.

**Table 5.2.** Fitting Parameters of Equation 1, Threshold Dissociation Energies at 0 K, and Entropies of Activation at 1000 K of $M^+$(ha18C6) Complexes[a]

| $M^+$ | $\sigma_0{}^{b}$ | $n^{b}$ | $E_0{}^{c}$ (eV) | $E_0(\mathrm{PSL})^{b}$ (eV) | Kinetic Shift (eV) | $\Delta S^{\dagger}(\mathrm{PSL})^{b}$ (J mol$^{-1}$•K•$^{-1}$) |
|---|---|---|---|---|---|---|
| $Na^+$ | 16.7 (2.2) | 1.1 (0.1) | 8.48 (0.08) | 3.38 (0.13) | 5.10 | 78 (2) |
| $K^+$ | 6.71 (0.4) | 1.0 (0.1) | 5.13 (0.14) | 2.30 (0.10) | 2.83 | 58 (2) |
| $Rb^+$ | 3.17 (0.3) | 1.0 (0.1) | 3.96 (0.05) | 1.93 (0.08) | 2.03 | 62 (2) |
| $Cs^+$ | 1.77 (0.2) | 1.5 (0.1) | 2.68 (0.14) | 1.55 (0.06) | 1.13 | 60 (2) |

[a] Present results, uncertainties are listed in parentheses. [b] Average values for a loose PSL TS. [c] No RRKM analysis.

**Table 5.3.** Bond Dissociation Enthalpies of $M^+$(ha18C6) Complexes at 0 K in kJ/mol[a]

| $M^+$ | TCID | B3LYP[b] | | | MP2[c] | | |
|---|---|---|---|---|---|---|---|
| | | $D_e$ | $D_0^d$ | $D_{0,BSSE}^{d,e}$ | $D_e$ | $D_0^d$ | $D_{0,BSSE}^{d,e}$ |
| $Na^+$ | 325.8 (12.8) | 305.3 | 290.7 | 288.7 | 343.5 | 328.9 | 299.6 |
| | | (396.1) | (379.3) | (377.2) | | | |
| | | *311.4* | *297.0* | *289.1* | *342.5* | *322.5* | *295.5* |
| $K^+$ | 221.8 (9.3) | 230.6 | 223.1 | 221.0 | 263.9 | 256.4 | 232.1 |
| | | (273.0) | (264.8) | | | | |
| | | *234.3* | *227.3* | *224.1* | *259.4* | *246.9* | *232.3* |
| $Rb^+$ | 186.1 (7.8) | 184.7 | 178.9 | 177.5 | 245.5 | 239.7 | 194.3 |
| | | (237.8) | (231.5) | (230.8) | | | |
| | | *170.2* | *163.2* | *161.0* | *208.5* | *193.6* | *165.2* |
| $Cs^+$ | 149.0 (5.8) | 149.8 | 145.0 | 143.3 | 205.8 | 201.0 | 172.7 |
| | | *132.3* | *123.8* | *121.7* | *187.2* | *173.2* | *146.1* |
| MAD[f] | 8.9 (3.0)[g] | | | 13.1 (16.4) | | | 16.8 (9.4) |
| | | | | *22.9 (14.6)* | | | *16.2 (12.0)* |

[a] Present results, uncertainties are listed in parentheses. [b] Calculated at B3LYP/def2-TZVPPD and *B3LYP/6-311+G(2d,2p)_HW//B3LYP/6-31+G*_HW* levels of theory. [c] Calculated at MP2(full)/def2-TZVPPD//B3LYP/def2-TZVPPD and *MP2(full)/6-311+G(2d,2p)_HW //B3LYP/ 6-31+G*_HW* levels of theory. [d] Including ZPE corrections with the B3LYP/6-31+G*_HW and B3LYP/def2-TZVPPD frequencies scaled by a factor of 0.9804. [e] Also includes BSSE corrections. [f] Mean absolute deviation. [g] Average experimental uncertainty.

**Table 5.4.** Bond Dissociation Enthalpies of $M^+$(ha18C6) Complexes at 0 K in kJ/mol using Polarizable Continuum Model for Water and Acetonitrile.[a]

| $M^+$ | conformer | $H_20$ | | | ACN | | |
|---|---|---|---|---|---|---|---|
| | | $D_e$ | $D_0^b$ | $D_{0,BSSE}^c$ | $D_e$ | $D_0^b$ | $D_{0,BSSE}^c$ |
| $Na^+$ | Na3(6N) | 18.2 | 7.8 | 5.8 | 23.3 | 12.5 | 10.5 |
| $K^+$ | K1(6N) | 34.8 | 31.0 | 27.7 | 38.0 | 34.7 | 31.5 |
| $Rb^+$ | Rb1(6N) | 12.1 | 10.5 | 9.8 | - | - | - |

[a] Calculated at B3LYP/def2-TZVPPD level of theory. [b] Including ZPE corrections with the B3LYP/def2-TZVPPD frequencies scaled by a factor of 0.9804. [c] Also includes BSSE corrections.

**Table 5.5.** Geometrical Parameters of the B3LYP/def2-TZVPPD Optimized Structures of Neutral ha18C6 and the M$^+$(ha18C6) Complexes$^a$

| M$^+$ | Conformer | r(M–N) (Å) | ∠NMN (°) | ∠NCCN (°) | ∠HNCC (°) | ∠CNCC (°) | ∠NMNH (°) | r(C–N) Å | r(N–H) Å |
|---|---|---|---|---|---|---|---|---|---|
| 18N6 | $C_{3v}$ | - | - | 66.5 | 55.6 | 177.0 | - | 1.455 | 1.016 |
| Na$^+$ | Na1(6N) | 2.918 | 60.8 | 62.8 | 62.8 | 177.7 | 98.6 | 1.464 | 1.016 |
| | Na2(6N) | 2.943 | 58.6 | 55.5 | 75.6 | 164.3 | 83.3 | 1.468 | 1.014 |
| | Na3(6N) | 2.571 | 71.8 | 58.2 | 127.3 | 112.0 | 120.1 | 1.470 | 1.012 |
| | Na4(6N) | 2.428 | 77.9 | 49.8 | 151.4 | 86.6 | 127.3 | 1.472 | 1.010 |
| K$^+$ | K1(6N) | 2.991 | 61.0 | 68.0 | 64.9 | 175.0 | 99.7 | 1.466 | 1.016 |
| | K2(6N) | 3.153 | 54.7 | 56.0 | 69.7 | 170.3 | 77.1 | 1.467 | 1.012 |
| | K3(6N) | 2.847 | 65.4 | 59.1 | 124.1 | 111.1 | 118.9 | 1.470 | 1.011 |
| | K4(6N) | 2.642 | 74.3 | 48.7 | 145.8 | 90.3 | 124.1 | 1.475 | 1.009 |
| Rb$^+$ | Rb1(6N) | 3.082 | 59.9 | 70.5 | 65.3 | 174.0 | 100.1 | 1.467 | 1.015 |
| | Rb2(*3*N) | 3.200 | 51.6 | 56.6 | 66.8 | 173.2 | 74.0 | 1.466 | 1.014 |
| | Rb3(4,*2*N) | 3.123 | 58.2 | 57.9 | 122.8 | 110.0 | 115.4 | 1.470 | 1.012 |
| | Rb4(6N) | 2.756 | 72.2 | 46.9 | 140.7 | 94.0 | 122.0 | 1.477 | 1.007 |
| Cs$^+$ | Cs1(6N) | 3.246 | 56.3 | 69.2 | 64.1 | 171.3 | 99.5 | 1.466 | 1.015 |
| | Cs2(*3*N) | 3.362 | 49.0 | 57.2 | 64.9 | 175.0 | 72.0 | 1.465 | 1.014 |
| | Cs3(2,*2*N) | 3.381 | 50.1 | 59.0 | 81.3 | 151.7 | 123.9 | 1.468 | 1.013 |
| | Cs4(6N) | 2.875 | 69.3 | 42.6 | 129.3 | 103.4 | 118.4 | 1.479 | 1.006 |

$^a$Average values are given for similar bond distances or angles, and represents the absolute average.

## 5.8. Figure Captions

**Figure 5.1.** Structure of hexacyclen (ha18C6, 1,4,7,10,13,16-hexaazacyclooctadecane). B3LYP/def2-TZVPPD optimized structures and relative energies at 0 K (in kJ/mol) of the stable low-energy conformations of ha18C6. The calculated dipole moments (μ) are also shown.

**Figure 5.2.** Cross section for collision-induced dissociation of $K^+$(ha18C6) with Xe as a function of kinetic energy in the center-of-mass frame (lower *x*-axis) and the laboratory frame (upper *x*-axis). Data are shown for a Xe pressure of ~0.2 mTorr, part a. Zero-pressure extrapolated cross section for collision-induced dissociation of the $K^+$(ha18C6) complex with Xe in the threshold region as a function of kinetic energy in the center-of-mass frame (lower *x*-axis) and the laboratory frame (upper *x*-axis). The solid line shows the best fit to the data using the model of eq 2.4 convoluted over the neutral and ion kinetic and internal energy distributions. The dashed line shows the model cross section in the absence of experimental kinetic energy broadening for reactants with an internal energy of 0 K, part b.

**Figure 5.3.** Cross sections for collision-induced dissociation of $M^+$(ha18C6) complexes, where $M^+ = Na^+$, $Rb^+$, and $Cs^+$, with Xe as a function of kinetic energy in the center-of-mass frame (lower *x*-axis) and the laboratory frame (upper *x*-axis). Data are shown for a Xe pressure of ~0.2 mTorr, parts a-c, respectively. Zero-pressure extrapolated cross sections for collision-induced dissociation of $M^+$(ha18C6) complexes, where $M^+ = Na^+$. $Rb^+$, and $Cs^+$, parts d-f respectively. The solid lines show the best fits to the data using the model of eq 2.4 convoluted over the neutral and ion kinetic and internal energy distributions. The dashed lines show the model cross sections in the absence of experimental kinetic energy broadening for reactants with an internal energy of 0 K.

**Figure 5.4.** B3LYP/def2-TZVPPD optimized geometries and relative free energies at 298 K (in kJ/mol) of the stable low-energy conformers of the $K^+$(ha18C6).

**Figure 5.5.** B3LYP/def2-TZVPPD optimized geometries and relative free energies at 298 K (in kJ/mol) of the stable low-energy conformers of the $Na^+$(ha18C6).

**Figure 5.6.** B3LYP/def2-TZVPPD optimized geometries and relative free energies at 298 K (in kJ/mol) of the stable low-energy conformers of the $Rb^+$(ha18C6).

**Figure 5.7.** B3LYP/def2-TZVPPD optimized geometries and relative free energies at 298 K (in kJ/mol) of the stable low-energy conformers of the $Cs^+$(ha18C6).

**Figure 5.8.** MP2(full) and B3LYP calculated versus TCID measured $M^+$–ha18C6 BDEs at 0 K (in kJ/mol), where $M^+ = Na^+$, $K^+$, $Rb^+$, and $Cs^+$. Single point energies calculated using the def2-TZVPPD (part a) and 6-311+G(2d,2p)_HW (part b) optimized geometries of the ground-state conformers. All values are determined here and taken from **Table 5.3**.

**Figure 5.9.** BDEs at 298 K (in kJ/mol) of the $M^+$(ha18C6) and $M^+$(18C6) complexes plotted versus the ionic radius of $M^+$, part a. Ionic radii are taken from reference 34. Comparison of TCID measured and B3LYP/def2-TZVPPD calculated $M^+$–ha18C6 and $M^+$–18C6 BDEs at 0 K (in kJ/mol), where $M^+ = Na^+$, $K^+$, $Rb^+$, and $Cs^+$, part b. All values for the $M^+$(ha18C6) complexes are determined here and taken from **Table 5.3**. Calculated values for the the $M^+$–18C6 BDEs are taken from **Table 5.1**. Measured values for the $M^+$–18C6 BDEs are taken from reference 20.

**Figure 5.10.** BDEs at 298 K (in kJ/mol) of the $M^+$(ha18C6) and $M^+$(ta12C4) complexes plotted versus the ionic radius of $M^+$, part a. Ionic radii are taken from reference 34. Comparison of TCID measured and B3LYP/def2-TZVPPD and MP2/def2-TZVPPD calculated $M^+$–ha18C6 and $M^+$–12N4 BDEs at 0 K (in kJ/mol), where $M^+$ = $Na^+$, $K^+$, $Rb^+$, and $Cs^+$, part b. All values for the $M^+$(ha18C6) complexes are determined here and taken from **Table 5.3**. Values for the $M^+$–ta12C4 BDEs are taken from reference 22. The solid line indicates values for which the $M^+$–ha18C6 and $M^+$–ta12C4 are equal, whereas the dashed line indicates values for which the $M^+$–ha18C6 BDEs exceed those of $M^+$–ta12C4 by 50 %.

Figure 5.1.

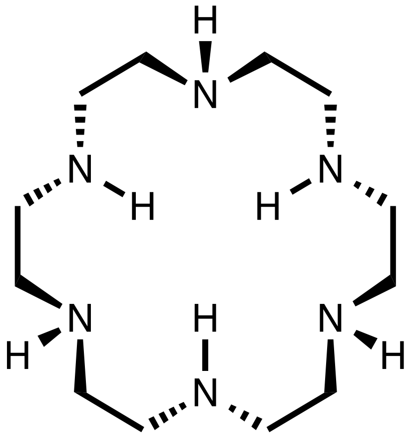

Hexacyclen (ha18C6)
1,4,7,10,13,16-hexaazacyclooctadecane

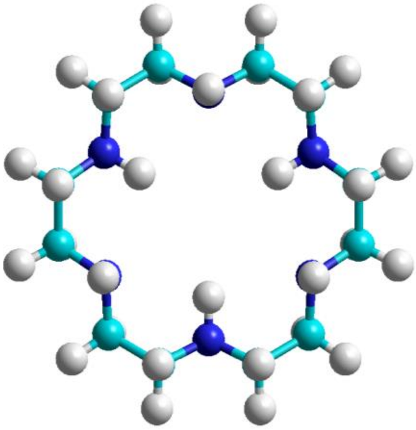

$C_{3v}$
0.0 kJ/mol
μ = 2.98 D

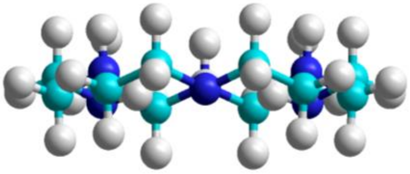

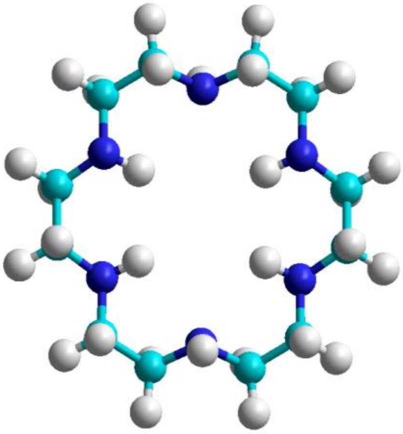

$C_{2h}$
7.9 kJ/mol
μ = 0.0 D

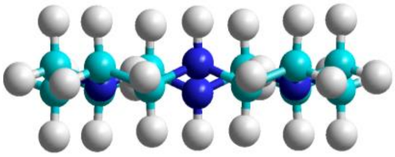

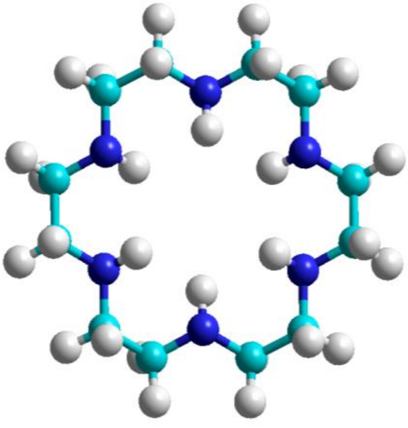

$C_i$
33.8 kJ/mol
μ = 0.0 D

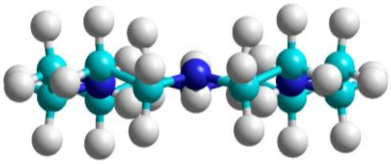

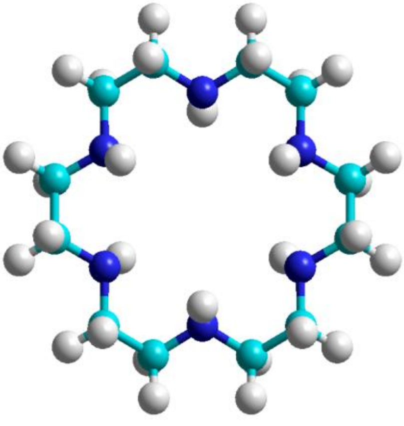

$D_{3d}$
58.9 kJ/mol
μ = 0.0 D

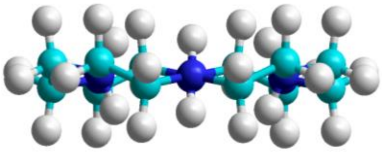

Figure 5.2.

a.

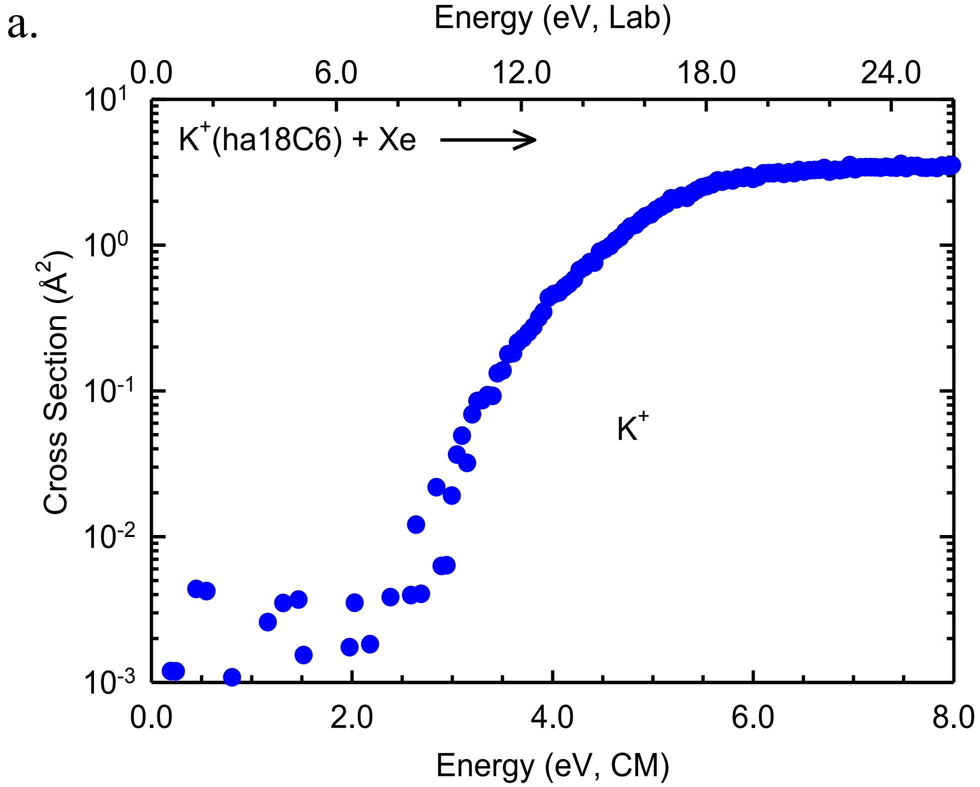
Energy (eV, Lab)
0.0
6.0
12.0
18.0
24.0
$10^1$
$10^0$
$10^{-1}$
$10^{-2}$
$10^{-3}$
Cross Section (Å$^2$)
K$^+$(ha18C6) + Xe
K$^+$
0.0
2.0
4.0
6.0
8.0
Energy (eV, CM)

b.

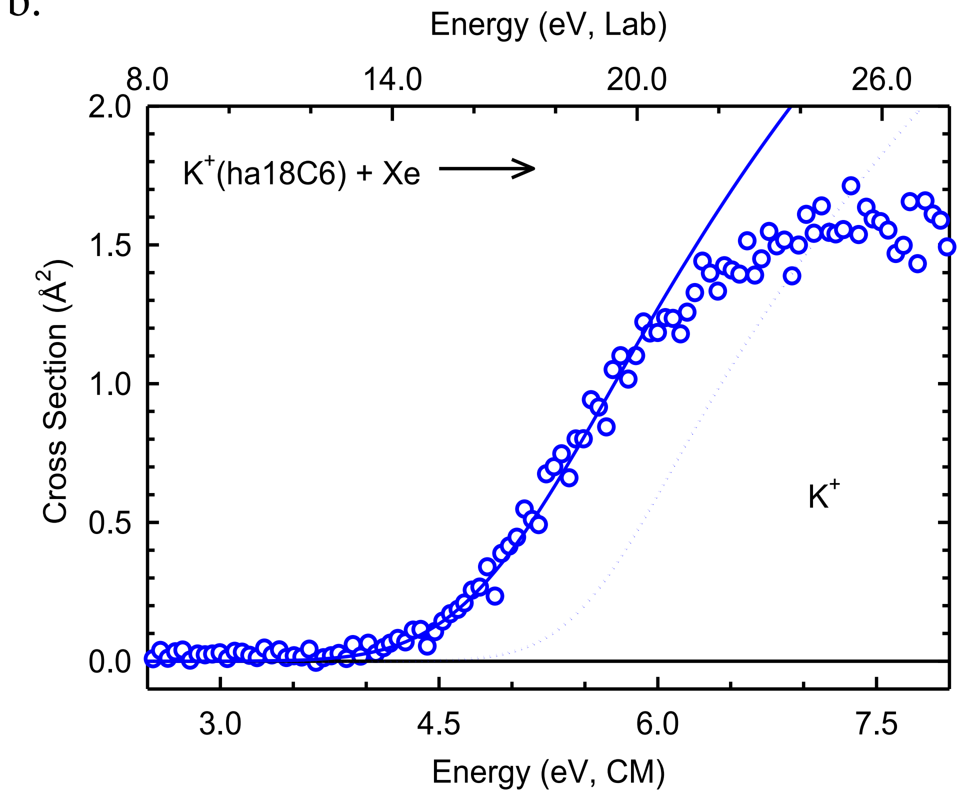
Energy (eV, Lab)
8.0
14.0
20.0
26.0
2.0
1.5
1.0
0.5
0.0
Cross Section (Å$^2$)
K$^+$(ha18C6) + Xe
K$^+$
3.0
4.5
6.0
7.5
Energy (eV, CM)

Figure 5.3.

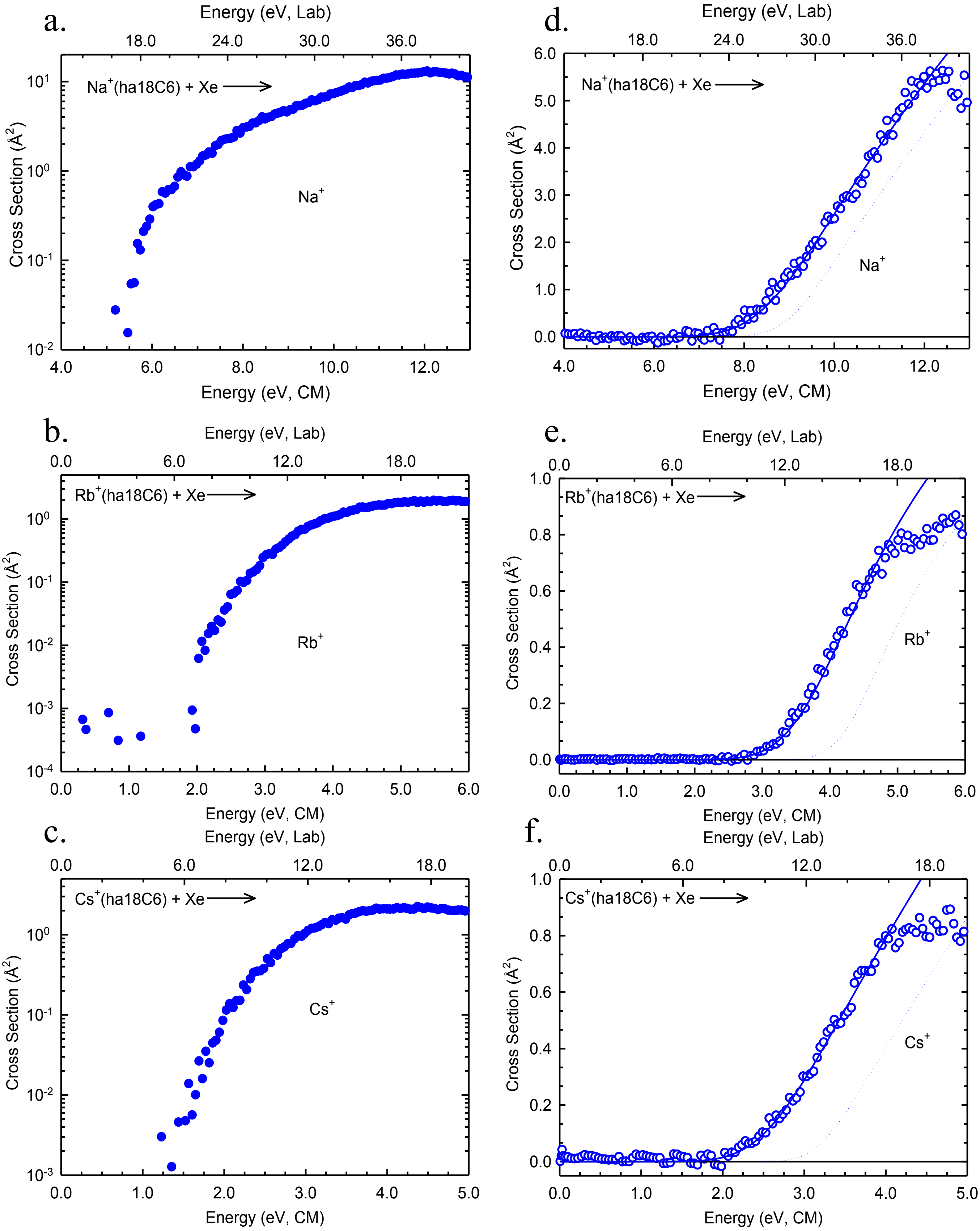
a.
Energy (eV, Lab)
18.0
24.0
30.0
36.0
Na⁺(ha18C6) + Xe →
Na⁺
Cross Section (Å²)
10¹
10⁰
10⁻¹
10⁻²
4.0
6.0
8.0
10.0
12.0
Energy (eV, CM)
d.
Energy (eV, Lab)
18.0
24.0
30.0
36.0
Na⁺(ha18C6) + Xe →
Na⁺
Cross Section (Å²)
6.0
5.0
4.0
3.0
2.0
1.0
0.0
4.0
6.0
8.0
10.0
12.0
Energy (eV, CM)
b.
Energy (eV, Lab)
0.0
6.0
12.0
18.0
Rb⁺(ha18C6) + Xe →
Rb⁺
Cross Section (Å²)
10⁰
10⁻¹
10⁻²
10⁻³
10⁻⁴
0.0
1.0
2.0
3.0
4.0
5.0
6.0
Energy (eV, CM)
e.
Energy (eV, Lab)
0.0
6.0
12.0
18.0
Rb⁺(ha18C6) + Xe →
Rb⁺
Cross Section (Å²)
1.0
0.8
0.6
0.4
0.2
0.0
0.0
1.0
2.0
3.0
4.0
5.0
6.0
Energy (eV, CM)
c.
Energy (eV, Lab)
0.0
6.0
12.0
18.0
Cs⁺(ha18C6) + Xe →
Cs⁺
Cross Section (Å²)
10⁰
10⁻¹
10⁻²
10⁻³
0.0
1.0
2.0
3.0
4.0
5.0
Energy (eV, CM)
f.
Energy (eV, Lab)
0.0
6.0
12.0
18.0
Cs⁺(ha18C6) + Xe →
Cs⁺
Cross Section (Å²)
1.0
0.8
0.6
0.4
0.2
0.0
0.0
1.0
2.0
3.0
4.0
5.0
Energy (eV, CM)

Figure 5.4.

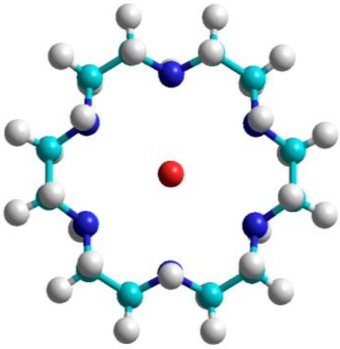

$K^+$– N = 2.991Å
∠N$K^+$N = 61.0°

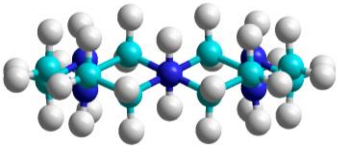

K1(6N)
0.0 kJ/mol

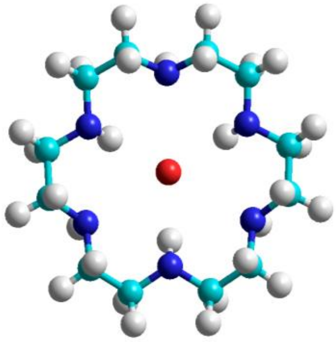

$K^+$– N = 3.153Å
∠N$K^+$N = 54.7°

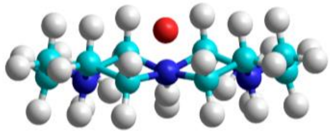

K2(6N)
44.0 kJ/mol

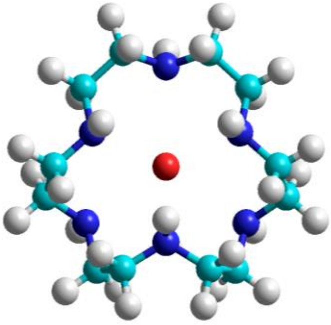

$K^+$– N = 2.847Å
∠N$K^+$N = 65.4°

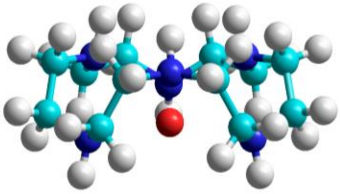

K3(6N)
71.5 kJ/mol

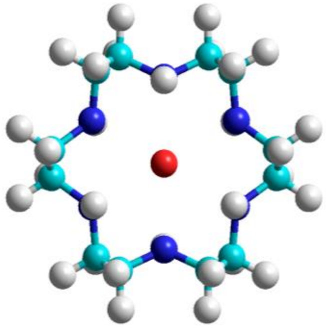

$K^+$– N = 2.642Å
∠N$K^+$N = 74.3°

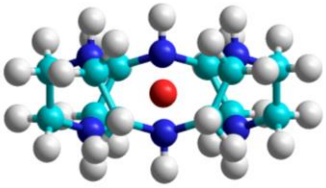

K4(6N)
199.1 kJ/mol, *i* = 1

$K^+$(ha18C6)

Figure 5.5.

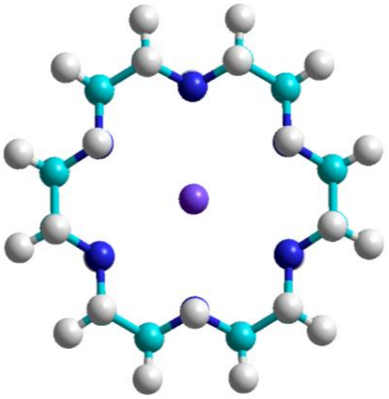

$\mathrm{Na^+}$– N = 2.918Å

$\angle \mathrm{NNa^+N} = 60.8^\circ$

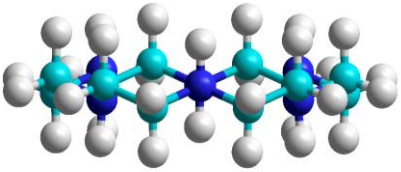

Na1(6N)

0.0 kJ/mol

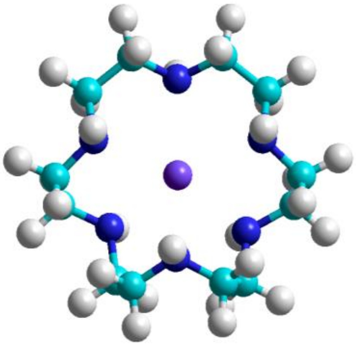

$\mathrm{Na^+}$– N = 2.571Å

$\angle \mathrm{NNa^+N} = 71.8^\circ$

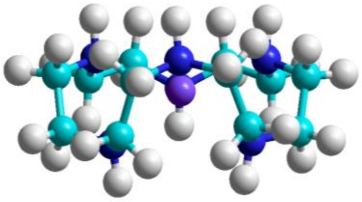

Na3(6N)

7.1 kJ/mol

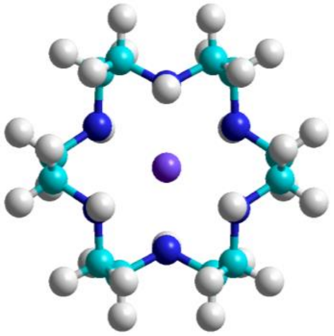

$\mathrm{Na^+}$– N = 2.428Å

$\angle \mathrm{NNa^+N} = 77.9^\circ$

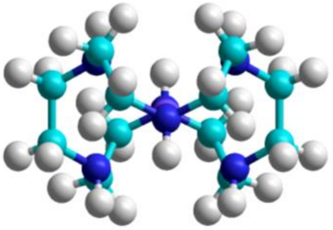

Na4(6N)

45.2 kJ/mol

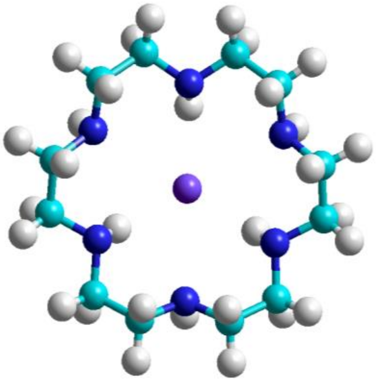

$\mathrm{Na^+}$– N = 2.943Å

$\angle \mathrm{NNa^+N} = 58.6^\circ$

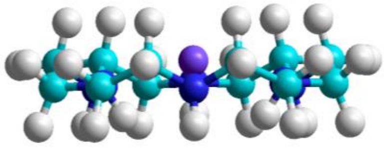

Na2(6N)

70.0 kJ/mol, *i* = 2

$\mathrm{Na^+}$(ha18C6)

Figure 5.6.

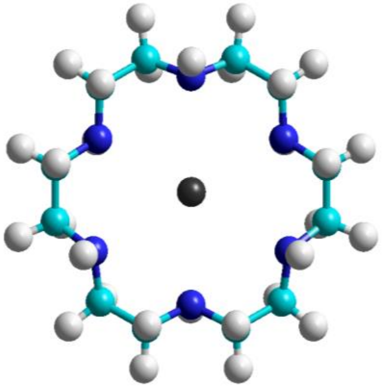

$Rb^+$– N = 3.082Å
∠N$Rb^+$N = 59.9°

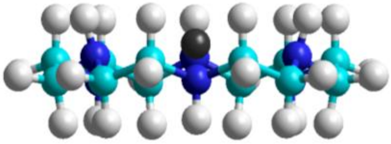

Rb1(6N)
0.0 kJ/mol

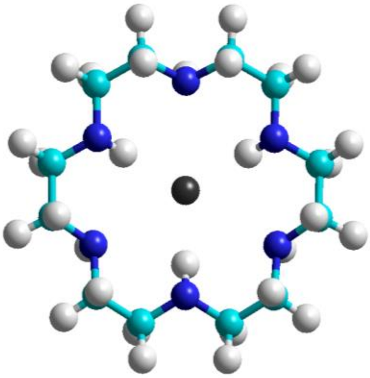

$Rb^+$– N = 3.200Å
∠N$Rb^+$N = 51.6°

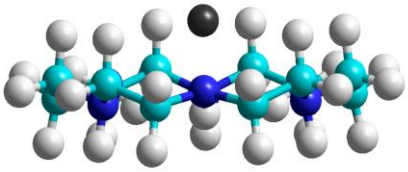

Rb2(*3*N)
18.8 kJ/mol

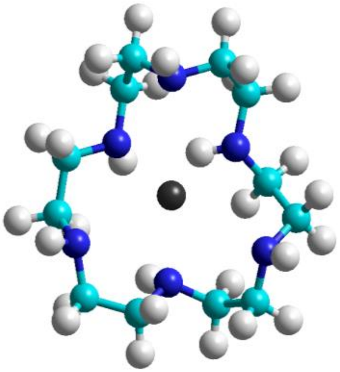

$Rb^+$– N = 3.123Å
∠N$Rb^+$N = 58.2°

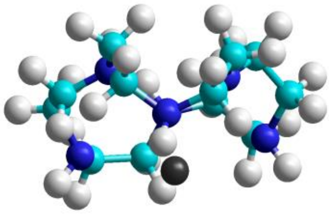

Rb3(4,*2*N)
71.0 kJ/mol

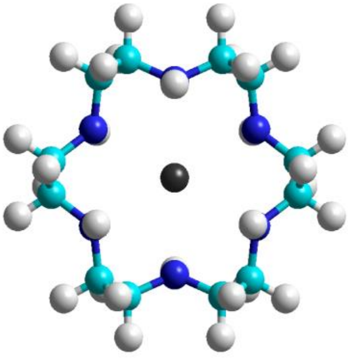

$Rb^+$– N = 2.756Å
∠N$Rb^+$N = 72.2°

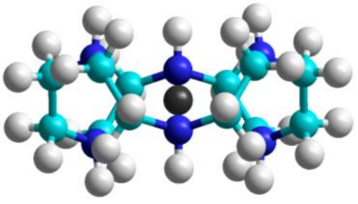

Rb4(6N)
272.9 kJ/mol, *i* = 1

$Rb^+$(ha18C6)

Figure 5.7.

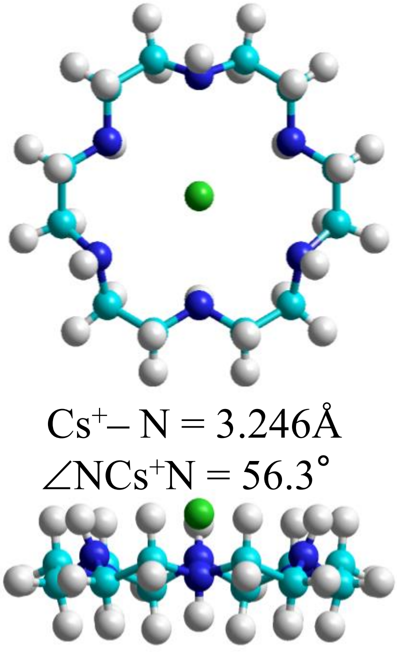
$Cs^+– N = 3.246$Å
∠$NCs^+N = 56.3°$

Cs1(6N)
0.0 kJ/mol

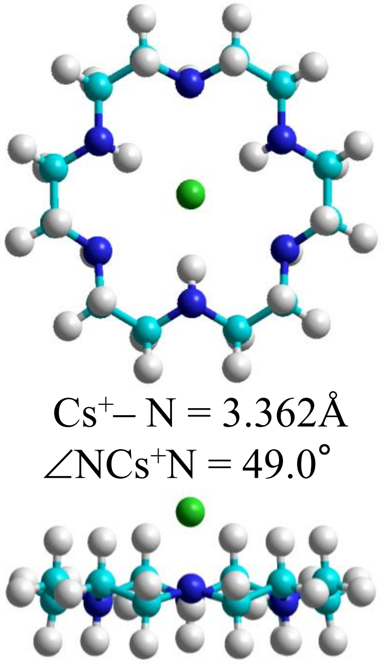
$Cs^+– N = 3.362$Å
∠$NCs^+N = 49.0°$

Cs2(*3*N)
7.5 kJ/mol

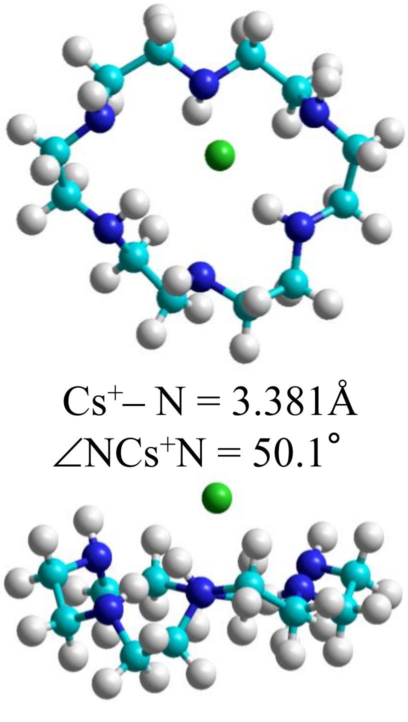
$Cs^+– N = 3.381$Å
∠$NCs^+N = 50.1°$

Cs3(2,*2*N)
42.6 kJ/mol

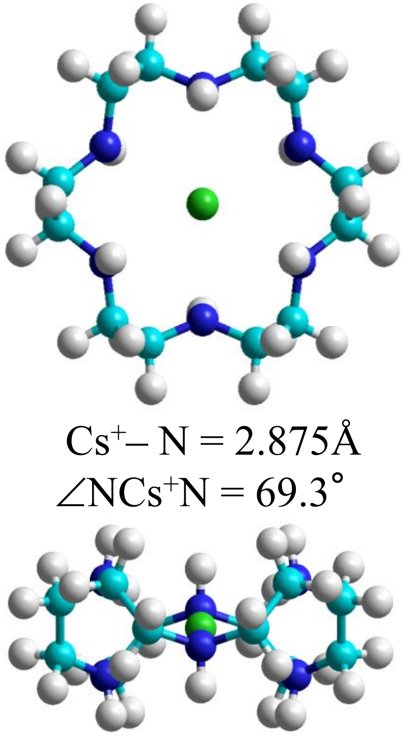
$Cs^+– N = 2.875$Å
∠$NCs^+N = 69.3°$

Cs4(6N)
358.8 kJ/mol, *i* = 1

$Cs^+$(ha18C6)

Figure 5.8.

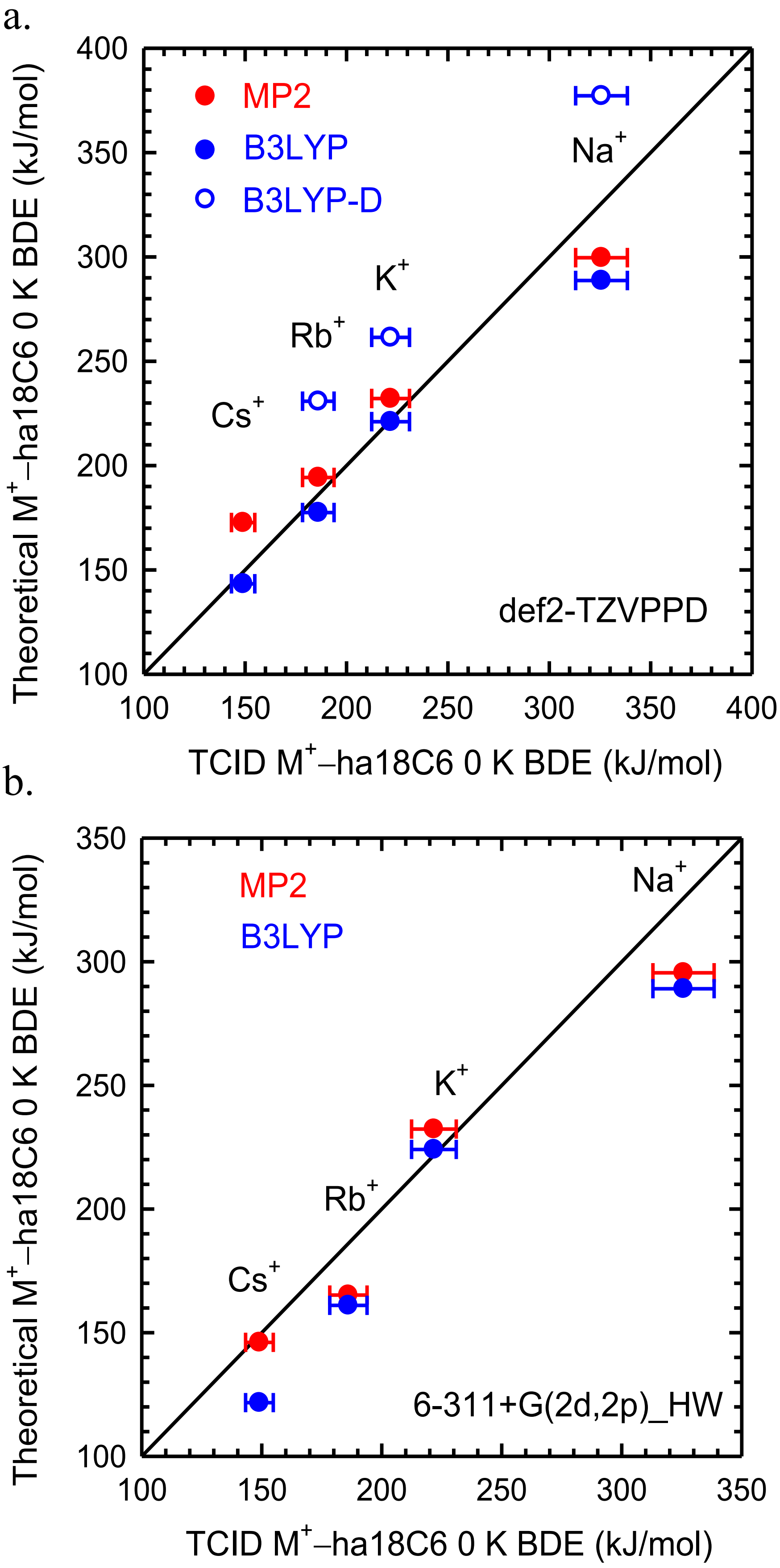
a.
MP2
B3LYP
B3LYP-D
Na+
K+
Rb+
Cs+
def2-TZVPPD
Theoretical M+–ha18C6 0 K BDE (kJ/mol)
TCID M+–ha18C6 0 K BDE (kJ/mol)
100
150
200
250
300
350
400
b.
MP2
B3LYP
Na+
K+
Rb+
Cs+
6-311+G(2d,2p)_HW
Theoretical M+–ha18C6 0 K BDE (kJ/mol)
TCID M+–ha18C6 0 K BDE (kJ/mol)
100
150
200
250
300
350

Figure 5.9.

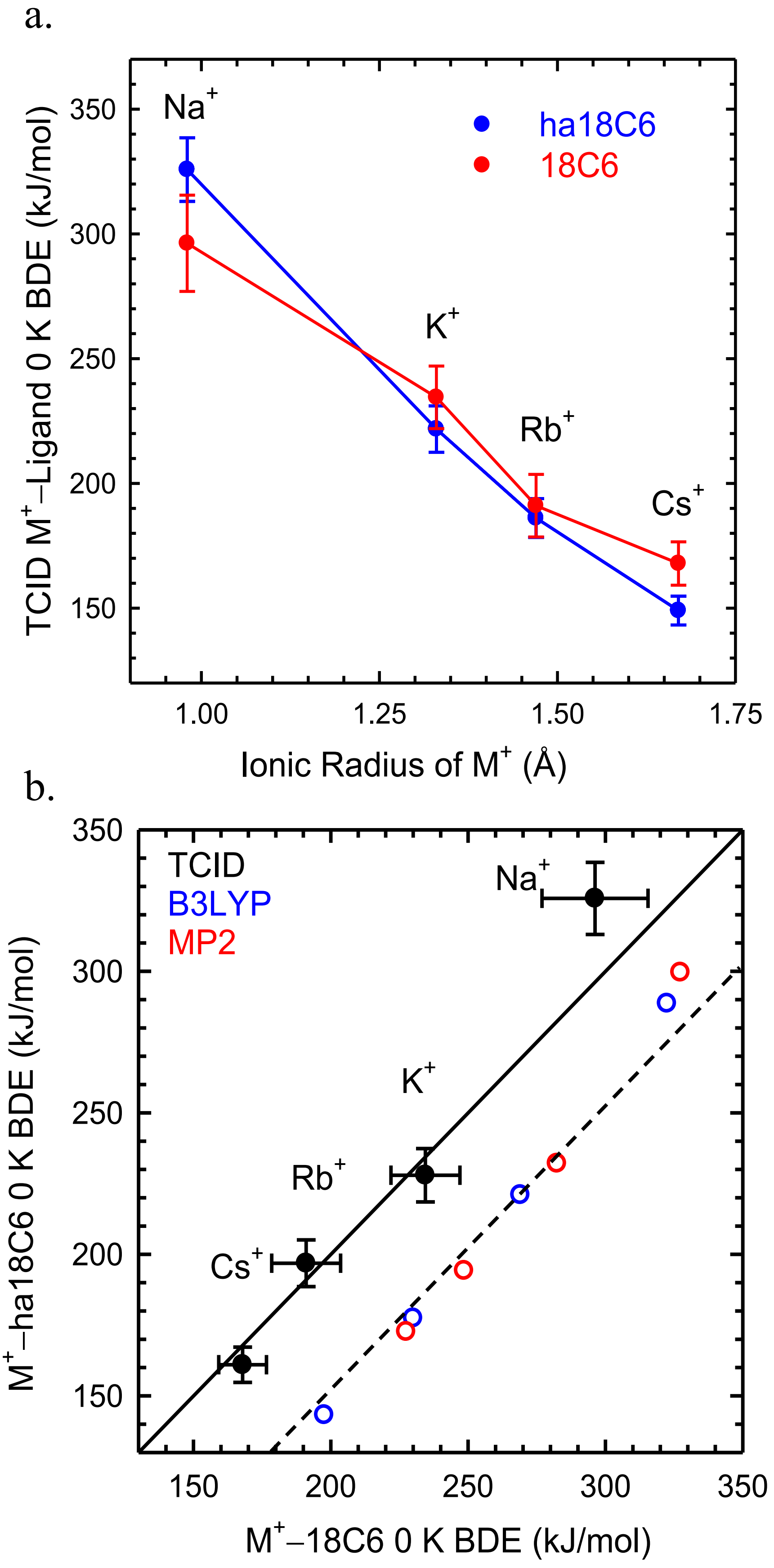
a.
Na$^+$
K$^+$
Rb$^+$
Cs$^+$
ha18C6
18C6
350
300
250
200
150
1.00
1.25
1.50
1.75
TCID M$^+$–Ligand 0 K BDE (kJ/mol)
Ionic Radius of M$^+$ (Å)
b.
TCID
B3LYP
MP2
Na$^+$
K$^+$
Rb$^+$
Cs$^+$
350
300
250
200
150
150
200
250
300
350
M$^+$–ha18C6 0 K BDE (kJ/mol)
M$^+$–18C6 0 K BDE (kJ/mol)

Figure 5.10.

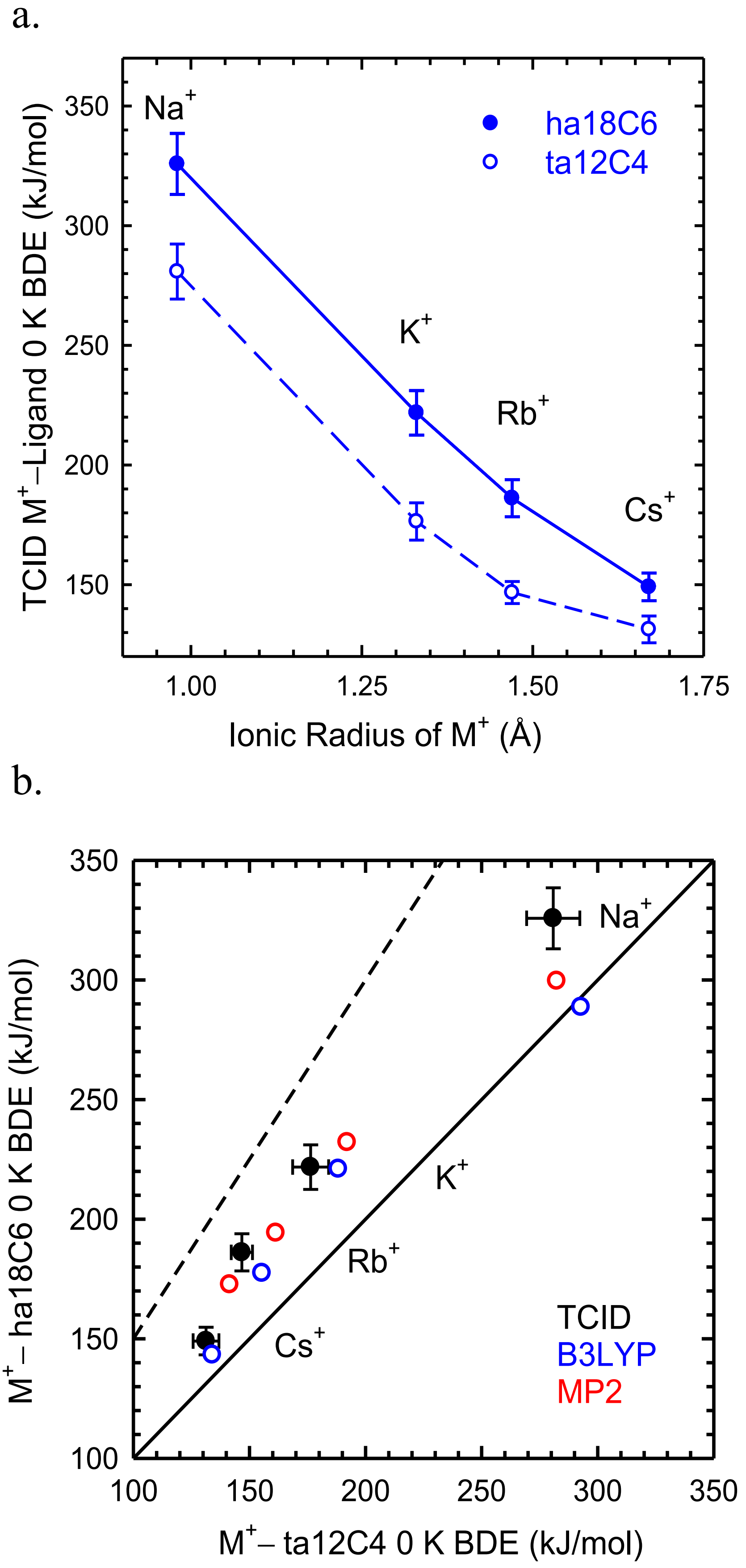
a.
Na$^+$
K$^+$
Rb$^+$
Cs$^+$
● ha18C6
○ ta12C4
TCID M$^+$–Ligand 0 K BDE (kJ/mol)
150
200
250
300
350
1.00
1.25
1.50
1.75
Ionic Radius of M$^+$ (Å)
b.
Na$^+$
K$^+$
Rb$^+$
Cs$^+$
TCID
B3LYP
MP2
M$^+$– ha18C6 0 K BDE (kJ/mol)
100
150
200
250
300
350
100
150
200
250
300
350
M$^+$– ta12C4 0 K BDE (kJ/mol)

# CHAPTER 6

# ALKALI METAL CATION – DIAZA-18-CROWN-6: EFFECTS OF ALKALI METAL CATION SIZE ON THE STRUCTURE AND BINDING ENERGIES

Portions of this chapter were reprinted with permission Austin, C.A. and Rodgers, M.T. Intrinsic Affinities of Alkali Metal Cations for Diaza-18-Crown-6: Effects of Alkali Metal Cation Size and Donor Atoms on the Binding Energies. Int. J. Mass Spectrom. dx.doi.org/10.1016/j.ijms.2014.06.033.

## 6.1. Introduction

There is considerable interest in the diaza-18-crown-6 (da18C6) ligand because it exhibits selectivity for specific metal cations, such as $Ag^+$. As its name suggests, diaza-18-crown-6 is an 18-crown-6 (18C6) analog where two of the oxygen donor atoms have been replaced by nitrogen donor atoms as shown in **Figure 6.1**. The properties attributed to the presence of two types of donor atoms symmetrically placed in the macrocycle have been investigated using solution phase methods [1]. The da18C6 ligand exhibits binding to the alkali and alkaline earth metal cations as well as transitions metal cations such as $Cu^+$ and $Ag^+$ in methanol and acetonitrile solutions [1–3]. The stability of metal cation–da18C6 complexes decreases in aqueous solution due to competition between the metal cation binding to da18C6 versus the water molecules. The stability of metal cation–da18C6 complexes increases with cage-functionalization of the da18C6 ligand as illustrated for alkali metal picrate extraction experiments [4], where the relative binding follows the order $K^+ > Na^+ > Rb^+ > Cs^+ > Li^+$. Using conductometric measurements, Aprano and Sesta found the relative binding order of the alkali metal cations to da18C6 in solution: $K^+ > Na^+ > Cs^+$ [2], consistent with the alkali picrate complexes.

Brodbelt and co-workers investigated the binding selectivity of da18C6 to the alkali metal cations in the gas phase using micro-electrospray ionization (MESI) coupled with quadrupole ion trap mass spectrometry analyses, where the relative order of alkali metal cation binding was found to parallel the solution phase trend, $K^+ > Na^+ > Rb^+$ [5]. A similar study investigated the competitive binding selectivity of the alkali metal cations in the presence of transition metal cations and showed that in methanol, da18C6 preferentially binds $Cu^{2+}$ over $Co^{2+}$, and $K^+$ over $Na^+$[6]. Theoretical investigations of the interactions of da18C6 with $Na^+$, $K^+$ [7], and $Ag^+$ [8], have been reported, whereas no work on the interactions of Rb+ and Cs+ with da18C6 has been published. There is relatively little quantitative [9] or theoretical data on the intrinsic interactions between the larger alkali metal cations and organic molecules. However, because $Rb^+$ and $Cs^+$ share chemical similarity to $K^+$ [10] and can bind to the same sites [11], but accumulate at different rates, $Rb^+$ and $Cs^+$ are used for medical imaging and cancer treatment [12–14].

To further extend the studies of molecular recognition of metal cations by macrocyclic ligands, accurate binding energies were measured for the $M^+$(da18C6) complexes of the alkali metal cations $Na^+$, $K^+$, $Rb^+$, and $Cs^+$ and compared to theoretical estimates. Results for the $M^+$(da18C6) complexes are also compared to the analogous $M^+$(1 8C6) and $M^+$(ha18C6) complexes to elucidate the influence of the donor atoms (O versus N) on the nature and strength of binding.

## 6.2. Collision–Induced Dissociation Experiments

Cross sections for collision-induced dissociation (CID) of four $M^+$(da18C6) complexes, where $M^+ = Na^+$, $K^+$, $Rb^+$, and $Cs^+$, are measured using a guided ion beam tandem mass spectrometer that has been described in detail **Chapter 2**. The $M^+$(da18C6) complexes are generated by electrospray ionization (ESI) [15]. Thermochemical analyses of the experimental results are explicitly discussed in **Chapter 2**.

## 6.3. Theoretical Calculations

To obtain model structures, vibrational frequencies, rotational constants, and energetics for the neutral da18C6 ligand and the M$^+$(da18C6) complexes, molecular dynamics simulated annealing procedures and ab initio and density functional theory calculations were performed using Hyperchem [16] and the Gaussian 09 suite of programs [17], respectively, and are describe in detail in **Chapter 2**. Starting structures for the M$^+$(da18C6) complexes are generated using four of the six low-energy neutral da18C6 structures (C1, C2, C3 and C6), as they are expected to provide the most favorable geometries for interaction with the alkali metal cation, and placing the alkali metal cation in the center of the macrocyclic ring of da18C6.

Vibrational analyses of the geometry-optimized structures were performed to determine the vibrational frequencies of the neutral da18C6 ligand and M$^+$(da18C6) complexes. When used to model the data or to calculate thermal energy corrections, the computed frequencies were scaled by a factor of 0.9804 [18]. Single-point energy calculations were performed at the B3LYP and MP2(full) levels of theory using 6-311+G(2d,2p)_HW and def2-TZVPPD basis sets and the B3LYP/6-31+G* _HW and B3LYP/def2-TZVPPD optimized geometries, respectively. To obtain accurate BDEs, zero-point energy (ZPE) corrections scaled by 0.98 were applied, and basis set superposition errors (BSSE) were subtracted from the computed BDEs in the full counterpoise correction [19,20]. The BSSE corrections are much smaller for B3LYP than MP2(full) calculations. The polarizabilities for the stable low-energy conformers of ha18C6 were calculated at the PBE0/6-311+G(2d,2p) level of theory using the B3LYP/6-31+G* optimized geometries. This level of theory has been shown to accurately reproduce experimental polarizabilities [21]. In addition, the polarizabilities for the stable low-energy conformers of ha18C6 were also calculated at the PBE0/def2-TZVPPD level of theory.

Several of the optimized structures of the M$^+$(da18C6) complexes exhibit imaginary frequencies. Attempts were made to eliminate imaginary frequencies by additional cycles of simulated annealing at 298 K, as well as by moving the metal cation along the path associated with the corresponding mode and re-optimizing. But even with tight convergence, several structures consistently converged to the same conformer with an imaginary frequency.

## 6.4. Results

### 6.4.1. Cross Sections for Collision–Induced Dissociation

Cross sections are measured for the collision-induced dissociation (CID) of four $M^+$(da18C6) complexes with Xe, where $M^+ = Na^+, K^+, Rb^+$, and $Cs^+$. **Figure 6.2** shows representative data for the $Rb^+$(da18C6) complex. The complexes to $Na^+$, $K^+$, and $Cs^+$ exhibit similar relative behavior and are provided as **Figure 6.3**. In all cases, the alkali metal cation is the only ionic product observed corresponding to endothermic loss of the intact da18C6 ligand in the CID reactions 6.1.

$$M^+(\text{da18C6}) + \text{Xe} \rightarrow M^+ + \text{da18C6} + \text{Xe} \qquad (6.1)$$

The magnitudes of the CID cross sections generally decrease and the apparent thresholds increase as the size of the alkali metal cation increases, consistent with the trend expected for binding based primarily on electrostatic interactions [22].

### 6.4.2. Threshold Analysis

Thresholds for CID reactions 6.1 are determined using the model of Eq. 2.4 for four M+(da18C6) complexes. Results of these threshold analyses are given in **Table 6.1**. A representative analysis is shown in **Figure 6.2** for the $Rb^+$(da18C6) complex, whereas an analogous set of figures for the complexes to $Na^+$, $K^+$, and $Cs^+$ are provided as **Figure 6.3**. The loose PSL TS accurately reproduces the experimental cross sections for CID reactions 6.1 for all four $M^+$(da18C6) complexes [23]. For noncovalently bound metal-ligand complexes, the loose PSL TS model provides the most accurate assessment of the kinetic shifts for CID processes [24–32]. The CID cross sections of the $M^+$(da18C6) complexes are reproduced over energy ranges exceeding 5.0 eV and cross section magnitudes of at least a factor of 1000 for the $M^+$(da1 8C6) complexes. **Table 6.1** also includes threshold values, $E_0$, obtained without including the RRKM lifetime analysis. A measure of the kinetic shifts for the $M^+$(da18C6) systems is obtained by taking the difference of the $E_0$ and $E_0$(PSL), which increase from 1.31 eV for the $Cs^+$(da18C6) complex to 4.42 eV for the $Na^+$(da18C6) complex. All of the $M^+$(da18C6) complexes possess the same number of vibrational modes, so the observed kinetic shifts should directly correlate with the measured $M^+$-da18C6 BDE, as observed (**Table 6.1**). The entropy of activation, $\Delta S^*$, is a measure of the looseness of the TS, but also depends on the threshold energy. The $\Delta S^*$(PSL) values for these systems at 1000 K exhibit modest variation, as expected on the basis of the similarity of these systems, and vary between 58 and 66 J $K^{-1}$ $mol^{-1}$. These entropies of activation compare favorably to those previously determined for a wide variety of noncovalently bound complexes that dissociate via simple noncovalent bond cleavage [24–32].

### 6.4.3. Theoretical Results

The ground-state and stable low-energy conformations of the da1 8C6 ligand and $M^+$(da18C6) complexes are calculated as described in the **Chapter 2**. $M^+$-da18C6 BDEs calculated at the B3 LYP and MP2(full) levels of theory using the def2-TZVPPD basis set and the B3LYP/def2-TZVPPD optimized geometries are summarized in **Table 6.2**. Also included are values calculated at the B3LYP and MP2(full) levels of theory using the B3LYP/6-311+ G(2d,2p)_HW basis set and the B3LYP/6–31+G*_HW optimized geometries. ZPE and BSSE corrections are also included in the computed BDEs.

#### 6.4.3.1. Neutral da18C6

Low -energy structures of the neutral da18C6 ligand are calculated as described above and shown in **Figure. 6.1**. Six distinct stable geometries are found. The various conformations of the neutral da18C6 ligand are designated based on their relative Gibbs free energies and the symmetry of the da18C6 ligand. Previous studies of the analogous $M^+$(ha18C6) complexes [24] and the smaller $M^+$(ta12C4) complexes [25] suggest energetics computed using the B3LYP/def2-TZVPPD level of theory are the most reliable among the levels of theory examined here. Therefore, the following discussion focuses on the geometries and energetics calculated at the B3LYP/def2-TZVPPD level of theory unless otherwise noted. The ground-state conformation C1 of neutral da18C6 adopts $C_{2h}$ symmetry, where the amine and oxygen donor atoms alternate up and down, whereas the hydrogen atoms of the amine donors are oriented toward the cavity of the macrocyclic ring with ∠HNCC dihedral angles of 56.4°. The local dipoles are anti-aligned for the C1($C_{2h}$) conformer leading to cancellation, and no net dipole moment. This conformation of da18C6 was previously reported as the ground-state by Freidzon et al. [8]. Two additional higher-energy conformers similar to the C1($C_{2h}$) conformer are found, C3($C_s$) and C6($C_{2h}$), which lie 18.4 and 40.7 kJ/mol higher in free energy, respectively. The major difference between the C3 and C6 conformations and the ground-state conformation is the position of the amino hydrogen atoms. For the C3 conformer, the average ∠HNCC dihedral angle is 56.5°, whereas for the C6 conformer, the average ∠HNCC dihedral angle is somewhat smaller, 50.9°. Similar to the C1 conformer, the local dipoles of the C6 conformer are anti-aligned leading to cancellation, and no net dipole moment, whereas the C3 conformer exhibits a large dipole moment of 1.456 D. The C2($C_1$) conformer is the second most stable conformer and is calculated to lie 18.0 kJ/mol higher in free energy as compared to the ground state. The C2 conformer is similar to the ground-state C1 conformer, the major difference being the ring of donor atoms is distorted from planarity. The C1, C2, C3, and C6 conformers of da18C6 adopt geometries similar to those observed when the macrocycle is complexed to a metal cation. In contrast, the C4($C_i$) and C5($C_i$) conformers adopt more rectangular geometries, similar to the ground-state determined for the 18C6 ligand [26], and are calculated to lie 29.3 and 31.4 kJ/mol higher in free energy than the ground-state C1 conformer. The C4 conformer was also identified by Freidzon et al. and calculated to lie 25.9 kJ mol higher in free energy than the ground-state C1 conformer using density functional methods with the PBE functional [8].

#### 6.4.3.2. $M^+$(da18C6)

The ground-state and low-energy structures of the $Rb^+$(da18C6) complex optimized at the B3LYP/def2-TZVPPD level of theory are shown in **Figure 6.4**. Similar conformations are also found for the complexes to the other alkali metal cations investigated and are shown as **Figure 6.5–6.7**. The nomenclature employed to describe these structures is of the form Mx(symmetry), where M identifies the metal cation, x indicates the relative order of stability among the low-energy conformers of the $K^+$(da1 8C6) complexes, and the symmetry is that of the ligand in its uncomplexed form. The ground-state conformation of the $M^+$(da18C6) complexes at 0 K determined at the B3LYP and MP2(full) levels of theory using the def2-TZVPPD basis set are very similar for the $K^+$, $Rb^+$, and $Cs^+$ complexes, compare **Figures 6.4**, **6.6–6.7**, and **6.8**. Although the analogous structure for the $Na^+$(da18C6) complex is calculated to be the most stable among those computed, this structure possesses an imaginary frequency and thus is not the true global minimum, but likely is very similar to the ground-state structure, and is therefore used as the ground-state structure for data analysis procedures and calculation of the $Na^+$-da18C6 BDE. The M1 conformer is calculated to be the lowest energy conformation for the alkali metal cations interaction with da18C6, **Figure 6.8**. The M1 conformer encapsulates the $Na^+$, $K^+$, and $Rb^+$ cations in the cavity created by the oxygen and nitrogen donor atoms. In contrast, the $Cs^+$ cation is too large to fit in the cavity and sits above the center of the macrocyclic ring, see **Figures 6.4–6.7**. In the M1 conformers, the da18C6 ligand is only slightly distorted from its ground-state conformation in the absence of the metal cation, with the largest differences being observed for the $Na^+$(da18C6) complex. In the M2 conformers, the metal cation sits above the plane created by oxygen donor atoms for all metal cations except $Na^+$. The M2 conformers are the only conformers where the amine hydrogen atoms are located on the same side of the macrocyclic backbone. The $Na^+$ cation only interacts with four of the donor atoms, whereas the larger alkali metal cations interact with all six donor atoms. M3 and M4 conformations adopt a hexagonal geometry (such that the ring created by the O and N donor atoms is nearly planar) upon binding of the large cations $K^+$, $Rb^+$, and $Cs^+$. The donor atoms of the macrocyclic rings of the M3 and M4 conformations distort from planarity to enable encapsulation or tighter binding to the $Na^+$ cation in a trigonal prismatic geometry.

#### 6.4.3.2.1. $K^+$(da18C6) and $Rb^+$(da18C6)

In the ground-state M1($C_{2h}$) conformations of $K^+$(da18C6) and $Rb^+$(da18C6) the metal cation sits in the center of the plane created by the oxygen and nitrogen donor atoms, see **Figure 6.4** and **6.6**. The average $Rb^+$–O 351 and $Rb^+$–N bond distances for the $Rb^+$(da18C6) complex are 2.946 Å and 3.060 Å, respectively, with corresponding average $\angle ORb^+O$ and $\angle NRb^+O$ angles of 58.0° and 59.2°, respectively (**Table 6.3**). Interestingly, the ground-state K1 conformer exhibits $K^+$–O (2.842 Å) bond distances that are longer than the average $K^+$–O bond distances for the K2($C_s$) and K3($C_s$) conformers, whereas the $K^+$–N (2.943 Å) bond distances are intermediate between those of the K2 and K3 conformers. In both the K2($C_s$) and Rb2($C_s$) conformers, the metal cation sits slightly above the plane created by the oxygen and nitrogen donor atoms. These M2 conformers are calculated to lie 15.3 and 23.2 kJ/mol higher in free energy than the ground-state M1 conformers, respectively. For the K3($C_s$) and Rb3($C_s$) conformers, the metal cation strongly interacts with the four oxygen donor atoms with corresponding average $M^+$–O bond distances of 2.786 Å and 3.004 Å, respectively, and only weakly interacts with the two nitrogen donor atoms with corresponding average $M^+$–N bond distances of 2.986 Å and 3.180 Å, respectively. The K3 conformer is calculated to lie 29.4 kJ/mol higher in free energy, whereas the Rb3 is calculated to lie 21.2 kJ/mol higher in free energy than the ground-state M1 conformers. The M4($C_{2h}$) conformers exhibit the shortest $M^+$–O and $M^+$–N bond distances compared to the M1, M2, and M3 conformers. The K4 conformer is calculated to lie 57.6 kJ/mol higher in free energy than the ground-state K1 conformer and possesses two imaginary frequencies associated with NH wagging with the metal cation moving up and down in the center of the macrocycle, whereas the other imaginary frequency corresponds to wagging of the C–C skeletal backbone. In contrast, the Rb4 conformer is calculated to lie 60.1 kJ/mol higher in free energy than the ground-state Rb1 conformer and possesses a single imaginary frequency associated with the metal cation moving up and down in the center of the macrocycle.

#### 6.4.3.2.2. $Cs^+$(da18C6)

The ground-state Cs1($C_s$) conformer of the $Cs^+$(da18C6) complex parallels that found for the analogous complexes of $K^+$ and $Rb^+$, however more significant distortions of the da18C6 ligand lead to a reduction in symmetry from $C_{2h}$ to $C_s$. The $Cs^+$ cation sits slightly above the plane of the donor atoms as it is too large to fit in the cavity of da18C6, see **Figure 6.7**. The next most stable conformer, Cs2($C_s$), is very similar. The $Cs^+$ cation again lies above the plane of the oxygen and nitrogen donor atoms, with slightly longer $Cs^+$–O and $Cs^+$–N average bond distances of 3.151 Å and 3.188 Å, respectively, than found in the Cs1 conformer and is calculated to lie 8.0 higher in free energy. The next most stable conformer, Cs3($C_s$), is calculated to lie 14.3 kJ/mol higher in free energy than the ground-state Cs1 conformer. However, in the Cs3 conformer, the $Cs^+$ cation strongly interacts with the four oxygen donor atoms with corresponding average $Cs^+$–O bond distances of 3.146 Å, and interacts weakly with the two nitrogen donor atoms with corresponding average $Cs^+$–N bond distances of 3.330 Å, parallel to that found for K3(Cs) and Rb3(Cs). The Cs4($C_{2h}$) conformer exhibits the shortest $Cs^+$–O and $Cs^+$–N 401 bond distances, but possesses an imaginary frequency that involves translation of the $Cs^+$ cation up and down in the center of the macrocyclic ring, similar to that found for the Rb4($C_{2h}$) conformer. The Cs4 conformer is calculated to lie 89.4 kJ/mol higher in free energy than the ground-state Cs1 conformer, with corresponding $Cs^+$–O and $Cs^+$–N average bond distances of 2.966 Å and 3.063 Å, respectively.

### 6.4.3.2.3. $Na^+$(da18C6)

The low-energy conformers of the $Na^+$(da18C6) complex at the B3LYP level of theory parallel those found for the complexes to the larger alkali metal cations, **Figures 6.5** and **6.8**. However, the most stable conformer computed, Na1($C_{2h}$), is not a true minimum as it possesses one imaginary frequency associated with the $Na^+$ cation moving back and forth in the plane of the oxygen and nitrogen donor atoms. The average $Na^+$–O (2.833 Å) and $Na^+$–N (2.755 Å) bond distances are significantly larger for the Na1 conformer than the other stable conformers computed. The average $Na^+$–O bond distance is longer than the average $Na^+$–N bond distance, whereas the $Na^+$–O bond distances are smaller than the $Na^+$–N bond distances in the other low-energy conformers of $Na^+$(da18C6). The next most stable conformer of the $Na^+$(da18C6) complex is found to have $C_1$ symmetry, Na2($C_1$), where the skeletal backbone exhibits much greater deviations from planarity than in the analogous complexes to the larger alkali metal cations, and is calculated to lie 6.7 kJ/mol higher in free energy than the Na1 conformer. The $Na^+$ cation binds to only four of the donor atoms with corresponding $Na^+$–O and $Na^+$–N average bond distances of 2.436 Å and 2.504 Å, respectively. The next most stable conformer, Na3(C1), exhibits average $Na^+$–O 429 and $Na^+$–N bond distances of 2.480 Å and 2.553 Å, respectively, longer than those of the Na2 ground-state conformer, and is calculated to be 20.5 kJ/mol less stable. Parallel to that found for the M4($C_{2h}$)

conformers of the larger alkali metal cations, the shortest average bond distances are found for the Na4($C_{2h}$) conformer. In contrast to the complexes to the larger alkali metal cations, the Na4 conformer has no imaginary frequencies. The Na4 conformer exhibits $Na^+$–O and $Na^+$–N average bond distances of 2.326 Å and 2.499 Å, respectively, and lies 53.1 kJ/mol higher in free energy than the Na1 conformer.

## 6.5. Discussion

### 6.5.1. Comparison of Theory and Experiment

The experimentally measured and theoretically calculated $M^+$–da18C6 BDEs are summarized in **Table 6.2**, whereas the agreement between the calculated and measured BDEs is illustrated in **Figure 6.9**. As can be seen in the figure, the B3LYP/def2-TZVPPD values exhibit very good agreement with the measured values. The mean absolute deviation (MAD) between theory and experiment is 4.5 ± 2.4 kJ/mol, and is roughly half the average experimental uncertainty (AEU) in these values, 10.4 ± 5.1 kJ/mol. The agreement between B3LYP/6-311+G(2d,2p)_HW theory and the measured $M^+$–da18C6 BDEs is not as good, **Table 6.2** and **Figure 6.9**, where the MAD is 9.8 ± 8.5 kJ/mol. When the measured BDEs are compared to the those calculated at the MP2(full)/def2-TZVPPD level of theory, the MAD is 17.1 ± 12.0 kJ/mol, almost double the AEU in these values. In contrast, the MAD improves to 6.5 ± 5.2 kJ/mol for values calculated at the MP2(full)/6-311+G(2d,dp)_HW level of theory, which compares well to the AEU in these values. Clearly, the best agreement between the measured and calculated $M^+$-da18C6 BDEs is found for the B3LYP/def2-TZVPPD results for all four alkali metal cations. In contrast, at the MP2(full)/def2-TZVPPD level of theory, the calculated BDEs are systematically high except for the $Na^+$(da18C6) complex, where excellent agreement is found.

### 6.5.2. Trends in the Binding of Alkali Metal Cations to da18C6

The measured $M^+$-da18C6 BDEs at 0 K are summarized in **Table 6.2** and shown pictorially in **Figure 6.9**. As the size of the alkali metal cation increases from $Na^+$ to $Cs^+$, the $M^+$–da18C6 BDEs are found to decrease monotonically, similar to behavior observed for many alkali metal cation-ligand complexes [22, 24–39]. This is the expected trend for binding based primarily on electrostatic interactions, because the increasing size of the alkali metal cation leads to longer metal-ligand bond distances [40]. The relative change in the ionic radii for the alkali metal cations becomes smaller with increasing size of the cation such that the difference in the $M^+$-da18C6 BDEs for adjacent metal cations becomes smaller as the size of the metal cation increases from $Na^+$ to $Cs^+$. The relative trend in the gas phase for alkali metal cation binding to da18C6, $Na^+ > K^+ > Rb^+ > Cs^+$, differs from that observed in competitive solution phase binding, where da18C6 shows selectivity in the order of $K^+ > Na^+ > Rb^+ > Cs^+$ as a result of competition with between the solvent and da18C6 ligand for binding to the alkali metal cations in solution [2-4].

### 6.5.3. Comparison with 18C6

The TCID measured and B3LYP/def2-TZVPPD and MP2(full)/def2-TZVPPD calculated $M^+$-da18C6 and $M^+$-18C6 BDEs [24,26] are compared in **Figure 6.10a**. Experimentally, alkali metal cation interactions with da18C6 and 18C6 are equal within experimental error, but do suggest a very minor enhancement in the binding of the larger alkali metal cations to 18C6. In contrast, both the B3LYP and MP2(full) levels of theory suggest that the alkali metal cations bind to 18C6 more strongly than da18C6, and that the preference for18C6 should increase slightly with the size of the alkali metal cation. Similar results were found for ha18C6, where theory suggests that the alkali metal cations should bind to 18C6 more strongly than ha18C6 and that the preference for 18C6 should increase with the size of the alkali metal cation [24]. Combining the results of these two studies suggest that theory either overestimates the strength of interaction with oxygen donor atoms or underestimates the strength of binding to nitrogen donor atoms.

### 6.5.4. Comparison with ha18C6

The measured and B3LYP/def2-TZVPPD calculated $M^+$-da18C6 and $M^+$-ha18C6 BDEs [24] are compared in **Figure 6.10b**. Experimentally, preferential binding of $Na^+$ to ha18C6 over da18C6 is observed, whereas theory suggests that the binding is equivalent. In contrast, both B3LYP and MP2(full) theory suggest that the larger alkali metal cations preferentially bind to da18C6 over ha18C6. This trend is very well reproduced in the experiments, where the larger alkali metal cations are found to bind to da18C6 slightly more strongly than ha18C6. However, the differences are small and within experimental error for all cations except $Cs^+$.

## 6.6. Conclusions

Thresholds for the loss of the intact da18C6 ligand determined from the kinetic energy dependence of the collision-induced dissociation of four $M^+$(da18C6) complexes, where $M^+ = Na^+$, $K^+$, $Rb^+$, and $Cs^+$, with Xe were determined. The effects of the kinetic and internal energy distributions of the $M^+$(da18C6) and Xe reactants, multiple collisions with Xe, and the lifetime of the activated $M^+$(da18C6) complexes using a loose PSL TS model were carefully considered to ensure accurate modeling of the experimental data. Theoretical calculations were performed at several levels of theory; B3LYP/def2-TZVPPD provided the best results and was therefore used for data analysis. Excellent agreement between the B3LYP/def2-TZVPPD calculated and experimentally determined BDEs was found for all four complexes, similar to the $M^+$(ta12C4) [25] and $M^+$(ha18C6) [24] complexes investigated using parallel approaches. Trends based primarily on electrostatic interactions were observed for the measured and theoretically calculated $M^+$-da18C6 BDEs. The BDEs decreased monotonically as the size of the alkali metal cation increases, whereas solution phase trends follow the order of $K^+ > Na^+ > Rb^+ > Cs^+$ as a result of competitive binding between the macrocycle and solvent. Preferential binding of

$Na^+$ to ha18C6 over da18C6 and 18C6 was observed, whereas the larger alkali metal cations exhibit a small preference for da18C6 and 18C6 versus ha18C6. Results suggested that the B3LYP and MP2(full) levels of theory either overestimate the strength of interaction to the oxygen donor atoms or underestimate the strength of binding to nitrogen donor atoms.

## 6.7. References

[1] H.K. Frensdorff, J. Am. Chem. Soc. 93 (1971) 600.

[2] A. D'Aprano, B. Sesta, J. Phys. Chem. 91 (1987) 2415.

[3] B.G. Cox, P. Firman, I. Schneider, H. Schneider, Inorg. Chem. 27 (1998) 4018.

[4] A.P. Marchand, H. Chong, Tetrahedron 55 (1999) 9697.

[5] S.M. Blair, J.S. Brodbelt, A.P. Marchand, H. Chong, S. Alihodzic, J. Am. Soc. Mass Spectrom. 11 (2000) 884.

[6] S.M. Williams, J.S. Brodbelt, Z. Huang, H. Lai, A.P. Marchand, Analyst 128 (2003) 1352.

[7] B. Çiçek, Ü. Çakır, A. Azizoglu, J. Incl. Phenom. Macro. 72 (2012) 121.

[8] A.Y. Freidzon, A.A. Bagaturyants, M.V. Alfimov, Russ. Chem. Bt. 56 (2007) 407.

[9] J-F. Gal, P-C. Maria, L. Massi, C. Mayeux, P. Burk, J. Tammiku-Taul, Int. J. Mass Spectrom. 267 (2012) 7.

[10] M. Winter, Web Elements Periodic Table of the Elements | Cesium | biological information, WebElements, 2012.

[11] H. Matsuda, H. Matsuura, A. Noma, J. Physiol. 413 (1989) 139.

[12] H. Jadvar, J.A. Parker, Clinical PET and PET/CT, Springer, London, 2005, pp. 70 part 3.

[13] C.K. Yen, Y. Yano, T.F. Budinger, R.P. Friedland, S.E. Derenzo, R.H. Huesman, A. O'Brien, J. Nucl. Med. 23 (1992) 532.

[14] T.S. Kehwar, J. Med. Phys. 34 (2009) 191.

[15] Y. Chen, M.T. Rodgers, J. Am. Chem. Soc. 134 (2012) 2313

[16] HyperChem Molecular Modeling Software Package, Version 7.5; Hypercube Inc.: Gainesville, FL, 2002.

[17] Frisch, M. J.; et al. Gaussian 09, revision A.1; Gaussian, Inc.: Wallingford CT, 2009.

[18] J.B. Foresman, M.J. Frisch, Exploring Chemistry with Electronic Structure Methods, 2nd ed, Gaussian; Pittsburgh, 1996, p. 64.

[19] S.F. Boys, R. Bernardi, Mol. Phys. 19 (1979) 553.

[20] F.B. van Duijneveldt, J.G.C.M. van Duijneveldt-van de Rijt, J.H. van Lenthe, Chem. Rev. 94 (1994) 1873.

[21] S.M. Smith, A.N. Markevitch, D.A. Romanov, X. Li, R.J. Levis, H.B. Schlegel, J. Phys. Chem. A 108 (2004) 11063.

[22] M.T. Rodgers, P.B. Armentrout, Mass Spectrom. Rev. 19 (2000) 215.

[23] M.T. Rodgers, K.M. Ervin, P.B. Armentrout, J. Chem. Phys. 106 (1997) 4499.

[24] C.A. Austin, M.T. Rodgers, J. Phys. Chem. A 118 (2014) 5488.

[25] C.A. Austin, Y. Chen, M.T. Rodgers, Int. J. Mass Spectrom. 330-332 (2012) 27.

[26] M.B. More, D. Ray, P.B. Armentrout, J. Am. Chem. Soc. 121 (1999) 417.

[27] D. Ray, D. Feller, M.B. More, E.D. Glendening, P.B. Armentrout, J. Phys. Chem. 100 (1996) 16116.

[28] M.B. More, D. Ray, P.B. Armentrout, J. Phys. Chem. A 101 (1997) 831.

[29] M.B. More, D. Ray, P.B. Armentrout, J. Phys. Chem. A 101 (1997) 4254.

[30] M.B. More, D. Ray, P.B. Armentrout, J. Phys. Chem. A 101 (1997) 7007.

[31] P.B. Armentrout, C.A. Austin, M.T. Rodgers, Int. J. Mass Spectrom. 330-332 (2012) 16.

[32] P.B. Armentrout, C.A. Austin, M.T. Rodgers, J. Phys. Chem. A (2014), doi:http://dx.doi.org/10.1021/jp4116172 Articles ASAP.

[33] M.T. Rodgers, J. Phys. Chem. A 105 (2001) 2374.

[34] M.T. Rodgers, P.B. Armentrout, J. Am. Chem. Soc. 122 (2000) 8548.

[35] R. Amunugama, M.T. Rodgers, Int. J. Mass Spectrom. 195-196 (2000) 439.

[36] M.T. Rodgers, J. Phys. Chem. A 105 (2001) 8145.

[37] H. Huang, M.T. Rodgers, J. Phys. Chem. A 106 (2002) 4277.

[38] R. Amunugama, M.T. Rodgers, J. Phys. Chem. A 106 (2002) 9092.

[39] R. Amunugama, M.T. Rodgers, J. Phys. Chem. A 106 (2002) 9718.

[40] R.G. Wilson, G.R. Brewer, Ion Beams: With Applications to Ion Implantation, Wiley, New York, 1973, pp. 118–124.

**Table 6.1.** Fitting Parameters of Equation (S1), Threshold Dissociation Energies at 0 K, and Entropies of Activation at 1000 K of $M^+$(da18C6) Complexes[a]

| $M^+$ | $\sigma_0$ | $n$ | $E_0$ [b] (eV) | $E_0$(PSL) (eV) | Kinetic Shift (eV) | $\Delta S^\dagger$(PSL) (J $mol^{-1}$ $K^{-1}$) |
|---|---|---|---|---|---|---|
| $Na^+$ | 4.90 (1.6) | 1.0 (0.1) | 7.49 (0.10) | 3.07 (0.18) | 4.42 | 61 (2) |
| $K^+$ | 3.07 (1.5) | 1.7 (0.8) | 5.02 (0.11) | 2.39 (0.10) | 2.63 | 58 (2) |
| $Rb^+$ | 1.08 (0.8) | 1.4 (0.1) | 3.86 (0.05) | 1.99 (0.08) | 1.87 | 65 (2) |
| $Cs^+$ | 0.8 (0.1) | 1.6 (0.1) | 2.98 (0.09) | 1.67 (0.07) | 1.31 | 66 (2) |

[a] Present results, uncertainties are listed in parentheses. Average values for a loose PSL TS. [b] No RRKM analysis.

**Table 6.2.** Bond Dissociation Enthalpies of $M^+$(da18C6) Complexes at 0 K in kJ/mol[a]

| $M^+$ | TCID | B3LYP[b] | | | MP2[c] | | |
|---|---|---|---|---|---|---|---|
| | | $D_e$ | $D_0$[d] | $D_{0,BSSE}$[d,e] | $D_e$ | $D_0$[d] | $D_{0,BSSE}$[d,e] |
| $Na^+$ | 296.4 (17.7) | 300.7 | 290.1 | 288.4 | 327.0 | 316.4 | 294.2 |
| | | *307.6* | *297.0* | *289.5* | *322.1* | *311.5* | *289.1* |
| $K^+$ | 230.5 (10.1) | 245.8 | 239.1 | 236.0 | 282.9 | 276.2 | 251.8 |
| | | *250.5* | *244.0* | *240.5* | *273.5* | *266.9* | *252.0* |
| $Rb^+$ | 192.0 (7.3) | 201.8 | 196.6 | 196.0 | 266.5 | 261.3 | 216.5 |
| | | *190.3* | *184.9* | *182.9* | *230.0* | *224.6* | *191.8* |
| $Cs^+$ | 160.6 (6.5) | 145.8 | 158.0 | 157.5 | 227.8 | 217.4 | 189.4 |
| | | *132.3* | *141.6* | *139.1* | *189.7* | *184.3* | *154.9* |
| MAD[f] | 10.4 (5.1)[g] | | | 5.2 (2.1) | | | 19.2 (11.1) |
| | | | | *11.9 (6.6)* | | | *8.6 (9.0)* |

[a] Present results, uncertainties are listed in parentheses. [b] Calculated at B3LYP/def2-TZVPPD and *B3LYP/6-311+G(2d,2p)_HW//B3LYP/6-31+G*_HW* levels of theory. [c] Calculated at MP2(full)/def2-TZVPPD//B3LYP/def2-TZVPPD and *MP2(full)/6-311+G(2d,2p)_HW //B3LYP/6-31+G*_HW* levels of theory. [d] Including ZPE corrections with the B3LYP/6-31+G*_HW and B3LYP/def2-TZVPPD frequencies scaled by a factor of 0.9804. [e] Also includes BSSE corrections. [f] Mean absolute deviation. [g] Average experimental uncertainty.

**Table 6.3.** Geometrical Parameters of the B3LYP/def2-TZVPPD Optimized Structures of Neutral and $M^+$(da18C6) Complexes.[a]

| $M^+$ | Conformer | Symm | r(M–N) (Å) | r(M–O) (Å) | $\angle M\mu_{N,O}$ (°) | $\angle M\mu_{O}$ (°) | ∠CNC (°) | ∠COC (°) | ∠NCCO (°) | ∠OCCO (°) | ∠CNCC (°) | ∠COCC (°) |
|---|---|---|---|---|---|---|---|---|---|---|---|---|
| da18C6 | C1 | $C_{2h}$ | - | - | - | - | 113.8 | 113.4 | 66.5 | 72.4 | 179.6 | 177.8 |
| $Na^+$ | Na1 | $C_{2h}$ | 2.755 | 2.833 | 61.6 | 57.8 | 111.4 | 112.9 | 61.7 | 58.3 | 179.9 | 175.0 |
| | **Na2** | **$C_1$** | **2.504** | **2.436** | **62.2** | **57.5** | **113.1** | **114.2** | **61.3** | **61.1** | **178.2** | **158.1** |
| | Na3 | $C_1$ | 2.553 | 2.480 | 70.4 | 69.4 | 115.3 | 116.5 | 57.5 | 52.5 | 119.3 | 111.2 |
| | Na4 | $C_{2h}$ | 2.499 | 2.326 | 74.9 | 74.7 | 118.5 | 120.0 | 49.5 | 45.8 | 89.3 | 99.1 |
| $K^+$ | **K1** | **$C_{2h}$** | **2.943** | **2.842** | **60.9** | **59.6** | **113.4** | **113.3** | **65.6** | **62.0** | **173.5** | **176.0** |
| | K2 | $C_s$ | 2.917 | 2.822 | 58.7 | 59.1 | 115.4 | 113.0 | 58.0 | 65.2 | 164.6 | 176.0 |
| | K3 | $C_s$ | 2.986 | 2.786 | 59.9 | 59.8 | 116.0 | 114.4 | 58.6 | 57.9 | 135.5 | 168.5 |
| | K4 | $C_{2h}$ | 2.895 | 2.829 | 61.6 | 59.3 | 118.8 | 113.8 | 53.5 | 69.7 | 132.4 | 170.3 |
| $Rb^+$ | **Rb1** | **$C_{2h}$** | **3.060** | **2.946** | **59.2** | **58.0** | **113.9** | **113.7** | **67.6** | **63.8** | **172.6** | **174.9** |
| | Rb2 | $C_s$ | 3.068 | 2.980 | 55.4 | 55.9 | 115.2 | 113.0 | 58.1 | 66.1 | 171.3 | 176.3 |
| | Rb3 | $C_1$ | 3.180 | 3.004 | 57.0 | 57.9 | 115.1 | 114.3 | 65.0 | 66.0 | 137.0 | 151.7 |
| | Rb4 | $C_{2h}$ | 2.971 | 2.893 | 59.1 | 62.0 | 119.7 | 114.2 | 55.6 | 74.8 | 129.0 | 169.4 |
| $Cs^+$ | **Cs1** | **$C_s$** | **3.186** | **3.127** | **55.6** | **54.4** | **113.9** | **11337** | **67.1** | **64.0** | **173.0** | **172.7** |
| | Cs2 | $C_s$ | 3.188 | 3.151 | 52.3 | 52.7 | 114.9 | 113.1 | 58.1 | 66.4 | 171.6 | 175.4 |
| | Cs3 | $C_s$ | 3.330 | 3.146 | 54.3 | 55.1 | 115.1 | 114.0 | 65.6 | 67.3 | 137.2 | 151.6 |
| | Cs4 | $C_{2h}$ | 3.063 | 2.966 | 58.8 | 62.5 | 120.5 | 114.6 | 58.5 | 81.0 | 124.0 | 168.1 |

[a] Average values are given for similar bond distances or angles, and represents the absolute average. The ground-state conformations are indicated in bold.

## 6.8. Figure Captions

**Figure 6.1.** Structure of da18C6. B3LYP/def2-TZVPPD optimized structures and relative energies at 0 K (in kJ/mol) of the stable low-energy conformations of da18C6. The calculated dipole moments (μ) are also shown.

**Figure 6.2.** Cross section for collision-induced dissociation of $Rb^+$(da18C6) with Xe as a function of kinetic energy in the center-of-mass frame (lower *x*-axis) and the laboratory frame (upper *x*-axis). Data are shown for a Xe pressure of ~0.2 mTorr, part a. Zero-pressure extrapolated cross section for collision-induced dissociation of the $Rb^+$(da18C6) complex with Xe in the threshold region as a function of kinetic energy in the center-of-mass frame (lower *x*-axis) and the laboratory frame (upper *x*-axis). The solid line shows the best fit to the data using the model of Eq (2.4) convoluted over the neutral and ion kinetic and internal energy distributions. The dashed line shows the model cross section in the absence of experimental kinetic energy broadening for reactants with an internal temperature of 0 K, part b.

**Figure 6.3.** Cross sections for collision-induced dissociation of $M^+$(da18C6) complexes, where $M^+ = Na^+$, $K^+$, and $Cs^+$, with Xe as a function of kinetic energy in the center-of-mass frame (lower *x*-axis) and the laboratory frame (upper *x*-axis). Data are shown for a Xe pressure of ~0.2 mTorr, parts a-c, respectively. Zero-pressure extrapolated cross sections for collision-induced dissociation of $M^+$(da18C6) complexes, where $M^+ = Na^+$. $K^+$, and $Cs^+$, parts d-f respectively. The solid lines show the best fits to the data using the model of Eq. (2.4) convoluted over the neutral and ion kinetic and internal energy distributions. The dashed lines show the model cross sections in the absence of experimental kinetic energy broadening for reactants with an internal temperature of 0 K.

**Figure 6.4.** B3LYP/def2-TZVPPD optimized geometries, relative energies at 0 K, and *Gibbs free energies at 298 K* (in kJ/mol) of the stable low-energy conformers of the $Rb^+$(da18C6) complex. *i* indicates number of imaginary frequencies.

**Figure 6.5.** B3LYP/def2-TZVPPD optimized geometries, relative energies at 0 K, and *Gibbs free energies at 298 K* (in kJ/mol) of the stable low-energy conformers of the $Na^+$(da18C6) complex. *i* indicates number of imaginary frequencies.

**Figure 6.6.** B3LYP/def2-TZVPPD optimized geometries, relative energies at 0 K, and *Gibbs free energies at 298 K* (in kJ/mol) of the stable low-energy conformers of the $K^+$(da18C6) complex. *i* indicates number of imaginary frequencies.

**Figure 6.7.** B3LYP/def2-TZVPPD optimized geometries, relative energies at 0 K, and *Gibbs free energies at 298 K* (in kJ/mol) of the stable low-energy conformers of the $Cs^+$(da18C6) complex. *i* indicates number of imaginary frequencies.

**Figure 6.8.** Variation in the relative energies at 0 K and Gibbs free energies at 298 K (in kJ/mol) of the four most stable conformations of the $M^+$(da18C6) complexes as a function of the alkali metal cation calculated at the B3LYP/def2-TZVPPD level of theory. Open symbols indicate low-energy structures that possess an imaginary frequency for the Na1($C_{2h}$) conformer.

**Figure 6.9.** B3LYP and MP2(full) calculated versus TCID measured $M^+$–da18C6 BDEs at 0 K (in kJ/mol), where $M^+$ = $Na^+$, $K^+$, $Rb^+$, and $Cs^+$. Single point energies calculated using the def2-TZVPPD (part a) and 6-311+G(2d,2p)_HW (part b) basis sets and the def2-TZVPPD and 6-31+G* optimized geometries of the ground-state conformers, respectively. All values are determined here and taken from **Table 6.2**.

**Figure 6.10.** Comparison of TCID measured and B3LYP/def2-TZVPPD calculated $M^+$–da18C6 and $M^+$–18C6 BDEs at 0 K (in kJ/mol) part a, and $M^+$–da18C6 and $M^+$–ha18C6 BDEs at 0 K (in kJ/mol) part b, where $M^+$ = $Na^+$, $K^+$, $Rb^+$, and $Cs^+$. All values for the $M^+$(da18C6) complexes are determined here and taken from **Table 6.2**. Calculated values for the $M^+$–18C6 BDEs are taken from reference 24.Values for the $M^+$- ha18C6 BDEs are taken from reference 24. Calculated values for the $M^+$–18C6 BDEs are taken from reference 26.

Figure 6.1.

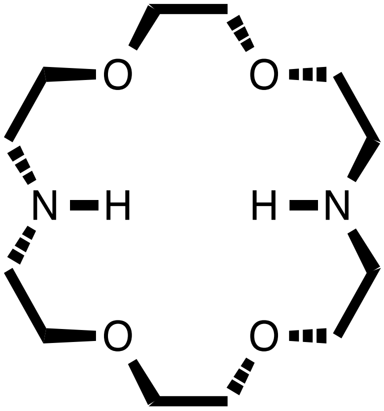

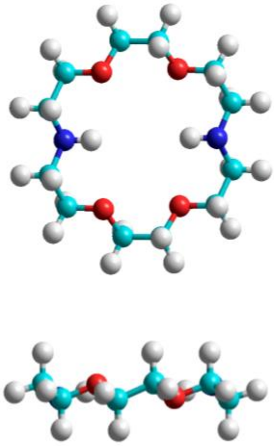

C1 ($C_{2h}$)
0.0 kJ/mol
μ = 0.0 D

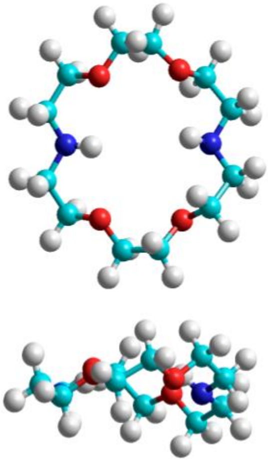

C2 ($C_1$)
18.0 kJ/mol
μ = 0.458 D

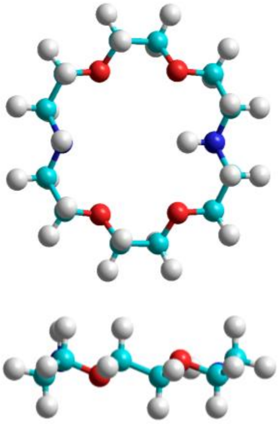

C3 ($C_s$)
18.4 kJ/mol
μ = 1.456 D

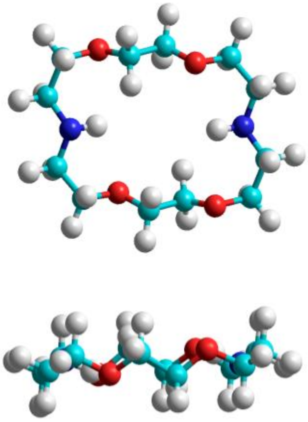

C4 ($C_i$)
29.3 kJ/mol
μ = 0.0 D

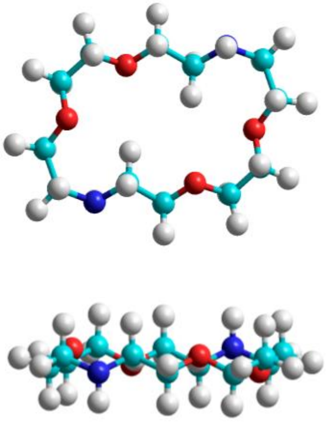

C5 ($C_i$)
31.4 kJ/mol
μ = 0.0 D

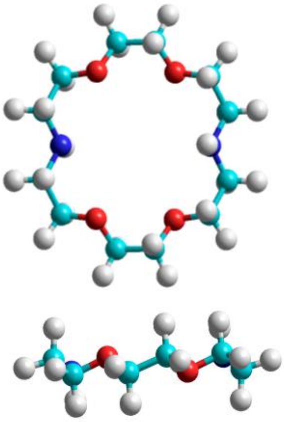

C6 ($C_{2h}$)
40.7 kJ/mol
μ = 0.0 D

Diaza-18-crown-6 (da18C6)
1,4,10,13-tetraoxa-7,16-diazacyclooctadecane

Figure 6.2.

a.

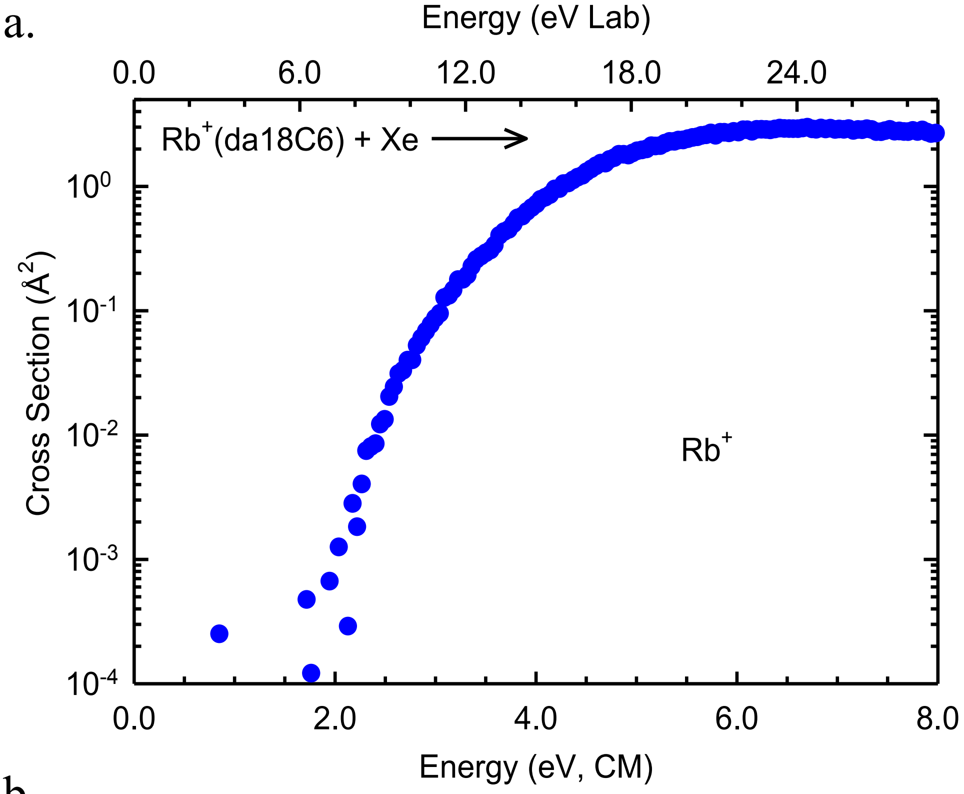
Energy (eV Lab)
0.0
6.0
12.0
18.0
24.0
Rb$^+$(da18C6) + Xe ⟶
$10^0$
$10^{-1}$
$10^{-2}$
$10^{-3}$
$10^{-4}$
Cross Section (Å$^2$)
Rb$^+$
0.0
2.0
4.0
6.0
8.0
Energy (eV, CM)

b.

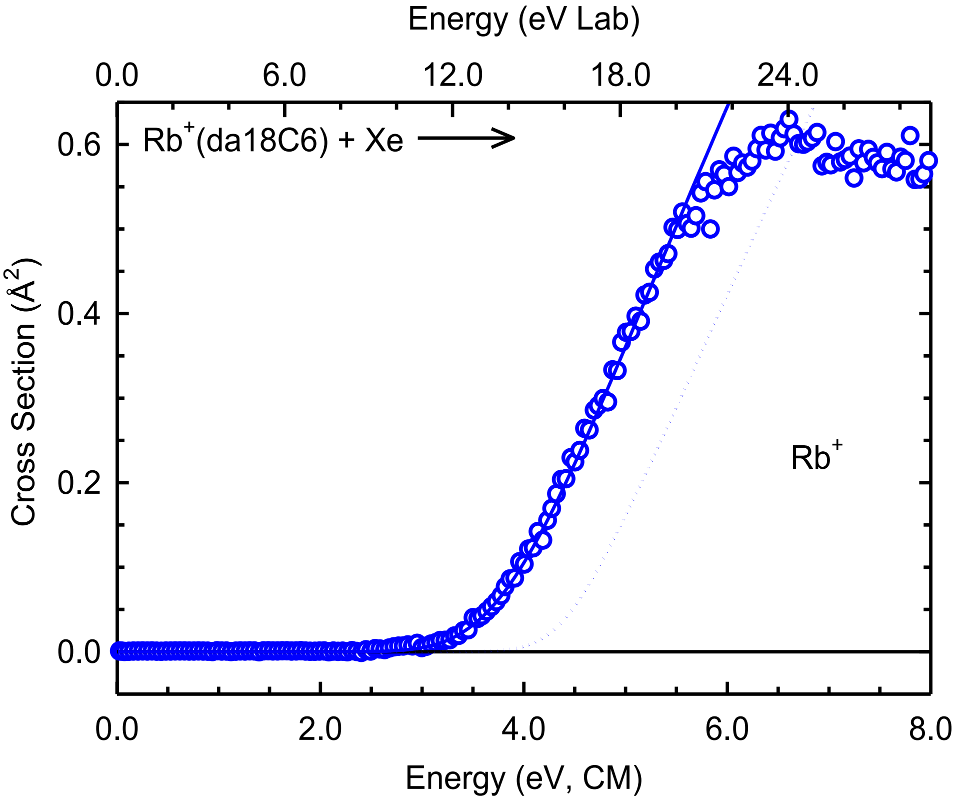
Energy (eV Lab)
0.0
6.0
12.0
18.0
24.0
Rb$^+$(da18C6) + Xe ⟶
0.6
0.4
0.2
0.0
Cross Section (Å$^2$)
Rb$^+$
0.0
2.0
4.0
6.0
8.0
Energy (eV, CM)

Figure 6.3.

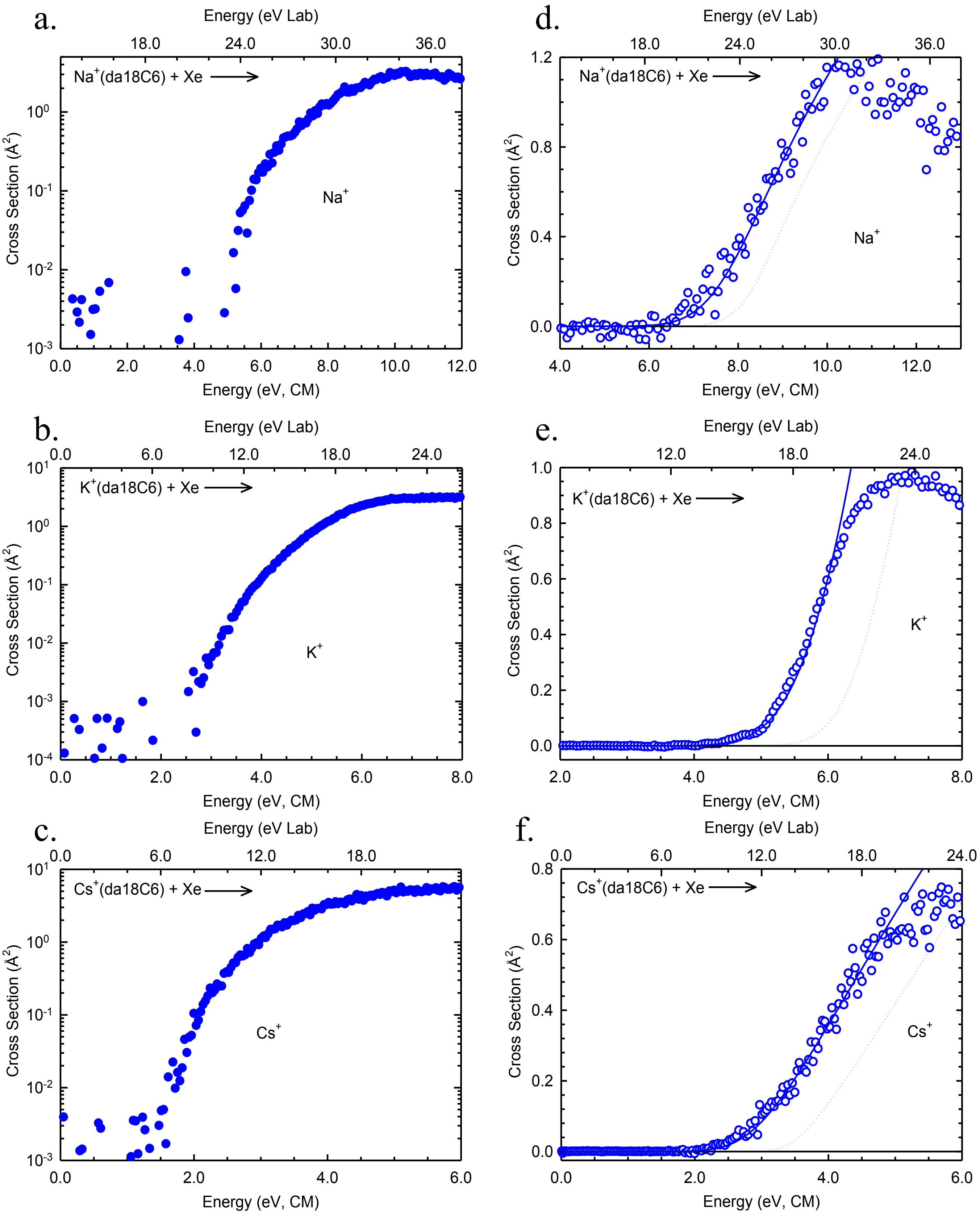
a.
Energy (eV Lab)
18.0
24.0
30.0
36.0
Na$^+$(da18C6) + Xe ⟶
Na$^+$
Cross Section (Å$^2$)
$10^0$
$10^{-1}$
$10^{-2}$
$10^{-3}$
0.0
2.0
4.0
6.0
8.0
10.0
12.0
Energy (eV, CM)
d.
Energy (eV Lab)
18.0
24.0
30.0
36.0
Na$^+$(da18C6) + Xe ⟶
Na$^+$
Cross Section (Å$^2$)
1.2
0.8
0.4
0.0
4.0
6.0
8.0
10.0
12.0
Energy (eV, CM)
b.
Energy (eV Lab)
0.0
6.0
12.0
18.0
24.0
K$^+$(da18C6) + Xe ⟶
K$^+$
Cross Section (Å$^2$)
$10^1$
$10^0$
$10^{-1}$
$10^{-2}$
$10^{-3}$
$10^{-4}$
0.0
2.0
4.0
6.0
8.0
Energy (eV, CM)
e.
Energy (eV Lab)
12.0
18.0
24.0
K$^+$(da18C6) + Xe ⟶
K$^+$
Cross Section (Å$^2$)
1.0
0.8
0.6
0.4
0.2
0.0
2.0
4.0
6.0
8.0
Energy (eV, CM)
c.
Energy (eV Lab)
0.0
6.0
12.0
18.0
Cs$^+$(da18C6) + Xe ⟶
Cs$^+$
Cross Section (Å$^2$)
$10^1$
$10^0$
$10^{-1}$
$10^{-2}$
$10^{-3}$
0.0
2.0
4.0
6.0
Energy (eV, CM)
f.
Energy (eV Lab)
0.0
6.0
12.0
18.0
24.0
Cs$^+$(da18C6) + Xe ⟶
Cs$^+$
Cross Section (Å$^2$)
0.8
0.6
0.4
0.2
0.0
0.0
2.0
4.0
6.0
Energy (eV, CM)

Figure 6.4.

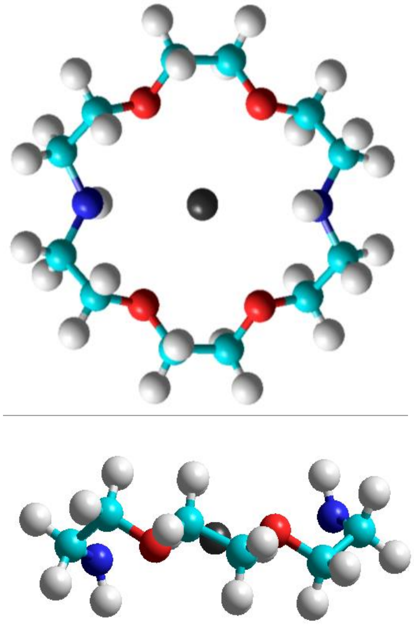

Rb1 ($C_{2h}$)
0.0 *(0.0)* kJ/mol

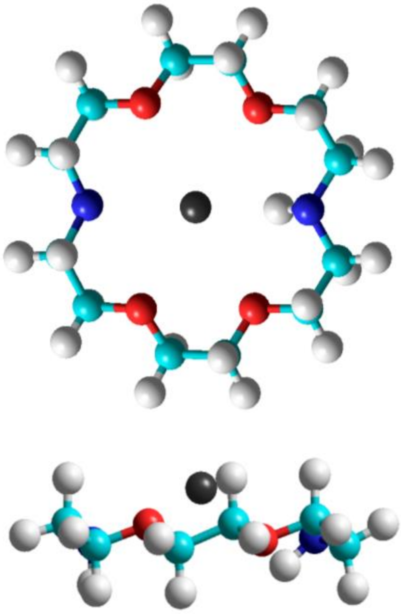

Rb2 ($C_s$)
17.1 *(15.3)* kJ/mol

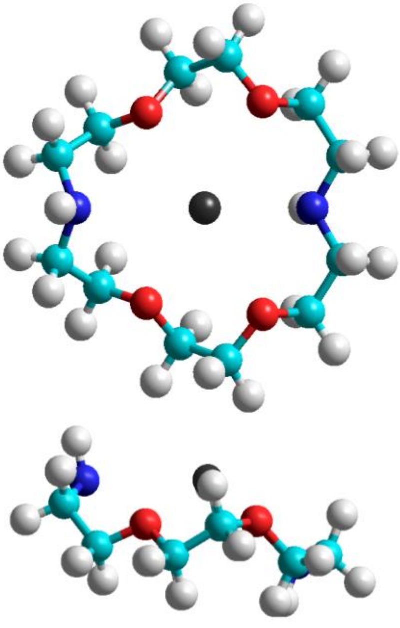

Rb3 ($C_1$)
23.5 *(21.2)* kJ/mol

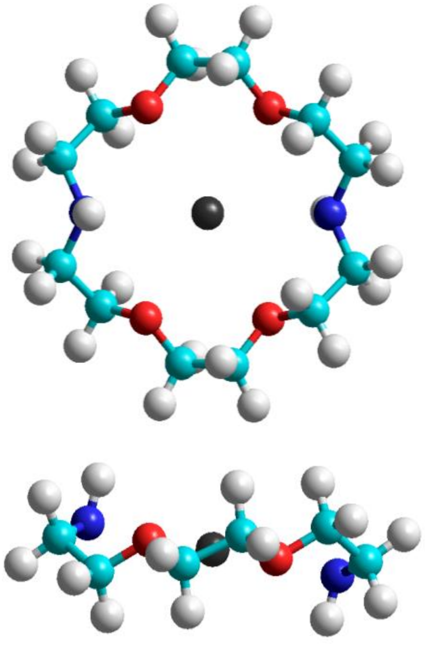

Rb4 ($C_{2h}$)
58.5 *(60.1)* kJ/mol, *i* = 1

Rb$^+$(da18C6)

Figure 6.5.

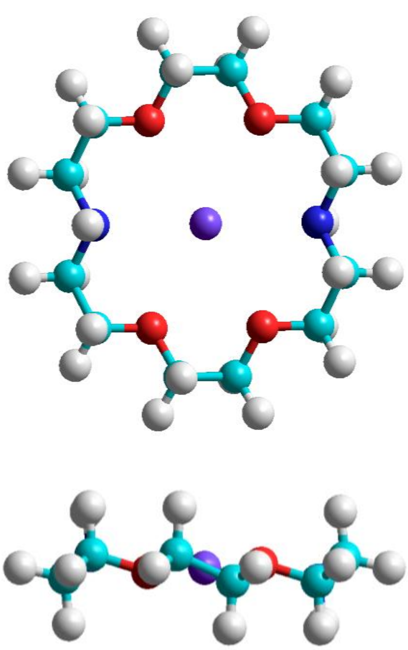

Na1 ($C_{2h}$)
0.0 *(0.0)* kJ/mol, *i* = 1

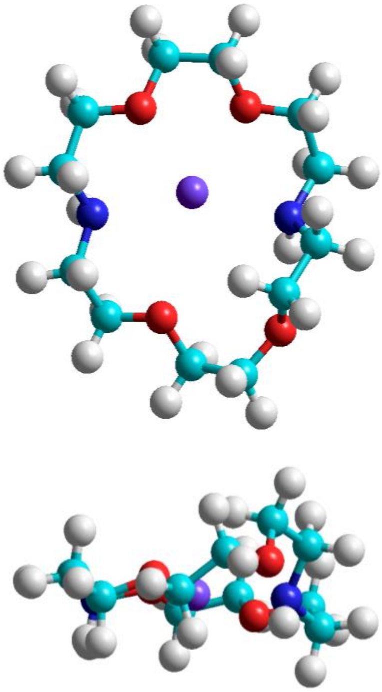

Na2 ($C_1$)
5.8 *(6.7)* kJ/mol

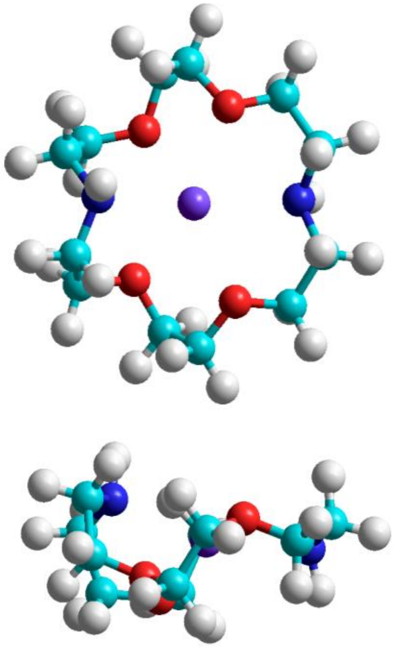

Na3 ($C_1$)
18.3 *(20.5)* kJ/mol

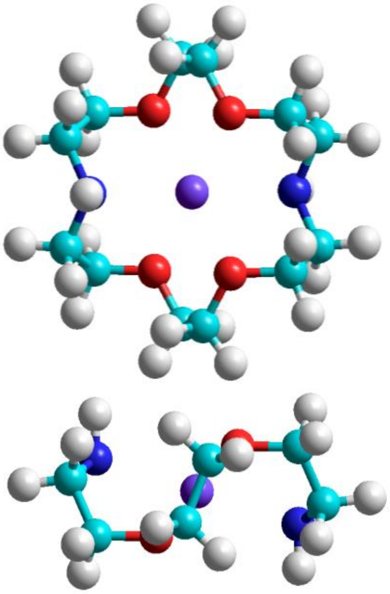

Na4 ($C_{2h}$)
48.6 *(53.1)* kJ/mol

$Na^+$(da18C6)

Figure 6.6.

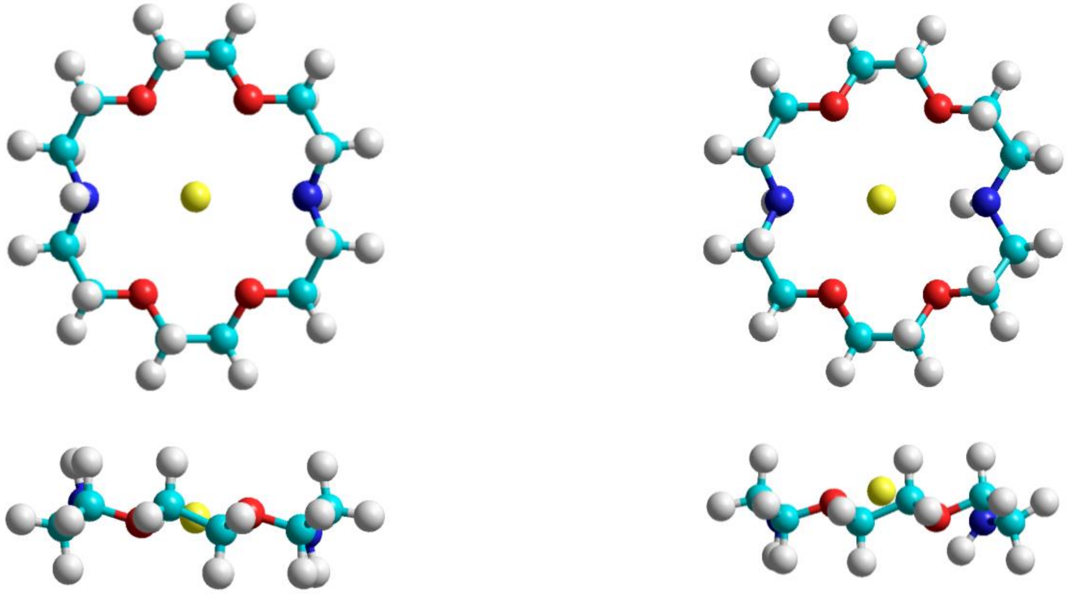

K1 ($C_{2h}$)
0.0 *(0.0)* kJ/mol

K2 ($C_s$)
25.1 *(23.2)* kJ/mol

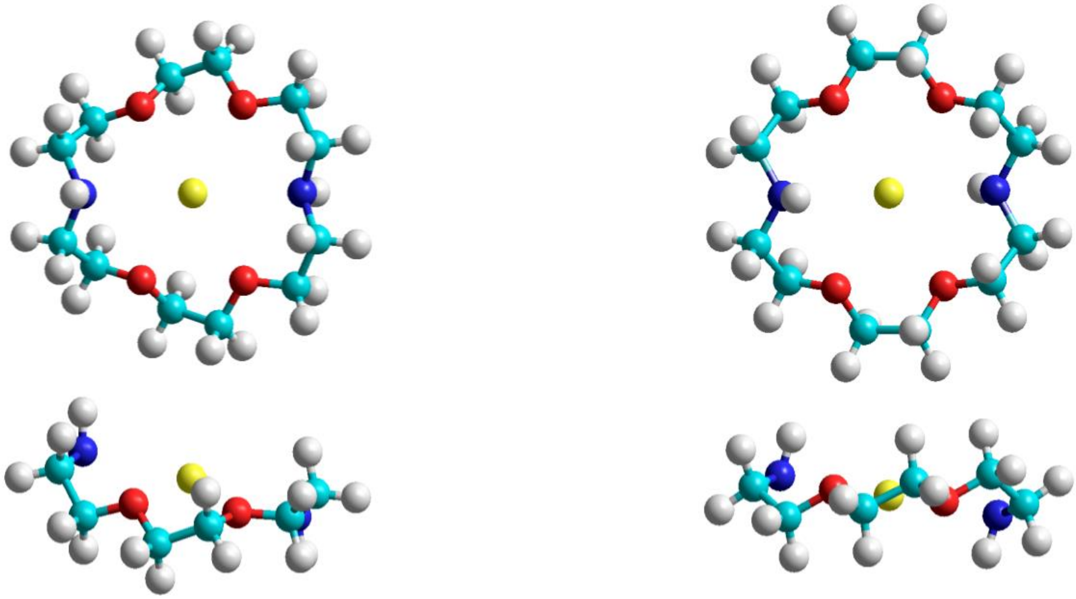

K3 ($C_s$)
30.1 *(29.4)* kJ/mol

K4 ($C_{2h}$)
53.4 *(57.6)* kJ/mol, $i = 2$

$K^+$(da18C6)

Figure 6.7.

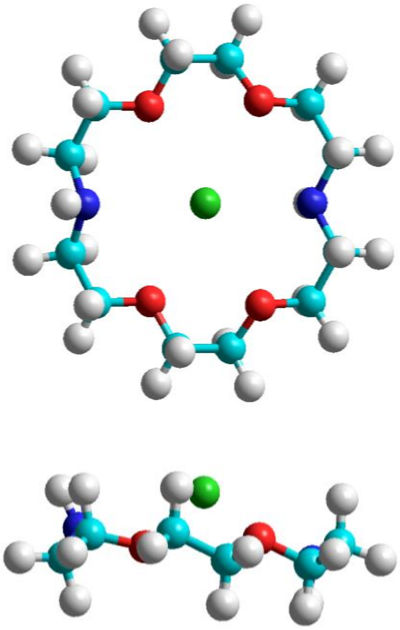

Cs1 ($C_s$)
0.0 *(0.0)* kJ/mol

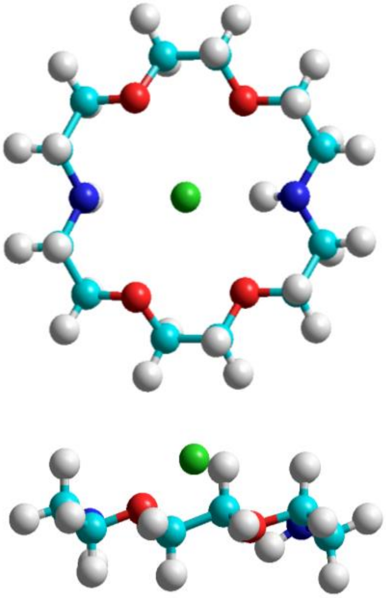

Cs2 ($C_s$)
8.1 *(8.0)* kJ/mol

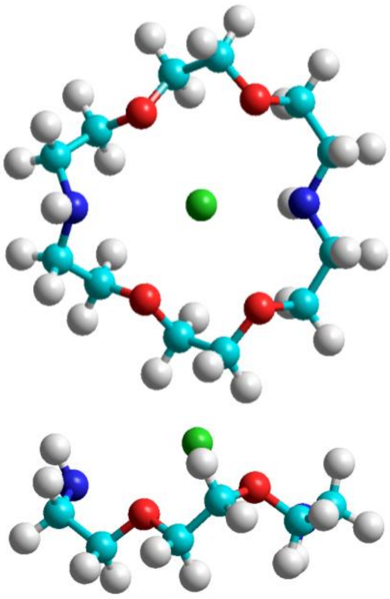

Cs 3($C_s$)
15.1 *(14.3)* kJ/mol

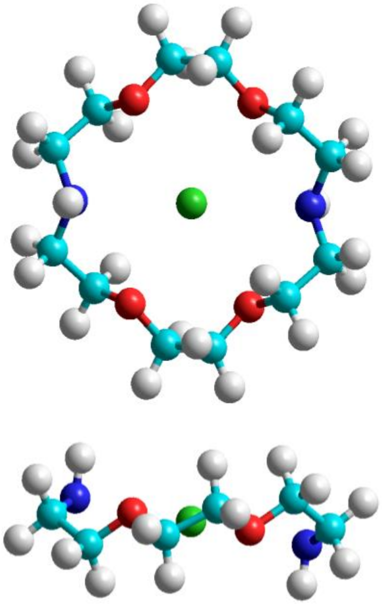

Cs4 ($C_{2h}$)
89.3 *(89.4)* kJ/mol, $i = 1$

$Cs^+$(da18C6)

Figure 6.8.

a.

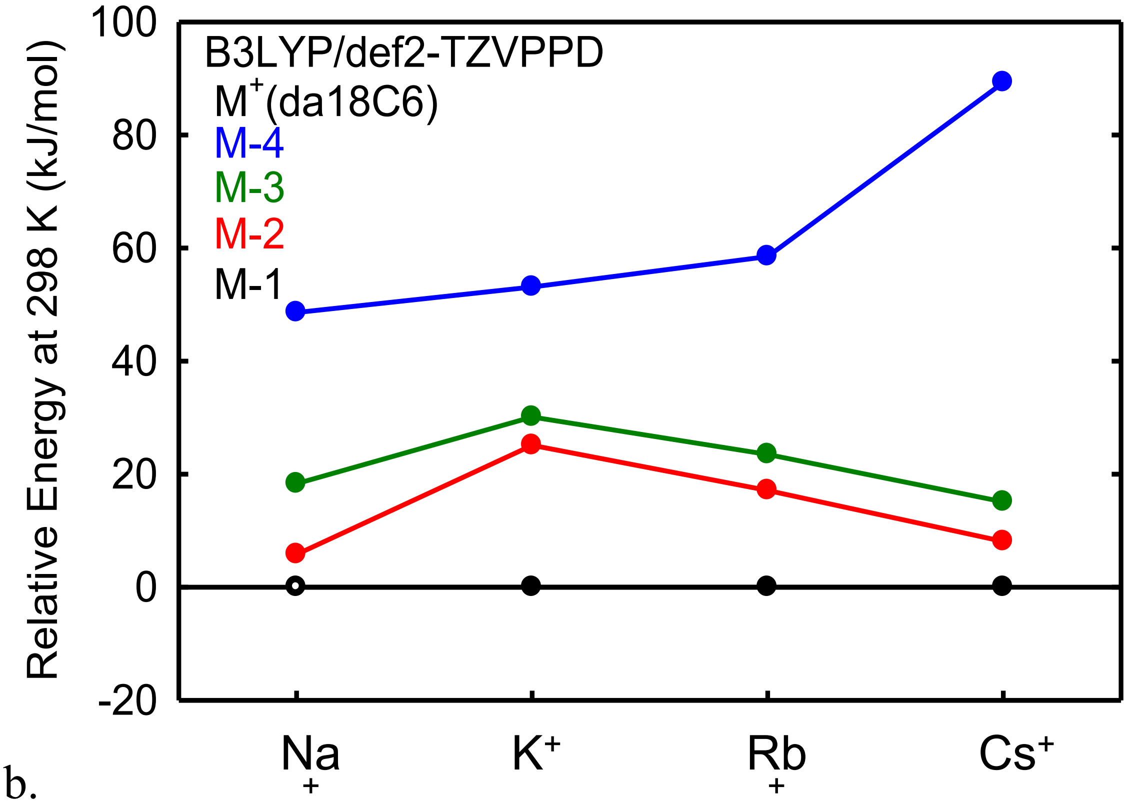
B3LYP/def2-TZVPPD
M+(da18C6)
M-4
M-3
M-2
M-1
Relative Energy at 298 K (kJ/mol)
100
80
60
40
20
0
-20
Na+
K+
Rb+
Cs+

b.

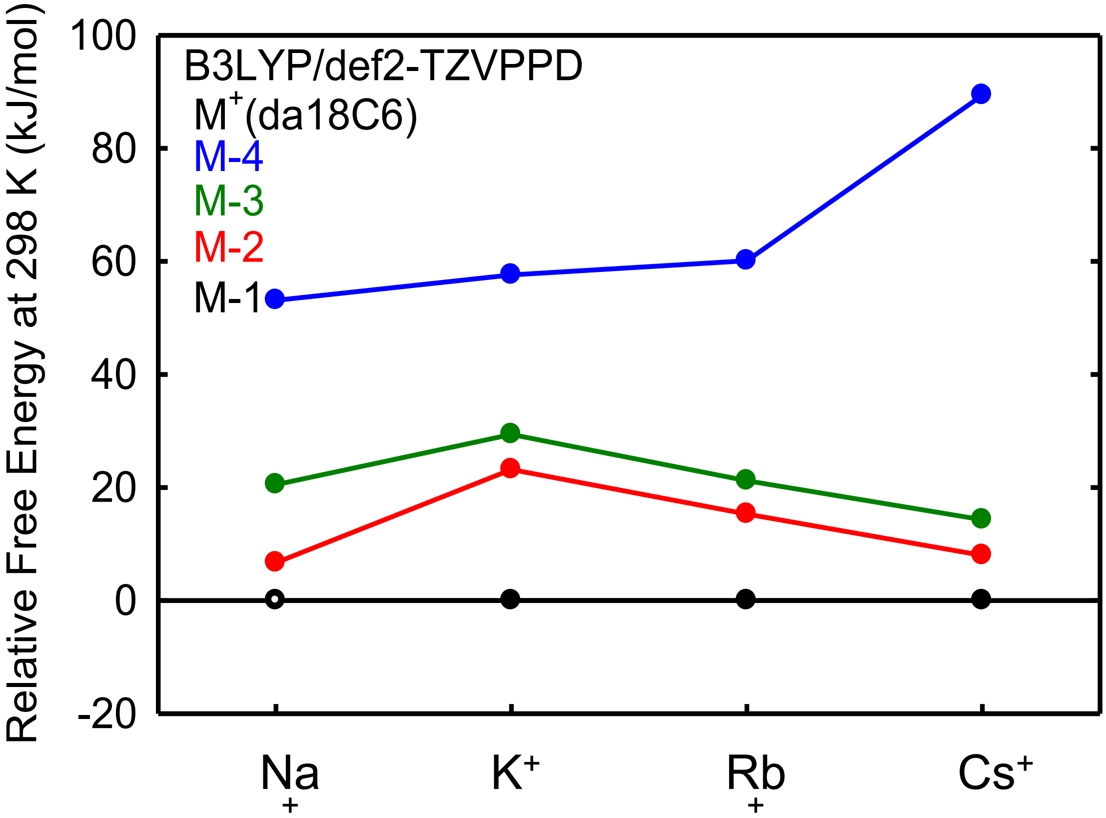
B3LYP/def2-TZVPPD
M+(da18C6)
M-4
M-3
M-2
M-1
Relative Free Energy at 298 K (kJ/mol)
100
80
60
40
20
0
-20
Na+
K+
Rb+
Cs+

Figure 6.9.

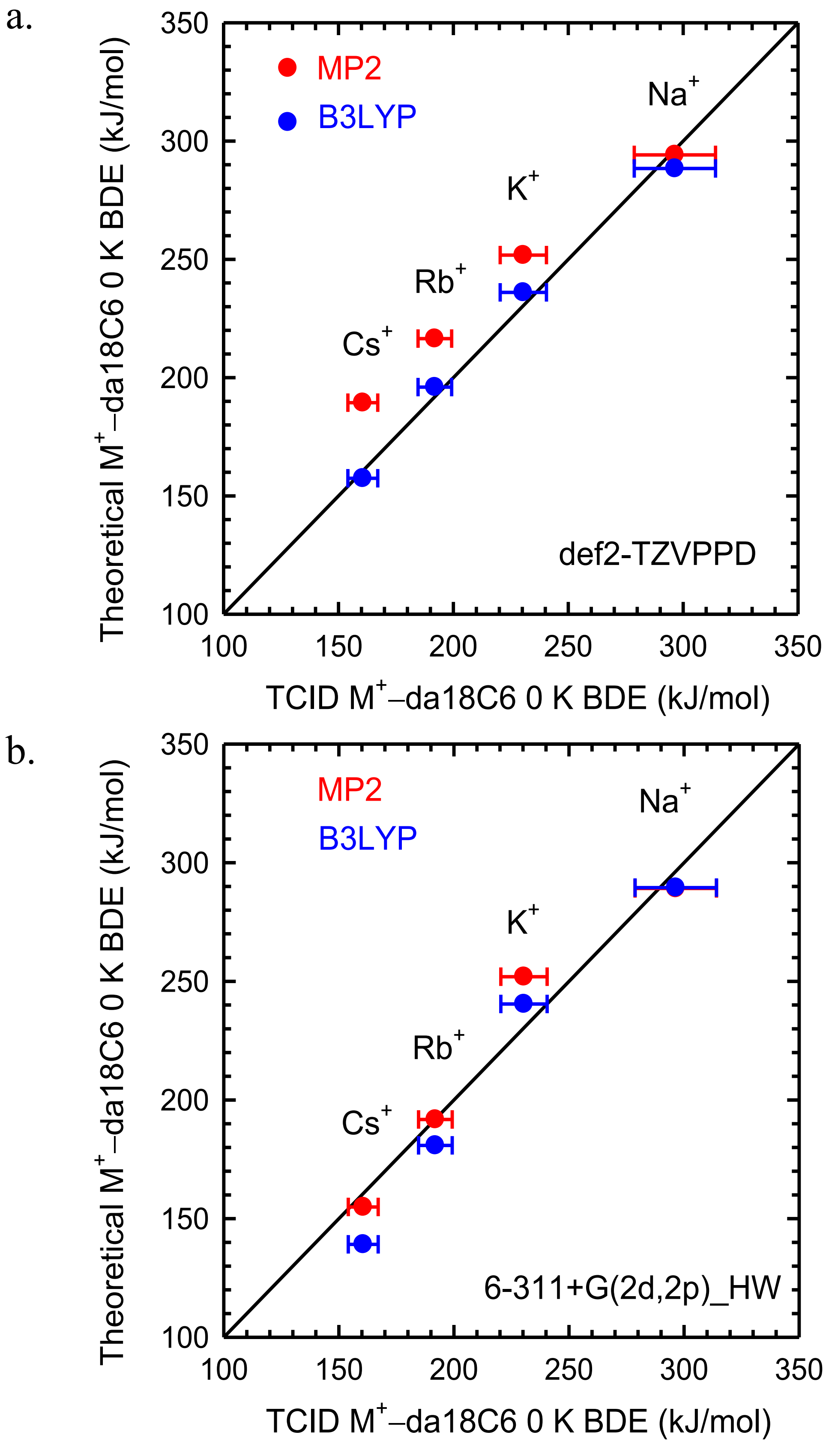
a.
MP2
B3LYP
Na$^+$
K$^+$
Rb$^+$
Cs$^+$
def2-TZVPPD
Theoretical M$^+$–da18C6 0 K BDE (kJ/mol)
TCID M$^+$–da18C6 0 K BDE (kJ/mol)
100
150
200
250
300
350
b.
MP2
B3LYP
Na$^+$
K$^+$
Rb$^+$
Cs$^+$
6-311+G(2d,2p)_HW
Theoretical M$^+$–da18C6 0 K BDE (kJ/mol)
TCID M$^+$–da18C6 0 K BDE (kJ/mol)
100
150
200
250
300
350

Figure 6.10.

a.

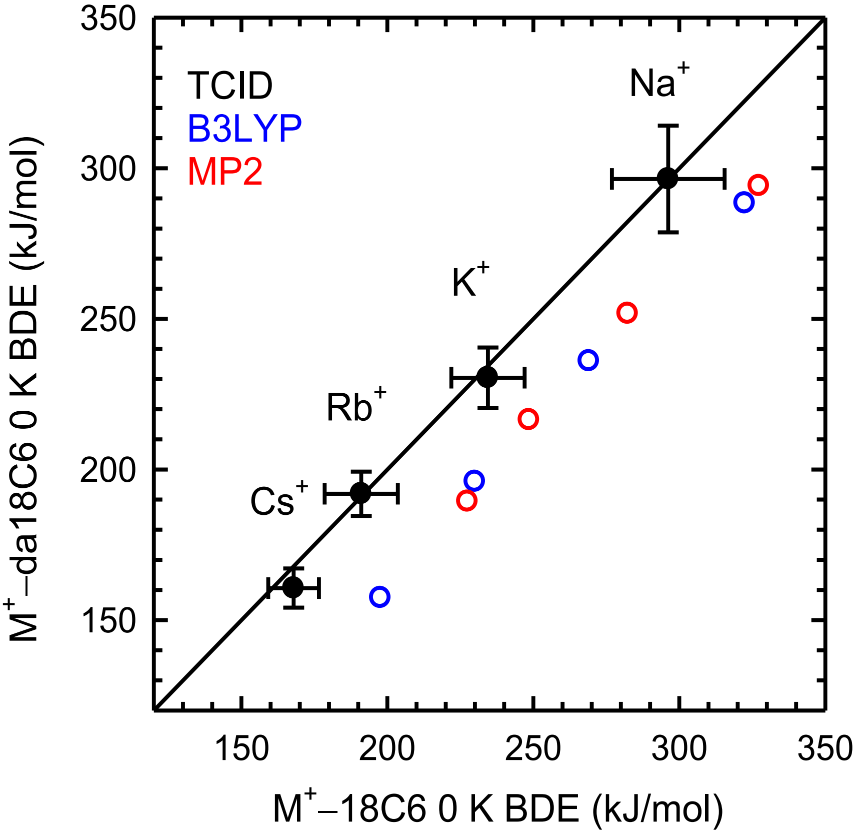

b.

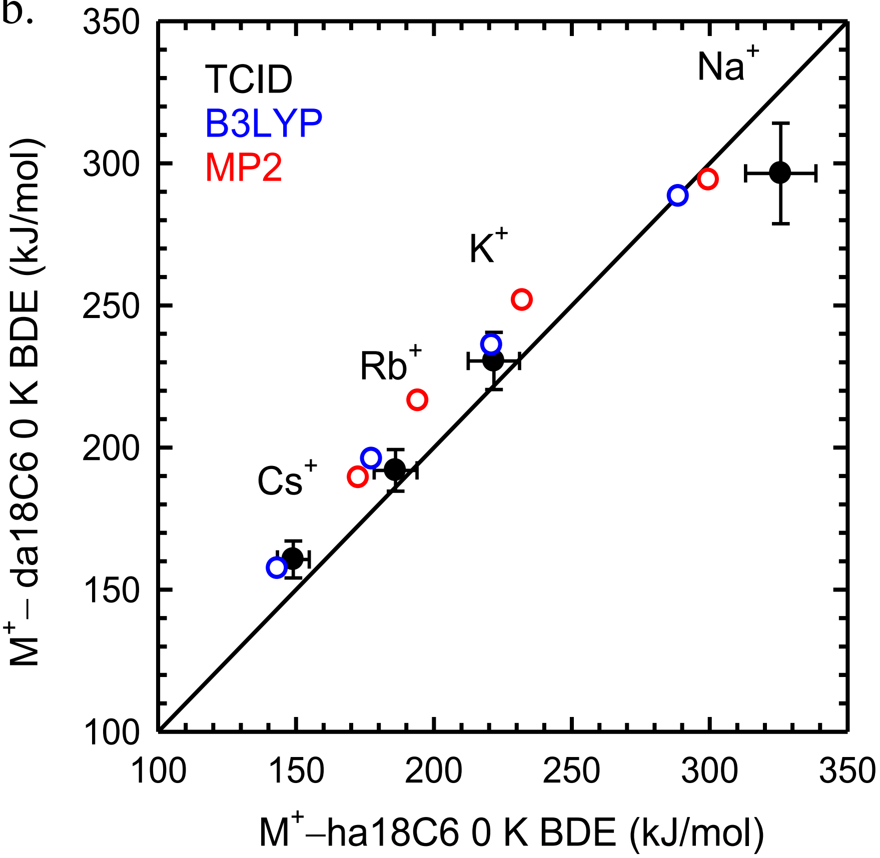

# CHAPTER 7

# Alkali Metal Cation – Hexathia-18-Crown-6: Effects of Alkali Metal Cation Size on the Structure and Binding Energies

## 7.1. Introduction

Hexathia-18crown-6 (1,4,7,10,13,16-hexathiacyclooctadecane, ht18C6) is a multidentate sulfur macrocycle and the thia analogue of 18-crown-6 (1,4,7,10,13,16-hexaoxacyclooctadecane, 18C6). The structure of ht18C6 is shown in **Figure 7.1**. To date, very little gas phase thermochemical and spectroscopic information has been reported for ht18C6 interactions with the alkali metal cations.

The purpose of this work was to further extend the studies of molecular recognition of metal cations by macrocyclic ligands by probing the nature of the binding interactions in alkali metal cation−ht18C6 complexes and providing accurate binding energies for the series of alkali metal cations including $Na^+$, $K^+$, $Rb^+$, and $Cs^+$. Results for the $M^+$(ht18C6) complexes are compared to the analogous $M^+$(18C6) and $M^+$(ha18C6) complexes to elucidate the influence of the donor atoms (S versus O and S versus N) on the nature and strength of binding. In aqueous solution, alkali metal cations preferentially bind to crown ethers over the analogous nitrogen and sulfur macrocycles [ 1 ]. Investigating the $M^+$(ht18C6) complexes in the gas phase thus allows separation of the intrinsic binding interactions. The effects of the alkali metal cations on the conformation of their complexes to ht18C6 were also investigated.

## 7.2. Collision–Induced Dissociation Experiments

Cross sections for collision-induced dissociation (CID) of four $M^+$(ht18C6) complexes, where $M^+ = Na^+$, $K^+$, $Rb^+$, and $Cs^+$, were measured using a guided ion beam tandem mass spectrometer that has been described in detail **Chapter 2**. The $M^+$(ht18C6) complexes were generated by electrospray ionization (ESI) [2]. Thermochemical analyses of the experimental results were explicitly discussed in **Chapter 2**.

## 7.3. Theoretical Calculations

To obtain model structures, vibrational frequencies, rotational constants, and energetics for the neutral ht18C6 ligand and the $M^+$(ht18C6) complexes, molecular dynamics simulated annealing procedures and ab initio and density functional theory calculations were performed using Hyperchem [3] and the Gaussian 09 suite of programs [4], respectively, and is described in detail in **Chapter 2**.

Starting structures for the $M^+$(ht18C6) complexes were generated using four of the five low-energy neutral ht18C6 structures, as they were expected to provide the most favorable geometries for interaction with the alkali metal cation, and placing the alkali metal cation in the center of the macrocyclic ring of ht18C6.

Vibrational analyses of the geometry-optimized structures were performed to determine the vibrational frequencies of the neutral ht18C6 ligand and $M^+$(ht18C6) complexes. When used to model the data or to calculate thermal energy corrections, the computed frequencies were scaled by a factor of 0.9804 [5]. Single-point energy calculations were performed at the B3LYP and MP2(full) levels of theory using 6-311+G(2d,2p)_HW and def2-TZVPPD basis sets and the B3LYP/6-31+G* _HW and B3LYP/def2-TZVPPD optimized geometries, respectively. To obtain accurate BDEs, zero-point energy (ZPE) corrections scaled by 0.98 were applied, and basis set superposition errors (BSSE) were subtracted from the computed BDEs in the full counterpoise correction [6,7]. The BSSE corrections are much smaller for B3LYP than MP2(full) calculations. The polarizabilities for the stable low-energy conformers of ht18C6 were calculated at the PBE0/6-311+G(2d,2p) level of theory using the B3LYP/6-31+G* optimized geometries. This level of theory has been shown to accurately reproduce experimental polarizabilities [8]. In addition, the polarizabilities for the stable low-energy conformers of ht18C6 were also calculated at the PBE0/def2-TZVPPD level of theory.

Several of the optimized structures of the $M^+$(ht18C6) complexes exhibit imaginary frequencies. Attempts were made to eliminate imaginary frequencies by additional cycles of simulated annealing at 298 K as well as by moving the metal cation along the path associated with the corresponding mode and re-optimizing, but even with tight convergence several structures consistently converged to the same conformer with an imaginary frequency.

## 7.4. Results

### 7.4.1. Cross Sections for Collision–Induced Dissociation

Cross sections were measured for the collision-induced dissociation (CID) of four $M^+$(ht18C6) complexes with Xe, where $M^+ = Na^+, K^+, Rb^+$, and $Cs^+$. **Figure 7.2a** shows representative data for the $K^+$(ht18C6) complex. The complexes to $Na^+$, $Rb^+$, and $Cs^+$ exhibit similar relative behavior and are provided as **Figure 7.3a-c**. In all cases, the alkali metal cation is the only ionic product observed corresponding to endothermic loss of the intact da18C6 ligand in the CID reactions 7.1.

$$M^+(\text{ht18C6}) + \text{Xe} \rightarrow M^+ + \text{ht18C6} + \text{Xe} \qquad (7.1)$$

The magnitudes of the CID cross sections generally decrease and the apparent thresholds increase as the size of the alkali metal cation increases except for the $Na^+$, consistent with the trend expected for binding based primarily on electrostatic interactions [9].

### 7.4.2. Threshold Analysis

Thresholds for CID reactions 7.1 are determined using the model of Eq. 2.4 for four $M^+$(ht18C6) complexes. Results of these threshold analyses are given in **Table 7.1**.

A representative analysis is shown in **Figure 7.2b** for the $K^+$(ht18C6) complex, whereas an analogous set of figures for the complexes to $Na^+$, $Rb^+$, and $Cs^+$ are provided as **Figure 7.3d-f**. The loose PSL TS accurately reproduces the experimental cross sections for CID reactions 7.1 for all four $M^+$(ht18C6) complexes [10]. For noncovalently bound metal-ligand complexes, the loose PSL TS model provides the most accurate assessment of the kinetic shifts for CID processes [11–19]. The CID cross sections of the $M^+$(ht18C6) complexes are reproduced over energy ranges exceeding 4.0 eV and cross section magnitudes of at least a factor of 1000 for the $M^+$(ht18C6) complexes. **Table 7.1** also includes threshold values, $E_0$, obtained without including the RRKM lifetime analysis. A measure of the kinetic shifts for the $M^+$(ht18C6) systems is obtained by taking the difference of the $E_0$ and $E_0$(PSL), which increase from 1.01 eV for the $Cs^+$(ht18C6) complex to 2.66 eV for the $Na^+$(ht18C6) complex. Because all of the $M^+$(ht18C6) complexes possess the same number of vibrational modes, the observed kinetic shifts should directly correlate with the measured $M^+$-ht18C6 BDE, as observed (**Table 7.1**). The entropy of activation, $\Delta S^*$, is a measure of the looseness of the TS, but also depends on the threshold energy. The $\Delta S^*$(PSL) values for these systems at 1000 K exhibit modest variation, as expected on the basis of the similarity of these systems, and vary between 76 and 112 J $K^{-1}$ $mol^{-1}$. These entropies of activation compare favorably to those previously determined for a wide variety of noncovalently bound complexes that dissociate via simple noncovalent bond cleavage [11–19].

### 7.4.3. Theoretical Results

The ground-state and stable low-energy conformations of the ht18C6 ligand and $M^+$(ht18C6) complexes were calculated as described in the **Chapter 2**. $M^+$-ht18C6 BDEs calculated at the B3 LYP and MP2(full) levels of theory using the def2-TZVPPD basis set and the B3LYP/def2-TZVPPD optimized geometries are summarized in **Table 7.2**. Also included are values calculated at the B3LYP and MP2(full) levels of theory using the B3LYP/6-311+ G(2d,2p)_HW basis set and the B3LYP/6–31+G*_HW optimized geometries. ZPE and BSSE corrections are also included in the computed BDEs.

### 7.4.3.1. Neutral ht18C6

Low-energy structures of the neutral ht18C6 ligand are calculated as described above and shown in **Figure. 7.1**. Five distinct stable geometries are found. The various conformations of the neutral ht18C6 ligand are designated based on their relative Gibbs free energies and the symmetry of the ht18C6 ligand. Previous studies of the analogous $M^+$(ha18C6) complexes [11] and the smaller $M^+$(ta12C4) complexes [12] suggest energetics computed using the B3LYP/def2-TZVPPD level of theory are the most reliable among the levels of theory examined here. Therefore, the following discussion focuses on the geometries and energetics calculated at the B3LYP/def2-TZVPPD level of theory unless otherwise noted. The ground-state conformation C1 of neutral da18C6 adopts $C_i$ symmetry, where four of the sulfur donor atoms are in exodentate position and two are endo. It has been previously shown by Cooper et al. that the crystal structural of ht18C6 have both endo and exodentate sulfur atoms [20]. The local dipoles are anti-aligned for the C1($C_i$) conformer leading to cancellation, and no net dipole moment. The next higher-energy conformer C2($C_{2h}$) which lie 28.7 kJ/mol higher in free energy, have a similar rectangular shape as the C1($C_i$) conformer, but all the sulfur atoms are found in the ring. Similar to the C1 conformer, the local dipoles of the C2 conformer are anti-aligned leading to cancellation, and no net dipole moment. The C3, C4, and C5 conformers of ht18C6 adopt geometries similar to those observed when the macrocycle is complexed to a metal cation, and are calculated to lie 56.1, 76.8, and 106.7 kJ/mol higher in free energy than the ground-state C1 conformer. In contrast, the C1($C_i$) and C2($C_{2h}$) conformers adopt more rectangular geometries, similar to the ground-state determined for the 18C6 ligand [13].

### 7.4.3.2. M$^+$(ht18C6)

The ground-state and low-energy structures of the K$^+$(ht18C6) complex optimized at the B3LYP/def2-TZVPPD level of theory are shown in **Figure 7.4**. Similar conformations are also found for the complexes to the other alkali metal cations investigated and are shown as **Figures 7.5–7.7**. The nomenclature employed to describe these structures is of the form Mx(symmetry), where M identifies the metal cation, x indicates the relative order of stability among the low-energy conformers of the Na$^+$(ht18C6) complexes, and the symmetry is that of the ligand in its uncomplexed form. The ground-state conformation of the M$^+$(ht18C6) complexes at 0 K determined at the B3LYP and MP2(full) levels of theory using the def2-TZVPPD basis set are very similar for the Na$^+$, Rb$^+$, and Cs$^+$ complexes, compare **Figures 7.5–7.7**, and **7.8**, but an a different ground-state conformation is observed K$^+$ cation. The M1 conformer is calculated to be the lowest energy conformation for the alkali metal cations interaction with ht18C6, (**Figure 7.8**). The M1 and M2 conformer encapsulates the Na$^+$ and K$^+$ cations in the cavity created by the sulfur donor atoms. In contrast, the Rb$^+$ and Cs$^+$ cations are too large to fit in the cavity and sit above the center of the macrocyclic ring, (see **Figures 7.4–7.7**). In the M1 conformers, the ht18C6 ligand is highly distorted from its ground-state conformation in the absence of the metal cation, with the largest differences being observed for the Cs$^+$(ht18C6) complex. In the M2 conformers, the metal cations sit above the plane created by sulfur donor atoms for all metal cations except Na$^+$ and K$^+$. In all cases, the metal cation is encapsulated in the center the ring for the M3 conformation.

#### 7.4.3.2.1. K$^+$(ht18C6)

In the ground-state conformation of the K$^+$(ht18C6) complex, K2($S_6$), the K$^+$ metal cation sits in the center of the nearly planar ring created by the sulfur donor atoms at an average K$^+$–S bond distance of 3.271 Å. There are large differences in the average

∠SCCS and ∠CSCC dihedral angles that describe the skeletal backbone of the macrocycle that occur upon binding of $K^+$, **Table 7.3**. Santos et al. concluded that for $M^+$(ha18C6) complexes to small metal cations such that the $M^+$–N bond distances are <2.6 Å, a more bent structure (trigonal prismatic) is preferred, whereas for larger metal cations, a planar hexagonal conformer is preferred [21,22]. The trend seems to be true for sulfur donor atoms binding to K. The next most stable conformer, K1($C_1$), is calculated to lie 3.4 kJ/mol higher in energy and has an average $K^+$–S bond distance of 3.445 Å. When the free energy is considered, the K1($C_1$) conformer is the ground-state and the K2($S_6$) conformer lie 4.3 kJ/mol higher in energy. In the K1($C_1$) conformer, three of the sulfur donor atoms are oriented toward the cavity, while the other three sulfur donor atoms are oriented towards the metal cation. The K1($C_1$) conformer skeletal backbone dihedral angles differ from the ht18C6 conformer by 80 to 31.5° , with the ∠SCCS and ∠CSCC dihedral angles contracting. The K3($C_{2h}$) conformer lies 188.2 kJ/mol higher in free energy and is similar to the trigonal prismatic structure observed for ha18C6 interactions with small metal cations [23,24,25]. The K3($C_{2h}$) conformer is more compact such that the average $K^+$–S bond distance is the shortest among the low–energy conformers computed, 2.979 Å. The K3($C_{2h}$) conformer exhibits the greatest distortion upon binding of $K^+$ of all of the stable conformers computed, see **Table 7.3.** Similar trends in the geometric parameters are found for all of the other alkali metal cation–hexathia 18-crown-6 complexes. The K3($C_{2h}$) conformer possesses an imaginary frequency corresponding to a ring-breathing mode where the metal cation moves up and down in the center of the ring as the ring stretches and shrinks. Calculations were performed using tight convergence in an attempt to remove this imaginary frequency; however, even tight convergence failed to eliminate the imaginary frequency.

#### 7.4.3.2.2. $Rb^+$(ht18C6) and $Cs^+$(ht18C6)

For $Rb^+$ and $Cs^+$, the Cs complexes, M1($C_s$) are preferred as found for the $Na^+$(ht18C6) complex. The cavity of ht18C6 is too small to accommodate these larger metal cations such that the metal cation sits above the ring in the complexes to $Rb^+$ and $Cs^+$, **Figure 7.6–7.7**. At the B3LYP/def2-TZVPPD level of theory, M2($C_{3v}$) conformers are calculated to lie 3.1 and 7.5 kJ/mol higher in free energy for $Rb^+$ and $Cs^+$ than the ground–state M1 conformers, respectively. The Rb1($C_s$) conformer has an average $Rb^+$–S bond distance of 3.601 Å, whereas the Rb2($C_{3v}$) conformer has an average $Rb^+$–S bond distance of 3.493 Å. Smaller bond distances generally suggest tighter binding, but not for the $Rb^+$(ht18C6). Similarity, the Cs1($C_s$) conformer has an average $Cs^+$–S bond distance of 3.758 Å, whereas the Cs2($C_{3v}$) conformer has an average $Cs^+$–S bond distance of 3.676 Å. For $Rb^+$(ht18C6), the Rb3($D_{3d}$) conformer is calculated to lie 261.7 kJ/mol higher in free energy than the ground–state Rb1($C_s$) conformer, with an average $Rb^+$–S bond distance of 3.096 Å. For $Cs^+$(ht18C6), the Cs3($D_{3d}$) conformer is calculated to lie 338.4 kJ/mol higher in free energy than the ground–state Cs1($C_s$) conformer, with an average $Cs^+$–S bond distance of 3.216 Å. The smallest average $M^+$–S bond distances are found for the M3($D_{3d}$) conformer. An imaginary frequency corresponding to a ring-breathing mode in which the metal cation moves up and down in the center of the ring as the ring expands and contracts, respectively is observed for the M3($D_{3d}$) conformer. Again, calculations were performed using tight convergence, but attempts failed to eliminate the imaginary frequency.

### 7.4.3.2.3. $Na^+$(ht18C6)

The low-energy conformers of the $Na^+$(ht18C6) complex at the B3LYP level of theory parallel those found for the complexes of the larger alkali metal cations, **Figures 7.5** and **7.8**. As shown in **Figure 7.8**, conformers Na1($C_s$) and Na2($S_6$) are of similar stability (free energy) only differing by 2.1 kJ/mol. At 0 K Na1($C_s$) is the ground-state conformation, whereas Na2($S_6$) is more stable at 298 K. For the Na2($S_6$) conformation, the average $Na^+$–S bond distance is 3.149 Å, suggesting a more weakly bound complex than the Na1($C_s$) conformation where the average $Na^+$–S bond distance is 2.853 Å. The next most stable conformer of the $Na^+$(ht18C6) complex was found to have $C_{2h}$ symmetry, Na3($C_{2h}$) and was calculated to lie 66.4 kJ/mol higher in free energy than the Na2 conformer with corresponding $Na^+$–S average bond distances of 2.742 Å. Parallel to that found for the M3($C_{2h}$) conformers of the larger alkali metal cations, the shortest average bond distances are found for the Na3($C_{2h}$) conformer and also possesses an imaginary frequency corresponding to a ring-breathing mode in which the metal cation moves up and down in the center of the ring as the ring expands and contracts. In contrast to the complexes to the larger alkali metal cations, the Na4 conformer has no imaginary frequencies. Again, calculations were performed using tight convergence, but attempts failed to eliminate the imaginary frequency.

## 7.5. Discussion

### 7.5.1. Comparison of Theory and Experiment

The experimentally measured and theoretically calculated $M^+$–ht18C6 BDEs are summarized in **Table 7.2**, whereas the agreement between the calculated and measured BDEs is illustrated in **Figure 7.9**. As can be seen in the figure, the B3LYP/def2-TZVPPD values exhibit very good agreement with the measured values. The mean absolute deviation (MAD) between theory and experiment is 7.9 ± 5.5 kJ/mol, and only roughly differs from the average experimental uncertainty (AEU) in these values, 6.7 ± 2.3 kJ/mol, by 1.2 kJ/mol. The agreement between B3LYP/6-311+G(2d,2p)_HW theory and the measured $M^+$–da18C6 BDEs is not as good, **Table 7.2** and **Figure 7.9**, where the MAD is 14.5 ± 9.7 kJ/mol, roughly double the AEU in these measurements. When the measured BDEs are compared to the those calculated at the MP2(full)/def2-TZVPPD level of theory, the MAD is 15.7 ± 11.9 kJ/mol, almost double the AEU in these values. In contrast, the MAD improves to 8.7 ± 2.8 kJ/mol for values calculated at the

MP2(full)/6-311+G(2d,dp)_HW level of theory, which compares well to the AEU in these values. Clearly, the best agreement between the measured and calculated $M^+$–da18C6 BDEs is found for the B3LYP/def2-TZVPPD results for all four alkali metal cations. In contrast, at the MP2(full)/def2-TZVPPD level of theory, the calculated BDEs are systematically high except for the $Na^+$(ht18C6) complex, where excellent agreement is found.

### 7.5.2. Trends in the Binding of Alkali Metal Cations to da18C6

The measured $M^+$–ht18C6 BDEs at 0 K are summarized in **Table 7.2** and shown pictorially in **Figure 7.10**. As the size of the alkali metal cation increases from $Na^+$ to $Cs^+$, the $M^+$–da18C6 BDEs are found to decrease monotonically, similar to behavior observed for many alkali metal cation-ligand complexes [9, 11–32]. This is the expected trend for binding based primarily on electrostatic interactions, because the increasing size of the alkali metal cation leads to longer metal-ligand bond distances [33]. The relative change in the ionic radii for the alkali metal cations becomes smaller with increasing size of the cation such that the difference in the $M^+$–ht18C6 BDEs for adjacent metal cations becomes smaller as the size of the metal cation increases from $Na^+$ to $Cs^+$. The relative trend in the gas phase for alkali metal cation binding to ht18C6 is $Na^+ > K^+ > Rb^+ > Cs^+$.

### 7.5.3. Comparison with 18C6

The TCID measured and B3LYP/def2-TZVPPD and MP2(full)/def2-TZVPPD calculated $M^+$–ht18C6 and $M^+$–18C6 BDEs [11,13] are compared in **Figure 7.11a**. Experimentally, alkali metal cation interactions have strong preference for 18C6 as compared to ht18C6. In contrast, both the B3LYP and MP2(full) levels of theory suggest that the alkali metal cations bind to 18C6 more strongly than ht18C6, and that the preference for 18C6 should increase slightly with the size of the alkali metal cation. Similar results were found for ha18C6, where theory suggests that the alkali metal cations should bind to 18C6 more strongly than ha18C6 and that the preference for 18C6 should increase with the size of the alkali metal cation [11]. The result of this study suggest that theory either overestimates the strength of interaction with oxygen donor atoms or underestimates the strength of binding to sulfur donor atoms.

### 7.5.4. Comparison with ha18C6

The measured and B3LYP/def2-TZVPPD calculated $M^+$-ht18C6 and $M^+$-ha18C6 BDEs [11] are compared in **Figure 7.11b**. Experimentally, in all cases preferential binding of the alkali metal cations to ha18C6 over ht18C6 is observed. B3LYP results reproduce the experimental trend, whereas the MP2(full) results suggest that the larger alkali metal cation $Cs^+$ binding is equivalent to ha18C6 as compared to ht18C6. This trend is slightly reproduced in the experiments, where the larger alkali metal cation $Cs^+$ are found to bind to ha18C6 slightly more strongly than ht18C6. However, the differences are small and within experimental error.

## 7.6. Conclusions

Thresholds for the loss of the intact ht18C6 ligand determined from the kinetic energy dependence of the collision-induced dissociation of four $M^+$(ht18C6) complexes, where M+ = $Na^+$, $K^+$, $Rb^+$, and $Cs^+$, with Xe were determined. The effects of the kinetic and internal energy distributions of the $M^+$(ht18C6) and Xe reactants, multiple collisions with Xe, and the lifetime of the activated $M^+$(ht18C6) complexes using a loose PSL TS model were carefully considered to ensure accurate modeling of the experimental data. Theoretical calculations were performed at several levels of theory; B3LYP/def2-TZVPPD provides the best results and is therefore used for data analysis. Excellent agreement between the B3LYP/def2-TZVPPD calculated and experimentally determined BDEs was found for all four complexes, similar to the $M^+$(ta12C4) [12] and $M^+$(ha18C6) [11] complexes investigated using parallel approaches. Trends based primarily on electrostatic interactions are observed for the measured and theoretically calculated $M^+$-ht18C6 BDEs. The BDEs decrease monotonically as the size of the alkali metal cation increases. When compared to the analogous 18C6 and ha18C6, preferential binding of the alkali metal cations to 18C6 and ha18C6 over ht18C6 was observed.

## 7.7. References

[1] L.F. Lindoy, The Chemistry of Macrocyclic Ligand Complexes; Cambridge University Press, Cambridge, 1989, p. 13.

[2] Y. Chen, M.T. Rodgers, J. Am. Chem. Soc. 134 (2012) 2313

[3] HyperChem Molecular Modeling Software Package, Version 7.5; Hypercube Inc.: Gainesville, FL, 2002.

[4] Frisch, M. J.; et al. Gaussian 09, revision A.1; Gaussian, Inc.: Wallingford CT, 2009.

[5] J.B. Foresman, M.J. Frisch, Exploring Chemistry with Electronic Structure Methods, 2nd ed, Gaussian; Pittsburgh, 1996, p. 64.

[6] S.F. Boys, R. Bernardi, Mol. Phys. 19 (1979) 553.

[7] F.B. van Duijneveldt, J.G.C.M. van Duijneveldt-van de Rijt, J.H. van Lenthe, Chem. Rev. 94 (1994) 1873.

[8] S.M. Smith, A.N. Markevitch, D.A. Romanov, X. Li, R.J. Levis, H.B. Schlegel, J. Phys. Chem. A 108 (2004) 11063.

[9] M.T. Rodgers, P.B. Armentrout, Mass Spectrom. Rev. 19 (2000) 215.

[10] M.T. Rodgers, K.M. Ervin, P.B. Armentrout, J. Chem. Phys. 106 (1997) 4499.

[11] C.A. Austin, M.T. Rodgers, J. Phys. Chem. A 118 (2014) 5488.

[12] C.A. Austin, Y. Chen, M.T. Rodgers, Int. J. Mass Spectrom. 330-332 (2012) 27.

[13] M.B. More, D. Ray, P.B. Armentrout, J. Am. Chem. Soc. 121 (1999) 417.

[14] D. Ray, D. Feller, M.B. More, E.D. Glendening, P.B. Armentrout, J. Phys. Chem. 100 (1996) 16116.

[15] M.B. More, D. Ray, P.B. Armentrout, J. Phys. Chem. A 101 (1997) 831.

[16] M.B. More, D. Ray, P.B. Armentrout, J. Phys. Chem. A 101 (1997) 4254.

[17] M.B. More, D. Ray, P.B. Armentrout, J. Phys. Chem. A 101 (1997) 7007.

[18] P.B. Armentrout, C.A. Austin, M.T. Rodgers, Int. J. Mass Spectrom. 330-332 (2012) 16.

[19] P.B. Armentrout, C.A. Austin, M.T. Rodgers, J. Phys. Chem. A (2014), doi:http://dx.doi.org/10.1021/jp4116172 Articles ASAP.

[20] J.R. Hartman, R.E. Wolf, B.M. Foxman, S.R. Copper, J. Am. Chem. Soc. 105 (1983) 131.

[21] M.A. Santos, M.G.B. Drew, J. Chem. Soc., Faraday Trans. 87 (1991)1321.

[22] M.G.B. Drew, M.A. Santos, Struct. Chem. 4 (1993) 5.

[23] M.A.A.F. de C.T. Corrondo, V. Félix, M.T. Durate, M.A. Santos, Poly-hedron 12 (1993) 931.

[24] M. Morooka, S. Ohba, K. Toriumi, Acta Crystallogr. Sect. B 48 (1992) 459.

[25] L. Ballester, A. Gutiérrez, M.F. Perpiñán, A.E. Sánchez, M. Fonari, M. Gdaniec, Inorg. Chem. 46 (2007) 3946.

[26] M.T. Rodgers, J. Phys. Chem. A 105 (2001) 2374.

[27] M.T. Rodgers, P.B. Armentrout, J. Am. Chem. Soc. 122 (2000) 8548.

[28] R. Amunugama, M.T. Rodgers, Int. J. Mass Spectrom. 195-196 (2000) 439.

[29] M.T. Rodgers, J. Phys. Chem. A 105 (2001) 8145.

[30] H. Huang, M.T. Rodgers, J. Phys. Chem. A 106 (2002) 4277.

[31] R. Amunugama, M.T. Rodgers, J. Phys. Chem. A 106 (2002) 9092.

[32] R. Amunugama, M.T. Rodgers, J. Phys. Chem. A 106 (2002) 9718.

[33] R.G. Wilson, G.R. Brewer, Ion Beams: With Applications to Ion Implantation, Wiley, New York, 1973, pp. 118–124.

**Table 7.1.** Fitting Parameters of Equation (S1), Threshold Dissociation Energies at 0 K, and Entropies of Activation at 1000 K of $M^+$(ht18C6) Complexes[a]

| $M^+$ | $\sigma_0$ | $n$ | $E_0$[b] (eV) | $E_0$(PSL) (eV) | Kinetic Shift (eV) | $\Delta S^\dagger$(PSL) (J $mol^{-1}$ $K^{-1}$) |
|---|---|---|---|---|---|---|
| $Na^+$ | 22.20 (2.7) | 1.2 (0.1) | 5.38 (0.17) | 2.72 (0.10) | 2.66 | 112 (2) |
| $K^+$ | 163.14 (18.1) | 1.2 (0.1) | 3.52 (0.04) | 1.84 (0.07) | 1.68 | 80 (2) |
| $Rb^+$ | 102.79 (10.8) | 1.4 (0.1) | 3.15 (0.08) | 1.70 (0.06) | 1.45 | 82 (2) |
| $Cs^+$ | 44.15 (5.1) | 1.7 (0.1) | 2.45 (0.06) | 1.44 (0.05) | 1.01 | 76 (2) |

[a] Present results, uncertainties are listed in parentheses. Average values for a loose PSL TS. [b] No RRKM analysis.

**Table 7.2.** Bond Dissociation Enthalpies of $M^+$(ht18C6) Complexes at 0 K in kJ/mol[a]

| $M^+$ | TCID | B3LYP[b] | | | MP2[c] | | |
|---|---|---|---|---|---|---|---|
| | | $D_e$ | $D_0$[d] | $D_{0,BSSE}$[d,e] | $D_e$ | $D_0$[d] | $D_{0,BSSE}$[d,e] |
| $Na^+$ | 262.6 (10.0) | 256.8 | 250.9 | 248.8 | 290.1 | 284.2 | 260.4 |
| | | *264.5* | *259.6* | *252.0* | *287.3* | *282.4* | *251.2* |
| $K^+$ | 177.7 (6.3) | 186.0 | 182.3 | 179.7 | 214.1 | 209.8 | 180.3 |
| | | *188.5* | *184.4* | *180.3* | *204.4* | *200.2* | *182.9* |
| $Rb^+$ | 163.8 (5.8) | 157.1 | 153.4 | 152.7 | 205.5 | 201.7 | 178.1 |
| | | *147.0* | *144.2* | *141.9* | *178.5* | *175.7* | *153.2* |
| $Cs^+$ | 138.4 (4.8) | 137.7 | 134.4 | 133.9 | 189.5 | 186.2 | 169.5 |
| | | *121.0* | *118.4* | *115.6* | *156.1* | *153.5* | *130.7* |
| MAD[f] | 6.7 (2.3)[g] | | 7.7 (3.9) | 7.9 (5.5) | | | 15.7 (11.9) |
| | | | | *14.5 (9.7)* | | | *8.7 (2.8)* |

[a] Present results, uncertainties are listed in parentheses. [b] Calculated at B3LYP/def2-TZVPPD and *B3LYP/6-311+G(2d,2p)_HW//B3LYP/6-31+G*_HW* levels of theory. [c] Calculated at MP2(full)/def2-TZVPPD//B3LYP/def2-TZVPPD and *MP2(full)/6-311+G(2d,2p)_HW //B3LYP/ 6-31+G*_HW* levels of theory. [d] Including ZPE corrections with the B3LYP/6-31+G*_HW and B3LYP/def2-TZVPPD frequencies scaled by a factor of 0.9804. [e] Also includes BSSE corrections. [f] Mean absolute deviation. [g] Average experimental uncertainty.

**Table 7.3.** Geometrical Parameters of the B3LYP/def2-TZVPPD Optimized Structures of Neutral and $M^+$(ht18C6) Complexes.[a]

| $M^+$ | Conformer | Symm | r(M–S) (Å) | ∠SMS (°) | ∠CSC (°) | ∠SCCS (°) | ∠CSCC (°) |
|---|---|---|---|---|---|---|---|
| ht18C6 | C1 | $C_i$ | - | - | 108.8 | 145.9 | 175.9 |
| $Na^+$ | Na1 | $C_s$ | 2.853 | 77.2 | 105.6 | 57.8 | 103.2 |
| | Na2 | $S_6$ | 3.149 | 64.3 | 100.6 | 64.3 | 167.0 |
| | Na3 | $C_{2h}$ | 2.742 | 82.4 | 110.4 | 42.6 | 79.7 |
| $K^+$ | K1 | $C_1$ | 3.445 | 60.0 | 101.6 | 65.9 | 144.4 |
| | K2 | $S_6$ | 3.271 | 64.4 | 102.3 | 72.2 | 166.0 |
| | K3 | $C_{2h}$ | 2.979 | 78.1 | 114.7 | 40.8 | 83.4 |
| $Rb^+$ | Rb1 | $C_s$ | 3.601 | 57.5 | 102.0 | 66.7 | 143.7 |
| | Rb2 | $C_{3v}$ | 3.493 | 58.1 | 102.0 | 65.7 | 166.8 |
| | Rb3 | $D_{3d}$ | 3.096 | 76.6 | 116.7 | 40.2 | 84.0 |
| $Cs^+$ | Cs1 | $C_s$ | 3.758 | 55.0 | 101.3 | 66.9 | 142.1 |
| | Cs2 | $C_{3v}$ | 3.676 | 54.3 | 101.8 | 63.3 | 163.1 |
| | Cs3 | $D_{3d}$ | 3.216 | 75.3 | 118.8 | 40.1 | 83.8 |

[a] Average values are given for similar bond distances or angles, and represents the absolute average.

**Table 7.4.** Enthalpies and Free Energies of $M^+$ Binding to ht18C6 at 298 K in kJ/mol[a]

| $M^+$(ht18C6) | $\Delta H_0$ | $\Delta H_0{}^b$ | $\Delta H_{298} - \Delta H_0{}^b$ | $\Delta H_{298}$ | $\Delta H_{298}{}^b$ | $T\Delta S_{298}{}^b$ | $\Delta G_{298}$ | $\Delta G_{298}{}^b$ |
|---|---|---|---|---|---|---|---|---|
| $Na^+$(ht18C6) | 262.6 (10.0) | 248.8 | 5.4 (1.3) | 268.0 (10.1) | 254.2 | 42.9 (2.7) | 225.1 (10.4) | 211.3 |
| $K^+$(ht18C6) | 177.7 (6.3) | 179.7 | 3.0 (0.8) | 180.7 (6.4) | 182.7 | 35.7 (3.6) | 145.0 (7.3) | 147.6 |
| $Rb^+$(ht18C6) | 163.8 (5.8) | 152.7 | 2.5 (0.8) | 166.3 (5.9) | 155.2 | 37.9 (3.6) | 128.4 (6.9) | 117.3 |
| $Cs^+$(ht18C6) | 138.4 (4.8) | 133.9 | 2.1 (0.6) | 140.5 (4.8) | 136.0 | 36.2 (7.0) | 104.4 (8.5) | 99.9 |

[a] Present results, uncertainties are listed in parentheses. [b] Density functional theory calculations at the B3LYP/def2-TZVPPD level of theory with frequencies scaled by 0.98.

## Figure Captions

**Figure 7.1.** Structure of ht18C6. B3LYP/def2-TZVPPD optimized structures and relative energies at 0 K (in kJ/mol) of the stable low-energy conformations of ht18C6. The calculated dipole moments (μ) are also shown.

**Figure 7.2.** Cross section for collision-induced dissociation of $K^+$(ht18C6) with Xe as a function of kinetic energy in the center-of-mass frame (lower *x*-axis) and the laboratory frame (upper *x*-axis). Data are shown for a Xe pressure of ~0.2 mTorr, part a. Zero-pressure extrapolated cross section for collision-induced dissociation of the $K^+$(ht18C6) complex with Xe in the threshold region as a function of kinetic energy in the center-of-mass frame (lower *x*-axis) and the laboratory frame (upper *x*-axis). The solid line shows the best fit to the data using the model of Eq (2.4) convoluted over the neutral and ion kinetic and internal energy distributions. The dashed line shows the model cross section in the absence of experimental kinetic energy broadening for reactants with an internal temperature of 0 K, part b.

**Figure 7.3.** Cross sections for collision-induced dissociation of $M^+$(ht18C6) complexes, where $M^+ = Na^+$, $K^+$, and $Cs^+$, with Xe as a function of kinetic energy in the center-of-mass frame (lower *x*-axis) and the laboratory frame (upper *x*-axis). Data are shown for a Xe pressure of ~0.2 mTorr, parts a-c, respectively. Zero-pressure extrapolated cross sections for collision-induced dissociation of $M^+$(ht18C6) complexes, where $M^+ = Na^+$. $K^+$, and $Cs^+$, parts d-f respectively. The solid lines show the best fits to the data using the model of Eq. (2.4) convoluted over the neutral and ion kinetic and internal energy distributions. The dashed lines show the model cross sections in the absence of experimental kinetic energy broadening for reactants with an internal temperature of 0 K.

**Figure 7.4.** B3LYP/def2-TZVPPD optimized geometries, relative energies at 0 K, and *Gibbs free energies at 298 K* (in kJ/mol) of the stable low-energy conformers of the $K^+$(ht18C6) complex.

**Figure 7.5.** B3LYP/def2-TZVPPD optimized geometries, relative energies at 0 K, and *Gibbs free energies at 298 K* (in kJ/mol) of the stable low-energy conformers of the $Na^+$(ht18C6) complex.

**Figure 7.6.** B3LYP/def2-TZVPPD optimized geometries, relative energies at 0 K, and *Gibbs free energies at 298 K* (in kJ/mol) of the stable low-energy conformers of the $Rb^+$(ht18C6) complex.

**Figure 7.7.** B3LYP/def2-TZVPPD optimized geometries, relative energies at 0 K, and *Gibbs free energies at 298 K* (in kJ/mol) of the stable low-energy conformers of the $Cs^+$(ht18C6) complex.

**Figure 7.8.** Variation in the relative energies at 0 K and Gibbs free energies at 298 K (in kJ/mol) of the four most stable conformations of the $M^+$(ht18C6) complexes as a function of the alkali metal cation calculated at the B3LYP/def2-TZVPPD level of theory.

**Figure 7.9.** B3LYP and MP2(full) calculated versus TCID measured $M^+$–ht18C6 BDEs at 0 K (in kJ/mol), where $M^+ = Na^+$, $K^+$, $Rb^+$, and $Cs^+$. Single point energies calculated using the def2-TZVPPD (part a) and 6-311+G(2d,2p)_HW (part b) basis sets and the def2-TZVPPD and 6-31+G* optimized geometries of the ground-state conformers, respectively. All values are determined here and taken from **Table 7.2**.

**Figure 7.10.** Measured and theoretically determined BDEs at 0 K (in kJ/mol) of the $M^+$(ht18C6), $M^+$(18C6), and $M^+$(ha18C6).

**Figure 7.11.** BDEs at 0 K (in kJ/mol) of the $M^+$(ht18C6), $M^+$(18C6), $M^+$(da18C6), and $M^+$(18C6) complexes plotted versus the ionic radius of $M^+$ (part a), and calculated BDEs at 0 K (in kJ/mol), using the B3LYP/def2-TZVPPD (part b), where $M^+$ = $Na^+$, $K^+$, $Rb^+$, and $Cs^+$. Ionic radii are taken from reference 45. All values for the $M^+$(ht18C6) complexes are determined here and taken from Table 2. Calculated values for the $M^+$–18C6 and $M^+$–ha18C6 BDEs are taken from reference [11] ($M^+$(ha18C6 TCID)). The measured values for the $M^+$–ha18C6 BDEs are taken from reference [11] ($M^+$(ha18C6 TCID)). Measured values for the $M^+$–18C6 BDEs are taken from reference 13(Armentrout). Measured and calculated values for the $M^+$–da18C6 BDEs are taken from reference [14] ($M^+$(da18C6 TCID)).

Figure 7.1.

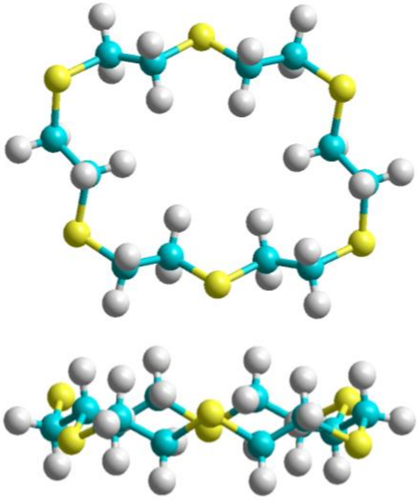

C1_$C_i$
0.0 kJ/mol
$\mu = 0.0$ D

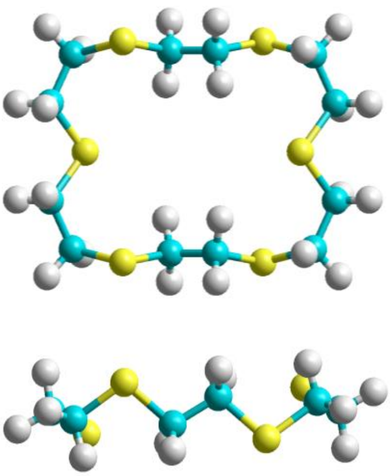

C2_$C_{2h}$
28.7 kJ/mol
$\mu = 0.0$ D

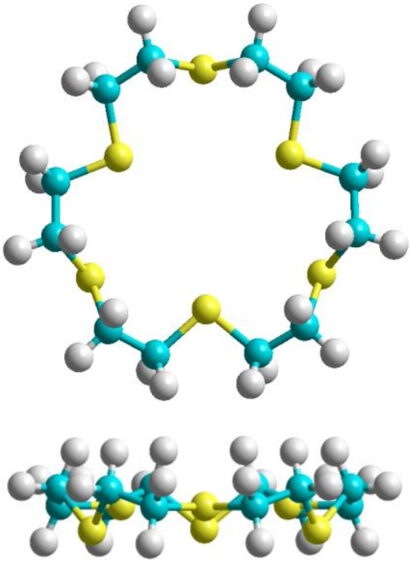

C3_$C_3$
56.1 kJ/mol
$\mu = 4.55$ D

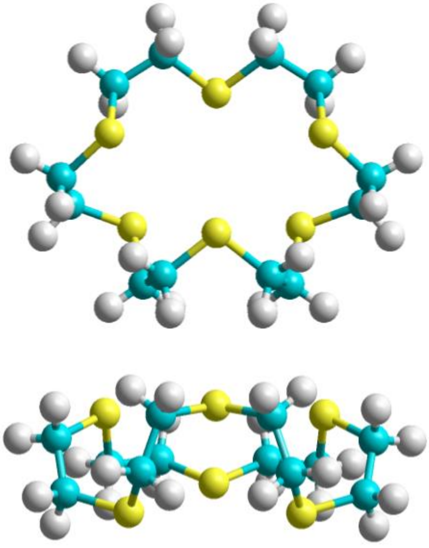

C4_$C_s$
76.8 kJ/mol
$\mu = 0.96$ D

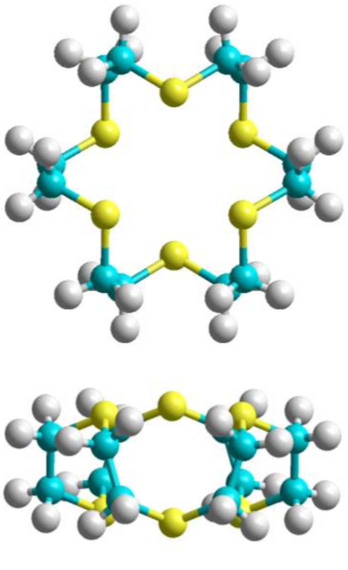

C5_$D_{3d}$
106.7 kJ/mol
$\mu = 0.0$ D

Hexathia-18-crown-6 (ht18C6)
1,4,7,10,13,16-hexathiacyclooctadecane

Figure 7.2.

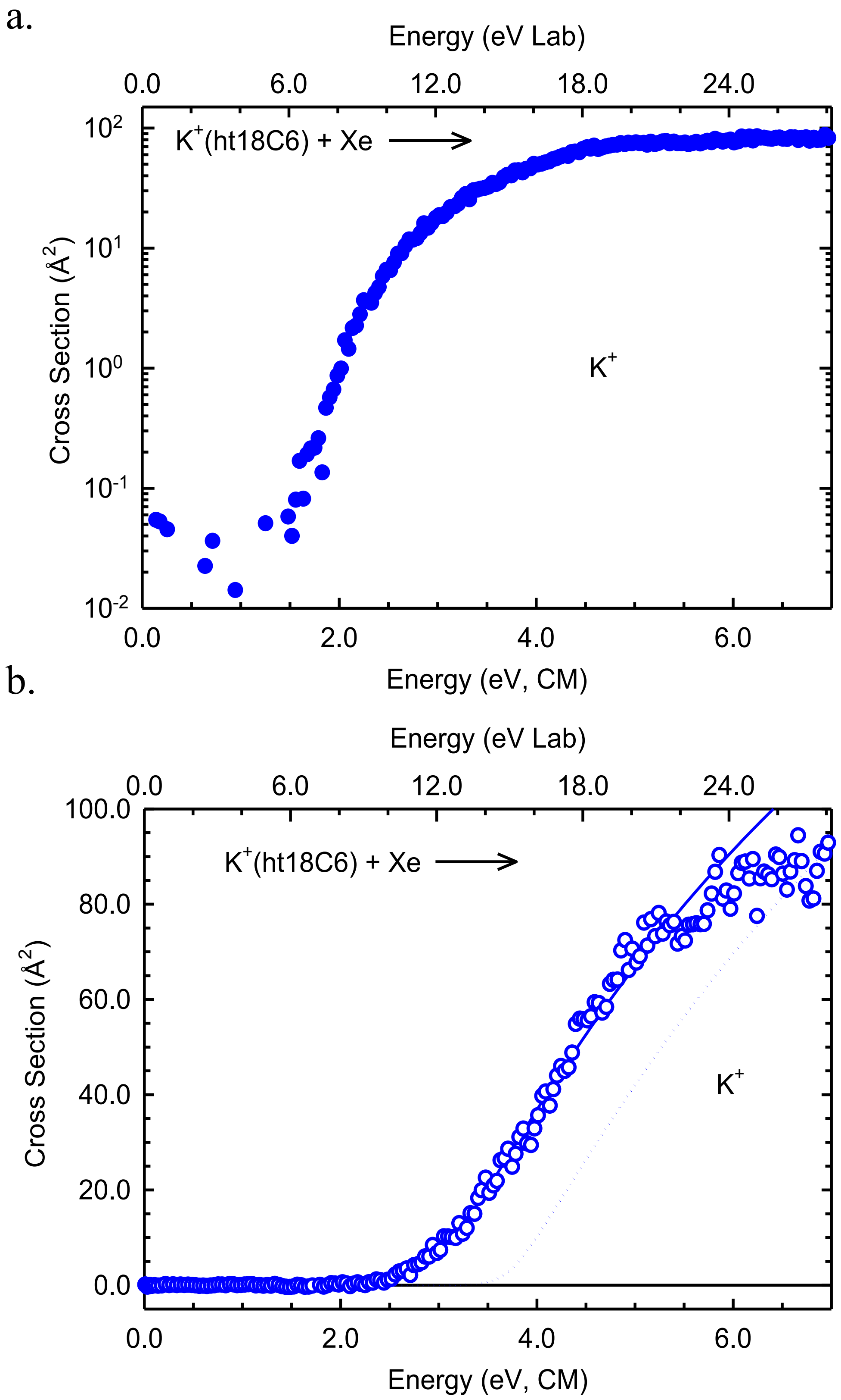
a.
Energy (eV Lab)
0.0
6.0
12.0
18.0
24.0
$10^2$
$10^1$
$10^0$
$10^{-1}$
$10^{-2}$
Cross Section (Å$^2$)
$K^+$(ht18C6) + Xe
$K^+$
0.0
2.0
4.0
6.0
Energy (eV, CM)
b.
Energy (eV Lab)
0.0
6.0
12.0
18.0
24.0
100.0
80.0
60.0
40.0
20.0
0.0
Cross Section (Å$^2$)
$K^+$(ht18C6) + Xe
$K^+$
0.0
2.0
4.0
6.0
Energy (eV, CM)

Figure 7.3.

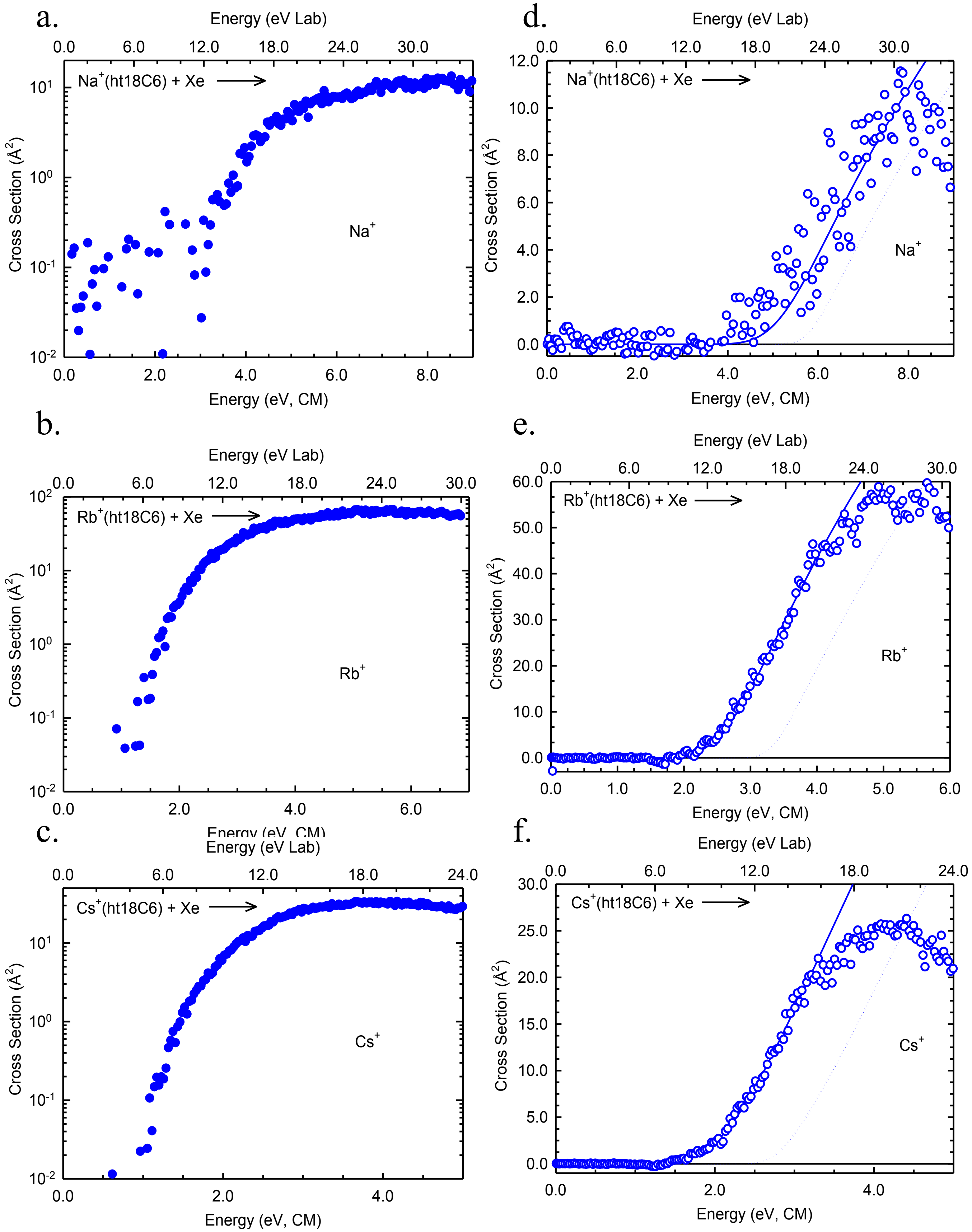
a.
Energy (eV Lab)
0.0
6.0
12.0
18.0
24.0
30.0
Na+(ht18C6) + Xe →
Na+
Cross Section (Å2)
10^1
10^0
10^-1
10^-2
0.0
2.0
4.0
6.0
8.0
Energy (eV, CM)
d.
Energy (eV Lab)
0.0
6.0
12.0
18.0
24.0
30.0
Na+(ht18C6) + Xe →
Na+
Cross Section (Å2)
12.0
10.0
8.0
6.0
4.0
2.0
0.0
0.0
2.0
4.0
6.0
8.0
Energy (eV, CM)
b.
Energy (eV Lab)
0.0
6.0
12.0
18.0
24.0
30.0
Rb+(ht18C6) + Xe →
Rb+
Cross Section (Å2)
10^2
10^1
10^0
10^-1
10^-2
0.0
2.0
4.0
6.0
Energy (eV, CM)
e.
Energy (eV Lab)
0.0
6.0
12.0
18.0
24.0
30.0
Rb+(ht18C6) + Xe →
Rb+
Cross Section (Å2)
60.0
50.0
40.0
30.0
20.0
10.0
0.0
0.0
1.0
2.0
3.0
4.0
5.0
6.0
Energy (eV, CM)
c.
Energy (eV Lab)
0.0
6.0
12.0
18.0
24.0
Cs+(ht18C6) + Xe →
Cs+
Cross Section (Å2)
10^1
10^0
10^-1
10^-2
0.0
2.0
4.0
Energy (eV, CM)
f.
Energy (eV Lab)
0.0
6.0
12.0
18.0
24.0
Cs+(ht18C6) + Xe →
Cs+
Cross Section (Å2)
30.0
25.0
20.0
15.0
10.0
5.0
0.0
0.0
2.0
4.0
Energy (eV, CM)

Figure 7.4.

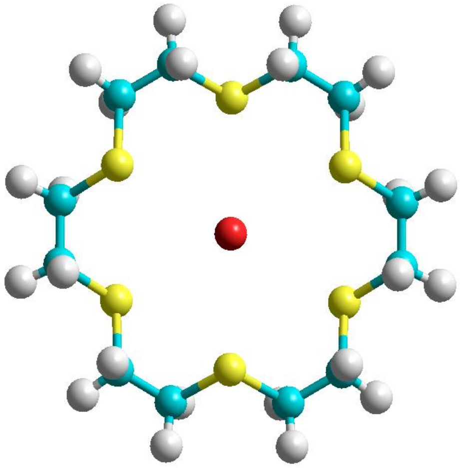

K$^+$– S = 3.271Å
∠SK$^+$S = 64.4°

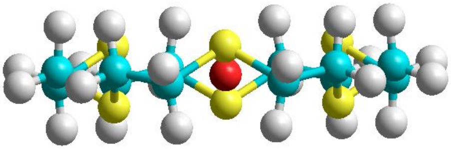

K2($S_6$)
0.0 (*4.3*) kJ/mol

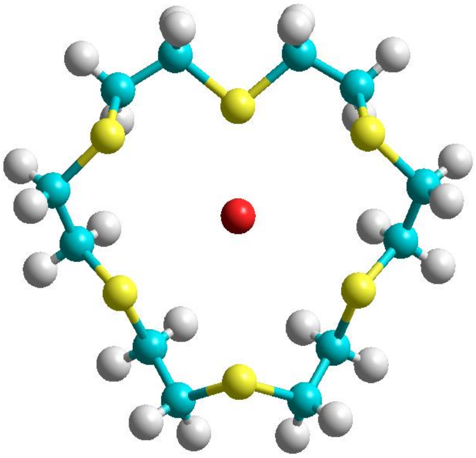

K$^+$– S = 3.445Å
∠SK$^+$S = 60.0°

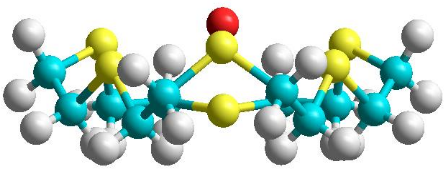

K1($C_1$)
3.4 (*0.0*) kJ/mol

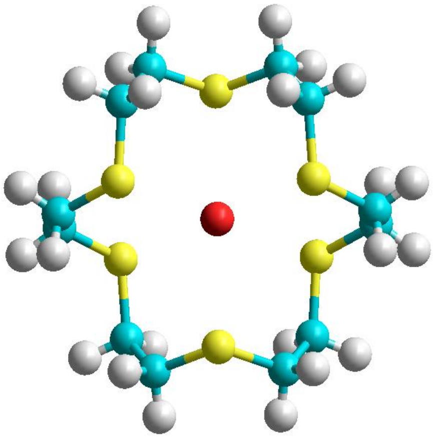

K$^+$– S = 2.979Å
∠SK$^+$S = 78.1°

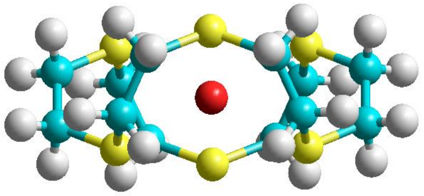

K3($C_{2h}$)
175.8 (*188.2*) kJ/mol
IF = 1

K$^+$(ht18C6)

Figure 7.5.

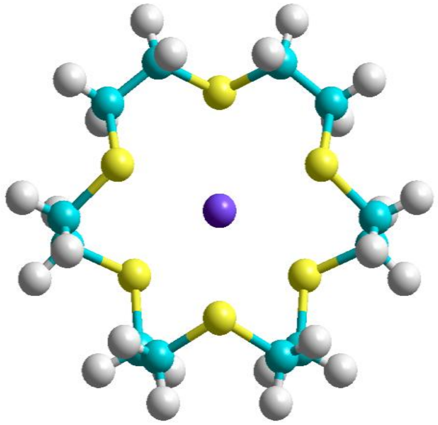

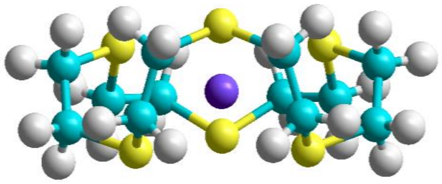

Na1($C_s$)
0.0 (*14.5*) kJ/mol

Na$^+$– S = 2.853Å
∠SNa$^+$S = 77.2°

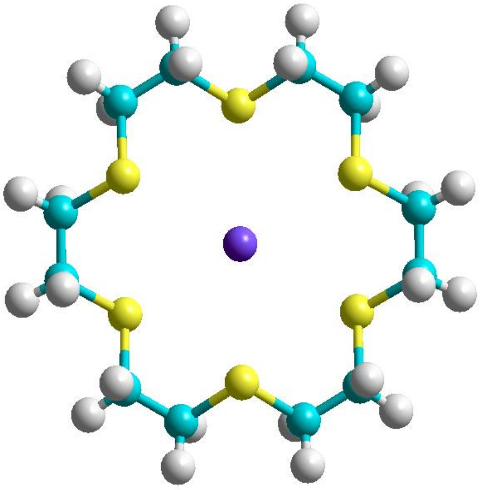

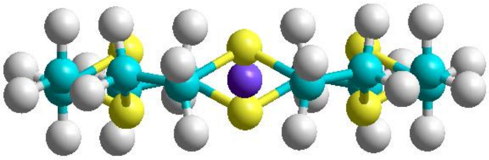

Na2($S_6$)
2.1 (*0.0*) kJ/mol

Na$^+$– S = 3.149Å
∠SNa$^+$S = 64.3°

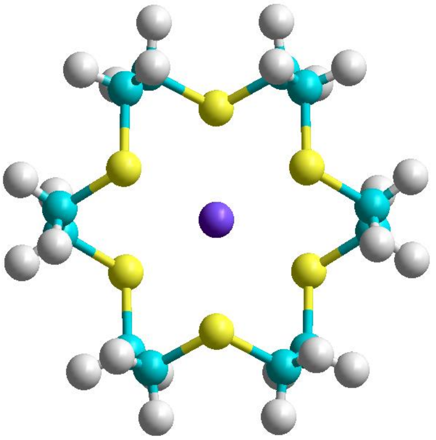

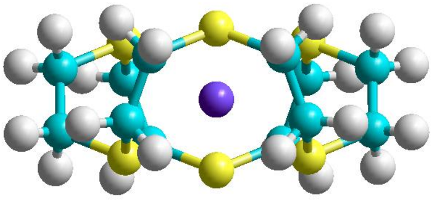

Na3($C_{2h}$)
46.7 (*66.4*) kJ/mol
IF = 1

Na$^+$– S = 2.742Å
∠SNa$^+$S =82.4°

Na$^+$(ht18C6)

Figure 7.6.

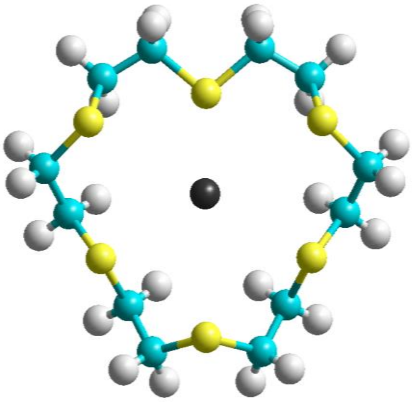

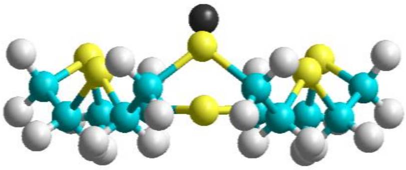

Rb1(C$_s$)
0.0 (*0.0*) kJ/mol

Rb$^+$– S = 3.601Å
∠SRb$^+$S = 57.5°

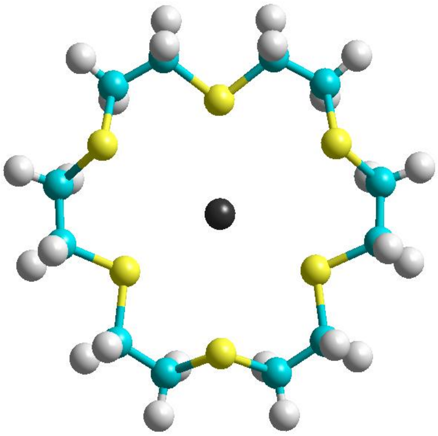

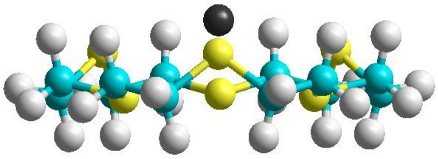

Rb2(C$_{3v}$)
4.3 (*3.1*) kJ/mol

Rb$^+$– S = 3.493Å
∠SRb$^+$S = 58.1°

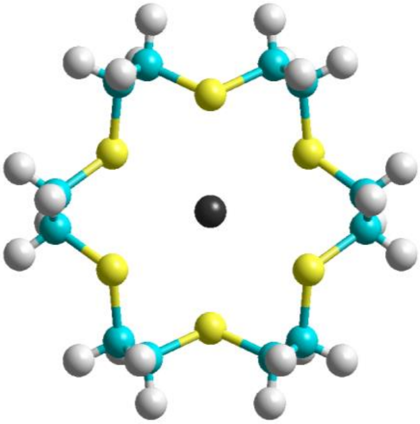

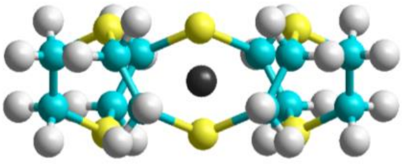

Rb3(D$_{3d}$)
248.9 (*261.7*) kJ/mol
IF = 1

Rb$^+$– S = 3.096Å
∠SRb$^+$S = 76.6°

Rb$^+$(ht18C6)

Figure 7.7.

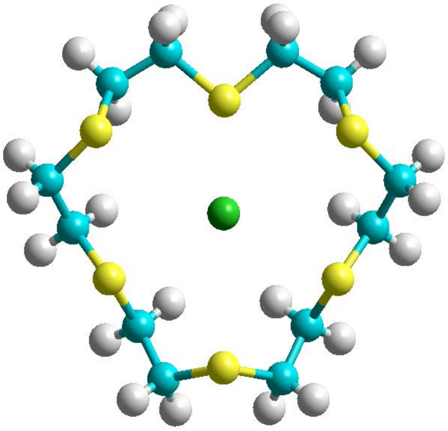

Cs$^+$– S = 3.758Å
∠SCs$^+$S = 55.0°

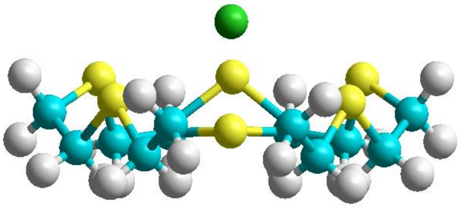

Cs1(C$_s$)
0.0 (*0.0*) kJ/mol

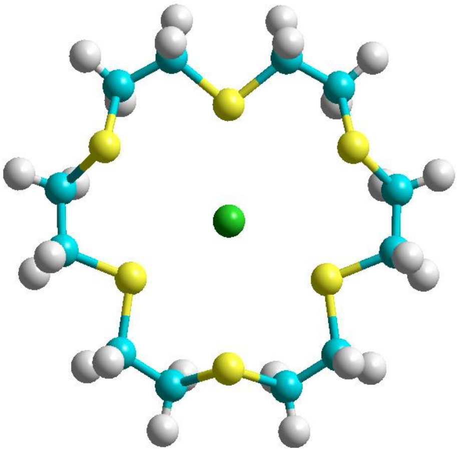

Cs$^+$– S = 3.676Å
∠SCs$^+$S = 54.3°

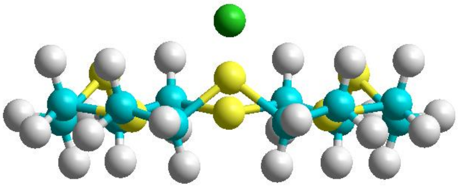

Cs2(C$_{3v}$)
6.9 (*7.5*) kJ/mol

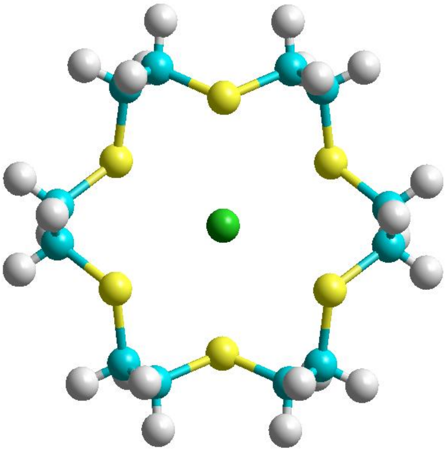

Cs$^+$– S = 3.216Å
∠SCs$^+$S =75.3°

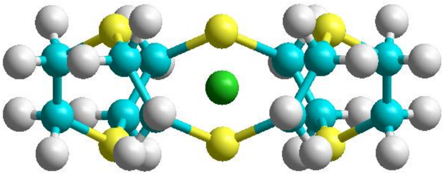

Cs3(D$_{3d}$)
337.7 (*338.4*) kJ/mol
IF = 1

Cs$^+$(ht18C6)

Figure 7.8.

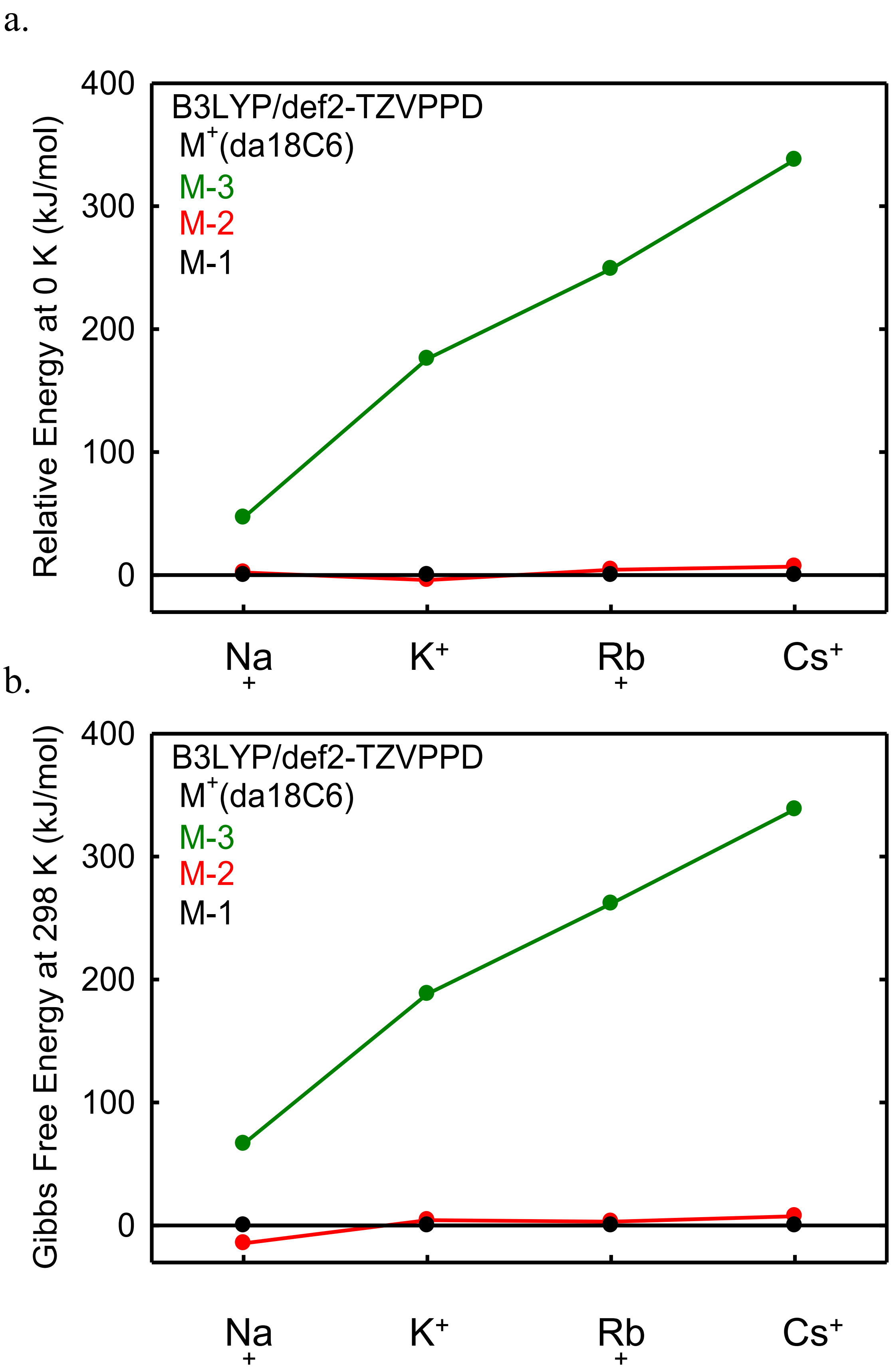
a.
B3LYP/def2-TZVPPD
M+(da18C6)
M-3
M-2
M-1
Relative Energy at 0 K (kJ/mol)
400
300
200
100
0
Na+
K+
Rb+
Cs+
b.
B3LYP/def2-TZVPPD
M+(da18C6)
M-3
M-2
M-1
Gibbs Free Energy at 298 K (kJ/mol)
400
300
200
100
0
Na+
K+
Rb+
Cs+

Figure 7.9.

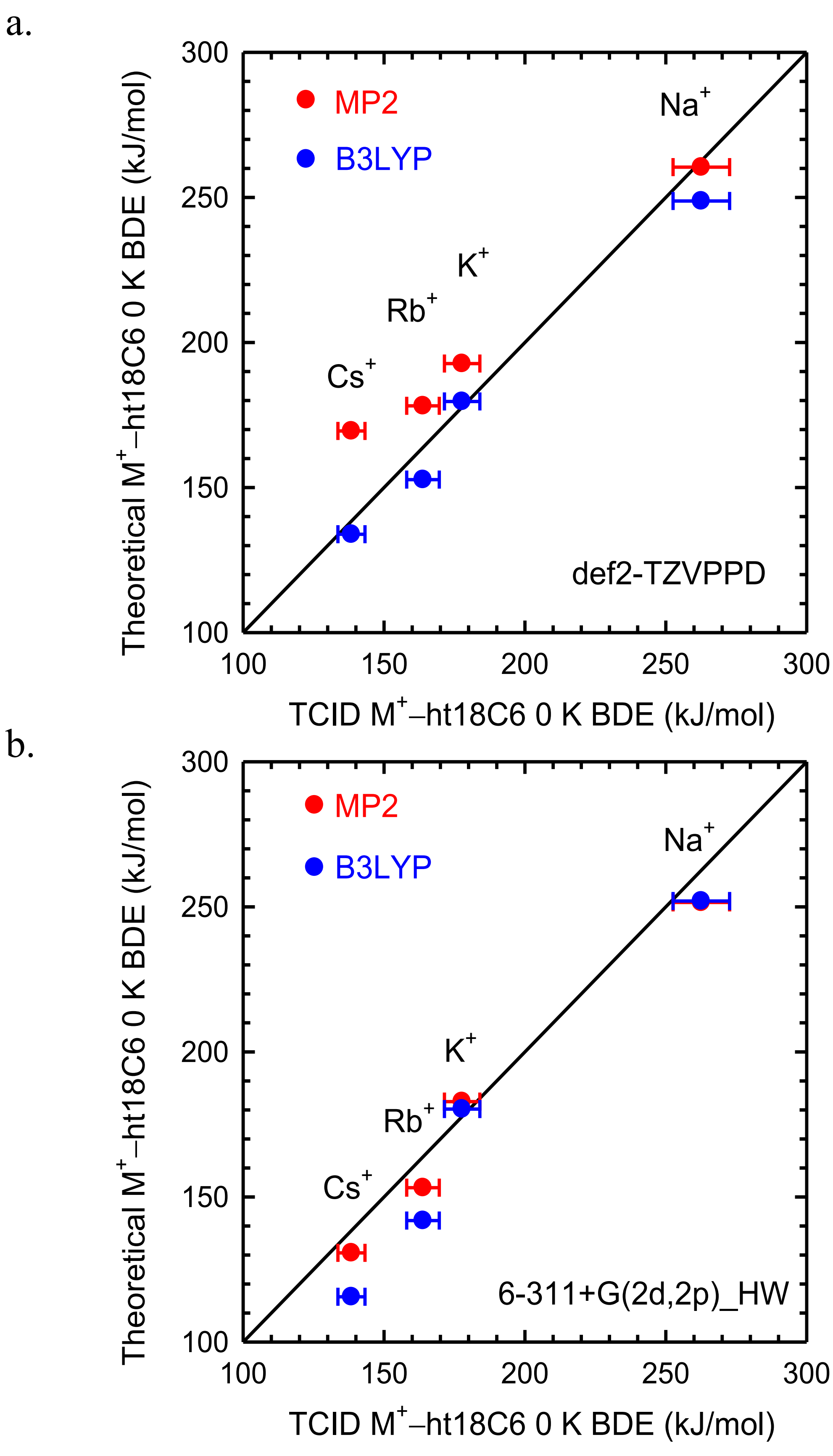
a.
MP2
B3LYP
Na$^+$
K$^+$
Rb$^+$
Cs$^+$
def2-TZVPPD
Theoretical M$^+$–ht18C6 0 K BDE (kJ/mol)
TCID M$^+$–ht18C6 0 K BDE (kJ/mol)
100
150
200
250
300
b.
MP2
B3LYP
Na$^+$
K$^+$
Rb$^+$
Cs$^+$
6-311+G(2d,2p)_HW
Theoretical M$^+$–ht18C6 0 K BDE (kJ/mol)
TCID M$^+$–ht18C6 0 K BDE (kJ/mol)
100
150
200
250
300

Figure 7.10.

a.

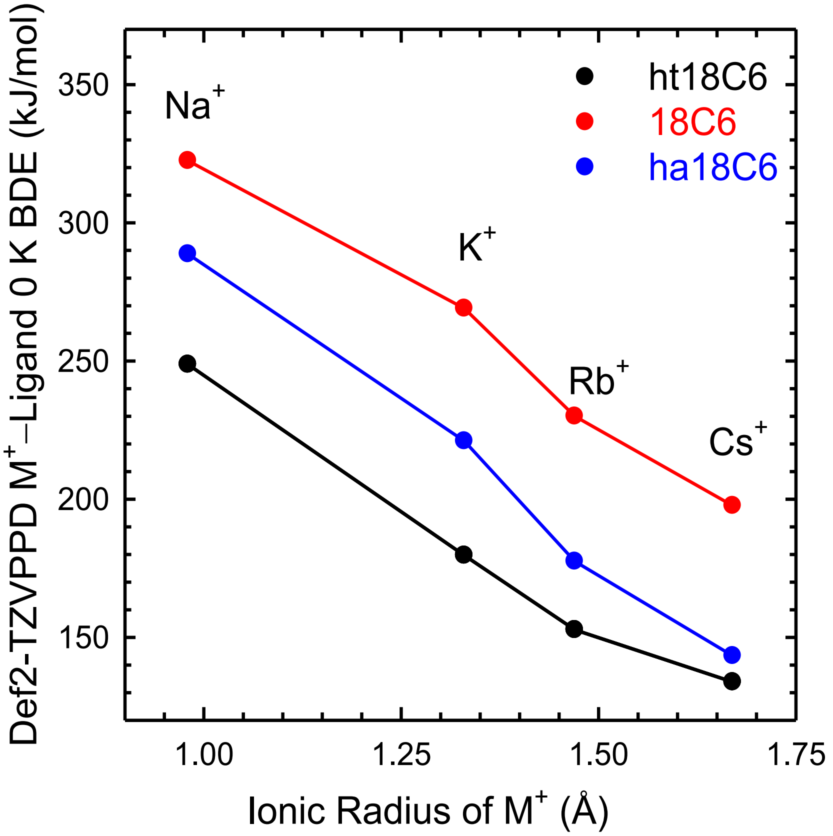

b.

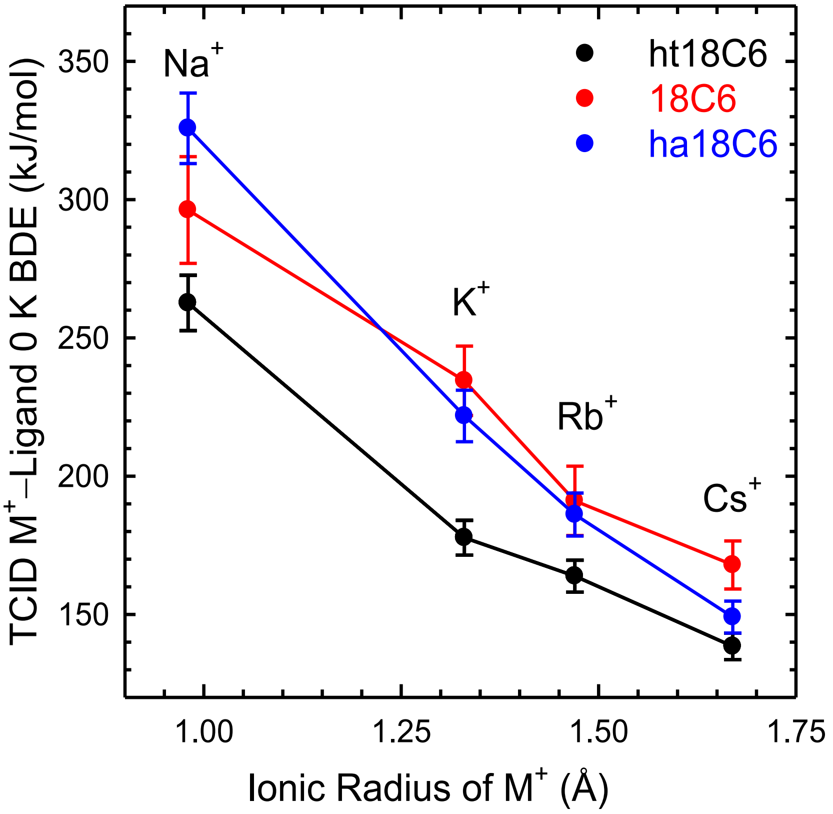

Figure 7.11.

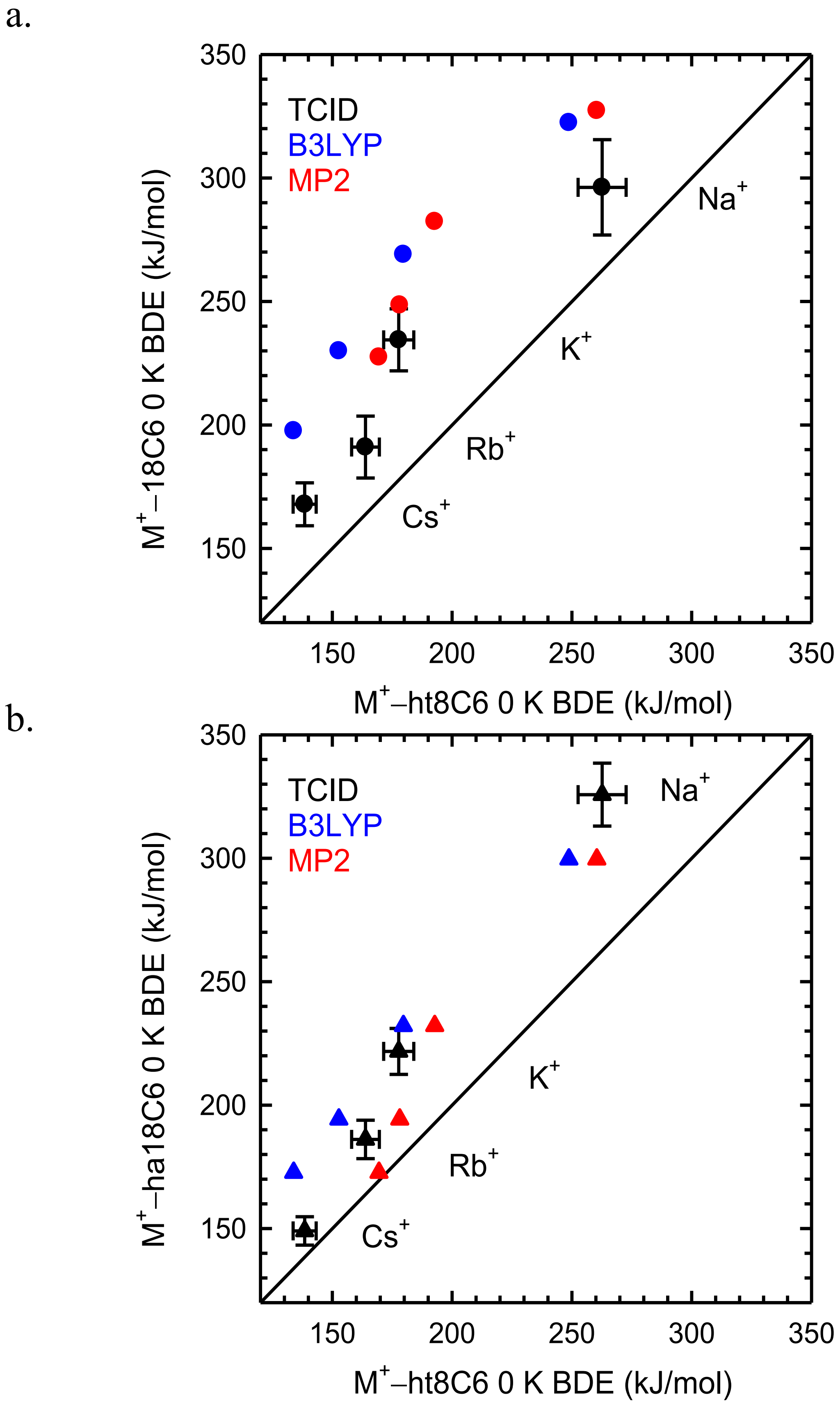
a.
TCID
B3LYP
MP2
Na$^+$
K$^+$
Rb$^+$
Cs$^+$
M$^+$–18C6 0 K BDE (kJ/mol)
150
200
250
300
350
M$^+$–ht8C6 0 K BDE (kJ/mol)
b.
TCID
B3LYP
MP2
Na$^+$
K$^+$
Rb$^+$
Cs$^+$
M$^+$–ha18C6 0 K BDE (kJ/mol)
150
200
250
300
350
M$^+$–ht8C6 0 K BDE (kJ/mol)

# CHAPTER 8

# CONCLUSIONS AND FUTUTRE WORK

## 8.1. Conclusion

Kinetic energy dependent cross sections for the interactions of the alkali metal cations ($Na^+$, $K^+$, $Rb^+$, and $Cs^+$) with cyclen, hexacyclen, diaza-18-crown-6, and hexathia-18-crown-6 were determined by collision-induced dissociation (CID), using a custom built guided ion beam tandem mass spectrometer (GIBMS). Complementary electronic structure theory calculations using B3LYP and MP2(full) functionals with the 6-31+G*_HW and def2-TZVPPD basis sets were preformed to determine the low-energy structures of the metal-ligand complexes and neutral ligand. Theoretical estimates of the strength of binding were calculated using B3LYP optimized structures with the 6-311+G(2d,2p)_HW and def2-TZVPPD basis set. These studies enable the characterization of the various binding geometries available to cation-macrocycle complexes and their relative stabilities as well as to accurately determine their absolute binding affinities metal-ligand complexes. The experimental and theoretical data has enabled the systematic evaluation of the effects of the size of the alkali metal cation, the nature and number of donor atoms, and the size of the macrocyclic ring has on the intrinsic binding interactions that control the geometry, and strength and selectivity of binding. In addition, using complementary infrared multiple photon dissociation (IRMPD) action spectroscopy experiments supported by theoretical electronic structure calculations, I was able to characterize the IR spectra of the cation-macrocycle complexes and definitively determine the structures of the complexes accessed under our experimental conditions.

In **Chapter 3**, simple CID leading to loss of the intact ta12C4 ligand was observed for all four alkali metal–ligand complexes. BDEs suggest that binding is based primarily on electrostatic interactions. The structures of the $M^+$(ta12C4) complexes are similar to those determined for the analogous $M^+$(12C4) complexes with only minor variations arising from the presence of the amino hydrogen atoms. Ta12C4 binds $Na^+$ more strongly than 12C4. In contrast, binding to $K^+$, $Rb^+$, and $Cs^+$ is slightly stronger to 12C4 than ta12C4. These results suggest that the N donor atoms of ta12C4 are more selective for hard metal cations whereas 12C4 is more selective for soft metal cations. In **Chapter 4**, IRMPD action spectra of alkali metal cation-ta12C4 complexes in the region extending from 600 to 1600 $cm^{-1}$ were obtained for four $M^+$(ta12C4) complexes where $M^+ = Na^+$, $K^+$, $Rb^+$, and $Cs^+$. For all four complexes, the loss of the intact neutral ta12C4 ligand was the only dissociation pathway observed, consistent with simple CID fragmentation behavior. Binding of alkali metal cations to ta12C4 produced similar IRMPD action spectra and yields for the $M^+$(ta12C4) complexes increased as the size the alkali metal cation increased, in accordance with the trends in the strength of alkali metal cation binding in these systems.

Spectral features in the IRMPD action spectra were retained throughout the entire series, while new spectral features were observed for the complexes to the larger alkali-metal cations. Comparison with IR spectra calculated at the B3LYP/def2-TZVPPD level of theory allowed the conformations present in the experiments to be identified. For the larger alkali metal cation $K^+$, $Rb^+$, and $Cs^+$, the IRMPD action spectrum was well reproduced by the calculated spectrum for the most-stable conformation, $C_4$(++++). Evidence for the presence of a minor population of excited conformations was observed for the complexes to $Rb^+$ and $Cs^+$.

In **chapter 5**, the CID behavior of the alkali metal cations interactions with hexacyclen (ha18C6) was investigated. Similar to what was observed for the ta12C4, the only dissociation pathway observed for all four complexes is loss of the intact ha18C6 ligand. Trends in the measured and calculated $M^+$–ha18C6 BDEs suggest that the binding is based primarily on electrostatic interactions as seen with ta12C4 ligand. For the larger alkali metal cations, $K^+$, $Rb^+$, and $Cs^+$, the nature of the binding to ha18C6 is similar, resulting in highly parallel stable low-energy conformations of these complexes. The ha18C6 ligand binds $Na^+$ more strongly than 18C6 as previously found for ta12C4 vs 12C4, whereas a slight preference for binding of 18C6 over ha18C6 to $K^+$, $Rb^+$, and $Cs^+$ is found, but this preference is smaller than the experimental error in these measurements for $K^+$ and $Cs^+$, suggesting that this binding preference is not very significant. Overall, the gas-phase trends in the binding further suggest that the N donors atoms of ha18C6 bind more strongly to hard metal cations, whereas the O donor atoms of 18C6 bind slightly more strongly to softer metal cations. In solvent, the binding interactions are weakened significantly, and the competition between the ha18C6 ligand and the solvent for the alkali metal cations leads to a change in the relative binding order, where ha18C6 is selective for $K^+$ over the other alkali metal cations. When the binding of the alkali metal cations to ha18C6 to ta12C4 are compared, binding of the alkali metal cations to ha18C6 is found to be 19 ± 6% stronger than to ta12C4, indicating that the number of donor atoms, the cavity size, and the flexibility of the ligand allow alkali metal cations to bind more strongly but that the enhancement in the binding falls off monotonically with each additional $M^+$–N interaction.

In **Chapter 6**, the mixed donor atom ligand diaza-18-crown-6 (da18C6) interactions with the alkali metal cations were investigated. As with the nitrogen donor atom ligands, the loss of the intact neutral da18C6 ligand was observed, further suggesting binding alkali metal cations with macrocycle is based primarily on electrostatic interactions. The BDEs decrease monotonically as the size of the alkali metal cation increases, whereas solution phase trends follow the order of $K^+ > Na^+ > Rb^+ > Cs^+$ as a result of competitive binding between the macrocycle and solvent. Preferential binding of $Na^+$ to ha18C6 over da18C6 and 18C6 was observed, whereas the larger alkali metal cations exhibited a small preference for da18C6 and 18C6 versus ha18C6. Lastly, in **Chapter 7**, the alkali metal - hexathia-18-crown-6 (ht18C6) BDEs were determined. Trends based primarily on electrostatic interactions were observed for the measured and theoretically calculated $M^+$-ht18C6 BDEs. The BDEs decrease monotonically as the size of the alkali metal cation increased as observed for ta18C6, ha18C6, and da18C6. When compared to the analogous 18C6 and ha18C6, preferential binding of the alkali metal cations to 18C6 and ha18C6 over ht18C6 was observed.

In summary, ta12C4 and 12C4 adopt similar ground-state conformations whereas different ground-state conformations are observed for the 6 donor atom ligands ha18C6, da18C6, ht18C6 as compared to 18C6. The def2-TZVPPD basis set produced consistent trends across the series investigated and compares well to the experimentally determined BDEs. For the comparison of the aza-macrocycles ta12C4 and ha18C6, the 6 donor atom ligand bind more strongly in all cases as compared to the 4 donor atom ligand. Similar behavior was observed for the analogous 12C4 and 18C6 ligands. The gas phase trend suggests that binding is determined by electrostatic interactions indicating the charge density of the cation is the major feature controlling binding. The gas phase trend also suggests that N donor atoms are more selective for hard metal cations, whereas O donor atoms are slightly more selective for softer metal cations, and S donor atoms bind the alkali metal cation the weakest.

Gas-phase binding energies can highlight the role solvent in the alkali metal cations interactions with the macrocycles investigated here. Previously Armentrout et al. [1] investigated the aqueous selectivity by considering the competition between the solvation of alkali metal cations and the complexation by 18C6 considering the total bond dissociation of $M^+(H2O)_x$ for $M^+ = Na^+$, $K^+$, $Rb^+$, and $Cs^+$, and the enthalpy for **Reaction 8.1**.

$$M^+(H_2O)_x + 18C6 \rightarrow M^+(18C6) + xH_2O \qquad (8.1)$$

Glendening et al. [2] used a similar analysis, but with only theoretical data. In both cases, the authors concluded the aqueous selectivity of 18C6 for the alkali metal cation can be reproduced when x = 5-6 water molecules. In this method, the extent to which $M^+(L)$

complex is solvated is not considered. In a similar approach, the competition the solvation of alkali metal cations and the complexation by da18C6 considering the total bond dissociation of $M^+(H2O)_x$ for $M^+ = Na^+$, $K^+$, $Rb^+$, and $Cs^+$, and the enthalpy for **Reaction 8.2**

$$M^+(H_2O)_x + da18C6 \rightarrow M^+(da18C6) + xH_2O \tag{8.2}$$

**Table 8.1** list the total gas-phase bond energies of $M^+(H2O)_x$ for $M = Na^+$, $K^+$, $Rb^+$, and $Cs^+$ for $x = 1 – 6$ [3], and the reaction enthalpy for **Reaction 8.2**. For $x = 1–3$, the reaction enthalpy parallels the gas-phase selectivity of da18C6 of $Na^+ > K^+ > Rb^+ > Cs^+$. For $x = 4$, the selectivity for $Na^+$ and $K^+$ are similar, whereas the solution phase behavior is observed for $x = 5 – 6$, $K^+ > Na^+ > Rb^+ > Cs^+$. A similar analysis is preformed for the ha18C6 by considering the total bond dissociation of $M^+(ACN)_x$ for $M^+ = Na^+$, $K^+$, $Rb^+$, and $Cs^+$ and ACN = acetonitrile, and the enthalpy for **Reaction 8.3**

$$M^+(ACN)_x + ha18C6 \rightarrow M^+(ha18C6) + xACN \tag{8.3}$$

**Table 8.2** list the total gas-phase bond energies of $M^+(ACN)_x$ for $M = Na^+$, $K^+$, $Rb^+$, and $Cs^+$ for $x = 1 – 6$ [4,5]. For $x = 1–3$, the reaction enthalpy parallels the gas-phase selectivity of ha18C6 of $Na^+ > K^+ > Rb^+ > Cs^+$. For $x = 4–6$, the reaction enthalpy changes from the gas-phase selectivity of ha18C6 to $Na^+ > Rb^+ > K^+ > Cs^+$. For ta12C4, considering the total bond dissociation of $M^+(ACN)_x$ for $M^+ = Na^+$, $K^+$, $Rb^+$, and $Cs^+$ and ACN = acetonitrile, and the enthalpy for **Reaction 8.4**

$$M^+(ACN)_x + ta12C4 \rightarrow M^+(ta12C4) + xACN \tag{8.4}$$

**Table 8.3** list the total gas-phase bond energies of $M^+(ACN)_x$ for M = $Na^+$, $K^+$, $Rb^+$, and $Cs^+$ for x = 1 – 6 [4,5]. For x = 1–2, the reaction enthalpy parallels the gas-phase selectivity of ta12C4 of $Na^+ > K^+ > Rb^+ > Cs^+$. For x = 3–6, the reaction enthalpy changes from the gas-phase selectivity of ta12C4 to $Na^+ > Cs^+ > Rb^+ > K^+$. For interactions in water, **Reaction 8.2** does well at reproducing the gas-phase and solution phase trend, whereas for interactions in acetonitrile **Reactions 8.2–8.3** does not preform well.

## 8.2. Future Work

The primary aims of the studies preformed in this thesis were to apply quantitative collision-induced dissociation (TCID) methods and electronic structure calculations to understand noncovalent interactions that occur in alkali metal cation ligand macrocyclic complexes. To date, accurate thermodynamic information on the O, N, and S 6 donor atom macrocycles, as well as information for the O and N four donor atom ligands have been investigated. Future experiments would involve extending the studies to the sulfur analogue of 12-crown-4. In addition studies involving mix donor atoms ligand in alkali metal cations can be examined in future studies.

Studying the binding interactions of alkali metal – ligand complexes in solvent and comparing to the gas-phase data will help elucidate the effects of solvent on the binding in these complexes. **In Chapter 5**, initial calculations were preformed on limited test set for the $M^+$(ha18N6) using the polarization continuum model (PCM) for water and acetonitrile. Future calculations will involved using PCM for water, methanol, and acetonitrile for all calculations presented here.

## 8.3. References

[1] M.B. More, D. Ray, P.B. Armentrout, J. Am. Chem. Soc. 121 (1999) 417.

[2] E.D.,Glendening, D. Feller, M.A., Thompson, J. Am. Chem. Soc. 116 (1994) 10657.

[3] I. Dzidic, P. Kebarle, J. Phys. Chem. 74 (1970) 1466.

[4] A.B. Valina, R. Aumungama, H. Huang, M.T. Rodgers, J. Phys. Chem. A 105 (2001) 11057.

[5] W.R. Davidson, P, Kebarle, J. Am. Chem. Soc. 98 (1976) 6125.

**Table 8.1**. Total Bond Dissociation of $M^+(H_2O)_x$ for M = Na, K, Rb, and Cs and the Enthalpy for the reaction $M^+(H_2O)_x + da18C6 \rightarrow M^+(da18C6) + xH_2O$.

| x | $Na^+(H_2O)_x$ | $\Delta H(Na^+)$ | $K^+(H_2O)_x$ | $\Delta H(K^+)$ | $Rb^+(H_2O)_x$ | $\Delta H(Rb^+)$ | $Cs^+(H_2O)_x$ | $\Delta H(Cs^+)$ |
|---|---|---|---|---|---|---|---|---|
| 0 | 0 | 292.2 | 0 | 232.1 | 0 | 193.2 | 0 | 161.5 |
| 1 | -100 | 192.2 | -75 | 157.1 | -66 | 127.2 | -57 | 104.5 |
| 2 | -183 | 109.2 | -142 | 90.1 | -123 | 70.2 | -110 | 51.5 |
| 3 | -249 | 43.2 | -197 | 35.1 | -174 | 19.2 | -156 | 5.5 |
| 4 | -307 | -14.8 | -247 | -14.9 | -221 | -27.8 | -201 | -39.5 |
| 5 | -359 | -66.8 | -292 | -59.9 | -265 | -71.8 | -242 | -80.5 |
| 6 | -403 | -110.8 | -333 | -100.9 | -306 | -112.8 | -281 | -119.5 |

**Table 8.2.** Total Bond Dissociation of $M^+(ACN)_x$ for M = Na, K, Rb, and Cs and the Enthalpy for the reaction $M^+(ACN)_x + ha18C6 \rightarrow M^+(ha18C6) + xACN$.

| x | $Na^+(H_2O)_x$ | $\Delta H(Na^+)$ | $K^+(H_2O)_x$ | $\Delta H(K^+)$ | $Rb^+(H_2O)_x$ | $\Delta H(Rb^+)$ | $Cs^+(H_2O)_x$ | $\Delta H(Cs^+)$ |
|---|---|---|---|---|---|---|---|---|
| 0 | 0 | 330.2 | 0 | 223.3 | 0 | 187.2 | 0 | 149.5 |
| 1 | -109 | 221.2 | -102 | 121.3 | -87 | 100.2 | -80 | 69.5 |
| 2 | -211 | 119.2 | -188 | 35.3 | -161 | 26.2 | -150 | -0.5 |
| 3 | -297 | 33.2 | -264 | -40.7 | -227 | -39.8 | -210 | -60.5 |
| 4 | -359 | -28.8 | -321 | -97.7 | -279 | -91.8 | -261 | -111.5 |
| 5 | -412 | -81.8 | -369 | -145.7 | -325 | -137.8 | -307 | -157.5 |
| 6 | -452 | -121.8 | -409 | -185.7 | -364 | -176.8 | -346 | -196.5 |

**Table 8.3.** Total Bond Dissociation of $M^+(ACN)_x$ for M = Na, K, Rb, and Cs and the Enthalpy for the reaction $M^+(ACN)_x + ta12C4 \rightarrow M^+(ta12C4) + xACN$.

| x | $Na^+(H_2O)_x$ | $\Delta H(Na^+)$ | $K^+(H_2O)_x$ | $\Delta H(K^+)$ | $Rb^+(H_2O)_x$ | $\Delta H(Rb^+)$ | $Cs^+(H_2O)_x$ | $\Delta H(Cs^+)$ |
|---|---|---|---|---|---|---|---|---|
| 0 | 0 | 285.1 | 0 | 178.3 | 0 | 149 | 0 | 133.1 |
| 1 | -109 | 176.1 | -102 | 76.3 | -87 | 62 | -80 | 53.1 |
| 2 | -211 | 74.1 | -188 | -9.7 | -161 | -12 | -150 | -16.9 |
| 3 | -297 | -11.9 | -264 | -85.7 | -227 | -78 | -210 | -76.9 |
| 4 | -359 | -73.9 | -321 | -142.7 | -279 | -130 | -261 | -127.9 |
| 5 | -412 | -126.9 | -369 | -190.7 | -325 | -176 | -307 | -173.9 |
| 6 | -452 | -166.9 | -409 | -230.7 | -364 | -215 | -346 | -212.9 |

# ABSTRACT

# NONOCOVALENT INETEACTIONS BETWEEN ALAKI METAL CATIONS AND AZA/THIA-CROWN ETHERS: MASS SPECTROMETRIC DISSOCAITAION TECNIQUES AND THEORETICAL STUDEIES

by

**CALVIN A. AUSTIN**

**August 2015**

**Advisor:** Dr. Matthew J. Allen

**Major:** Chemistry (Analytical)

**Degree:** Doctor of Philosophy

Macrocyclic complexes have been useful in understanding many systems encountered in biology, along with having widespread use in analytical, pharmaceutical, and synthetic chemistry. My goal was to provide a quantitative experimental and theoretical description of cation-aza-crown and thia-crown ether interactions with alkali metal cations. Infrared multiple photon dissociation (IRMPD) action spectroscopy and energy-resolved collision-induced dissociation (CID) techniques were used in conjunction with theoretical electronic structure calculations to characterize the structures, binding interactions, and stability of cation-aza-crown ether interactions. Quantum chemical calculations at several levels of theory were employed to characterize the structures and stabilities of the isolated cations and aza-crown and thia-crown ethers, as well as noncovalently bound complexes comprised of these species. Quantum chemical calculations were also used to generate linear IR spectra and provide theoretical bond dissociation energy (BDEs) for comparison to IRMPD action spectra and experimentally determined BDEs, respectively. Guided ion beam tandem mass spectrometry techniques were used to characterize the energy dependence of the collision-induced dissociation behavior of these cation-aza-crown ether complexes. The photodissociation experiments were carried out in a 4.7 T Fourier transform ion cyclotron resonance mass spectrometer (FT-ICR MS) coupled to a wavelength tunable free electron laser (FEL). The gas phase trend suggests that binding is determined by electrostatic interactions indicating the charge density of the cation is the major feature controlling

binding for the alkali metal cations complex macrocyclic ligand. The gas phase trend also suggests that N donor atoms are more selective for hard metal cations, whereas O donor atoms are slightly more selective for softer metal cations, and S donor atoms bind the alkali metal cation the weakest. Results here suggests that the nitrogen donor atoms macrocycles can selectivity and strongly bind the alkali metal cations in the proper environment similar to oxygen donor atoms macrocycles.

# AUTOBIOGRAPHICAL STATEMENT

## Calvin A. Austin

### Education

**Ph.D. Analytical Chemistry** May 2015

Wayne State University, Detroit, MI

Doctorate Research Advisor: Professor Mary T. Rodgers

**M. Sc. in Chemistry** August 2008

Youngstown State University, Youngstown, OH

Master Research Advisor(s): Professor Brian D. Leskiw and Professor Peter Norris

**B.Sc. in Applied Science (Chemistry Minor)** August 2006

Youngstown State University, Youngstown, OH

Undergraduate Research Advisor(s): Dr. Chet Cooper and Dr. Peter Norris

### Awards

(1) YSU Quest 2008 Dean's Award, Youngstown State University, 2008

(2) Department Citation for Excellence in Teaching Service in Chemistry, Wayne State University, 2009

(3) GRC Travel Fellowship to attend the 2011 Gordon Research Conference on Gaseous Ions: Structure, Energetics, and Reactions, Galveston, TX, February 27 – March 4, 2011

(4) A. Paul and Carol C. Schaap Endowed Distinguished Graduate Student Fellowship 2012-2013

(5) Wayne State University Graduate School Summer Dissertation Fellowship Summer 2013

(6) David F. Boltz Graduate Award in Analytical Chemistry 2013

(7) The Emory University Laney Graduate School STEM Research and Career Symposium Diversity Travel Award 2014